SAND76-5547
Unlimited Release

Transactions

Conference on Fuel and Clad Motion Diagnostics in LMFBR Safety Test Facilities

November 11-12, 1975

Sandia Laboratories

Issued by Sandia Laboratories, operated for the United States Energy Research & Development Administration by Sandia Corporation.

NOTICE

SF 1004-DF (3-75)

Printed in the United States of America

Available from
National Technical Information Service
U. S. Department of Commerce
5285 Port Royal Road
Springfield, Virginia 22151
Price: Printed Copy $11.75; Microfiche $2.25

Add $2.50 per copy for foreign price.

Form ERDA 427
(2/75)
ERDAM 3201

U.S. ENERGY RESEARCH & DEVELOPMENT ADMINISTRATION

MAJOR CONTRACTOR'S RECOMMENDATION FOR DISPOSITION OF SCIENTIFIC AND TECHNICAL DOCUMENT

*See Instructions on Reverse

1. ERDA Report No.
SAND76-5547

2. Subject Category No.

3. Title
Transactions - Conference on Fuel and Clad Motion Diagnostics in LMFBR Safety Test Facilities

4. Type of Document ("X" one)

- [x] a. Scientific and Technical Report
- [ ] b. Conference paper:
  - Title of conference
  - Date of conference
  - Exact location of conference
- [ ] c. Other *(Specify, Thesis, Translation, etc.)**

5. Copies Transmitted ("X" one or more)

- [ ] a. Copies being transmitted for standard distribution by ERDA-TIC.
- [ ] b. Copies being transmitted for special distribution per attached complete address list.*
- [x] c. Two completely legible, reproducible copies being transmitted to ERDA-TIC.

6. Recommended Distribution ("X" one)

- [x] a. Normal handling (after Patent clearance): no restraints on distribution except as may be required by the security classification.
- [ ] b. Make available only to U.S. Government agencies and their contractors.
- [ ] c. Make available only within ERDA and to ERDA contractors.
- [ ] d. Make available only within ERDA.
- [ ] e. Make available only to those listed in item 12 below.
- [ ] f. Other *(Specify)**

7. Recommended Announcement ("X" one)

- [x] a. Normal procedure may be followed.*
- [ ] b. Recommend following announcement limitations:

8. Reason for Restrictions Recommended in 6 or 7 above.

- [ ] a. Preliminary information.
- [ ] b. Prepared primarily for internal use.
- [ ] c. Other *(Explain)*

9. Patent Clearance ("X" one)

- [x] a. ERDA patent clearance has been granted by responsible ERDA patent group.
- [ ] b. Document has been sent to responsible ERDA patent group for clearance.

10. National Security Information *(For classified document only; "X" one)*

- [ ] a. Document does contain national security information other than restricted data.
- [ ] b. Document does not contain national security information other than restricted data.

11. Copy Reproduction and Distribution

a. Total number of copies reproduced 244

b. Number of copies distributed outside originating organization 96

12. Additional Information or Remarks *(Continue on separate sheet, if necessary)*

13. Submitted by *(Name and Position) (Please print or type)**
W. L. Garner - Supervisor

14. Organization
Sandia Laboratories

15. Signature

16. Date October 25, 1976 jz

September 1, 1976

MEMORANDUM OF RECORD

Subject: Review and Approval of SAND76-5547, Transactions of the Conference on Fuel and Clad Motion Diagnostics in LMFBR Safety Test Facilities

Reviews and approvals for papers written by Sandia Laboratories authors and included in the subject report were secured individually under the following numbers:

SAND75-6066	Biggs/Renken
SAND76-5834	Dolce
SAND76-5835	Halbleib
SAND76-5833	Posey
SAND76-5832	McArthur/Kelly
SAND76-5831	Kelly/McArthur
SAND76-5830	Hessel/Stalker
SAND75-6081	Cooper/Kurowski/McKenzie
SAND75-6067	Dupree
SAND76-5829	Edwards

In total these approvals comprise approvals necessary for unlimited release of the subject report.

W. L. Garner - 3151

WLG:3151:jz

Copy to:
3151 R. S. Gillespie

SAND76-5547
Unlimited Release
Printed October 1976

TRANSACTIONS
CONFERENCE ON FUEL AND CLAD MOTION DIAGNOSTICS IN LMFBR SAFETY TEST FACILITIES

November 11-12, 1975
Sandia Laboratories
Albuquerque, New Mexico 87115

Co-Sponsored by

U.S. Nuclear Regulatory Commission
U.S. Energy Research and Development Administration
Sandia Laboratories

CONTENTS

CONTENTS (Cont)

Introduction

On November 11 and 12, 1975, a conference on Reactor Fuel and Clad Motion Diagnostics was held in Albuquerque, New Mexico. The meeting was sponsored by the U. S. Nuclear Regulatory Commission (NRC) and the U. S. Energy Research and Development Administration (ERDA), and was hosted by Sandia Laboratories. The purpose of the conference was to exchange technical information on needs, capabilities, and current research in the field of fuel and clad motion diagnostics for LMFBR safety test facilities.

The conference was attended by representatives from virtually every major U. S. laboratory working in the LMFBR field, as well as from private industry and universities. In addition, representatives were present from France, Germany, the United Kingdom, and Japan.

Twenty-six papers were presented on subjects ranging from experimental needs to specific devices. From the "needs" papers it is clear that substantial improvements will have to be made in the diagnostics to provide the required data for future LMFBR safety tests.

For the past ten years the fast neutron hodoscope has been the only device available for use in fast reactor safety studies. It is currently being improved. Some new technologies developed for the medical, weapons, and space programs are now being applied to the material motion detection problem. They have the potential for providing improved resolution and in some cases three dimensional imaging. However, their capabilities must be proven in reactor environments under test conditions. Both NRC and ERDA are currently funding development programs in these areas.

Although the meeting addressed needs and capabilities for safety test facilities in general, a large vein of interest in the proposed SAfety

Research Experiment Facility (SAREF) permeated the meeting.* This was reflected in Dave Rose's paper on the SAREF assessment (Section VI) and in Charlie Kelber's and Bill Hannum's comments (Sections II and III) which concluded the meeting. It was evident at the end of the meeting that as work on SAREF and other facilities progresses there will probably be a need for additional information exchanges on this subject.

In conclusion I want to thank Bob Wright of the NRC for his help with the technical program and Wilma Salisbury, Don Hosterman, Hank Willis and Ann McFarland for their help with the many details of the meeting.

J. E. Powell
Program Chairman

*At the time of this meeting, November 1975, the term SAREF was used to denote a planned single large LMFBR safety test facility. The term was so used at this meeting and in these transactions. By July, 1976 the term SAREF was used to denote a program for the construction of several test and support facilities to be used for LMFBR safety research in the U.S.

Comments

C. N. Kelber
U. S. Nuclear Regulatory Commission

As we came to this meeting, two facts were evident:

1. Fuel motion detection yielding high quality data is vital to confirmation of FBR safety analyses.
2. Incorporation of fuel motion detection capability into safety test facilities makes a profound impact on facility design and function.

These considerations furnish the impetus for this work and the information exchange.

Coming away from the meeting I carried these additional thoughts:

3. There is no universal solvent:
   - coded apertures are good for 3-D viewing over small to intermediate volumes, at high intensities;
   - the technical basis for improving the fast neutron hodoscope exists, but an analytical prediction of its ultimate capability is in dispute;
   - linear electron accelerators have good potential at low intensities, but are limited by build-up considerations;
   - totally contained ("in-core") detection remains an outside possibility worthy of further investigation: it may be most useful for large proof tests where the motion is expected to be well characterized;
   - the provision of two slots to provide 3-D capability is probably insufficient in large tests.
4. There exists a solid analytic and experimental foundation for further development. Well before the construction is completed of

major new facilities it should be possible to specify the modes of fuel motion detection.

Finally, I wish to complement Sandia and Jim Powell for such fine assistance in carrying out the fuel motion detection meeting. The meeting was successful because of these efforts.

Comments

W. H. Hannum
U. S. Energy Research and Development Administration

The current subject of fuel and clad motion diagnostics is a very timely topic. We appreciate the opportunity to participate in this meeting. We would like to approach this topic not as a reactor problem but as an experimental technique problem.

In fact, there are two different problems we are addressing with the subject techniques. The first is basically differential; that is, we need to understand the basic mechanisms that would be associated with loss of fuel integrity. This requires that we observe detailed and differential (in space) motions. The second problem is that, should there be a gross core failure, there could be fuel motion. Since the subsequent course of events is strongly influenced by reactivity changes, and these in turn could be controlled by fuel and clad motions, we need to "observe" gross fuel and clad motions as might characterize such situations. Specifically, there is good reason to believe that all gross fuel motions following gross failure would be dispersive rather than compactive. It would be useful to be able to observe such gross motions differentially in time. Both of these "observations" would be in the presence of very high background.

As we begin, it would appear that there is a need for invention here. Timing is also important, in that we are actively considering a new facility (SAREF) and we need to know what is available.

Among other things, I will be listening for the following factors in the various approaches being discussed:

Availability
Technical feasibility
Sensitivity to background
Density, time, space resolution
R&D required & probability of success
Cost
Facility implications

The following represents a personal summary of lessons learned at the Sandia Conference on Fuel and Clad Motion Diagnostics in LMFBR Safety Test Facilities, November 11-12, 1975.

I divide the fuel and clad motion problem into three basic areas; that of sources; means of information extraction and transmission; and information recording.

Sources

As for sources, one can use internal radiation sources or external sources. For internal sources, optical monitoring is, of course, not feasible for LMFBR tests. This leaves in practice only gammas and neutrons. For clad motion, effectively gammas are the only potential source. It is in principle possible to use external gammas (x-rays) to radiograph test elements during the test, but very high power x-ray sources would be required for this. It is judged that very substantial development effort would be required to develop multiple pulsing capability in the very large accelerators in order to produce satisfactory sources for this. There are several approaches for the smaller tests. A linear electronic accelerator might be feasible and is reasonably well developed. Concepts costing in the $1M to $10M range might be available to provide such a source. For the larger tests, the much larger machines corresponding to Sandia's HERMES, or LASL's PHERMEX machine, either being upgraded to multiple pulse capability, would be required. This, in my judgment, is not feasible for SAREF. This judgment is colored somewhat with the fact that the internal sources appear to be generally adequate for the sort of information which is required.

The major question is that of sensitivity. The required fuel motions appear to be the order of 1% density change. This is discussed a bit further below, under the topic of Information Recording.

Information Extraction

As for information extraction, this is somewhat different and apparently aligns reasonably directly as to whether one is speaking of neutrons

or gammas as the source. For neutrons, the concept of the hodoscope or something very similar appears to be the only feasible technique. This combines collimation and high discrimination bandpass so as to observe neutrons in the presence of extremely high gamma background. Developments at Argonne under de Volpe, which are also now being tried by the French for CABRI, give good evidence of the feasibility of this approach.

If gamma rays are used as the source, there are two alternate approaches that are, in principle, available here. One is the matter of collimation and the other is that of coded apertures. The apertures, in principle, appear feasible for gammas, giving the substantially increased information at little increased cost. The only counterforce here is that of energy discrimination. With current approaches and techniques, it does not appear straightforward to apply energy discrimination to a coded aperture type recording. The information density requires essentially continuous recording and continuous recorders are not well suited to energy discrimination. The significance of energy discrimination is that the gamma source from a steel clad is much higher in average energy than that from the fuel. Thus, with energy discrimination, it may well be feasible to observe and differentiate between clad motion and fuel motion.

The basic developments required here are the reduction to practice of a coded image gamma type device. This is being pursued as part of the RSR Sandia program for ACPR. If it is demonstrable on that scale, it should be fairly readily adaptable to existing and proposed devices having external beam capability.

The only supplemental work that appears to be appropriate for consideration would be to try to combine energy discrimination with coded aperture recording. This can probably wait until a proof-of-principle demonstration is accomplished at ACPR.

Recording

For information recording, again the hodoscope and the gamma are quite separate in terms of the available techniques. For the hodoscope,

these are two techniques normally used. One is a Hornack button and the other is fission counters. These appear to be generally satisfactory for the application. It was suggested at this meeting that dielectric recording might be capable of higher sensitivity and better precision than either the counters or the Hornack buttons. This would be a low cost development and adaption of the hodoscope. Current experimental evidence indicates 2% density discrimination from a hodoscope which is close to the required 1%, but this is viewed by some with a bit of skepticism. Gamma detectors with the collimator type device, where one uses a fairly gross mesh recording, can be done with counters so as to apply an energy pulse height discrimination. In using the coded image type apertures, essentially continuous spatial recording is required. To date, all work on this has used a converter of gammas to optical light, and then normal optical imaging and recording on films, orthicons, etc.

The counter type recording has a fairly high sensitivity, whereas the optical recording techniques to date have been demonstrated to no better than 5% density discrimination. This may be a problem in trying to gain substantially improved sensitivity.

Internal Fuel Motion Monitors

Internal counters for fuel motion monitoring would perform both the extraction and recording functions, and with dramatically reduced configuration demands. There are three approaches that were discussed. One is a fission counter of some sort which has spatial discrimination, such as Compton diode. The response of this system, based on preliminary experiments at ANL, is very poorly understood leading to substantial uncertainty as to the development potential of this instrument. The second type is a diamond detector, which apparently has the sensitivity and background capability, but again will require significant development so as to be at a usable point. The third approach is that of using a fission couple. This requires rather complex unfolding, in order to have any time resolution at all.

Sandia estimates that the development of a usable fission couple device would require 4 to 5 years, and a diamond detector type scheme much longer than that. The ANL work on this is substantially further along (Applied Physics Division) and is focusing primarily on the Compton diode.

Summary

In an overall sense, we can conclude that the neutron hodoscope as a complete system is clearly feasible. For smaller tests, it should have the appropriate sensitivity. There is some lingering doubt as to whether the sensitivity and background discrimination will be adequate but indications are favorable. The cost, except for the facility application, of having to have a large slot (or probably several slots) does not appear prohibitive and the continuing R&D costs appear again reasonable. The major difficulties or shortcomings with this system are some limitation in resolution. For larger tests, there remain substantial questions as to sensitivity, and no indication of any capability for clad motion diagnostics.

As for external devices based on gamma rays, the coding imaging approach appears quite promising, but is not yet an established capability. The potential will be demonstrated in the RSR ACPR program. The sensitivity appears to be significantly less than that required. At this point, there is in principle the capability of differentiating between clad and fuel motion, but that will require considerable further development.

External gamma devices based on the collimator type principle are quite clearly feasible and should be able to distinguish fairly readily between clad and fuel motion but will be significantly limited in sensitivity and resolution.

I see no basis for pursuing solely for our own purposes the development of external sources for x-raying in situ during tests. These developments may be accomplished on other (weapons) programs. There are also questions as to cost scale for test reactor applications.

The attractiveness of internal counters in terms of their reduced impact on facility must be pursued. All three of the approaches proposed at this point are at a preliminary stage and little confidence of final success is assured. The development costs at this point also are quite modest.

A few minor miscellaneous points based on the meeting. With an external beam capability, the feasibility of in situ radiography appears to be, in principle, straightforward. The direct use of Godiva type thermal expansions in existing pulse reactors represents a readily available test bed for fuel motion monitors.

A rather wild idea, but one which appears at least worthy of further discussion (from Albrecht from the University of Washington) is the concept of coding fuel tests with recoverable microsphere tracers; for example, small tungsten spheres containing fuel which could be tagged and recovered, giving a traceability of fuel motion in large disruptive tests.

All in all, the meeting was quite beneficial and, in my judgment, a large number of people, including myself, developed a significantly better comprehension of the state of the art relative to fuel and clad motion diagnostic techniques.

Experiment Needs and Measurement Requirements*

by

J. F. Marchaterre

Reactor Analysis and Safety Division
Argonne National Laboratory
9700 South Cass Avenue
Argonne, Illinois 60439

My discussion of experiment needs and measurement requirements focuses on in-pile testing needs associated with core-disruptive accidents or potential initiators of core-disruptive accidents. This is true by definition since if we are interested in measuring fuel motion we are studying core-disruptive phenomena or a potential initiator of core disruption. It should be kept in mind, however, that fast reactor safety includes much more than the study of core-disruptive phenomena and that the solution to fast reactor safety problems requires more than in-pile tests. A complete discussion of safety research needs is beyond the scope of this paper, but it should be noted that extensive analysis and out-of-pile testing is also required.

The key safety issues which we have identified are as follows: (Figure 1)

(1) Protection Against and Propagation of Local Faults -- This means that a combination of design features and understanding of phenomena must be shown to preclude single-subassembly faults (i.e., blockages, failure propagation) as whole-core initiators to an acceptably low level of probability.

(2) Establish that there are No Autocatalytic Effects in the Initiating Phase of Accidents -- Our studies of FFTF and CRBR have led to the conclusion that in a reactor with a small or negative sodium void coefficient

* This work supported by the U. S. Energy Research & Development Administration

the most likely course of a whole-core loss-of-flow accident with failure to scram is a gradual core meltdown with no energetic burst.

This same conclusion would be true for a large reactor in which the large positive sodium void coefficient had been designed out. The same conclusion may not be true for a reactor with a large positive sodium void coefficient where combined fuel and coolant motion could lead to large reactivity insertions. Even if the sodium void coefficient is made small or negative we must still establish that there are no combined effects which could lead to large reactivity insertion rates.

It should be noted that the fact that there are some accident paths (i.e., transient overpower accidents with failure to scram) which lead to early termination does not change the conclusion that the important issue is to show that there are no mechanisms for changing a mild initiator to a severe excursion.

(3) Accident Energetics and Recriticality -- If we assume that the answer to (2) above is that a gradual meltdown is the most probable course of an unprotected accident (or the dominate path that must be considered) then the next key issues are to show that no recriticalities can occur and lead to severe excursions and that the large amount of molten fuel involved in a whole-core meltdown cannot interact rapidly with sodium (vapor explosion). It is our current belief that dispersive mechanisms will prevent any energetic recriticalities and that true vapor explosions cannot occur between UO_2 and sodium.

(4) Radiological Consequences and Postaccident Heat Removal -- The central issue, of course, in LMFBR safety is assuring that the radiological consequences of any accident are acceptable. This means assuring that the melted core does not lead to breaching the containment and evaluating the adequacy of the containment or confinement systems following various postulated accidents.

The accident scenarios and experiment needs derived from them must always be considered in terms of these key issues. In determining experiment needs we have considered three scenarios as representative. They

are (1) fuel failure propagation, (2) transient overpower accidents, and (3) loss-of-flow accidents. (Figures 2, 3, and 4)

Fuel Failure Propagation (Figure 5)

The primary objective of studies of fuel failure propagation is to provide reactor designers and reactor operators with the information needed to make the most reasonable design choices to minimize the potential for failure propagation in LMFBRs. For convenience, failure propagation studies can be divided into two areas: pin-to-pin and subassembly-to-subassembly phenomena. Fuel pin failures during normal reactor operation and off-normal transients may occur both randomly and coherently. Pin-to-pin failure propagation studies are concerned with the potential of these failures propagating to make continued operation unsafe, or gross subassembly failure imminent. Subassembly failure propagation studies are concerned with assessing the probability of a gross subassembly failure propagating to adjacent subassembly and ultimately to a whole-core accident.

Current studies have shown that rapid fuel pin failure propagation is unlikely and that longer term effects can be investigated in existing or planned facilities. Current studies are also showing that rapid subassembly-to-subassembly failure propagation from any credible local fault initiator can be demonstrated to be very small, but an evaluation of the consequences is necessary in order to establish:

(a) That if these potential local faults do occur, they can be detected and the reactor shut down in a timely manner.

(b) If these local faults are undetected, the effects can be confined to a single subassembly.

(c) If unprotected subassembly-to-subassembly failure propagation does occur, the inherent shutdown mechanisms (e.g., fuel dispersion) and/or design modifications will limit the event to consequences which are within the "whole-core" accident envelope.

The confinement of malfunctions and their effects to a single subassembly is an important line of assurance for LMFBR safety. If it can be shown that local faults do not propagate beyond the confines of a single subassembly, public safety is not endangered.

The implications for LMFBR design and licensing are:

(1) Establishing what protection systems against local malfunctions are required, e.g., subassembly instrumentation.

(2) Enabling the consequences of the accident to be determined for risk assessment.

Core-Disruptive Accidents

The course of an LMFBR whole-core disruptive accident is, in general, controlled by reactivity effects. In turn, the reactivity history depends on a number of interrelated phenomena and, most importantly, those involving core material displacement. In a large LMFBR, sodium voiding can add sufficient reactivity to lead to a rapid power excursion. A fast reactor also is very sensitive to fuel motion, and compactive motion can also produce an excursion. In situations in which the reactor protective system is assumed not to be effective, some form of dispersive fuel motion (reactor disassembly) is required to provide sufficient negative reactivity to terminate a given accident sequence.

The whole-core accidents usually considered in evaluating the safety of LMFBRs can be classified in two broad categories: (1) transient undercooling (usually loss-of-flow) without scram accidents, and (2) reactivity-insertion (or transient overpower) without scram accidents. These accidents can be further subdivided into an initiating phase and a core-disruptive phase. The accident can either terminate at the end of the initiating phase with a largely intact core, or proceed into complete core disruption either by gradual melting of the whole core or by a severe prompt-critical excursion which directly disassembles the core. An unprotected loss-of-cooling accident can itself lead potentially to the addition of significant amounts of reactivity. However, during the initial stages, important differences exist

between loss-of-cooling and reactivity-insertion accidents. One basic difference lies in the temporal sequence in which the temperatures of the fuel and cladding rise. In the case of a reactivity-insertion accident, it is the fuel temperature that rises first.

Transient Overpower Accidents (Figure 6)

Inasmuch as coolant temperatures rise relatively slowly in a transient overpower accident, considerable fuel melting can occur before sodium voiding and, at some point, fuel-pin failures (cladding ruptures in the core region) can occur. The reactor protection system should be designed to prevent fuel failures for anticipated transients. After fuel-pin failure, rapid sodium expulsion from the coolant channels potentially can be induced because of the ejection of molten fuel and fission-product gas (for irradiated fuel) from the fuel pins. Particularly in large LMFBRs, sodium voiding can lead to rapid reactivity insertions. However, the expulsion of fuel from the reactor core region through sweepout by sodium vapor and liquid or through expansion of the fission gas-fuel mixture, can counteract with negative reactivities and tend to terminate the excursion. If this is not effective, the sodium void reactivity, in combination with the initiating reactivity, possibly can lead to a prompt-critical excursion with a resultant core disassembly due to high fuel vapor pressures. The interplay between the positive and negative reactivity effects is complex and depends on the fuel-pin failure times, locations and modes, and on the magnitudes of the fuel and sodium reactivity worths.

The key problems in the initiating phase of transient overpower accidents that require in-pile testing are:

(1) An understanding of transient fuel performance and fuel failure thresholds to determine operating design margin.

(2) The nature and location of fuel pin failures.

(3) The rate and direction of fuel and coolant movements following fuel pin failure.

(4) The characteristics of extended motion of fuel, including any freezing or plugging and ultimate coolability of the core, if the initiating phase of the accident does not lead directly to a mechanical disassembly.

The implications of these key problems in the design and licensing of LMFBRs are the following:

(1) A knowledge of transient fuel performance and fuel failure thresholds is necessary to set operating limits for LMFBR cores, and thus directly affects reactor performance.

(2) An ability to predict the nature and location of fuel pin failures, the rate and direction of fuel and coolant movements following pin failures are essential to analyze transient overpower accidents. In large reactors with a large sodium void coefficient this may be the bounding accident which sets the structural design basis of the plant.

Loss-of-Flow Accidents (Figure 7)

Whole-core loss-of-flow accidents potentially can be initiated in several ways. However, the initiating event usually considered is that of loss of off-site power with a resultant coastdown of all pumps and with an assumed failure of the protection system. In such a flow coastdown without scram accident, the first substantial temperature increase occurs in the coolant and the cladding. If no protective action is taken, this leads to sodium boiling near the top of the core. After sodium boiling and ejection from an assembly, a thin liquid film remains on the fuel pin, but the film dries quickly. Following this sodium-film dryout, essentially no heat transfer occurs from the fuel. This fuel temperature increases rapidly while simultaneously the temperature distribution within each pin tends to become flat. In the meantime, the cladding melts and can be followed by fuel melting and slumping, which may add significant amounts of reactivity and lead to a prompt-critical excursion, or by fuel dispersal which will rapidly reduce power.

For a small LMFBR, the reactor power may remain fairly low during the voiding phase of a flow-coastdown accident, and, as noted above, fuel

temperatures may increase little until after the cladding melts. However, for larger reactors, the larger positive sodium-void worths can lead to fairly rapid increases in power because of sodium voiding in the hotter assemblies. For the large portion of the core that remains unvoided, the accident appears much like a reactivity-insertion accident, and fuel melting with consequent fuel failures may occur before sodium voiding in the unvoided channels. Again, the interplay of reactivity effects will strongly determine the detailed sequence of events.

The key problems in the initiating phase of a loss-of-flow accident that require in-pile testing are:

(1) The rates of sodium voiding and clad movement in the first assemblies to boil.

(2) The rate and direction of early fuel movements in the first assemblies to melt and specifically whether clad and fission gases can cause early fuel dispersal.

(3) The rate and direction of fuel and coolant movements in unvoided channels.

(4) The nature and extent of any cladding or fuel plugs which would inhibit fuel dispersal.

The implications of these key problems in the design and licensing of LMFBRs are the following:

(1) An ability to predict the consequences of this accident will probably be a necessity for licensing LMFBRs, and may set the structural design basis for the plant.

(2) If a large sodium void coefficient in large LMFBRs causes adverse fuel and coolant movements in the unvoided channels, then core design will be affected (i.e., spoiled geometries).

Transition Phase and Disassembly (Figures 8, 9, and 10)

For both loss-of-flow and transient overpower accidents, the initial motion of core material may result in a neutronic shutdown. If stable cooling of the partially disrupted core can be established at that point,

then the accident would be terminated prior to gross core disruption. If not, the accident will proceed to either a complete and rapid disassembly of the core, if reactivity-insertion magnitudes and rates are high, or to a more gradual meltdown.

In recent years, as the methods used to analyze whole-core disruptive accidents have become more detailed, the initial excursions have been shown to be milder than anticipated. The net result of this is that the accident sequence tends to proceed into a gradual meltdown of the core, instead of ending in an early disassembly excursion. This does not mean that a disassembly excursion cannot be induced at some point in the accident, but merely that it is less likely in the initial phase. This is particularly true for smaller reactors in which sodium voiding reactivity is not dominating.

As the subassemblies successively progress through the stage of coolant voiding and melting, the pressures generated may be too low to cause a massive dispersal of molten fuel from the core region. The subassembly duct walls are quickly melted and growing regions of molten fuel and steel begin to form in the hottest portions of the core. This stage of the accident can be accompanied by a number of mild excursions induced by continued fuel motion in other parts of the core, or possibly by the reentry of fuel that was temporarily dispersed by mild pressurizations. This state of the accident has been termed the "transition phase."

Once an accident has entered the transition phase, it appears likely to proceed into whole-core involvement. Thus, ensuring an end to the neutronics events requires attainment of a subcritical configuration through the permanent dispersal of a large fraction of the core. This dispersal can result either from an energetic excursion ending in a classical disassembly, or from more gradual mechanisms such as boil-out and melt-out. It is currently believed that the most likely termination of a core-disruptive accident of this type is a gradual fuel ejection.

A common point to all fast reactor whole-core accident scenarios in which loss of active shutdown devices is assumed is that irreversible dispersive fuel motion must occur in order to provide permanent neutronic shutdown. Thus, without regard to initiating events, three generalized accident scenarios involving somewhat different fuel dispersion processes can be identified, although these may overlap.

(1) Situations in which small amounts of fuel can be removed permanently through hydraulic forces or mild internal pressurization from fission products, cladding vapor, and/or fuel vapor. Subassembly geometries could be retained and in-place cooling maintained or established under low fission power or decay heat conditions.

(2) Situations similar to (1) above, but in which either permanent fuel removal or in-place cooling are not maintained or established early in the accident sequence and which proceed to the "transition" phase involving a gradual loss of subassembly geometry. Fuel removal and neutronic shutdown would occur either through a series of mild pressurization events or through gradual melt-out and boil-out processes.

(3) Situations in which gross fuel removal occurs due to a general "mechanical" disassembly. In this case, sufficient internal pressurization is implied such that the core is well dispersed. The damage consequences from this type of event can vary significantly depending on whether the pressurization that causes the disassembly is by fuel vapor pressure or gaseous fission products.

During and following the events leading to termination of the accident, the thermal energy generated and stored in core materials can be converted to work energy. Work can come from either the expansion of the core materials or the interaction of these materials with the sodium coolant. Once the energy partition is established, the response of the system can be determined. After the work energy is released and imparted to the system structure and containment, the whole-core disruptive accident enters its final phase involving long-term decay heat removal from the

fuel. The final disposition of core materials and the measures required to assure cooling of the core debris are, of course, dependent on the reactor size and design.

The key problems in the transition phase and disassembly of the core-disruptive whole-core accident which require in-pile tests are:

(1) The nature of extended motion of core materials following a non-energetic meltdown. It is currently believed these are dispersive and would essentially preclude severe secondary criticalities.

(2) In cases where an accident proceeds to disassembly with sodium in the core, the rate of transfer of heat from the fuel to sodium must be established.

(3) Whether fission gases can exert pressures to disassemble the core at low fuel temperatures must be established.

(4) The ultimate coolability and containment of core debris.

The implications for design and licensing of these key problems are the following:

(1) Demonstration of the dispersive nature of a disrupted core which would preclude secondary criticalities would eliminate one of the major accident issues for LMFBRs, allowing the structural design basis for the reactor to be set by considerations of the initiating accident.

(2) If fission gases can exert pressures to disassemble at low core temperatures, accident energetics are correspondingly reduced, thus reducing design requirements for containing the accident.

(3) It is our current belief that heat transfer from fuel to sodium cannot occur on a rapid enough time scale to significantly add to the damage potential from an excursion. Verification of this for sodium in excursions is required.

(4) Ultimate coolability of disrupted core materials must be shown. How this ultimate coolability is achieved will vary with reactor design but requires at least small-scale demonstration tests.

Fuel Motion Measurement Requirements (Figures 11-17)

Other papers at this conference will address in more detail fuel and clad motion measurement requirements but the following examples illustrate the approach we have used in setting requirements for SAREF. Three accident calculations which were carried out for CRBR were examined to establish the calculated rate of change of fuel density. From these requirements for measuring fuel density changes and time resolution were determined.

The three accidents which were examined were a transient undercooling, transient overpower, and a core disassembly (from ANL/RAS 75-29). Examination of the fuel motion calculated in these accidents indicated that the rate of density change for both the transient undercooling and transient overpower accidents was approximately 0.02 $gm/cm^3/msec$, and that 5 msec would be an acceptable resolution time. The rate of density change for the core disassembly accident was 0.12 $gm/cm^3/msec$ and a time resolution of 0.5 msec would be required.

KEY SAFETY ISSUES

In terms of the need for the measurement of fuel and clad motion, they are focused on phenomena of importance in the analysis of core-disruptive accidents.

Protection against and propagation of local faults.

Possible autocatalytic effects in initiating phase.

Transition phase behavior - recriticality - disassembly.

Figure 1

SEQUENCE OF EVENTS - FUEL FAILURE PROPAGATION

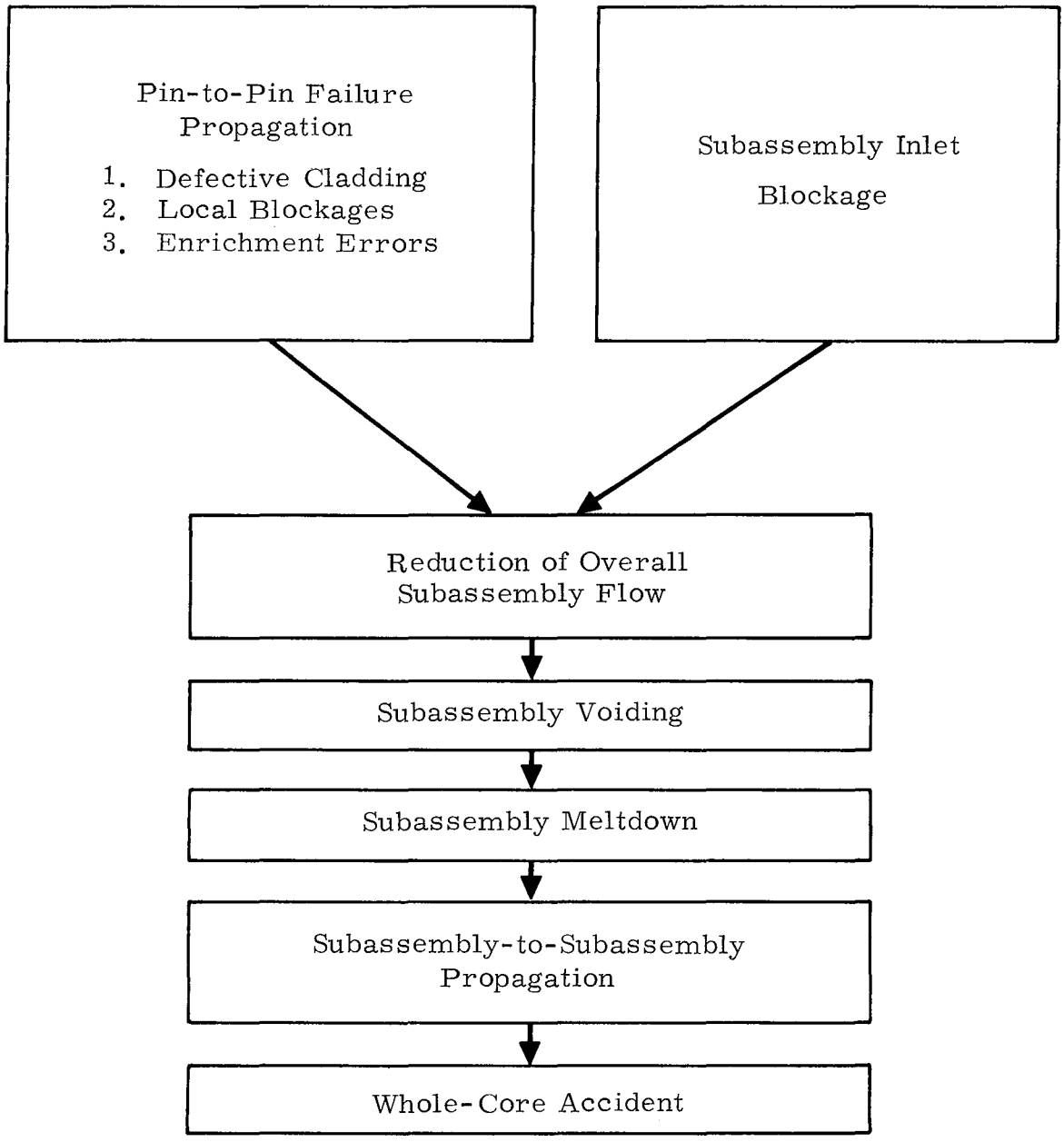

Figure 2

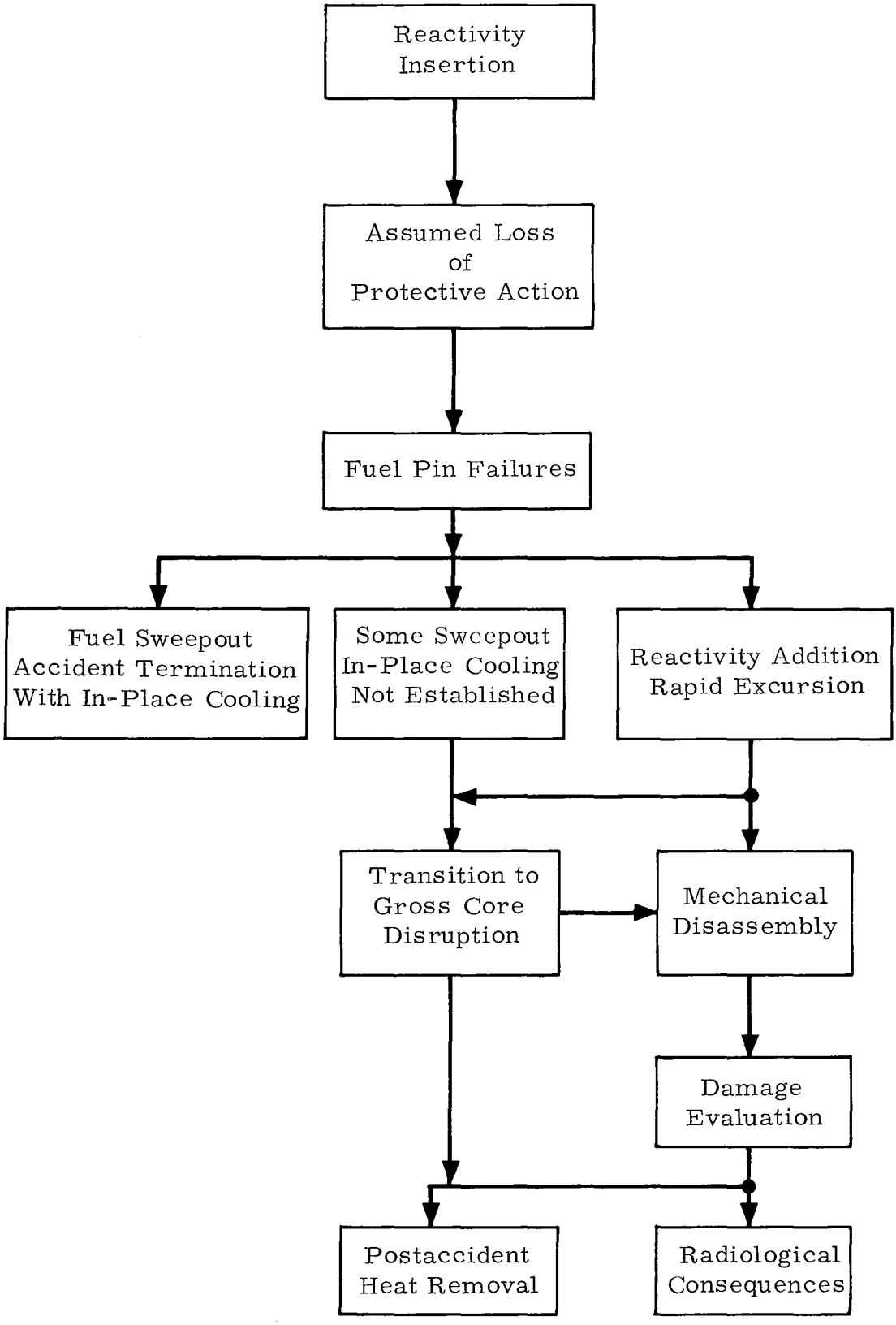
Reactivity Insertion
Assumed Loss of Protective Action
Fuel Pin Failures
Fuel Sweepout Accident Termination With In-Place Cooling
Some Sweepout In-Place Cooling Not Established
Reactivity Addition Rapid Excursion
Transition to Gross Core Disruption
Mechanical Disassembly
Damage Evaluation
Postaccident Heat Removal
Radiological Consequences

Figure 3

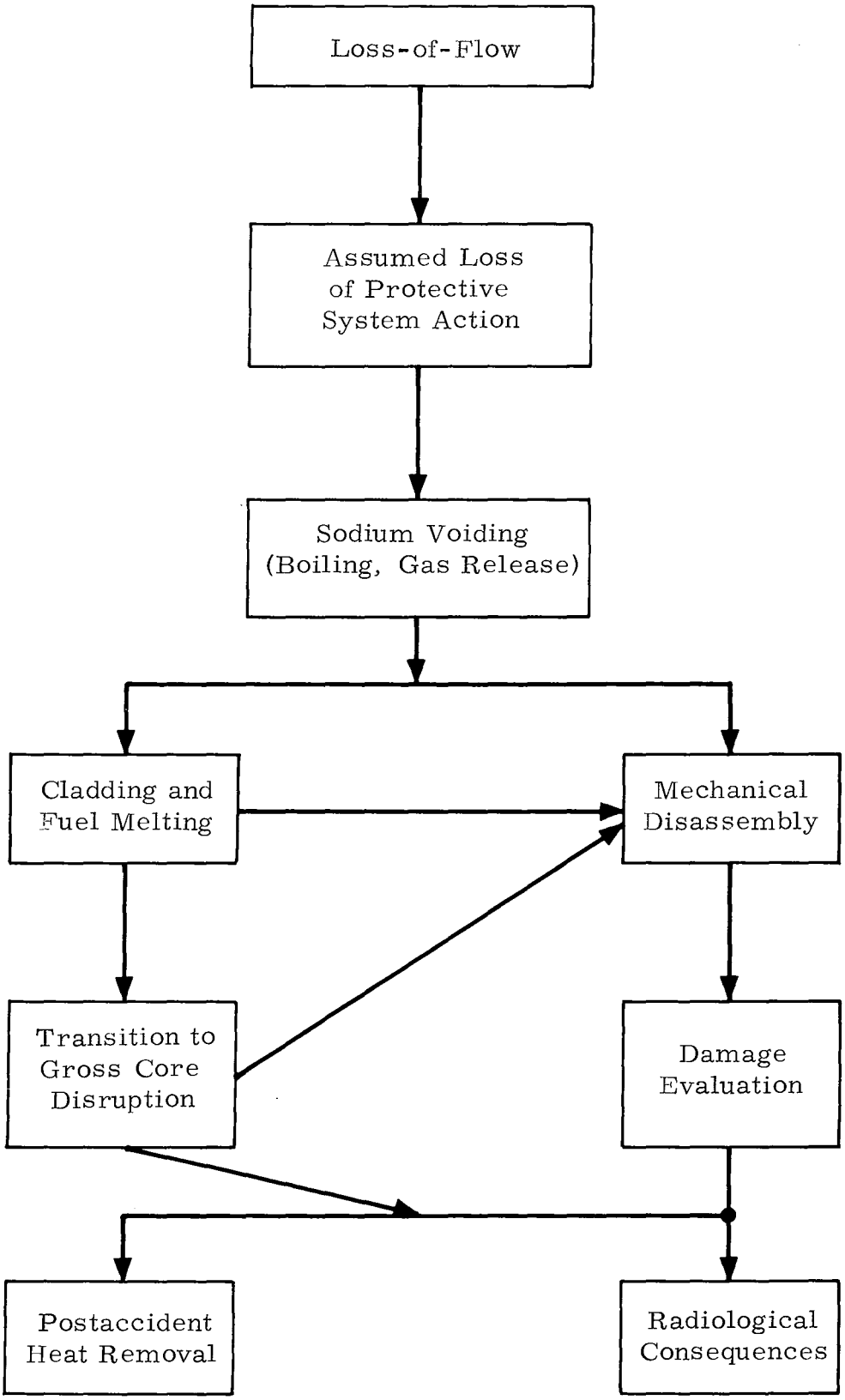
Loss-of-Flow
Assumed Loss of Protective System Action
Sodium Voiding (Boiling, Gas Release)
Cladding and Fuel Melting
Mechanical Disassembly
Transition to Gross Core Disruption
Damage Evaluation
Postaccident Heat Removal
Radiological Consequences

Figure 4

FUEL FAILURE PROPAGATION

Key Issues

(1) Pin-to-pin failure propagation

(2) Effects of meltdown of an LMFBR subassembly

Design Implications

(1) Protection system requirements

(2) Consequences of accident for risk assessment, i.e., is it a whole-core initiator

Fuel and Clad Motion Implications

(1) Clad motion important in blockage formation

(2) Fuel motion may determine heat load on adjacent fuel assemblies

Figure 5

TRANSIENT OVERPOWER ACCIDENTS

Key Issues

(1) Transient fuel performance and fuel failure thresholds

(2) Nature and location of fuel pin failures

(3) Rate and direction of fuel and coolant movements following fuel pin failure

(4) Extended motion of fuel materials

Design Implications

(1) Operating limits

(2) Structural design basis for reactor

(3) Core design

Fuel and Clad Motion Implications

(1) Clad motion probably not important

(2) Fuel motion determines whether early termination is possible

Figure 6

LOSS-OF-FLOW ACCIDENTS

Key Issues

(1) Rates of sodium voiding and clad movement

(2) Rate and direction of early fuel movements

(3) Rate and direction of fuel and coolant movements in unvoided channels

(4) Nature and extent on any cladding or fuel plugs

Design Implications

(1) Structural design basis for reactor

(2) Core design

Fuel and Clad Motion Implications

(1) Clad motion important both because of its role in blockage formation and its reactivity effects

(2) Fuel motion determines course of accident

Figure 7

TRANSITION PHASE AND CORE DISRUPTION

Key Issues

(1) Nature of extended motion of core materials following a nonenergetic meltdown

(2) For sodium in disassembly, the rate of heat transfer from fuel to sodium must be established

(3) Whether fission gases can exert pressures to disassemble the core at low fuel temperatures must be established

(4) The ultimate coolability and containment of core debris must be shown

Figure 8

TRANSITION PHASE AND CORE DISRUPTION

Design Implications

(1) Demonstration of the dispersive nature of a disrupted core which would preclude secondary criticalities would eliminate one of the major accident issues for LMFBRs, allowing the structural design basis for the reactor to be set by considerations of the initiating accident.

(2) If fission gases can exert pressures to disassemble at low core temperatures, accident energetics are correspondingly reduced, thus reducing design requirements for containing the accident.

(3) It is our current belief that heat transfer from fuel to sodium cannot occur on a rapid enough time scale to significantly add to the damage potential from an excursion. Verification of this for sodium in excursions is required.

(4) Ultimate coolability of disrupted core materials must be shown. How this ultimate coolability is achieved will vary with reactor design but require at least small-scale demonstration tests.

Figure 9

FUEL AND CLAD MOTION IMPLICATIONS

(1) Clad motion is of interest but steel is probably dispersed in fuel

(2) Extended motion of core materials determines ultimate dispersal

(3) Small scale, short-time scale fuel motion is of importance in disassembly phenomena

Figure 10

ACCIDENTS CHOSEN TO SET REQUIREMENTS

Transient Undercooling

Transient Overpower

Core Disassembly

Figure 11

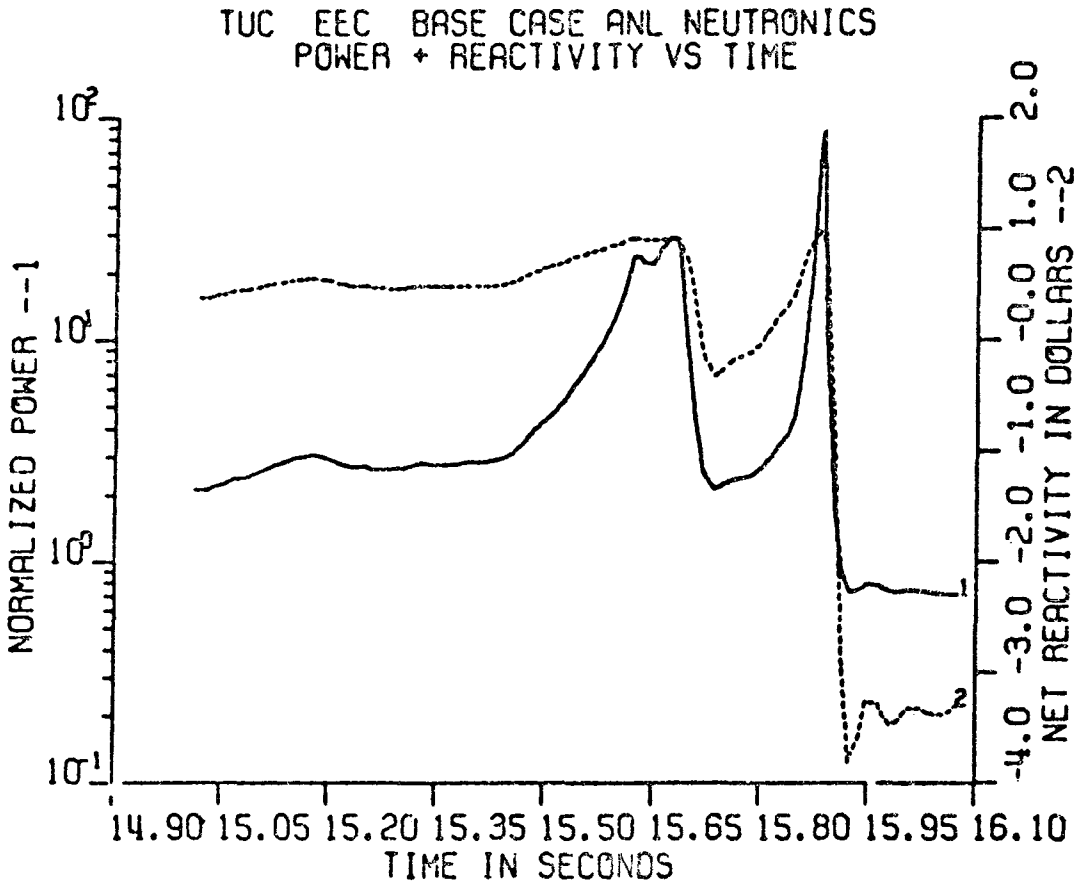
TUC EEC BASE CASE ANL NEUTRONICS
POWER + REACTIVITY VS TIME
NORMALIZED POWER --1
10^2
10^1
10^0
10^{-1}
2.0
1.0
-0.0
-1.0
-2.0
-3.0
-4.0
NET REACTIVITY IN DOLLARS --2
1
2
14.90 15.05 15.20 15.35 15.50 15.65 15.80 15.95 16.10
TIME IN SECONDS

Figure 12

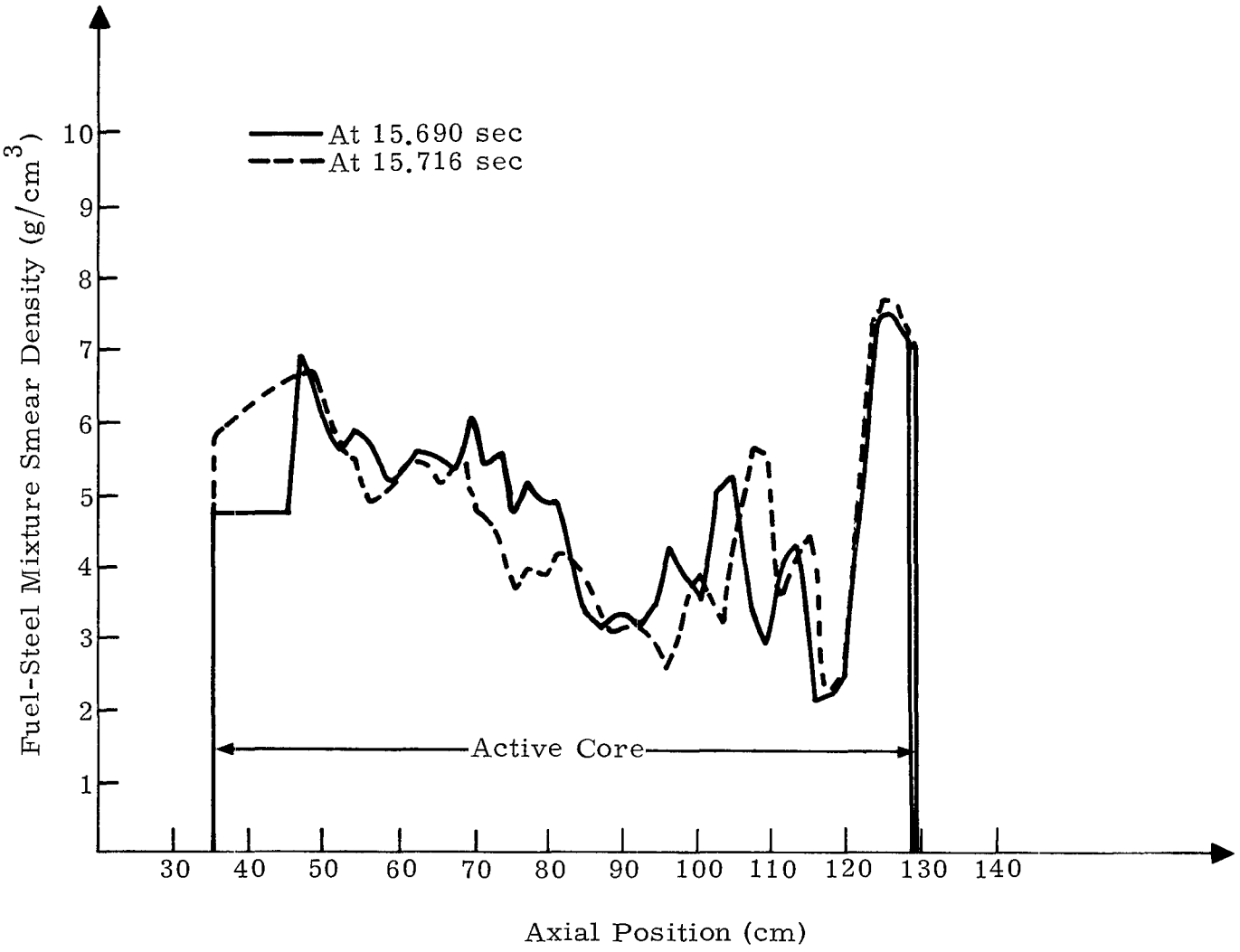
At 15.690 sec
At 15.716 sec
Fuel-Steel Mixture Smear Density (g/cm^3)
10
9
8
7
6
5
4
3
2
1
Active Core
30
40
50
60
70
80
90
100
110
120
130
140
Axial Position (cm)

Figure 13

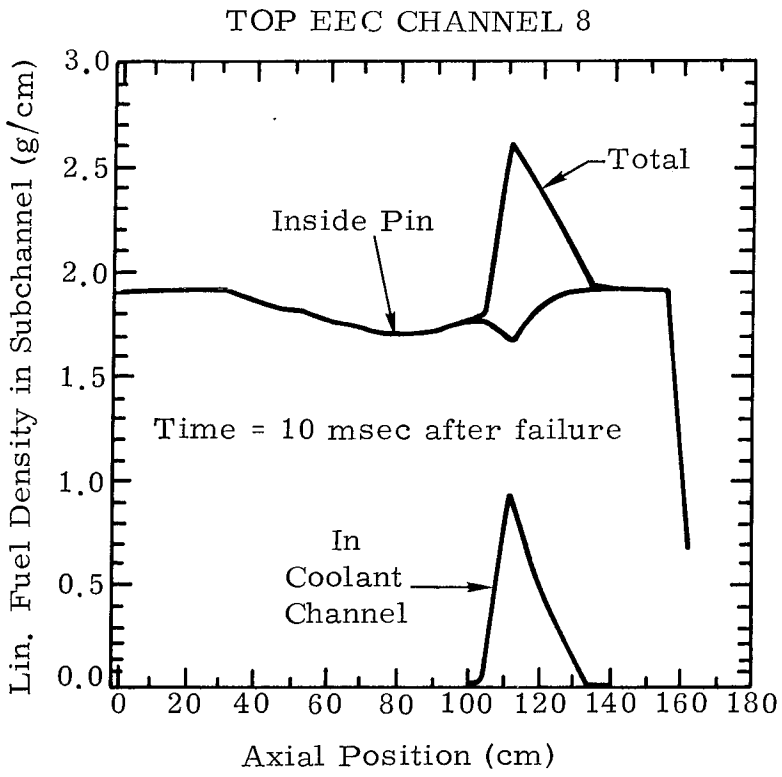
TOP EEC CHANNEL 8
Lin. Fuel Density in Subchannel (g/cm)
3.0
2.5
2.0
1.5
1.0
0.5
0.0
Total
Inside Pin
Time = 10 msec after failure
In
Coolant
Channel
0 20 40 60 80 100 120 140 160 180
Axial Position (cm)

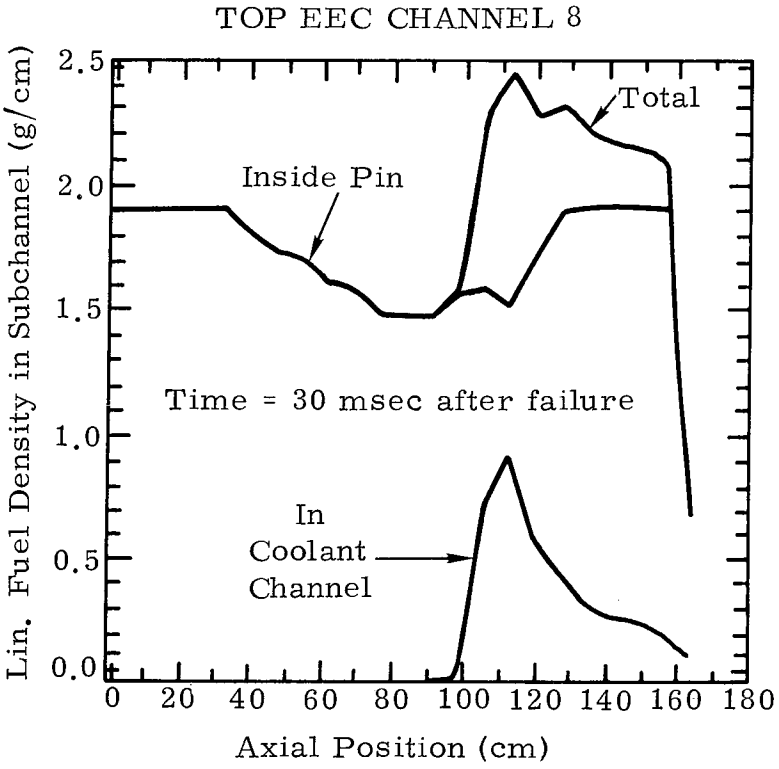
TOP EEC CHANNEL 8
Lin. Fuel Density in Subchannel (g/cm)
2.5
2.0
1.5
1.0
0.5
0.0
Total
Inside Pin
Time = 30 msec after failure
In
Coolant
Channel
0 20 40 60 80 100 120 140 160 180
Axial Position (cm)

Figure 14

TRANSIENT UNDERCOOLING

First Event

Rate of density change per msec is approximately $0.02 g/cm^3/msec$

Event lasted 40 msec

5 msec is an acceptable resolution time

Figure 15

TRANSIENT OVERPOWER

Average absolute difference between total fuel distributions is approximately $0.4 g/cm^3$. Time difference is 20 msec

Rate of density change is again $0.02 g/cm^3/msec$

Figure 16

CORE DISASSEMBLY

Rate of fuel density change found from VENUS calculations to be 0.12g/cm^3/msec

Time resolution of 0.5 msec required

Figure 17

Fast Reactor Safety Experiment Needs and Measurement Requirements*

by

M. G. Stevenson

Reactor Safety and Technology Division
Los Alamos Scientific Laboratory
University of California
Los Alamos, New Mexico 87545

The usefulness of in-reactor safety experiments depends strongly on the quality and quantity of data which can be obtained to extend our knowledge of phenomena and to allow detailed comparison with theoretical models. It is imperative that the design of new safety research facilities optimizes data acquisition possibilities within the constraints of other experiment requirements. This is most important in relation to fuel and cladding motion diagnostics.

In the analysis of postulated LMFBR core disruptive accidents (CDA), there are five key considerations or questions, as listed in Figure 1, each of which is related to an accident phase or to the threshold between major accident phases. Each of these also defines an analysis area and the type of analytical techniques used for that area. For situations in which fuel pins and subassembly cans are intact, computational methods are relatively straightforward. Detailed analysis is not only feasible, but also can be well verified. Beyond fuel pin failure, both analysis and related experiments become more difficult.

It is generally assumed in CDA analysis that some potentially disruptive accident has been initiated, and that the normal reactor scram is unavailable. Therefore, neutronic shutdown processes involving substantial

* Work performed under the auspices of the United States Energy Research and Development Administration and the Nuclear Regulatory Commission.

fuel removal and dispersal from the core region are necessary so that further fission energy generation does not occur. Fuel removal could occur either through a relatively brief and energetic disassembly process or through the more gradual boilout and dispersal typical of transition phase behavior.[1] In any case, the sequence leading to neutronic shutdown is important in defining accident energetics and the final energy state of the core materials.

Primary system integrity is obviously a critical question, since if it is maintained indefinitely no substantial hazard to the public can occur. The energetics of the neutronic shutdown processes and of any subsequent interactions between molten core materials and liquid sodium determine whether the primary system integrity is in immediate jeopardy due to mechanical damage. A subsequent question is whether molten core materials and solid debris can be cooled and/or retained, if not in the primary system, then in a configuration that does not lead to an unacceptable release of radioactive material to the environment.

It is the final consideration that determines the ultimate severity of the accident. Obviously, radioactive material transport occurs throughout the disruptive accident sequence and must be analyzed sufficiently to determine its disposition and any leakage through barriers (fuel pin, primary system boundary, final confinement system boundary) if loss of barrier integrity occurs.

In the analysis of disruptive accidents, technical problems can be defined in four major areas as shown in Figure 2. Similar sets of in-reactor experiment types are shown in Figure 3. These analysis areas and the related experiments are bound closely together and must be directed towards answering the key questions discussed above.

Before discussing experiment information needs, it is prudent to look for a moment at some current developments in analysis methods. To be successful, new methods must be based on and verified thoroughly by experimental information. As an example, the SIMMER code,[2] being developed

at the Los Alamos Scientific Laboratory, is a complex two-dimensional coupled neutronics-hydrodynamics code. It is intended primarily for the analysis of core disassembly and extended fuel motion but also offers the capability of analyzing transition phase sequences as well. Further, the methods used in SIMMER may be applicable to the analysis of phenomena related to postaccident heat removal.

As shown in Figure 4, the SIMMER code uses, as a framework, a fixed Eulerian grid for the two-dimensional coupled neutronics-hydrodynamics calculation. Within each grid mesh, considerable modeling detail is allowed through the use of a two-field calculational technique[3] treating liquid and vapor flow with separate conservation equations and, in addition, a pseudo-field[4] which allows the inclusion of structural elements (intact fuel pins, cladding and wire wraps, and subassembly can walls). Subassembly can walls, if intact, restrict radial motion between cells. In this way, the methodology can encompass a multichannel treatment as in initiating phase codes.

The modeling framework allows, in principle, the inclusion of thermal and mechanical interactions between any phase (solid, liquid, or vapor) of any component (sodium, steel, fuel) and another phase of the same component or any phase of another component. This is indicated in Figure 4 by the arrows. The liquid phase is represented by dispersed droplets and is in a continuous vapor field which is a mixture of the three component vapors.

Achieving experimental verification of a code of this complexity will be difficult. A reasonable procedure is to develop and verify the detailed modeling as much as possible through laboratory experiments using simulant materials. This can be followed by proof-testing using the reactor materials in in-reactor experiments. Although this is an involved process, it could be simpler than with a less complex code since there are less restrictive assumptions. Further, a more detailed code allows a greater capability to extrapolate from one experiment to another and, finally, to reactor conditions.

In any case, verification of analysis methods requires in-pile experiments, since fission heating is the best, if not only, way to achieve proper thermal conditions using actual reactor materials in a reasonable-sized experiment. Further, the usefulness of the experiments depends on the quality of the data obtained. Since the final check on the analysis validity is with material motions, the monitoring of these motions, i.e., "visual" data, is essential.

The next figures delineate what we believe are good targets for fuel motion monitoring resolutions in various experiments. Figures 5 and 6 note single-pin behavior. In these experiments we wish to investigate the transition from pin geometry to either an early shutdown and cooled configuration or to a disrupted subassembly situation. Of particular interest is detailed fuel motion near the time of fuel pin failure. We wish to resolve fuel motion to the extent that initial expulsion into the coolant channels and motion inside the fuel pin can be determined. This leads to a desired radial resolution of about 1 mm. In a rapid TOP-FCI we need to know the spread in fuel failure times and this leads to a time resolution of 1 ms. Time resolutions for slower transients probably do not need to be shorter than 10 ms unless detailed resolution of the ejection process cannot be achieved through out-of-pile experiments.

In larger experiments, the spatial fuel density resolution requirements are much less stringent since we are no longer interested in single-pin detail but in gross fuel and steel motion. Figures 7 and 8 indicate the kind of information needed for resolution subassembly-scale experiments. It is convenient in this case to express resolution requirements in terms of a mass motion, i.e., a mass moving through a distance. We have listed here a requirement of distinguishing the motion of a fuel mass of 10 - 100 g moving through a radial distance of 1 cm and an axial distance of 10 cm in a time of 10 ms.

This requirement can be viewed in several different ways. Figure 9 provides a rationale for the order of magnitude of desired resolution. If

we look at an FTR-sized subassembly, as shown in Figure 10, we can envision that with overcooling of the outer two pin rows and possibly with a power gradient across the subassembly, we might wish to resolve fuel motion down to groups of about 20 - 40 pins. If we wish to detect density variations of 10% along an axial resolution element of 10 cm, then we need resolution of about 400 g-cm. Relating this to reactivity feedback and assuming an average fuel worth gradient we get a resolution of .1 - .2¢/ subassembly. If we assume that groups of 10 - 20 subassemblies behave reasonably coherently, then these numbers translate to a resolution of a few cents in the whole core accident calculation. Thus, if we can acquire fuel motion data with a density resolution as noted, and if these agree with numerical models, then the reactivity history for the accident shall be accurate within a few cents provided that the neutronics calculations are accurate also.

Figure 11 indicates that the resolution for multi-subassembly experiments needs to be on the same level. This is based on an interest in the transition from subassembly geometry to a molten region. Thus, fuel motion between subassemblies as they fail is of interest, and this requires tight resolution.

Achieving high resolution fuel motion information is difficult and obviously adds considerable expense to the experimental program. It is a necessary part of the program, however, since it is required for the development and verification of models sufficiently detailed to permit extrapolation to the reactor accident conditions.

REFERENCES:

1. J. F. Jackson, M. G. Stevenson, J. F. Marchaterre, R. H. Sevy, R. Avery, and K. O. Ott, "Trends in LMFBR Hypothetical Accident Analysis," Proc. of the Fast Reactor Safety Meeting, Beverly Hills, CA, April 2-4, 1974, CONF-740401, Vol. 3, p. 1241.

2. L. L. Smith, et al., "SIMMER Program Manual," Los Alamos Scientific Laboratory report (to be published).

3. F. H. Harlow and A. A. Amsden, "Numerical Calculations of Multiphase Fluid Flows," J. Comp. Phys. 17, 19 (1975).

4. K. D. Lathrop, "Transport Theory, Reactor Theory, and Reactor Safety," July 1 - September 30, 1975, Los Alamos Scientific Laboratory report LA-6137-PR (1975).

KEY CONSIDERATIONS

Pin and subassembly can integrity

Permanent neutronic shutdown

Primary system integrity

Core material retention and cooling

Radioactive material transport and release

Figure 1

ACCIDENT ANALYSIS

Initiating Phase

Fuel behavior and pin failure

Sodium boiling

Initial cladding and fuel motion

Transition Phase

Subassembly disruption

Fuel/steel expulsion, plugging, reentry

Thermal interactions

Accident Energetics and Consequences

Neutronics/material motion coupling

Energy/work conversions

System damage

Material transport and release

Post Accident Heat Removal

Figure 2

REACTOR EXPERIMENTS

Small Bundle

Fuel pin failure

Initial cladding and fuel motion

Fuel/steel/sodium phenomenological behavior

Subassembly

Extended dispersive fuel/steel motion

Rapid fuel/steel expulsion

Fuel/steel reentry

Subassembly disruption

Accident sequences

Multiple Subassembly

Transition phase dynamics

Large-scale energetics

Neutronics/material motion coupling

Fission product transport

Material retention and cooling

Accident sequences

Figure 3

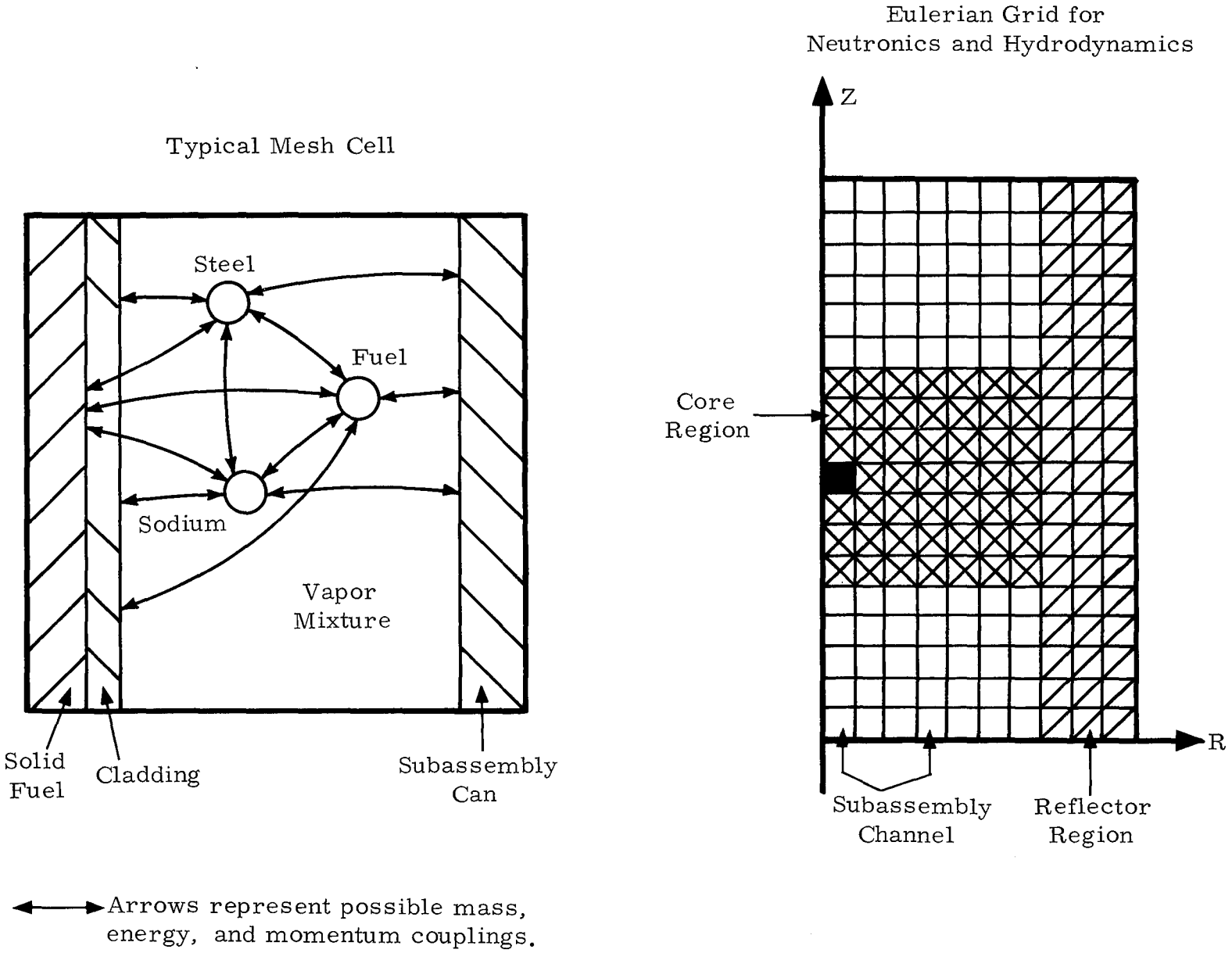

Figure 4. Typical SIMMER Calculation

SMALL BUNDLE EXPERIMENTS

Experiment

Pin failure and fuel motion (TOP)

Key Questions

Loss of pin integrity

Neutronic shutdown process

Post shutdown cooling

Phenomena of Interest

Pin failure time, location, and mode

Internal fuel motion

Fuel expulsion and motion in channel

Fuel sweepout, plugging, reentry

Coolability

Visual Data Requirements

1 mm Radial

10 mm Axial

10-50 ms Time

Figure 5

SMALL BUNDLE EXPERIMENTS

Experiment

Rapid TOP FCI

Key Questions

Neutronic shutdown process

Energy conversion (system damage)

Phenomena of Interest

Pin failure conditions

Coherence of failure

Internal fuel motion

Fuel-coolant mixing

Visual Data Requirements

1 mm Radial

10 mm Axial

1 ms Time

Figure 6

SUBASSEMBLY EXPERIMENTS

Experiment

Fuel/steel motion during LOF-induced TOP

Key Questions

Neutronic shutdown process

Subassembly failure threshold

Post-shutdown cooling

Phenomena of Interest

Pin failure conditions

Fuel/steel expulsion, plugging, removal

Fuel/steel reentry dynamics

Can failure

Melting attack

Visual Data Requirements

100-1000 g-cm Axial

10-100 g-cm Radial

10 ms Time

Figure 7

SUBASSEMBLY EXPERIMENTS

Experiment

Fuel/steel boilup

Primary Objective

Neutronic shutdown process

Subassembly failure threshold

Post-shutdown cooling

Phenomena of Interest

Initiation of motion

Fuel/steel dispersive motion

Plugging, axial melting attack

Can failure

Visual Data Requirements

500 g-cm Axial

100 g-cm Radial

10-50 ms Time

Figure 8

SUBASSEMBLY SCALE VISUAL RESOLUTION

Consider FTR-size subassembly (9 rows, 217 pins)

Might have groups of 20-40 pins behaving coherently

Suppose we wish to detect axial fuel motion of 10% of fuel in 10 cm of length in 20 pins

This gives about 400 g-cm of fuel motion
(2 g/cm/pin x 20 pin x 10 cm x .1 x 10 cm)

This translates to .1 - .2¢/subassembly or of the order of a few cents in the accident progression

Figure 9

Fuel ρ = 10 gm/cm^3
Na ρ = 1 gm/cm^3
Neglect clad
0.63 cm dia. rods
217 pins
0.75 cm pitch

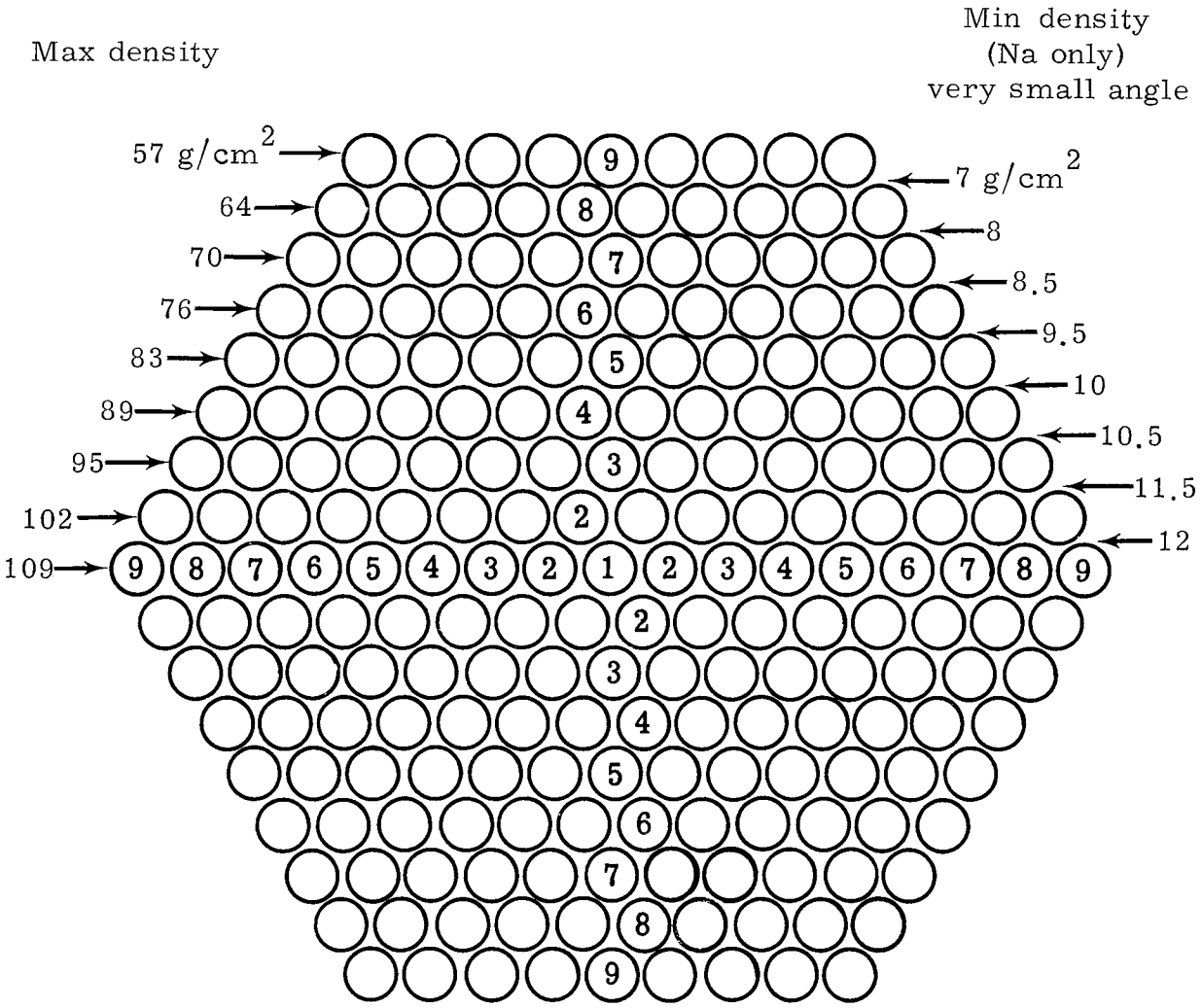

Figure 10. Arrangement of a 217 pin subassembly showing fuel and sodium areal densities.

MULTI-SUBASSEMBLY EXPERIMENTS

Experiment

Transition to Molten Region

Key Questions

Neutronic shutdown process

Subassembly failure threshold

Post-shutdown cooling

Phenomena of Interest

Initiation of motion

Can failure

Gross axial fuel motion

Plugging, axial melting attack

Radial fuel motion

Visual Data Requirements

1000 g-cm Axial

100 g-cm Radial

10-50 ms Time

Figure 11

Methods Used and Kind of Results Obtained in SCARABEE Facility About Fuel and Clad Motion Diagnostics

Previsional Development
for SCARABEE N and CABRI Facilities

by

J. Bardy
G. Manent
L. Roche
A. Tattegrain

Department de Surete Nucleaire
Service D'Essais de Surete
CEN/CADARACHE

I - INTRODUCTION

Since 1971, the Division of Nuclear Safety have performed an experimental program on L M F B R loss of flow studies using first single pin, then seven pin bundle tests. This program, called Scarabée, was completed in July 1974.

Now two further projects are in progress. They will begin operating in the beginning of 1977 and their objectives are:

SCARABEE N to continue the former program with irradiated fuel and increasing bundle size (up to a maximum of 37 pins). A study of the feasability of an experiment on the P. A. H. R. is just starting up.

CABRI the study of transient over power (following or not a loss of flow), with a single pin device first with fresh then with irradiated fuel.

In this paper, we have in view:

- first to present the techniques used for the previous Scarabée program to point out the fuel and clad motions. This presentation will be illustrated by pictures giving some results obtained with seven pin bundles.

- second to present the methods we think appropriate for the experiments in the new facilities, taking into account their objectives and emphases.

II - MEANS USED FOR SCARABEE PROGRAM

The Scarabee facility has been installed in an existing building. It was not possible to carry out extensive modifications such as for example, the installation of an hodoscope.

It has been necessary to use less sophisticated methods. You can see, on the following table, the methods used and the associated results obtained (Table 1).

The techniques are not new, but we have obtained interesting results using the following methods:

- The most important part of the work was to perform experiments one after the other, increasing each time test condition severity or inserting only one new condition
With this method, we can fix the fuel state after tests of increasing severity and try to understand the fuel movements.

- The neutron radiographs and the gamma scanning are performed in the test reactor building itself with a minimum of handling, the stringer remaining in the vertical position.

- Two gamma scannings have been done, before and after the transport between the test reactor building and the hot cells where the macrographic sections are done.

TABLE 1

Method	Kind of Results
Neutron radiography	- length of the fissile column - qualitative axial distribution of fuel and clad
Gamma Scanning (Na I detector)	- length of the fissile column - quantitative axial distribution of fuel
Macrographs Autoradiographs	- radial distribution of fuel and clad on some points - granulometry - temperature of fuel amount of molten fuel
Power trace of driver core	time detection of fast molten fuel movements
Thermocouples in sodium or in the external wall of an experimental channel	time detection of molten material movement

III - RESULTS

III. 1 - Single pin tests.

We have only seen large fuel displacements on one single pin stringer (Scarabee 17).

In this test the clad failure was obtained with the following conditions:

- linear power $\simeq 1$ 400 w/cm
- internal pressure 90 bars
- outlet sodium temperature 850°C

The Rod Drop was initiated 2.8 sec after the clad failure.

You can see the state of the fuel after this test in the upper part of the test section in the Fig. 1. We have no information on the dynamics of the phenomena.

III. 2 - Seven pin tests.

In these tests we have tried to obtain information about fuel and clad motion during loss of flow. We have performed the tests in various conditions as given in Table 2.

The postmortem examination has given the following information:

Test 7.1 - Fig. 2 and Fig. 3

In this test, no fuel melting occurred, the clads have melted and the material is located in the inner part of the bundle in a kind of crucible

shape about 2 cm high and against the Niobium containment above this crucible.

TABLE 2

Number of Test	State of Fuel	Power When Clad Failure Occurs	Observations
7.1	Fresh	0.5 P_N †	Power held 10 sec after zero flow
7.3	Fresh	0.3 P_N	Power held 30 sec after zero flow
7.5	Fresh Internal pressure of 30 bar (cold)	0.3 P_N	Power held 10 sec after clad failure
7.6	Fresh Internal pressure of 30 bar (cold)	0.3 P_N	Power held 60 sec after clad failure
7.7	Fresh Internal pressure of 30 bar (cold)	0.36 P_N	Power held 50 sec after clad failure

† P_N = Nominal power.

A shortening of the fissible zone of about 5% can be seen in Fig. 3 due to the rearrangement of the pellets after the clad movement. The problem is to separate the effects of the test and the handling.

Test 7.2 - Fig. 4 and Fig. 5

We can see the same kind of fuel and clad arrangement as in the test 7.1 except that the whole of the clad material seems to be located in crucible on the first 15 cm of the fissile zone.

The same shortening of the fissile zone can be seen in Fig. 5.

Test 7.5 - Fig. 6 and Fig. 7

In this test, the pins were pressurized at 30 bars in (cold conditions). The blockage is located 10 cm after the inlet of the fissile zone. No fuel melting can be observed.

No shortening of the fissile zone occurred (Fig. 7).

It is difficult to separate the influences of the pressurization and the power level when we compare this test with 7.1.

Test 7.6 - Fig. 8 and Fig. 9

The conditions of this test are the same as those of 7.5 except the time of rod drop. The power was held for 60 sec after clad failure.

The blockage is 10 cm high beginning at the inlet of the experimental channel. The major part of the clad material is located in this zone.

The length of the fissile zone is unchanged but you can see on the neutron radiographs (Fig. 8) and on the gamma-scanning that the central parts of the pellets above the blockage have melted out. This molten fuel is located above the blockage as you can see in Fig. 9.

Test 7.7 - Fig. 10

The conditions of this test were the same than of 7.6 except that the power was 20% higher.

You can see on the gamma-scanning a large difference in the location of the fuel and an increase in the length of the fuel column.

It seems that a new phenomenon has appeared, perhaps clad vaporization, and the fuel has been displaced towards the inlet and outlet of the experimental channel.

Information on the dynamics of this phenomenon can be found on the power trace of the driver core.

It seems that with all the information in various conditions given by these experiments, we begin to have an understanding of the phenomena which may follow a loss of cooling accident. We have now to write the corresponding code which will be tested against the experiments in larger bundle up to a maximum of 37 pins.

IV - METHODS IN PROGRESS

IV.1 - Scarabee

As the general limitations of the installation are still the same the methods we intend to develop are:

a/ Gamma scanning

The previous equipment will be improved and will be made automatic. A collimator and a semiconductor spectrometer will be

installed. The fission product distribution in the test pin or bundle will be deduced from these measurements. The results will be obtained using a self-calibration method. Provided there is no migration of fission products in the fuel, the relocation of the fission products gives the new configuration of the fuel.

When this assumption is not valid the location of fuel will be obtained by carrying out a gamma scan after a low power reirradiation with low fuel temperatures, to be done in the loop itself.

b/ Reactivity variations

This method seems to be usable in spite of the low reactivity worth of pins or bundles. It is now being studied and it is necessary to perform:

- Neutronic calculations checked by experiments carried out in a critical mock-up on a few typical arrangements, to be performed about March 76.

- Local flux measurements in the loop near the tested fuel in order to observe fuel movement. This is difficult because of the neutron background from the driver core.

- Reactivity and flux measurements after the experiment, at low temperature level, in order to observe any difference between the state of the fuel immediately after the experiment while it is still hot, and after it has cooled.

- A perfect knowledge of the driver core reactivity and of all the factors influencing it.

An on line computer could be necessary.

c/ Other methods

Other methods (neutron radiographs, micrographic sections, temperature, etc.) will still be used.

IV. 2 - Cabri

Taking into account both the brevity of events and the magnitude of reactivity insertions in the cabri experiments it has been decided to fit a fast neutron hodoscope, which has been described by Herr BLUHM.

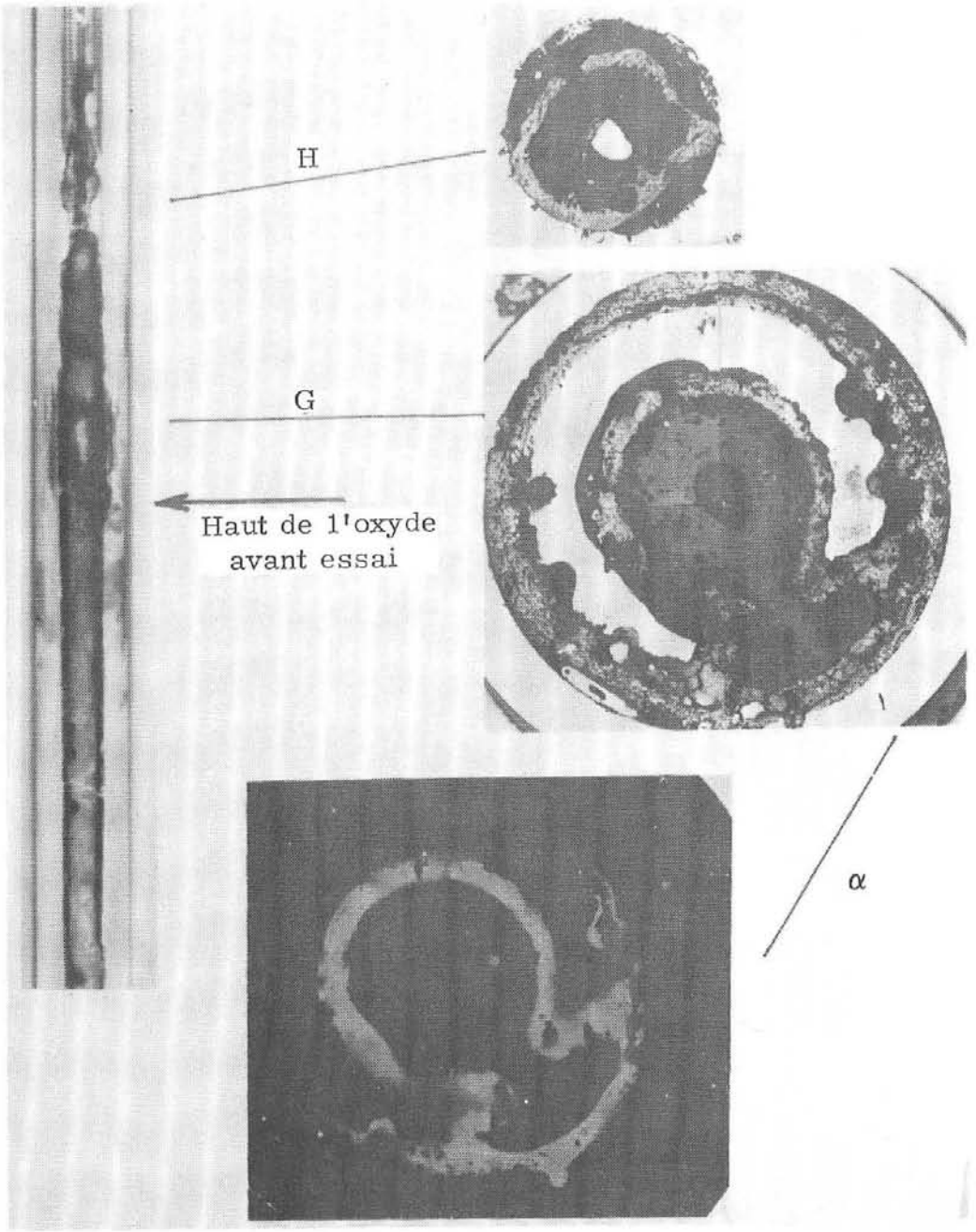

Figure 1. SCARABEE 17

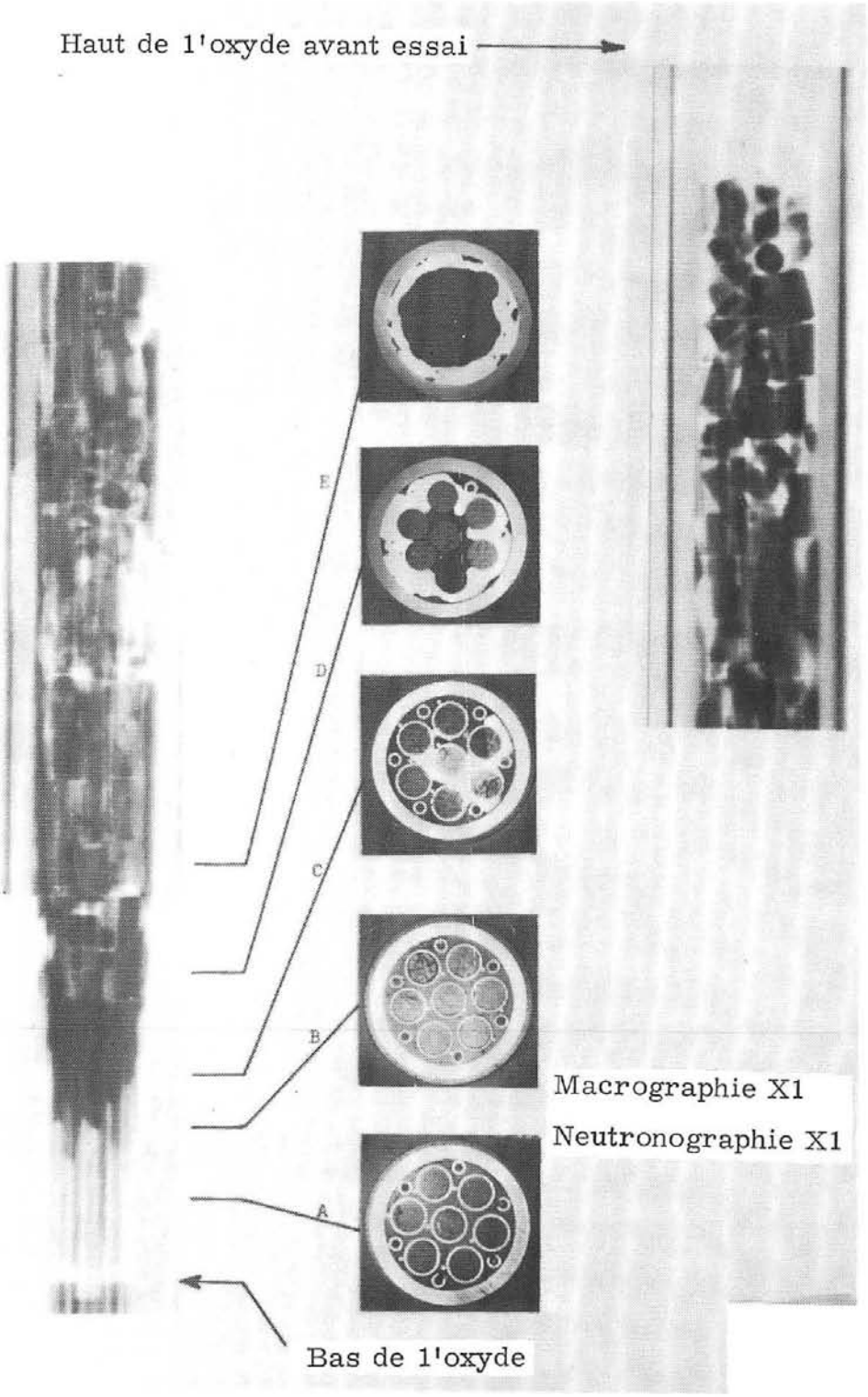

Figure 2. SCARABEE 7-1

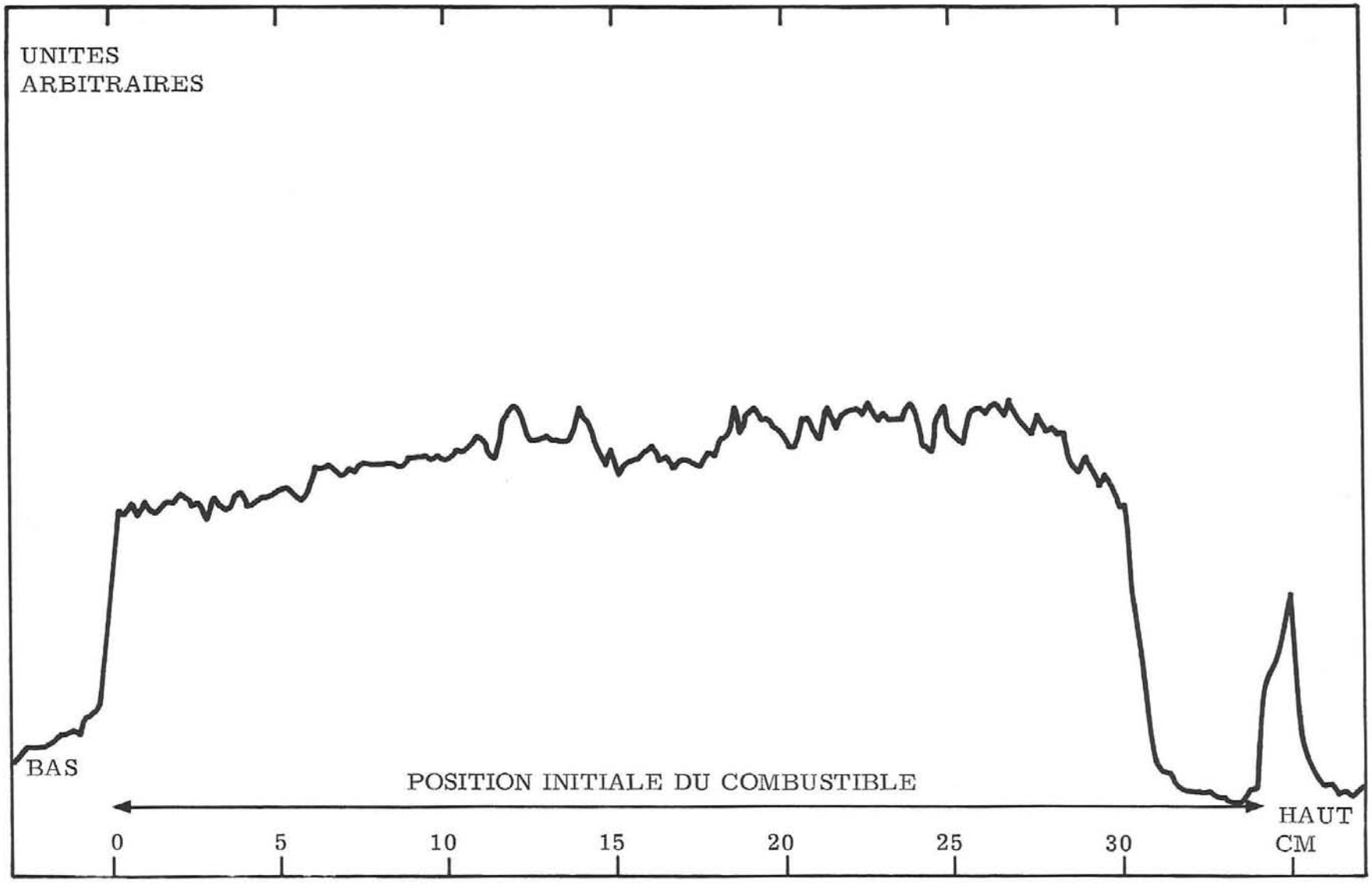

Figure 3. SCARABEE 7-1

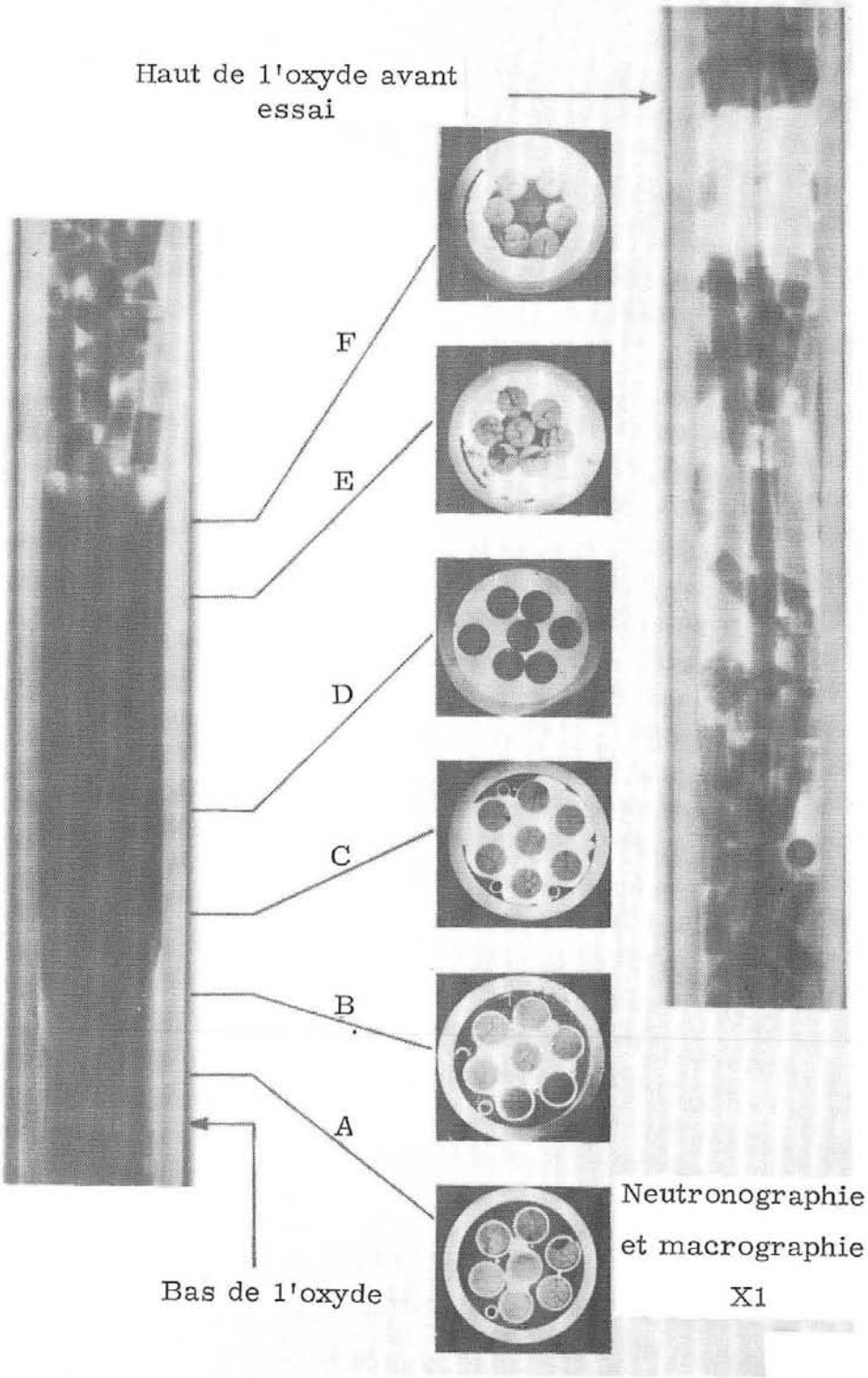

Figure 4. SCARABEE 7-3

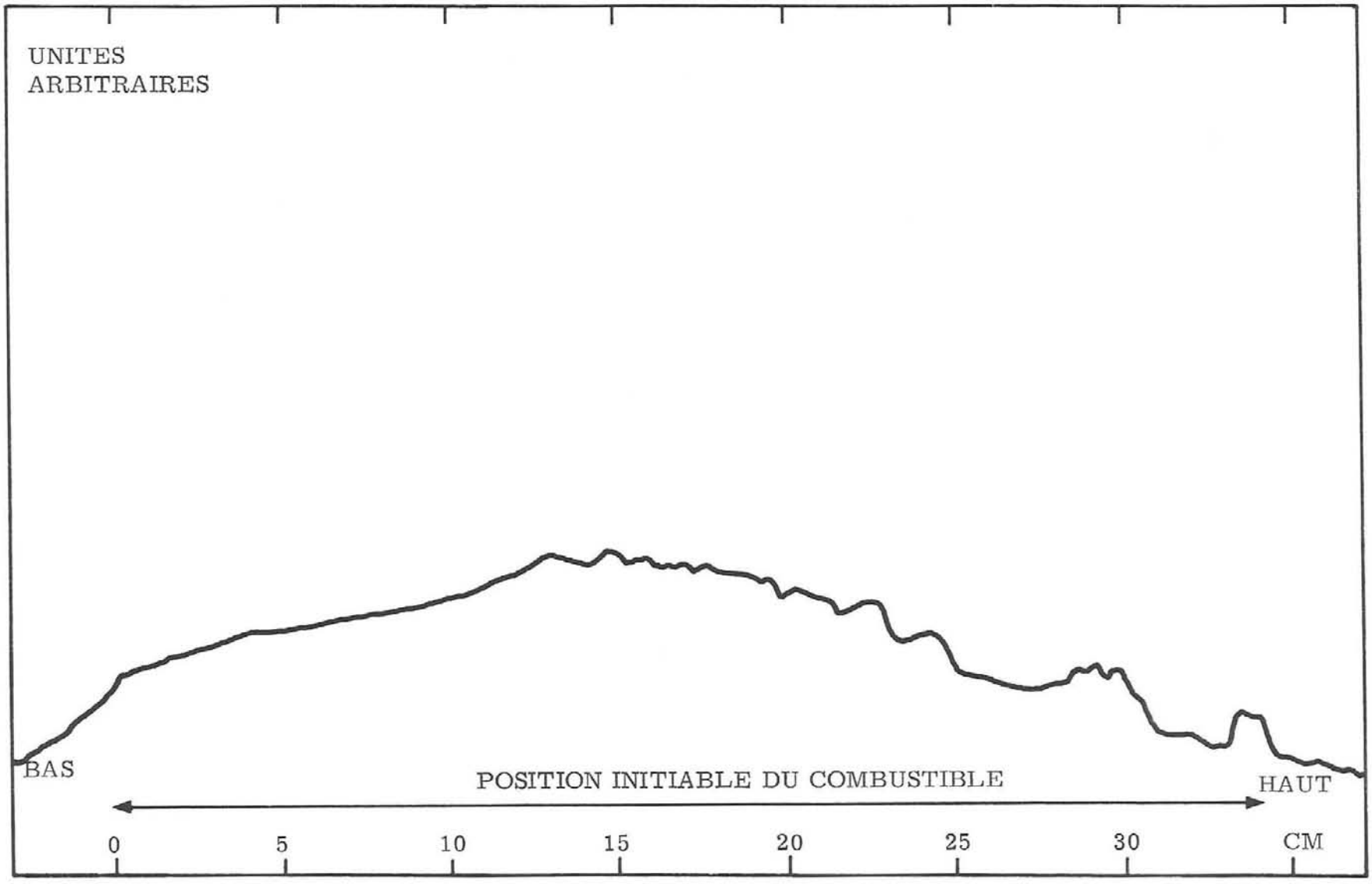

Figure 5. SCARABEE 7-3

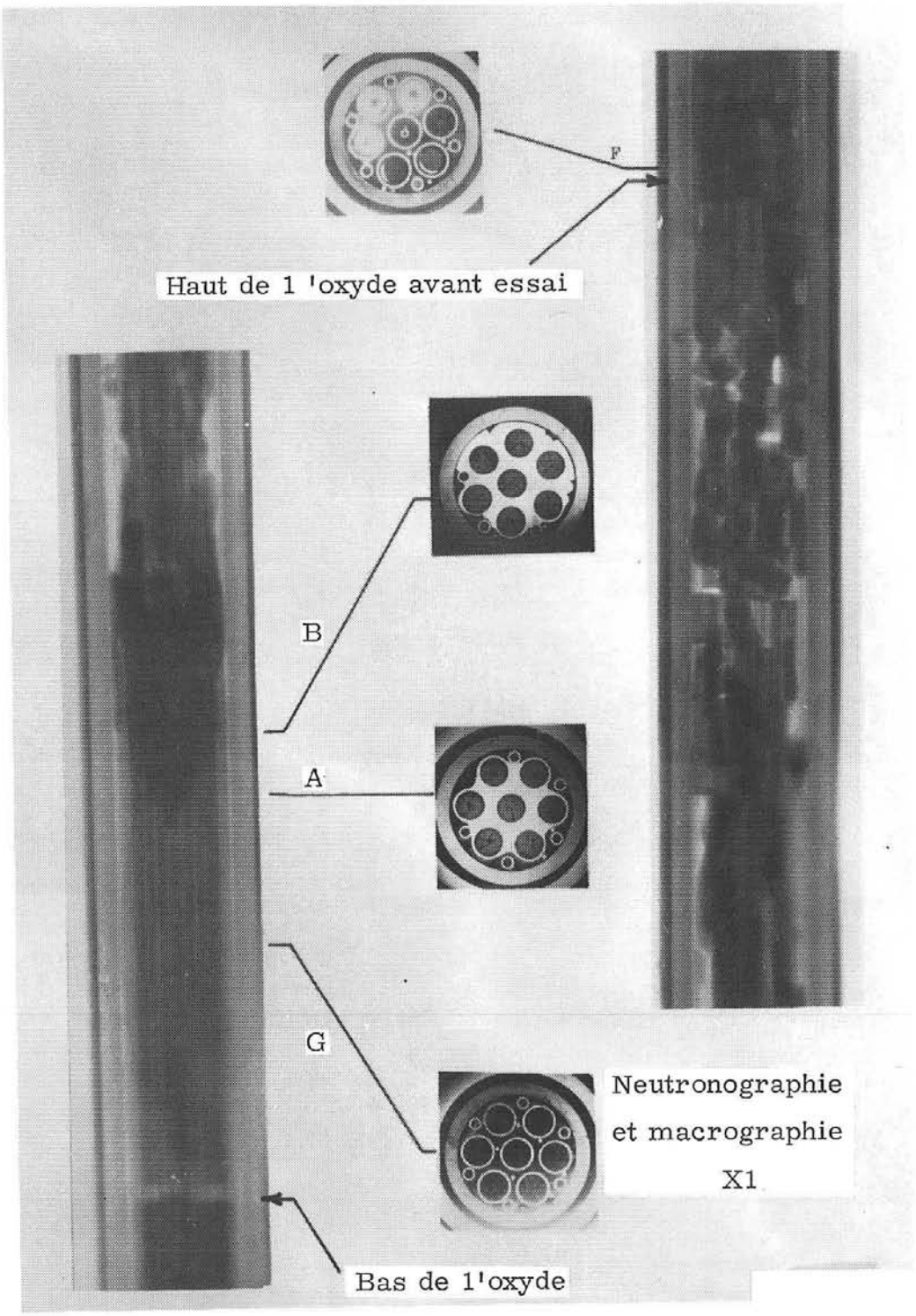

Figure 6. SCARABEE 7-5

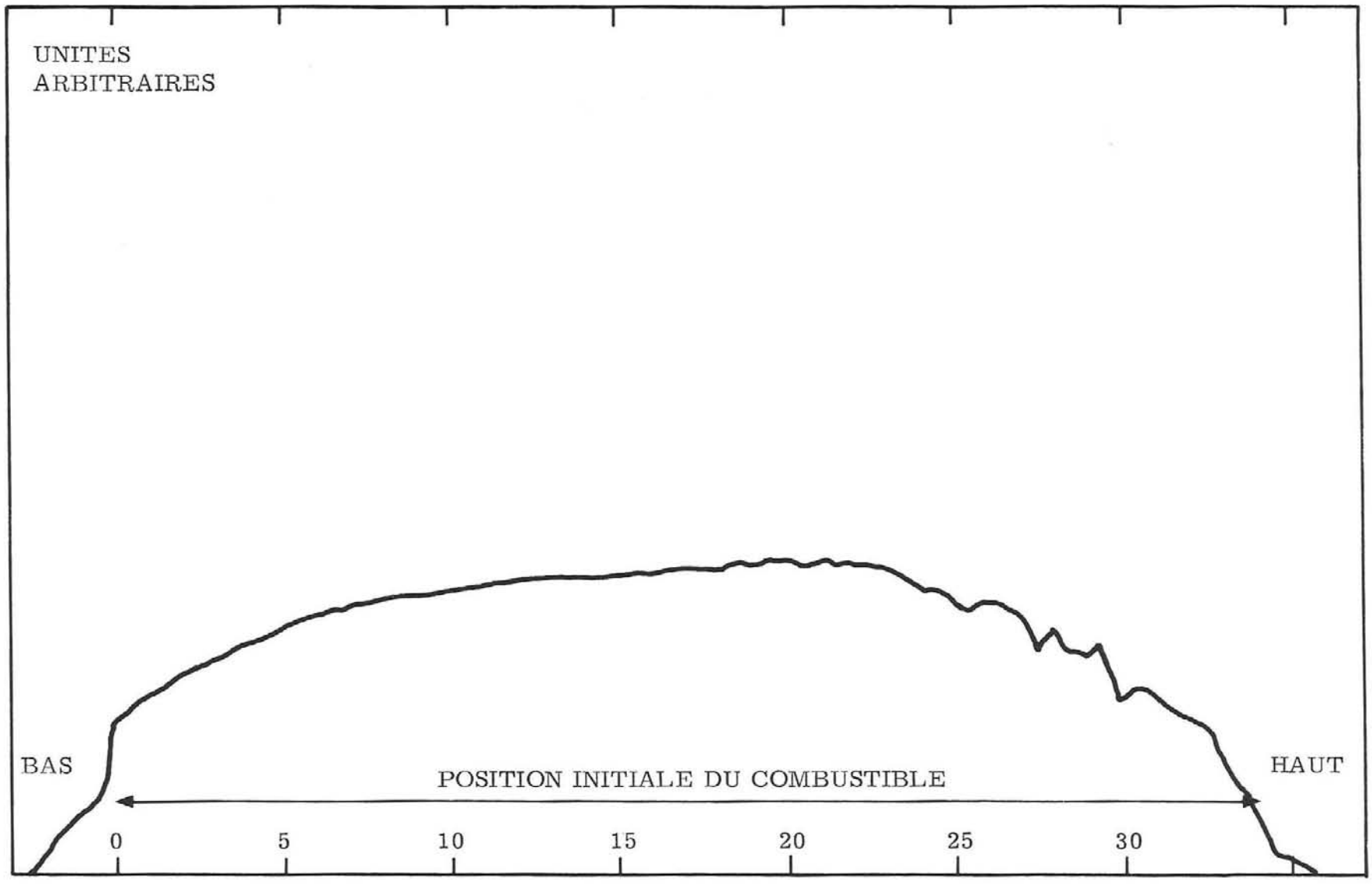

Figure 7. SCARABEE 7-5

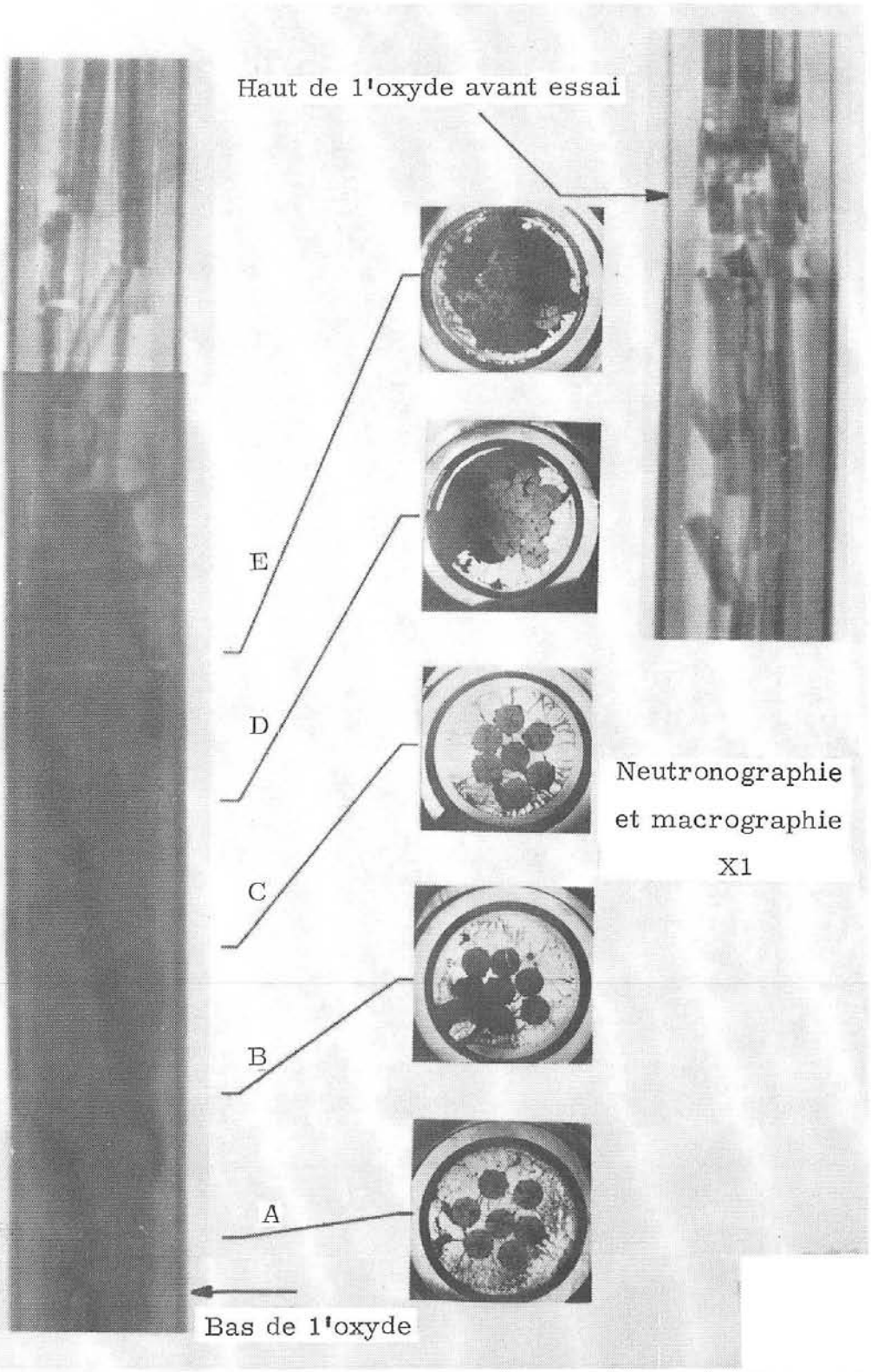

Figure 8. SCARABEE 7-6

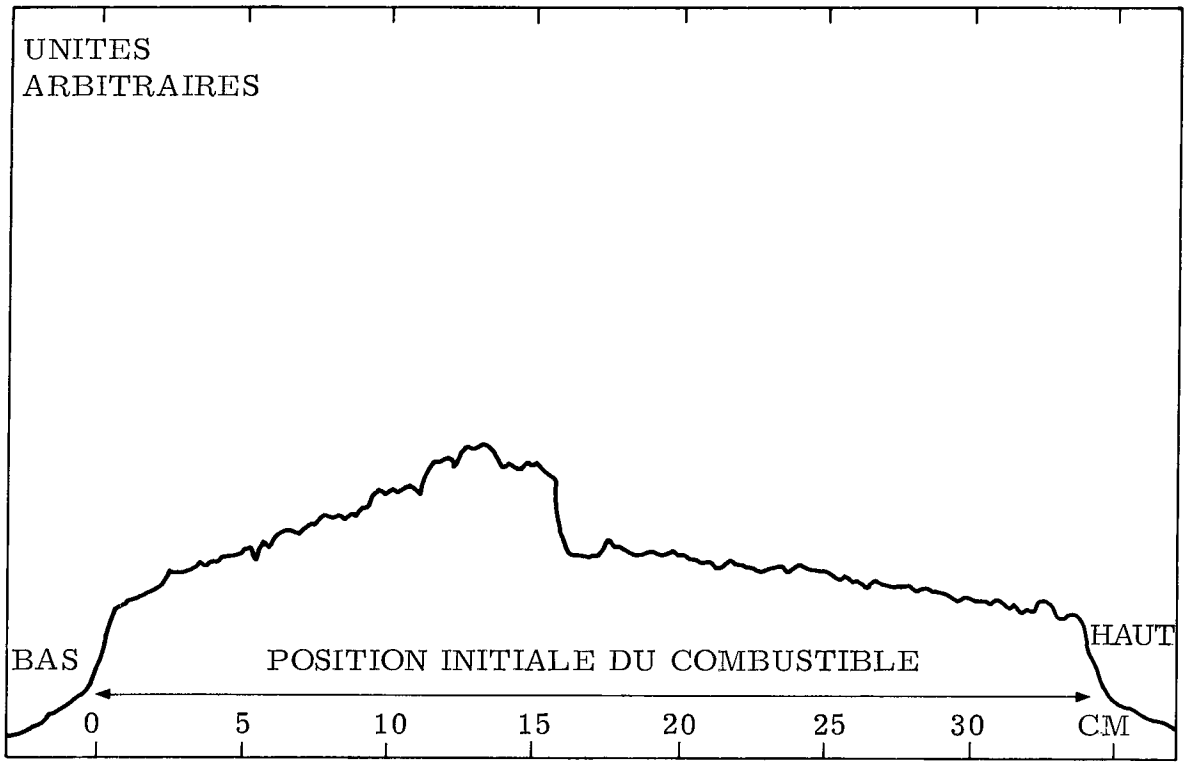

Figure 9. SCARABEE 7-6

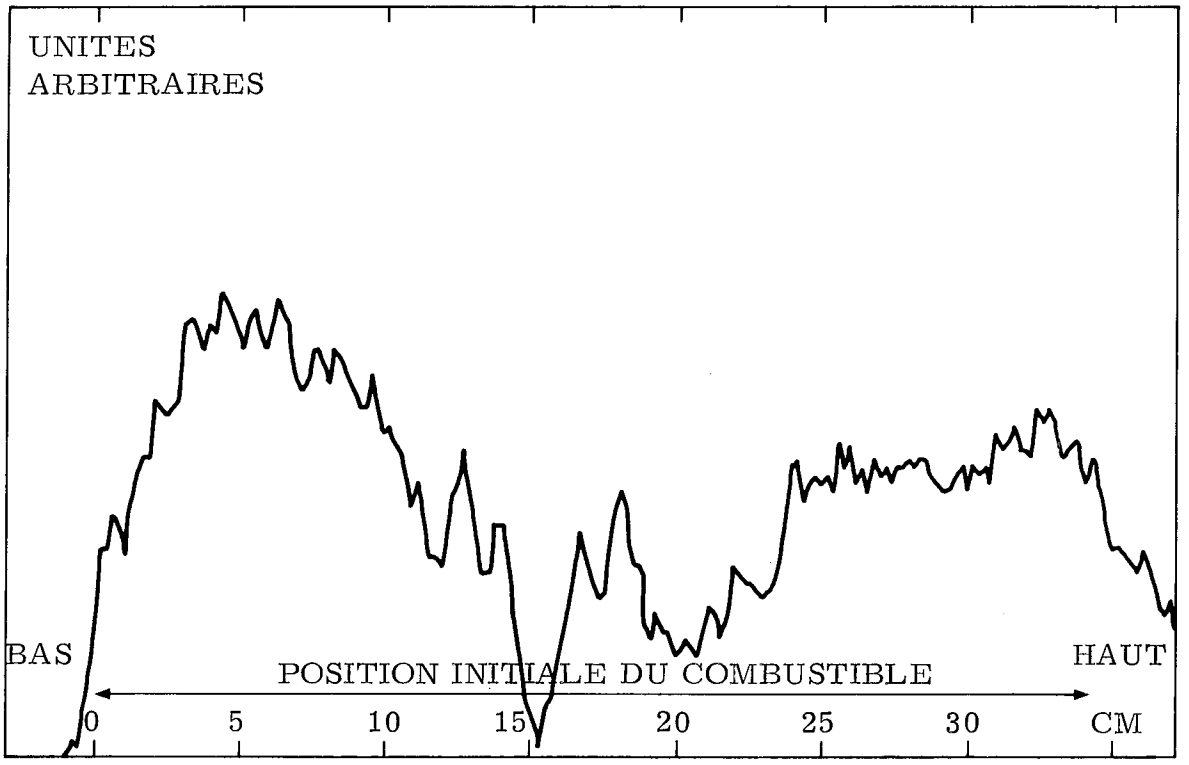

Figure 10. SCARABEE 7-7

Current Developments in TREAT Hodoscope Technology*

by

A. De Volpi

Reactor Analysis and Safety Division
Argonne National Laboratory
Argonne, Illinois 60439

Abstract

The development of fuel motion monitoring is traced from its inception, through present operation, and into future programs. After noting the role of fuel motion studies in terms of safety assurance for the LMFBR, the history of in-pile fuel monitoring is reviewed. The operational record of the present TREAT fast neutron hodoscope is summarized with attention to various performance features. Development plans for the TREAT hodoscope are described in some detail. Application of the hodoscope has been considered for eight safety facilities other than TREAT. In addition, there is a possible role for fuel monitoring techniques to be extended to real-time ex-vessel core surveillance in operating reactors. Certain intrinsic strengths of the hodoscope technique for material monitoring are identified. The pattern of development may be characterized as an adaptation of several technologies to fit available requirements and resources.

---

*Work performed under the auspices of the U.S. Energy Research and Development Administration.

Introduction

Assurance of ultimate safety in nuclear reactors depends on preventing accidents, limiting core damage, containing postulated excursions, and attenuating possible radiological impact. The activities reported in this paper deal with experimental efforts aimed at observation of the initiating, sustaining, and terminating aspects of various accident scenarios.

The overall program is characterized by substantial theoretical modeling and experimental simulation of accident sequences. On one extreme, measures -- such as clad integrity -- which prevent or limit core disturbance have been the subject of extensive testing. On the other extreme, measures which lead to final containment of a hypothetical core disruption -- such as postaccident heat removal -- are just becoming the subject of close attention. Between the two extremes of failure threshold and core debris, there has been a need to monitor core condition during accident simulations.

Of greatest interest has been fuel motion detection, although the integrity or dismemberment of any structure in the reactor core are of concern to safety evaluations. Clearly, information desired in such a comprehensive program can be acquired in a variety of complementary ways. Out-of-pile testing can clarify underlying physical phenomena. In-pile testing causes the experimental simulation to be more prototypical of an operating reactor environment.

There are roles in-pile for both steady-state irradiations and for transient experiments, though the most significant safety issues apparently are best addressed through brief high-power reactor-driven exposures. Although the remainder of this paper deals primarily with in-pile fuel motion monitoring from its original application at the transient reactor TREAT, possible applications to other reactor systems will be discussed.

Observation of fuel redistribution has always been a difficult problem because of a number of factors that stretch the limits of available technology. Perhaps foremost has been the requirement for time-resolved diagnostics. Compounding the problem are the inevitable containment, structure, and coolant placed around a sample tested in a burst reactor environment. As a result, the standard techniques of radiography have been inapplicable, and it has been necessary to search for new methods.

---

*Work performed under the auspices of the U.S. Energy Research and Development Administration.

History of In-Pile Fuel Monitoring

Initial success in monitoring fuel motion was achieved by direct photographic techniques at TREAT. Because of plans for use of opaque coolants, alternatives were examined and development of a gamma ray scheme was commissioned in 1957 prior to beginning of the experimental work in TREAT. Although gamma ray methods failed to achieve adequate sensitivity, the door was opened for neutron techniques which did prove successful. A continuing search has been underway for improvements and additional alternatives.

Photographic

High-speed color photography of fuel element tests was performed soon after the TREAT reactor was placed in operation.[1] In order to provide an optically clear path, the sample was placed in an elongated capsule faced with a transparent window at one end. The transparent capsule fitted into a slot running half way through the core. A high-speed framing camera, triggered by the transient program timer, was focused on the area surrounding the fuel pin. Self-illumination from the source and a low level zenon floodlight caused the film exposure.

The results from experiments on LMFBR pins were excellent, leading to observation and discovery of a number of phenomena dealing with clad damage and fuel motion.

Clouds of vaporized sodium from the fuel-cladding bond caused limitations on the technique by obscuring results during part of the experiments. More serious limits were inability to use sodium as a coolant, to use fuel clusters, to use high pressure autoclaves, or to use plutonium fuel.

Gamma

The Naval Research Laboratory was requested by Argonne prior to 1960[2-4] to develop an instrument to observe the position and motion of fuel utilizing emitted gamma radiation. The desired space resolution was 2.5 mm at 1 msec intervals.

Early investigations were directed towards a gamma-ray pinhole camera. The intention was to view with a TV chain an image of fuel elements formed upon a sodium-iodide screen. NRL concluded that "improved time resolution and dynamic range with greater flexibility and reduced cost" could be achieved with the same space resolution by an alternate system.[3] They proposed to replace the pinhole camera with a rotating cylinder having a large number of small collimating holes scanning across the test section. Signals from scintillation detectors placed behind the drum would intensity-modulate multi-gun oscilloscopes. A continuously moving film camera would record these sweeps.

Reference 4 recounts the development from initial stages through termination. The radiation scanning device proposed by NRL was built and tested at TREAT. An appraisal of the technique[4] indicates that the

fuel signal could not be measured in strong contrast with signals from background sources. During a steady-state scan for a 6%-enriched pin the signal/background achieved was about 0.65. During a transient, this would probably be reduced by a factor of about two because decay gammas would not be available to contribute to the signal. In addition, these measurements had been made under artificial conditions in which the amount of extraneous steel and other gamma-producing materials was minimized.

Neutron

In 1963, as a result of experience with new techniques in fast neutron detection, scanning of fission neutrons was proposed, and adequate support for the calculations was obtained from tests at TREAT.[5] Signal/background ratios were found to be typically 7.0 for transparent capsules and about 2.5 for sodium loops. Various stages of development ensued until 1969, when the system in essentially its present form became operational with the full quota of 334 detection channels.

The leading physical reason why the hodoscope system has been successful is the choice of fast neutrons. The neutrons are specific to the fission process in fuel, the source term is distributed throughout the volume of the fuel, and fast neutrons tend to lose energy when subjected to a deflecting collision.

To take advantage of these features, it was necessary to develop a multi-channel collimator; high-efficiency neutron detectors; simple, reliable, and inexpensive electronics; and a cost-effective, dependable data recording system.

Early phases of hodoscope development benefited substantially from prior photographic and gamma methods of fuel motion detection. The data accumulated from gamma ray scanning acted as a steppingstone for calculations of gamma effects and as an example of successful scanning techniques. The photographic data resulted in movies which allowed direct verification of simultaneous hodoscope and optical results.

Alternatives

There has been a continuing evaluation of alternative methods of fuel motion detection not only for TREAT but for other applications. In particular, the generation of neutron or gamma beams for transmission through test sections has been frequently reexamined. The possible use of detectors placed in-core in close proximity to the test section has also been evaluated. As improvements occur in these techniques, reconsideration will be given to possible use either as a substitute or companion to proven methods. It should, of course, be recognized that some alternatives may be better suited to special requirements or facility constraints.

Operational Record at TREAT

Because the fast neutron hodoscope is still the only operational device in the fuel motion field, it is difficult to make a comparative

judgement on performance. With exceptions to be mentioned later, spatial and temporal specifications have been met by a system which has been acceptably reliable and operationally ready. The recovery and analysis of quantitative data is a lengthy process which is intrinsic to the level of detail required. The results of over a decade of development and experience serve not only as a basis for further improvements but also for extrapolation to other reactors.

Transient Shots

The hodoscope with the full digital system since 1969 has participated in 76 transient experiments. These run the range from low power flattops, short bursts, or flattops followed by bursts. Experiments simulated loss-of-flow, transient-overpower, fuel-coolant interaction, and threshold-of-failure conditions. Power levels have peaked at 22 to 16,000 MW.

Fuel configurations span single pins, three pins, and seven pins, with lengths of 15 to 91 cm. Special configurations included various forms of flux shaping, thermal neutron filtering, and nuclear-fission heated walls. The experiments have been designed not only by Argonne (East and West Divisions) but also by General Electric and Hanford Engineering Development Laboratory. Various forms of containment, pressure vessels, loops and other apparatus have been associated with the experiments.

Many experiments have been simply calibrations or trials and have not required analysis of data. The visual results from six of these transients have been reconstructed into a series of film strips to be shown later as a movie. Quantitative results are compiled in reports to the experimenters.

Performance

Of the 76 experiments, hodoscope data for two essential shots has been lost due to technical failure.[6] The data from a few other transients is of minimum value due to nonlinearity or synchronization problems. Operationally, the hodoscope can be reliably readied for an experiment with half a day of checkout and calibration. Maintenance has been performed with little impact on the experiment schedule.

Documentation of development,[5] design,[7] operation,[8] and results[6] is now complete.

Quality assurance measures are employed to maintain a high level of reliability in functioning prior to and during transients and in data recovery following experiments.

Performance, as measured in terms of fuel motion detection, is summarized in Table 1.

TABLE 1. TREAT Hodoscope Performance Summary

*Lateral spatial resolution as small as 0.25 mm
*Vertical spatial resolution as small as 6.2 mm
*Data collection intervals 1.5 msec and longer
*Sensitivity limit about 0.02 in signal/background, corresponding to about 50 mg of fuel under good conditions
*Penetration of opaque containment, such as steel walls over 1 cm thick
*Power levels up to 20,000 MW
*Sensitive to fuel motion during postscram delayed neutron phase

Performance may also be characterized by phenomena observed:

Distortion. Fuel pins are usually subjected to warpage or other forms of distortion. If the experiment consists of a single pin, then detailed bending and bulging has been noticed. If the experiment contains a cluster, there may be either coherent or incoherent motions of the pins with respect to each other.

Expansion. Both axial and radial time-dependent expansion have been observed.

Fuel Ejection. The ejection of fuel, which can follow the failure of cladding, has been detected either directly in terms of outflow or indirectly in terms of losses within the pin.

Prefailure Fuel Motion. Internal fuel motion prior to clad failure has been detected in single-pin experiments. This has occurred either by virtue of the filling of an expansion space above the pin or by the movement of molten or highly plastic material within central voids. The opening and closing of central voids with diameters less than 1 mm have been monitored.

Slumping. Draining of fuel following meltoff of cladding has been observed in multi-pin experiments to lead to losses at higher elevations and accumulations of fuel at lower elevations of the test pins.

Dispersal. In short burst experiments, fuel dispersal or disappearance of fuel from the field of view has been observed.

Eructations. One of the most dramatic phenomena identified has been a mechanism for moderately energetic dispersal of fuel caused, apparently, by the vaporization of steel intimately mixed and heated by fuel.

Compaction. No coherent or rapid compaction has been observed.

Problem Areas

All techniques have weaknesses. The fact that we provide significant ventilation of these matters should not be mistaken as an indication that overall system performance is inadequate. In general, the problems may be characterized as current limitations, all of which are subject to remedial development depending on the availability of modest resources.

Our biggest problem has been a nonlinear response of the Hornyak button neutron detector at high power levels. This is subject to both hardware and software accommodation to be described later.

Performance of our film recording system has been poor in the range of 1.2 to 1.5 msec and works best at 6 msec or longer. Only a few transients have required the shortest data collection intervals, and it has been possible, with added effort, to recover data taken in the marginal range.

There is need for additional redundancy in data storage in order to reduce the risk of total data failure. In addition, turnaround time could be improved by going to a system of recording which is more directly computer-compatible.

In an array of 334 channels, each with differing characteristics of detector, phototube, and electronics, there is an inherent problem with nonuniformity of response from detector to detector -- as well as individual nonuniformity in response to power level changes. Although these irregularities have not limited transient fuel diagnostics, they do hamper performance in terms of more subtle localized space-dependent phenomena.

Development Plans for TREAT Hodoscope

Improvements planned at TREAT incorporate two objectives: a larger scope of effort in material monitoring and correction of known deficiencies or limitations.

Collimator for Full-length FFTF Pins

A new collimator has been designed, fabricated, and is in process of installation for viewing a height and width of 122 by 6.6 cm.[9] At the same time, improvements in scanning, calibration, and operation have been introduced. The existing detectors and data storage system are to be reused. The original 51-cm collimator will be relocated to the South face of the reactor where it will be utilized in single-pin experiments requiring higher resolution.

The new collimator has cross-focusing beams both horizontally and vertically. Figures 1 and 2 illustrate the design.

Fission-Counter Array

In order to circumvent the problems of nonlinear response of the Hornyak button detectors, an array of fission counters has been devised for use at high power levels.[10] A 31-channel prototype, instrumented with ten active channels, has been tested at TREAT. A wide variety of operating conditions have been evaluated, including choice of fissile isotope, coating thickness, gas filling, plate spacing, high voltage, and condensed electronic circuitry. The special electronic circuits are appended directly to the parallel plates of the fission counters, as shown in Fig. 3. Cost and space limitations were major factors in the design. This prototype will be brought up to full complement of detectors and placed in tandem behind the 51-cm hodoscope collimator for use particularly with a forthcoming equation-of-state (EOS) series.

A larger array containing at least 108 plates of ^{237}Np will be installed behind the new collimator. Although the fission chamber response has been shown to be quite linear, its efficiency relative to the Hornyak button may be pushed up to a few percent.

Magnetic Recording System

Conceptual design has been completed for a magnetic recording system. The intent here is to provide more rapid turnaround for data and to establish a level of redundancy. Magnetic recording techniques have improved sufficiently in the last decade to warrant acquisition of off-the-shelf hardware components as central elements in the design. Because of risk associated with bit dropout and reliability in magnetic tape systems, we have selected a high-speed head-per-track disk as the basic storage medium. We are designing for collection intervals of 0.6 msec minimum (although smaller intervals may be employed by adding modular units). The system will be portable so that it can be shared with another reactor at the Idaho National Engineering Laboratory site. After a transient, data stored on disk will be transferred to magnetic tape in a computer-compatible form. A potential for real time or posttransient replay of qualitative features of the experiment may become possible.

Redundancy will occur because the disk system will become the primary data recording medium, but the existing digital photographic system will be retained for backup recording. We also plan to increase the total number of channels recorded.

Upgraded Analysis Facility

Until involved in actual analysis of data, it is often difficult to appreciate the effort level required. Both hardware and software capability is needed to extract the maximum amount of information on a time scale compatible with the overall experimental program. Naturally a

heavy reliance is placed on computers; in our case, we make maximum use of dedicated facilities with interactive features. On the basis of experience and in step with new technological developments, we plan to introduce an extended computational capability, greater interactive use, and a high visual graphics content.

Clad Blockage Detection

It is recognized that cladding may play an active role in the potential accident progression. Over a number of years we have conducted experiments which indicate that unambiguous clad blockage detection may become feasible by making modifications to the TREAT hodoscope.[11] Note that the words "clad motion" have been deliberately avoided in favor of "clad blockage." Although our experimental data do not exclude clad motion capability, we have not sufficiently demonstrated the required level of sensitivity. We have, however, discovered that high energy capture gammas from steel may be isolated from the background caused by fuel within the field of view and that resolution comparable to that achieved for fuel motion may be attainable for clad accumulations.

Figure 4 is a photograph of the hodoscope at TREAT depicting the tandem enclosure arrangement for sodium iodide detectors. Also in view is the prototype 31-channel fission-counter array mounted between the neutron and gamma detector bays.

Sodium Void Detection

Exploratory experiments have been done regarding ex-core detection of the voiding of large volumes of sodium. Gamma rays characteristic of capture in sodium have been examined, but the intensity available in typical experiments does not appear to be adequate. Although investigation will continue, it may be necessary to find an alternative scheme to meet the sodium void requirement.

Radiography

The hodoscope could be considered as a system for time-resolved radiography. One major difference is that resolution is nominally limited by the interdetector spacing. However, when the fuel moves past the hodoscope slot projections, spatial resolution of about 0.25 mm can be achieved. Conversely, it is well established in medical radiography that if collimated detectors are scanned across a stationary subject, then high resolution can evolve. This effect is illustrated in Fig. 5, which shows a hodoscope scan of a single pin. Count rate differentials corresponding to separations of 0.25 mm are observable.

Consequently, we have in mind an extension of hodoscope application to that of in-situ radiography.[12] We have found that sometimes after an experiment the radiography produced ex-core fails to agree with the disposition of fuel at scram as measured by the hodoscope. Effects which could contribute to this discrepancy are contraction upon cooling, sodium slug reentry, or mechanical disturbance upon removal of test section from the reactor.

Our plan would be to make pretest and posttest measurements in-situ using the hodoscope in its scanning mode. The reactor would be brought up to a nominal power level to act as a source. The collimator would be placed under remote motorized scanning control, and all channels would record data simultaneously.

Data taken in this mode comprise a form of digital radiography which is potentially inherently advantageous for quantitative analysis. By using fast neutrons as the detection medium, a high level of penetration into large clusters is assured. Consistent with prior remarks about clad blockage detection, it should be possible to differentiate the location of fuel and steel; in fact, data substantiating clad blockage distinction is already on hand.

The possibility of 3-dimensional projections, based on reconstructions through transaxial tomography, is not to be excluded. This may be accomplished either by rotating the test section or by having two hodoscope collimators at 90°.

Miscellaneous Developments

Additional activities underway include the design of a uniform plate of fissile material to be used as a plane calibration source. Experimental support to the hodoscope project includes (1) studies of the response function of the Hornyak button to neutron energy and flux intensity, (2) efficiency of various detectors, and (3) effects of materials such as steel, lead, or plastic placed ahead of the detectors.

Recent analytical support covers calculations of efficiency, count rates, and response functions to large-bundle test sections.

Considerable successful effort has gone into profile curve fitting and into corrections for the nonlinear response of the Hornyak button. The deviation, which is supralinear, has been found to behave reasonably according to a quadratic model which uses the linear power as an independent variable and which depends on adjustment of two parameters for a fit. As a result, the supralinear effect can be compensated, even for high power experiments, and the fuel motion data linearized.

Technology Export to Other Reactors

I am aware of eight reactors or reactor concepts besides TREAT which have considered specific hodoscope installations.

FARET. Possible incorporation of a hodoscope collimator within the reactor vessel was considered in late design stages.

PBF. Use of a hodoscope with PBF was foresightedly anticipated by APDA during conceptual design stages, and reports recommending provision for future installation were issued.[13] These provisions were actually carried out in the design so that current consideration of implementation is not adversely affected by structural limitations. There is a mortered region in the biological shield for inclusion of a collimator;

the potential viewing path through the core loading to the test section is clear of impediments; and there is space adjacent to the reactor wall for instrumentation. The physics and engineering impact of a slot through the fueled core and other factors are now being evaluated.

STF. Initial studies of a Fast Safety Test Reactor[14] included a significant role for a radiation hodoscope intended for ex-core gamma and neutron monitoring.

CABRI. A multi-national effort to obtain fuel monitoring during transient overpower experiments is underway at Cadarache.[15] A fast neutron hodoscope system is being designed with low and high range instrumentation. Data collection efforts must cope with short-burst sub-millisecond time resolution.

ACPR. Not only is a hodoscope with a different type of data recording system being considered, but at least one other alternative method of fuel monitoring is being studied for application to ACPR.[16]

SAREF. A comprehensive assessment[17] of generalized material monitoring systems for a hard spectrum or fast reactor safety test facility is being carried out. Particular problems addressed are response to multi-subassembly experiments and sensitivity to clad blockage. In addition, both real-time and posttransient 3-dimensional diagnostic instrumentation are desired. Different versions of the facility by ANL, GE, and LASL have called for a hodoscope or alternative material motion monitoring device.

DMT. An integral experiment on fuel boilup and dispersal is being examined.[18] A conceptual review will be made of functional requirements and reactor features in order to incorporate some type of ex-core fuel monitoring system.

ETR. Because of the importance of fuel motion in certain integral LMFBR experiments being conducted in ETR, ANC personnel are making an appraisal of potential diagnostic techniques and implications.[19]

Breeder Reactor Ex-Vessel Core Surveillance

Applications discussed so far have been with regard to direct visualization in safety test facilities. There is, additionally, a potential extension of these techniques to the real-time surveillance of operating power reactor cores. Not only is there incentive to provide technical and public assurance of safety, but there is a strong economic motivation for the reactor operator to be aware of and to minimize core disruption, should such occur.

Within the framework of the four lines of assurance for ultimate reactor safety, a role exists for an ex-vessel detection system capable of tracking the fuel disposition of an LMFBR core at all times. A key element of such an ex-vessel system is ability to remain immune to damage resulting from hypothesized core destruction. Although existing material monitoring systems require a clear slot through the reactor in

order to realize high spatial resolution, no such slot nor such stringent spatial requirement exists in an operating power reactor. The information needs from an ex-vessel monitoring system include real-time approximate fuel location, power level, reactivity ramps, sodium voiding, steel plugging, and debris bed status.

The most obvious detection problems in fuel surveillance are caused by the substantial core size and the reflector and core barrel zones surrounding the fuel region.

Table 2 contains an application matrix for an ex-vessel detection system. The reactor status is partitioned into "operating" and "scrammed," and conditions considered are divided into "normal" and "abnormal." A rough estimate of relative probability of success in achieving these goals and of their relative importance is indicated by special markings. Some features relate to limitations on incident consequences; others relate to postincident consequence limitation.

While it is a big jump from current technology to possible achievement of just a few of these goals, it may be wise to initiate such development, particularly using SAREF as an intermediate testing facility.

Discussion

The development of material monitoring has been traced, noting various steppingstones required for advancement. An updating of current activities indicates that incremental improvements are being introduced into existing facilities and being planned for new facilities. The field is approaching nearly 20 years of development, which includes time when gamma ray and visual photographic techniques were pursued. It is clear that the technology is complex, requiring assimulation of techniques from many fields, for example, neutron and reactor physics, nuclear detection, nuclear electronics, large arrays, integrated circuits, data recording, photography, nuclear medical scanning, radiography, computers, graphic displays, and analytical models.

The path to success has been serpentine; many false steps are possible. Although there is room for development of radically new techniques, each must travel a similar tortuous path to sidestep the numerous pitfalls.

Because of the complexity of the combined techniques, the considerable established base, and the potential for new features, it is likely that the hodoscope will continue to be in the forefront of material monitoring. There are a number of intrinsic features which strengthen its future serviceability: The hodoscope capitalizes upon a distributed fission source, has a high penetrability through large test sections, can have a response specific to various materials under surveillance; is relatively insensitive to local variations in reactivity; and neither perturbs nor is destroyed by melting or disruption of the test object.

TABLE 2. Ex-vessel Detection System

Application Matrix

LMFBR	NORMAL CONDITIONS (PREINCIDENT)	ABNORMAL CONDITIONS (POSTINCIDENT)	
OPERATING REACTOR (Neutrons from prompt fission; gammas from capture)	Independent Power Monitor (T) + ***	Independent Reactivity Monitor (T) + ***	Incident consequence-limitation
	Base-line Fuel Condition (T,S) + *	Early-warning Fuel Motion (T,S) +++ *	
		Fuel Motion Confirmation (S) ++ *	
SCRAMMED REACTOR (Neutrons from spontaneous fission; gammas from decay)	Subcriticality Assurance Monitor + ***	Subcriticality Assurance Monitor + *	Postincident consequence-limitation
		Fuel Location Detection (FFP/Core Meltdown/PAHR) (S) +++ **	

Incident Prevention

	high	medium	low
Success probability	***	**	*
Relative importance	+++	++	+

S = space resolution required

T = time resolution required

Limitations in these applications have in fact been budgetary rather than technical.

The monitoring of material motion should contribute significantly to several lines of assurance for nuclear reactor safety, not only through current and future application in test reactors but also through possible extension of these techniques to operating reactors.

References

1. C. E. Dickerman, G. H. Golden, and L. E. Robinson, "In-Pile Photographic Studies of EBR-II Mark-I and Fermi Core -- A Sample Meltdown," Nucl. Sci. & Eng. 14: 30-36 (1962).

2. C. E. Dickerman, private communication.

3. References contained in "Progress Report on Fast Breeder Reactor Safety Studies," unpublished NRL Memorandum Report 803, by L. A. Beach, A. G. Pieper, and M. P. Young (undated, circa 1958); also NRL Memorandum Reports 936 (May 1959) and 975 (September 1959).

4. L. A. Beach, A. G. Pieper, M. P. Young, "Gamma-Ray Scanning Techniques for Fast Breeder Reactor Safety Studies," NRL Report 5625, unpublished (July 12, 1961).

5. A. De Volpi, R. Pecina, D. Travis, R. Stewart, and E. Rhodes, "Fast-Neutron Hodoscope at TREAT: Development and Operation," Nucl. Techn. (in press, Nov 1975).

6. A De Volpi, R. R. Stewart, J. P. Regis, G. S. Stanford, and E. A. Rhodes, "Fast-Neutron Hodoscope at TREAT: Data Processing, Analysis, and Results," submitted to Nucl. Techn.

7. W. C. Kaiser (Editor), "System Design Description for TREAT Fast Neutron Hodoscope," Argonne National Laboratory internal report R0206-1000-SA-00 (November 21, 1974).

8. W. C. Kaiser (Editor), "TREAT Fast Neutron Hodoscope Operating Manual," Argonne National Laboratory internal report R0206-1002-SA (to be issued).

9. A. De Volpi et al., "Hodoscope Collimator for 122-cm Viewing Height at TREAT," (proceedings this conference).

10. A. De Volpi, W. C. Kaiser, and John J. Eichholz, "Multi-Detector Integrated Fission Counter Array," Proceedings of IEEE Symp. on Nucl. Sci., San Francisco, California (November 1975).

11. A. De Volpi, C. L. Fink, and R. R. Stewart, "Monitoring Clad Blockages," (proceedings this conference).

12. A. De Volpi, "High-resolution Fast-neutron and Gamma Digital Radiography," Proceedings of the IEEE Symp. on Nucl. Sci., San Francisco, California (November 1975).

13. C. E. Branyon and G. L. Ball, "Fast Reactor Fuel Meltdown Test Facility Requirements," Atomic Power Development Associates Report APDA-173 (August 31, 1965); C. E. Branyon et al., "Application of the Power Burst Facility to Fast Reactor Fuel Meltdown Tests," APDA-177 (August 31, 1965).

14. C. N. Kelber et al., "Safety Problems of Liquid-Metal-Cooled Fast Breeder Reactors," Argonne National Laboratory Report ANL-7657 (February 1970).

15. M. Kuchle, private communication (September 1975).

16. J. Powell, private communication (September 1975).

17. D. Rose (proceedings of this conference).

18. J. B. Heineman, private communication (October 1975).

19. A. Bowman, private communication (October 1975).

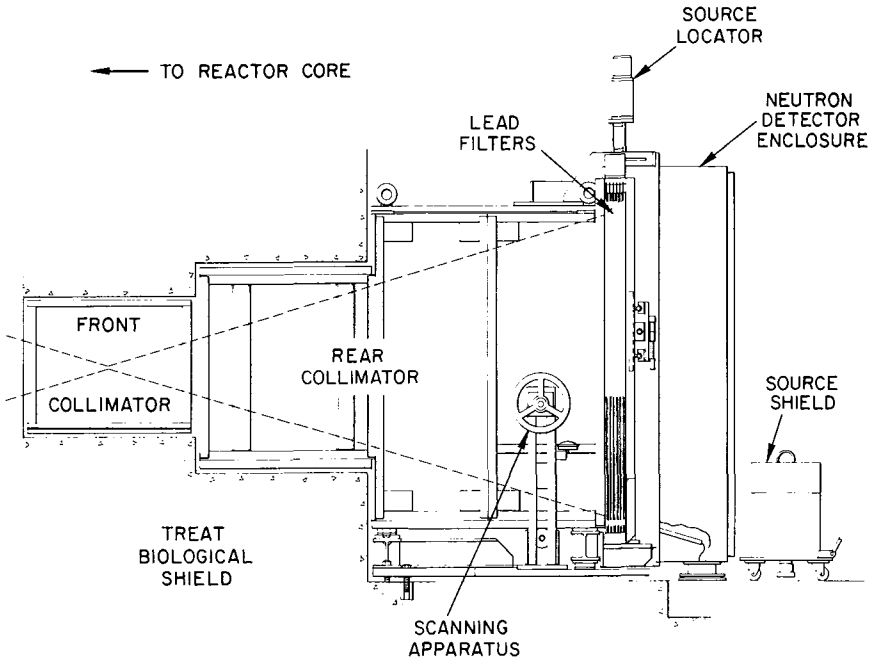

Figure 1. Schematic of Assembly of New TREAT Hodoscope Collimator for Full-Length Fuel Pins

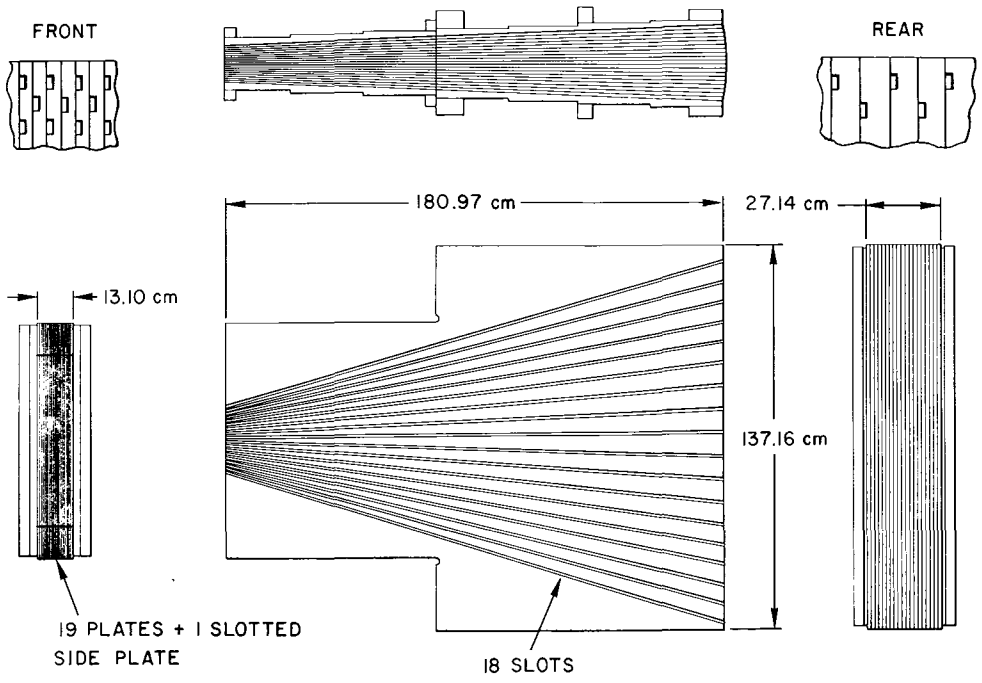

Figure 2. Details of Design of a Typical Steel Plate for New TREAT Hodoscope Collimator

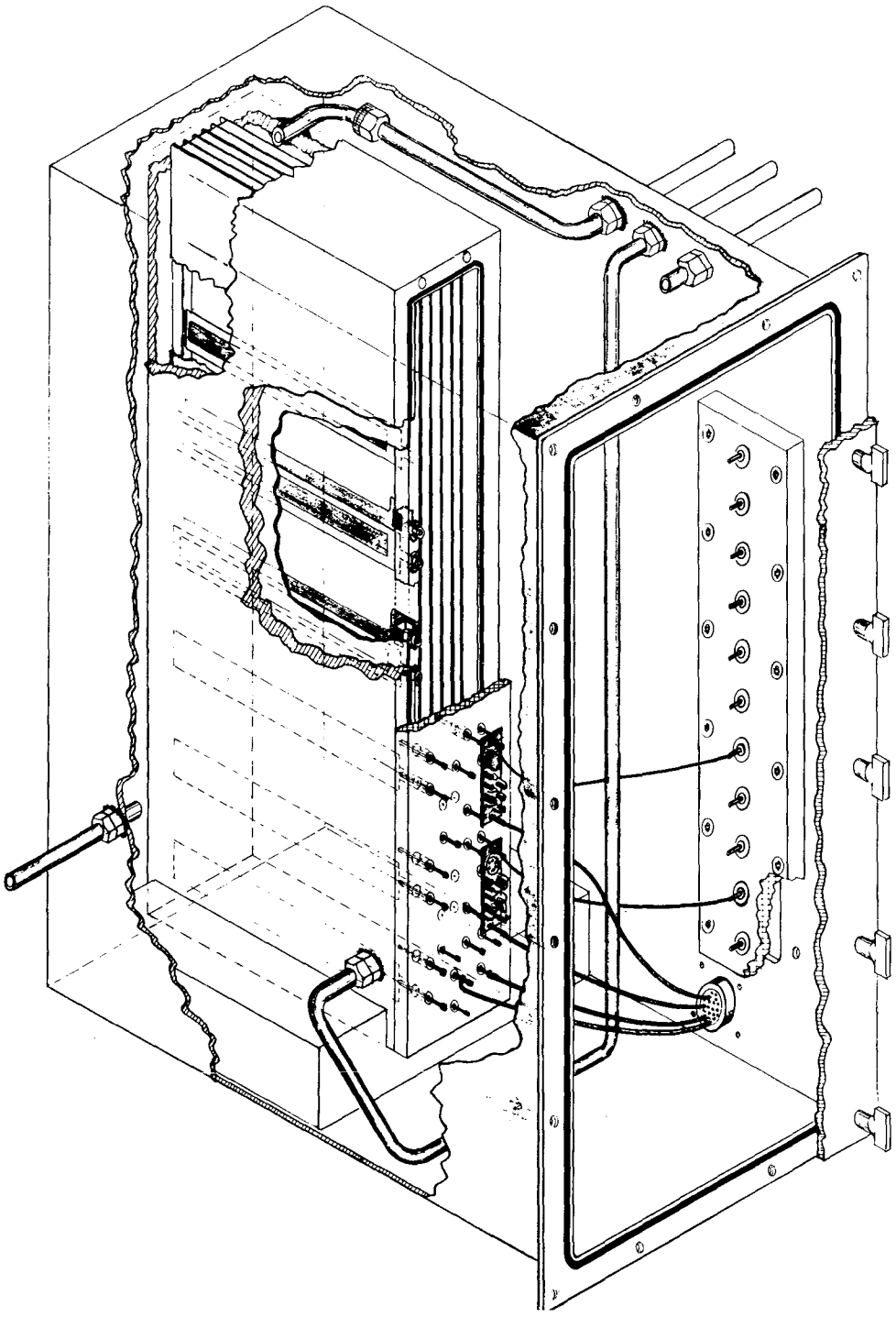

Figure 3. Cutaway View of 31-Channel Fission Counter Array

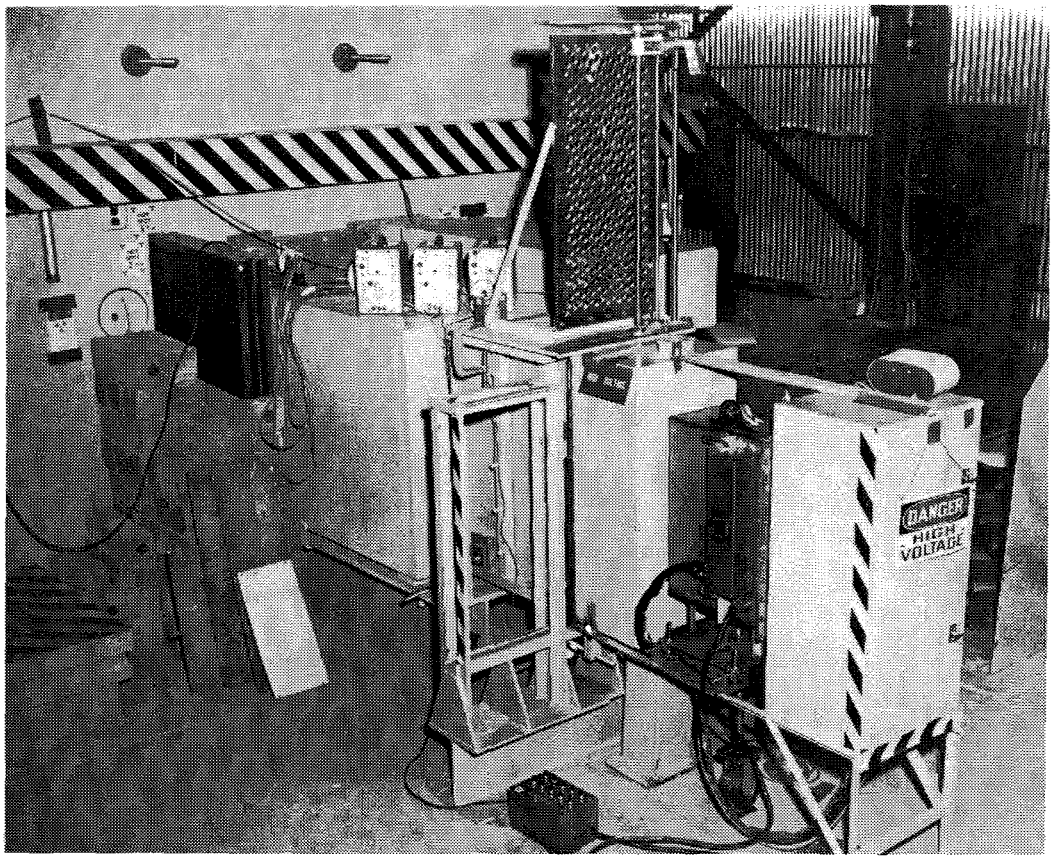

Figure 4. Photograph of 51-cm Hodoscope Collimator at TREAT with Three Tandem Detector Bays

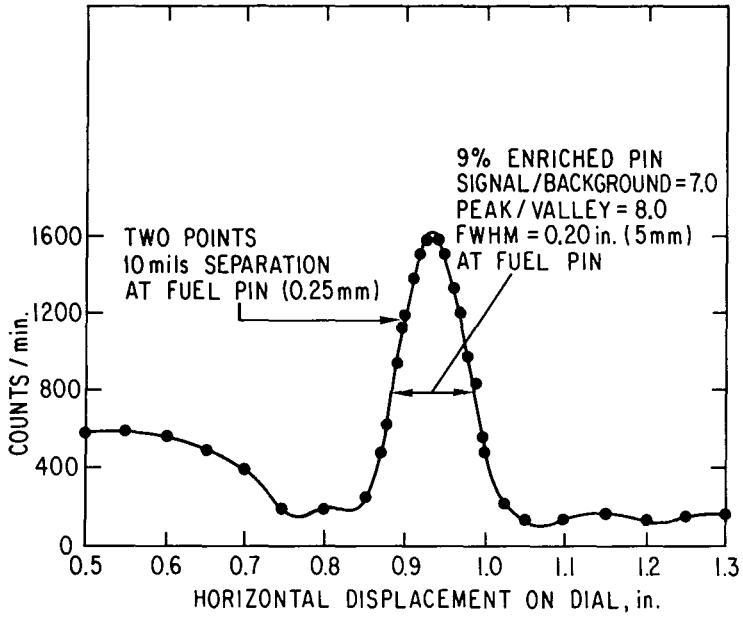

Figure 5. Hodoscope Neutron Scan of Single Pin in TREAT

Design Characteristics of the CABRI-Neutron Hodoscope

by

H. Bluhm, K. Bohnel, M. Kuchle, H. Werle
Institut fur Neutronenphysik und Reaktortechnik

GfK, 75, Karlsruhe, Germany

and

R. Agaisse, J. M. Aujollet, J. Dadillon

CEN/SES Cadarache, France

1. Objectives of the CABRI-Hodoscope

The hodoscope to be described in the present paper will be installed at the CABRI transient overpower test facility which consists of a thermal swimming pool type driver reactor and a sodium test loop. The driver core contains fuel rods of UO_2 enriched to about 6% and allows to establish preburst power levels corresponding to about 450 W/cm in the test pin for a period of up to 30 minutes. Ramp rates of 10 to 100 \$/sec leading to pulse widths at half maximum of between 5 and 200 msec are obtained, by rapid depressurization of ^3He tubes located inside the core. The reactor will become critical in the second half of 1976 and a test programme of about five years duration has been planned (1).

One principal goal of the CABRI-TOP experimental programme will be to provide experimental data allowing to check and validate theoretical models to be incorporated in whole-core accident analysis code systems.

Since only single-pin experiments have been projected, the tasks of the CABRI hodoscope have been restricted mainly to the determination of vertical fuel density changes, because these are most important for negative reactivity feedbacks. To be more precise, we understand fuel density changes to mean variations of the fuel mass contained in a vertical segment of the coolant channel.

At first it was necessary to clarify which sensitivity and which spatial and time resolution the hodoscope must have. According to theoretical investigations published (2,3) we expect maximum fuel density

changes of 30% right after pin failure and near the location of failure. Mean values of about 10% are more likely. Therefore, the hodoscope should be able to detect 5% variations of the fuel density.

Up to now the finest mesh used in most calculations is 10 cm; therefore, this spatial resolution would generally be adequate for a comparison with theoretical predictions.

The time resolution should be connected to the spatial resolution via the velocity at which the fuel is ejected from the coolant channel. We expect values between 1 and 6 cm/msec and, therefore, require a time resolution of 2-10 msec. The hodoscope measurements should start when the CABRI reactor is brought to preburst full-power operation and should be continued until reactor shutdown. Therefore, data acquisition times of several minutes will be necessary.

A large dynamic range of neutron fluxes has to be covered by the hodoscope detector system with sufficient statistics. A factor of 200 is expected between the highest and lowest power levels at which rapid fuel movement can occur.

2. Setup of the Hodoscope

a. Collimator

Figure 1 shows an artist's view of the collimator and slot arrangement in the reactor tank. The slot, which divides the reactor into two parts, consists of empty aluminum boxes extending to both sides of the test loop. Their inner width is 5 cm and their height 120 cm. In the

direction of the collimator the box widens after 50 cm to match the dimensions of the inner collimator surface which is directly attached to the slot at a distance of 100 cm from the center of the test loop. The inner collimator surface is 142 cm high and 7.53 cm wide.

The collimator itself is a prismlike block of iron containing three columns of 51 channels. They diverge up to a distance of 4.5 cm between their axes at the collimator end. The rectangularly shaped collimator slits have dimensions of 1.5 cm in the vertical and of 0.75 cm in the horizontal direction at the collimator entrance, which enlarge to become 2 cm x 1 cm at the collimator outlet. The overall length of the collimator block is 300 cm.

b. Detectors

To cover a wide dynamic range of neutron fluxes, two detectors are positioned behind each collimator slit, a fission chamber for high and a proton recoil counter for low neutron intensities. The Np-237 fission chamber (f. c.) contains 100 plates covered with 1 mg Np/cm^2 on both sides. The total amount of 400 mg Np-237 in the chamber produces an efficiency of $6 \cdot 10^{-4}$ for fission neutrons. The efficiency of the proton recoil proportional counter (p. r.) can be adjusted between 10^{-2} and 10^{-3} according to experimental requirements. The counter dimensions are: diameter: 2.54 cm, length: 20 cm.

c. Preamplifier-Discriminator System

The detectors are connected to fast current sensitive preamplifiers which directly attack a fast discriminator. Base line drifts in the

amplifiers are avoided by differentiation of the current signal. The p. r. preamplifiers differ from the f. c. preamplifiers by a larger rise time and a greater differentiation time constant. This and the additional use of an adapter increases their signal to noise ratio by a factor of five relative to that of the f. c. amplifiers. Pulse pair resolution of less than 100 nsec and 200 nsec has been obtained for the f. c. and p. r. systems, respectively.

Special μ-metal shielded coaxial cables are used to connect the detectors with the preamplifiers. Although cable lengths of 35 m are used, practically no electrical noise pickup has been observed in a reactor environment.

d. Data Acquisition System

Figure 2 shows a block diagramme of the data acquisition system. It consists of 320 12-bit 10 MHz scalers which are attacked by the discriminator outputs, via optical isolated gates. In addition twenty registers are available to take over further data of interest such as the reactor time, the flux monitor counting rate, the gas pressure, high voltage, etc.

Every 1 to 10^4 msec the contents of all 340 scalers are transferred to a buffer in less than 1 μsec. Immediately after the transfer the scalers are ready for counting again.

The buffer consists of 10 large 420-bit parallel-in serial-out shift registers in which all data belonging to the same recording track are combined and after conversion to the two-phase Miller code written onto 10 tracks of a 14 track analog magnetic tape. 350 words make up a block which is separated from its follower by a synchronisation word. By special tape selection the dropout rate can be kept within acceptable limits.

The analog magnetic tape is run at a speed of 120 ips. It can be read into the computer at reduced speed which will write the data on digital tapes in an IBM-compatible form.

The time autonomy of the system is given by the length of the analog tape and is about 28 minutes.

The system is able to handle data rates of 5.4 Mbit per sec which could easily be expanded by a factor of 1.4. It has been regarded as one of the essential tasks of the data acquisition system to facilitate and to accelerate all calibrations and adjustments necessary for the hodoscope. Therefore, lower data rates can be directly taken over by the computer, evaluated and, for instance, displayed instantaneously. Also it is possible to set computer controlled levels for all discriminators via digital to analog converters.

3. Considerations Leading to the Present Hodoscope Design

Due to the distance between the collimator and testsection, parts of the testsection are viewed by the detectors, which are not located in the field obtained by direct prolongation of the collimator slit. The counting rate in the detector originating from a point source versus the source position is shown on the right hand side of Figure 3. It has a trapezoidal shape. Therefore, in our case, the effective view field of one channel has the dimensions 1 cm x 2 cm. The distance between neighbouring slits is chosen in such a way that the outer edges of the view fields overlap and the effective view fields just touch each other in the pin plane. Only in this case the sum of count rates of adjacent channels has a flat response.

Since it has been decided that only vertical fuel density changes need be detected, it would be sufficient to have only two arrays of slits, one looking onto the testpin and the other for background determination. It would be adequate to make the slits sufficiently wide to confine all possible horizontal fuel movements in their region of flat response.

We have, however, chosen two smaller channels to look at the pin. The main advantages of this solution are:

1. A maximum counting rate can be obtained which is greater by a factor of two.

2. A certain sensitivity to horizontal fuel movements is maintained.

3. Redundance.

It has already been mentioned that a spatial resolution of about 10 cm in the vertical direction might be sufficient. Also in some phases of the experiment a more detailed resolution would be desirable, especially at the beginning of pin failure. However, since the maximum counting rate attainable with one detector is limited, it was necessary to use 5 slits over this region to obtain the required sensitivity of the hodoscope. For the expected fuel velocities, it should be possible to take pictures of the fuel distribution at least every msec in order to be able to make use of this spatial resolution in favourable situations.

4. Results of Detector and Preamplifier Test Measurements

Several prototype detectors and preamplifier discriminator systems have been tested in stationary and transient neutron fluxes to demonstrate

that their performance is adequate for the application intended. Especially, we wanted to find out the maximum possible counting rates, the behaviour under fast pulse rate changes, and the recovery time following high overloads.

By use of a very fast current-sensitive preamplifier, the pulse width at 1/10 of the maximum for our fission chambers has been determined to be about 70 nsec. The preamplifier finally selected which had a much better signal to noise ratio, gives 80 nsec. Figure 4 shows the plateau curve for the final detector preamplifier system. At the lower end of the curve restrictions are already imposed by α-pileup. Therefore, it is useless to increase further the signal to noise ratio.

Figure 5 represents the dead time losses for the f. c. preamplifier-discriminator system. The ratio of measured counts to fission pulses generated in the chamber has been plotted versus the number of these pulses. Up to at least $4 \cdot 10^6$ fission pulses in the chamber, the measured curve coincides with the theoretical curve obtained for a dead time of 85 nsec. This results in counting losses of about 8% at 10^6 cps.

Transient measurements have been carried out in a beam geometry at a TRIGA-reactor. The experimental conditions were quite similar to those expected for the CABRI hodoscope. Generally the behaviour of the f. c. system was completely identical to that during stationary measurements. Space charge effects and drifts in electronics did not lead to abnormal results of counting rates below $7 \cdot 10^6$/sec. Following very high pulse rates of about $4 \cdot 10^7$/sec the system recovers immediately when the counting rate has dropped again below $7 \cdot 10^6$/sec. This is shown in Figure 6 where the same reactor pulse has been measured twice with the same equipment, the only difference being that for one measurement the

thermal neutrons from the reactor had been also used. This was possible since the f. c. contained some additional U-235. The measurement performed with only fast neutrons (open circles in the drawing) has been normalized to the thermal neutron measurement in the postburst region. Above about $7 \cdot 10^6$ counts/sec the applied dead-time corrections did no longer lead to an agreement between both measurements. It is suspected that space charge effects in the chamber are responsible for this behaviour.

To overcome the high noise levels of the current sensitive preamplifiers, large internal gas amplifications of about 70 had to be applied in the p. r. counters. However, these high gas multiplications lead to additional counting losses, since the magnitude of space charges originating from pulse rates above $1\text{-}2 \cdot 10^5$/sec is big enough to reduce the electric field strength and thereby the gas amplification. The higher the original gas multiplication and the discriminator levels are, the higher are the additional counting losses. However, it was demonstrated that for counting rates up to 10^6/sec gas multiplication factors of about 10 are just tolerable for our proportional counters. Since we want to obtain these counting rates of about 10^6/sec with the p. r. system, we had to reduce the noise level of the preamplifiers. Until now a factor of five has been gained in the signal to noise ratio through the modifications mentioned in section 2 above.

However, by these changes the pulse width at 1/10 of the maximum increased from 150 nsec to 220 nsec. Figure 7 shows the counting loss curve for the cld and the modified preamplifier together with the theoretical curve obtained for a dead time of 200 nsec. It appears that for the modified preamplifier allowing lower gas multiplications a satisfactory agreement has been attained with the theoretical curve.

Figure 8 shows a reactor burst resulting from a relatively small reactivity input. In this case the deviation of the in-core fission chamber monitor, which was sensitive to γ-rays too, from the exact neutron signal is not greater than about 15%. Although this measurement has been carried out with the unmodified p. r. preamplifier and only an approximate correction for the counting losses could be applied, the agreement with the monitor is quite satisfactory.

In Figure 9 the response of the unmodified p. r. system to a large reactor burst is compared to the monitor. The difference clearly results from space charge effects in the counter. It is concluded from the non-symmetrical form of the proton recoil measurement that about 5 msec are necessary to remove the space charge. Therefore, in this case, the system was correctly counting again (as under steady state conditions) when the input pulse rate had dropped below $0.6 \cdot 10^6$ cps.

Summarizing we have now established an f. c. system which is able to handle pulse rates of about $7 \cdot 10^6$/sec with dead-times of about 85 nsec and a p. r. system which can treat pulse rates of about 10^6/sec with dead-times of about 200 nsec.

5. Capabilities of the Present Hodoscope Design

The question of interest to be discussed in this section is:

Is our hodoscope capable of meeting the requirements necessary for a reasonable comparison with fuel movements predicted theoretically?

To answer this question we must know the signal to background ratio which has been estimated to be 0. 96 in case the full diameter of the

test pin is within the view field of one channel, and 0.48 in case the test-pin is viewed by two horizontal channels. This estimation might however be rather conservative since it has been deduced from the central neutron flux of the undisturbed reactor core and differences between signal and background spectrum have not been taken into account.

The most straight forward way of background correction consists of subtracting the count rate of channel 3 from the count rates of channels 1 and 2 (Figure 3). A more sophisticated background correction would use the sum of all background channels or a separate accurate neutron flux measurement together with preburst calibration factors. Then the error in the background determination could be practically neglected.

Figure 10 presents the hodoscope sensitivity for both kinds of background correction and two extreme experimental situations which are possible in the CABRI test program. A very mild and a very energetic excursion are considered, leading to total energy inputs of 0.4 and 3.4 KJ/g, respectively, in the test pin. During the first transient which might be applied to a fuel pin with high burn-up, pin failure is expected to occur after the peak power has been reached. In the second transient, which might be used for fresh fuel pins, pin failure will occur most likely before or at the peak. Rapid fuel movement is suspected within 30 msec after pin failure.

The results presented in Figure 10 have been obtained for 5 rows and are integrated over 5 msec. Although the cases presented in Figure 10 are extreme ones, we remain below the 5% sensitivity margin, at least within the 30 msec time interval after pin failure. It can also be concluded from Figure 10 that in some regions 5-10% variations of the fuel density can also be detected for much finer space and time resolutions. Therefore, a reasonable strategy would be to add the results of channels and to integrate overtime intervals depending on experimental progress.

Literature

1. J. Bailly, G. Kessler, and H. J. Teague, "In-Pile Safety Tests on Fast Reactor Fuels," Nuclear Energy Maturity, Paris, April 1975 ANS-Transactions Vol. 20 (1975) 527.

2. H. U. Wider, J. F. Jackson, and L. L. Smith, "An improved analysis of fuel motion during an overpower excursion," Conf. -740401 p. 1541 (1974).

3. E. T. Rumble, W. E. Kastenberg, D. Okrent, and J. O. Cermak, "Fuel movement investigations during LMFBR overpower excursions using a new model," Conf. -740401 p. 1556 (1974).

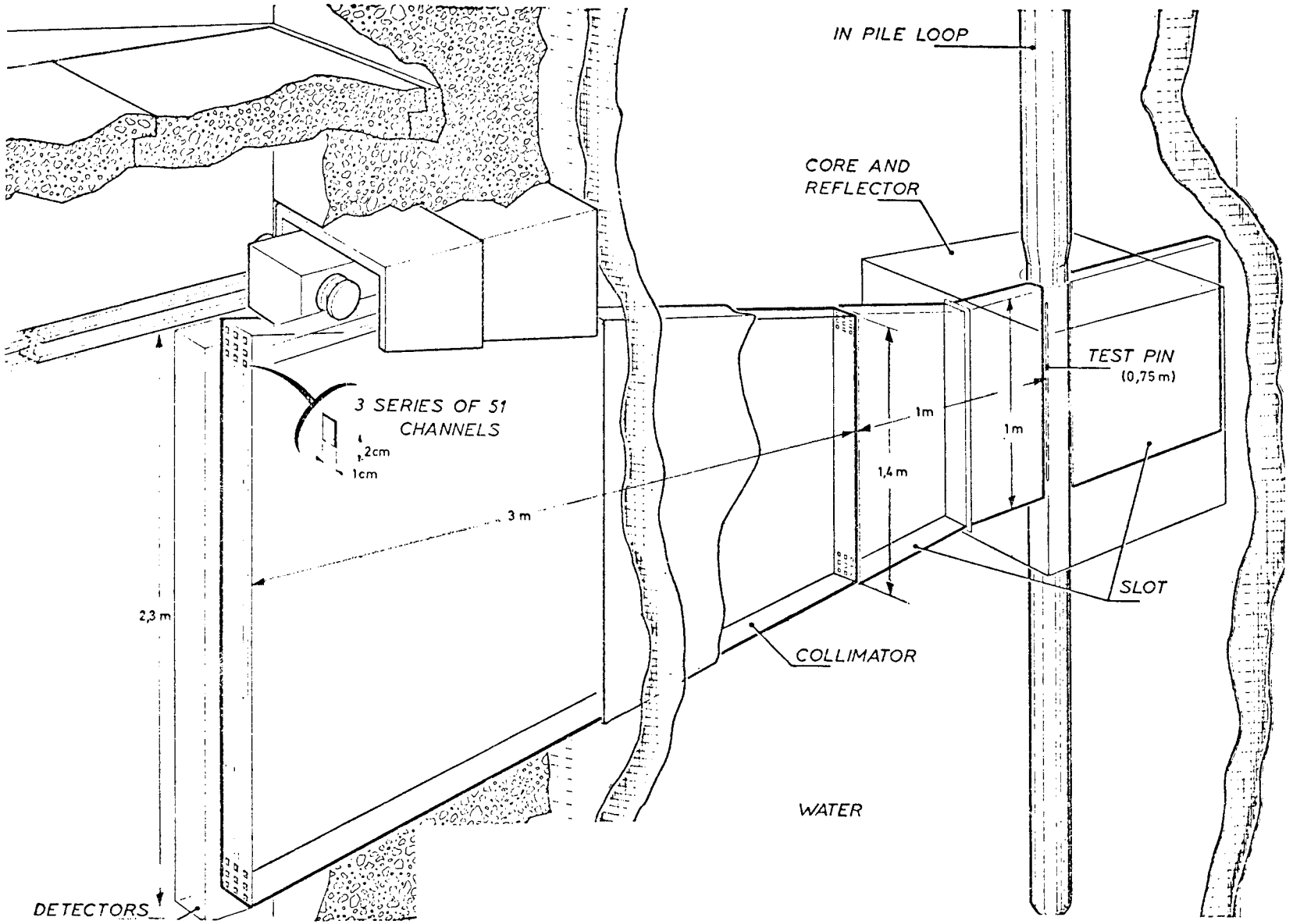

Figure 1. Artist's view of the hodoscope and slot arrangement in the CABRI reactor.

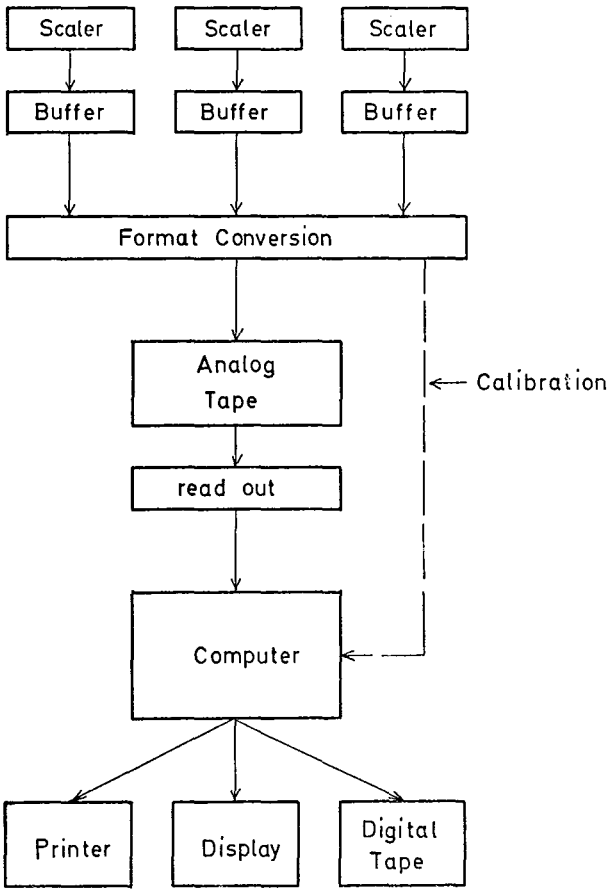

Figure 2. Schematic diagramme of the data acquisition system.

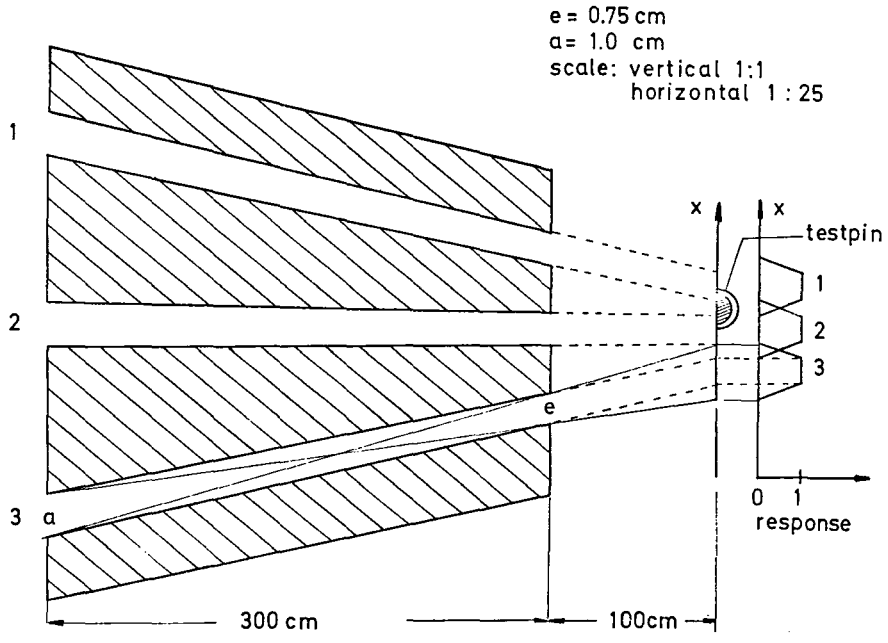

Figure 3. Response of a three-channel collimator to a point source.

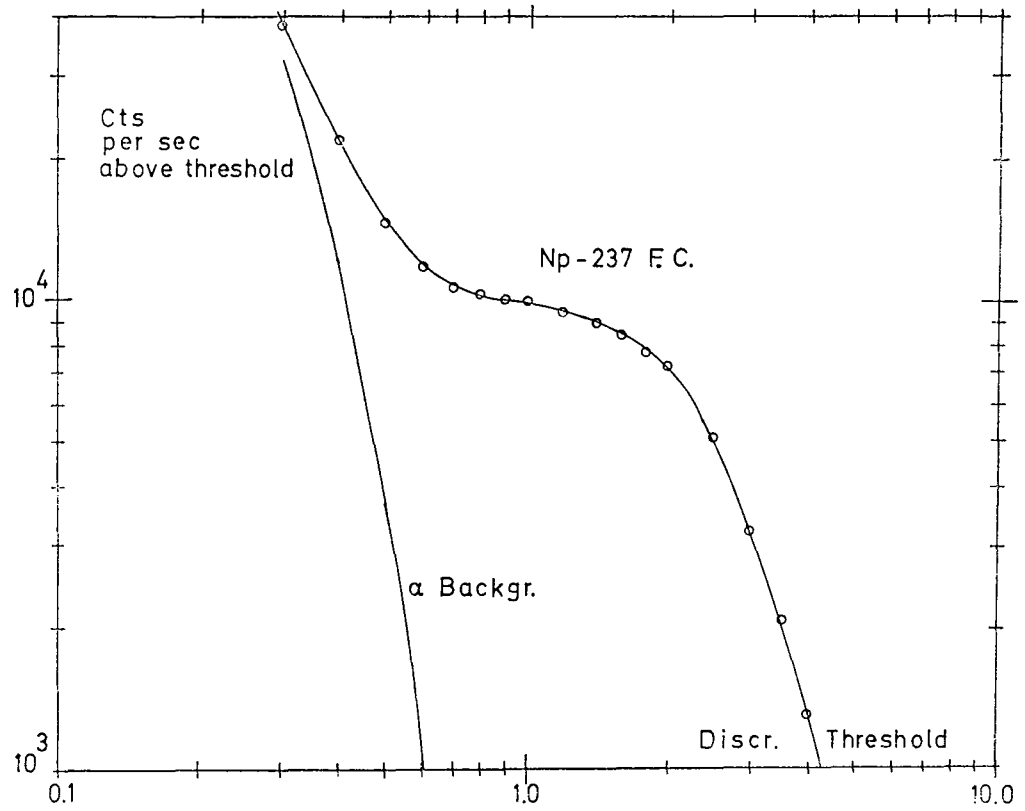

Figure 4. Integral bias curve for the Np-237 fission chamber.

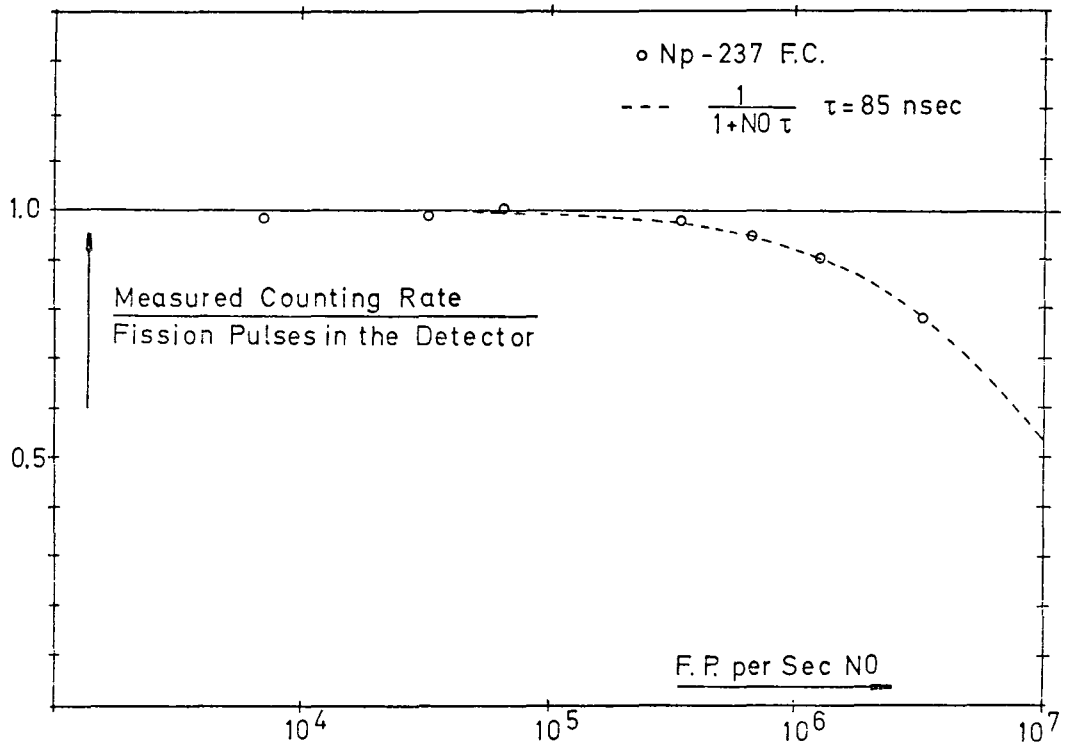

Figure 5. Dead time losses of the f. c. preamplifier-discriminator system versus fission pulse rate above threshold in the chamber.

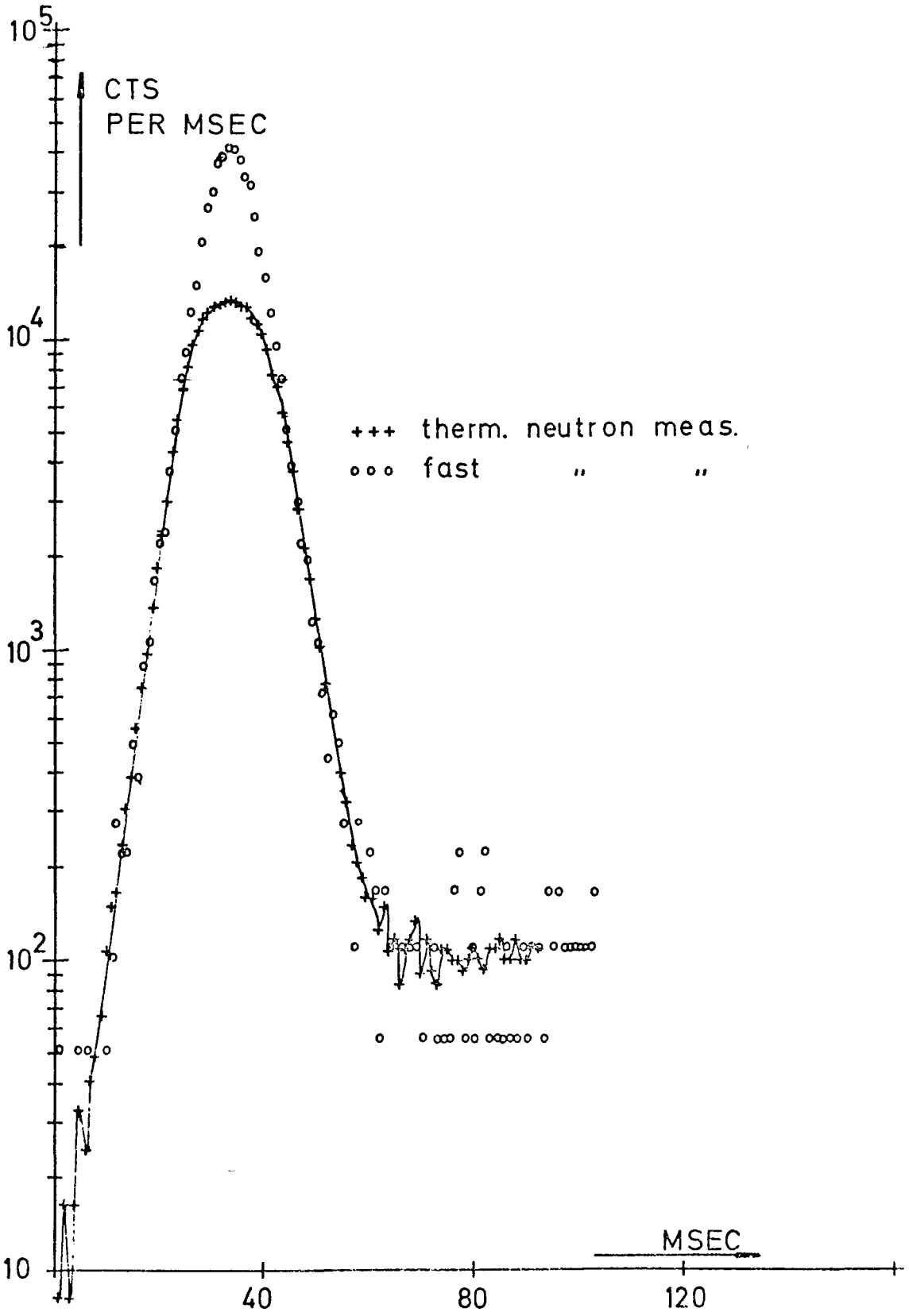

Figure 6. Comparison of reactor transients measured with the f. c. pre-amplifier system once with high and once with low efficiency of the f. c.

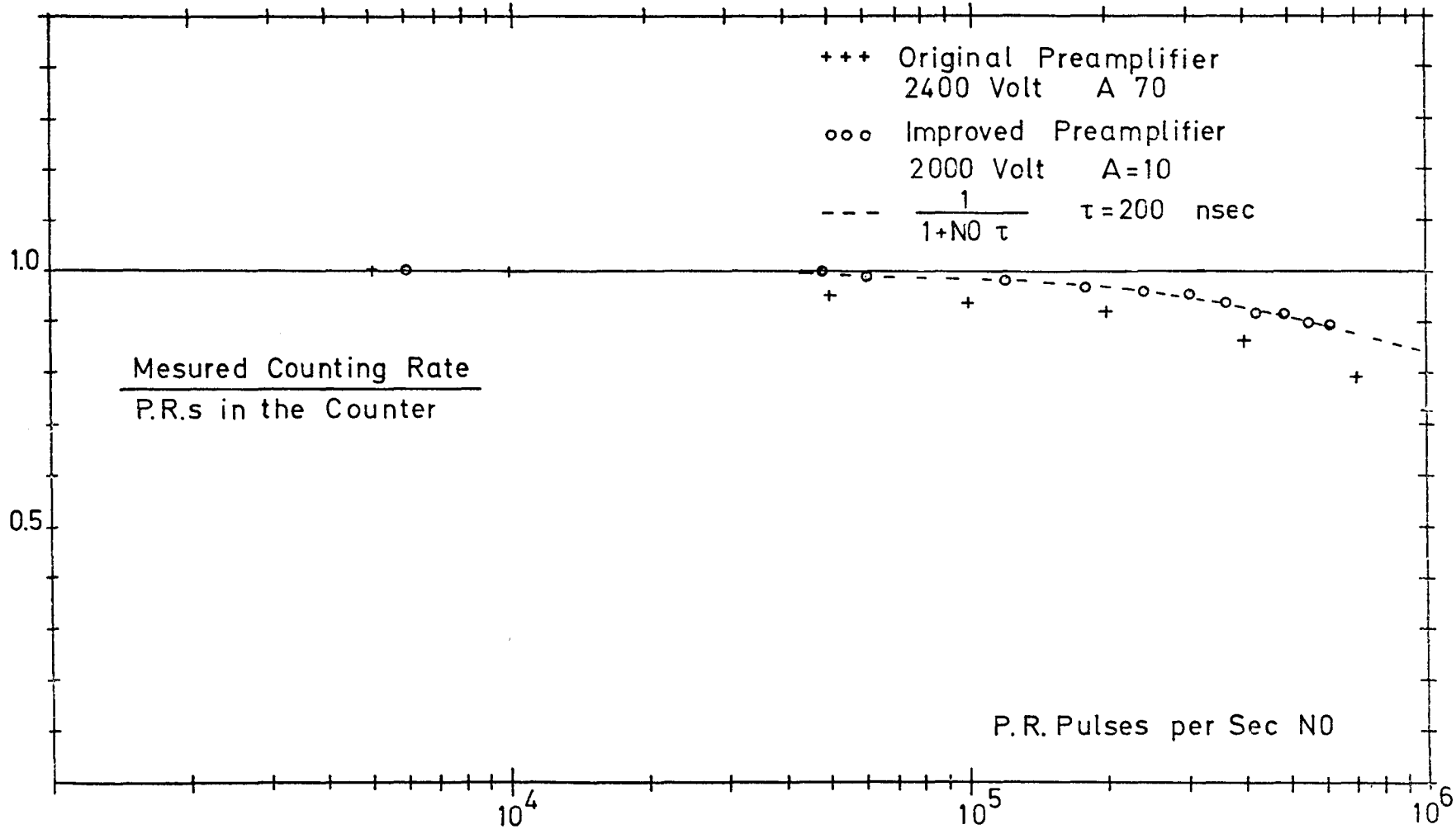

Figure 7. Counting losses of the p. r. system versus p. r. pulse rate above threshold in the counter.

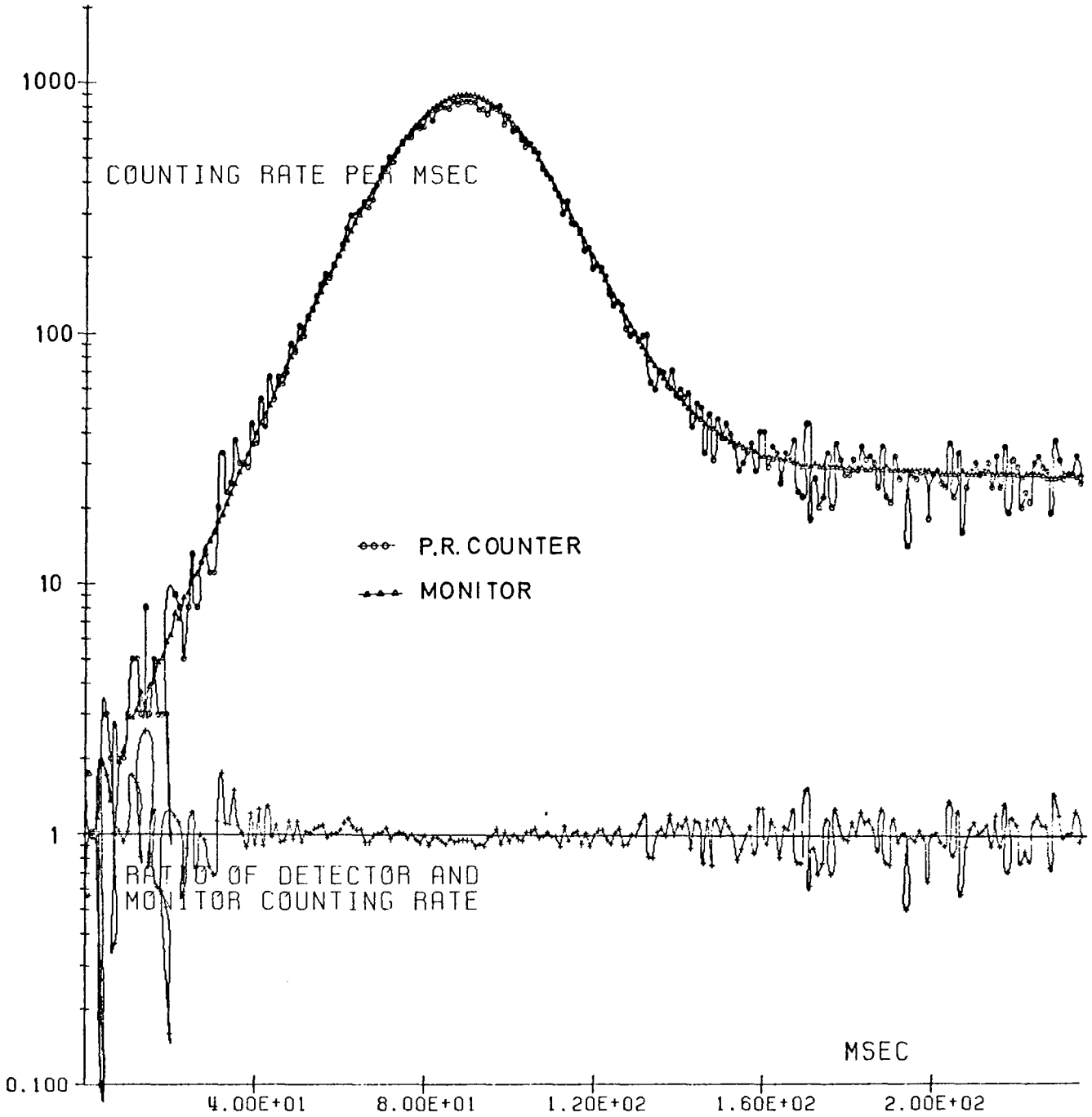

Figure 8. Mild reactor excursion measured with the nonimproved p. r. system.

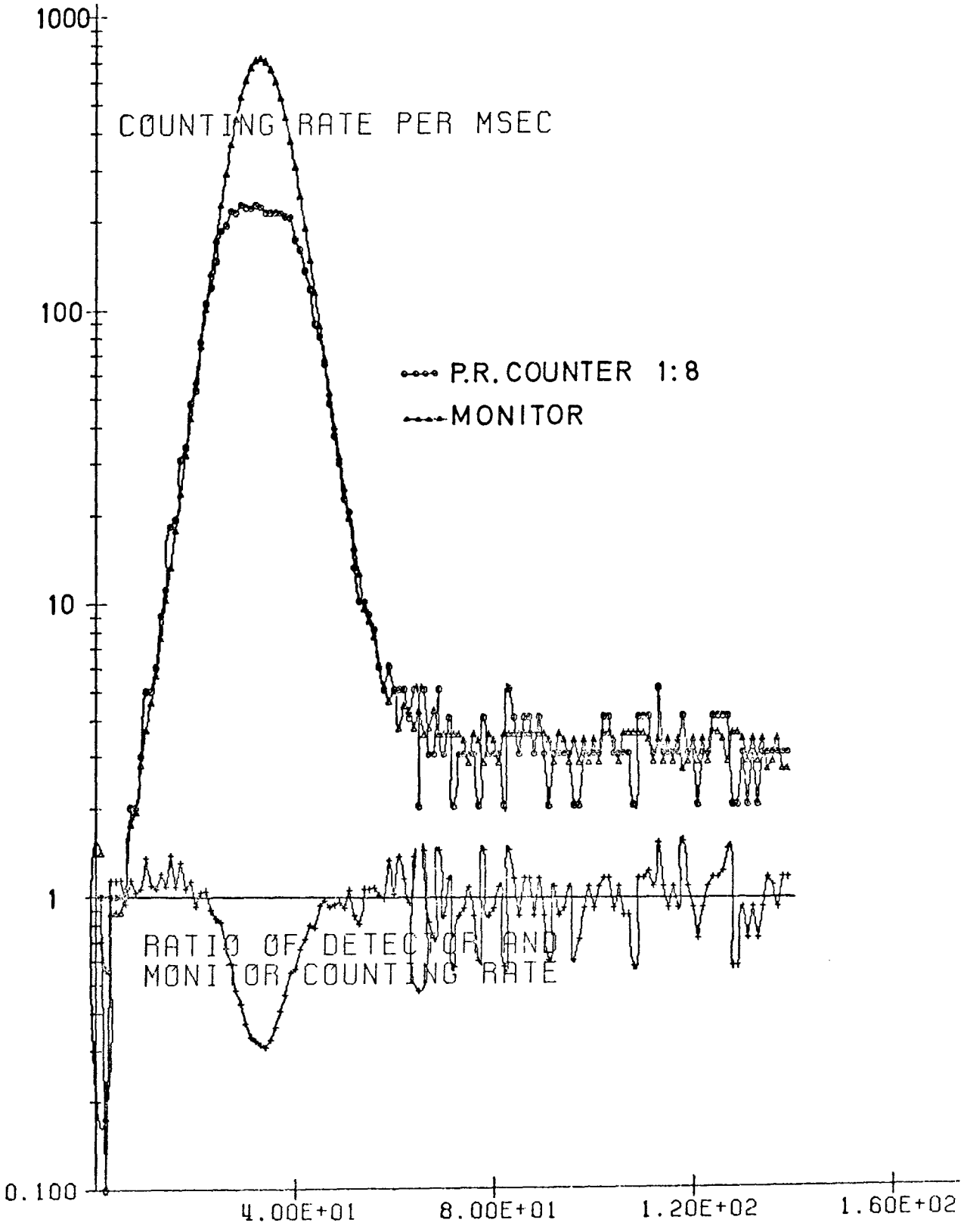

Figure 9. Energetic reactor excursion measured with the nonimproved p. r. system.

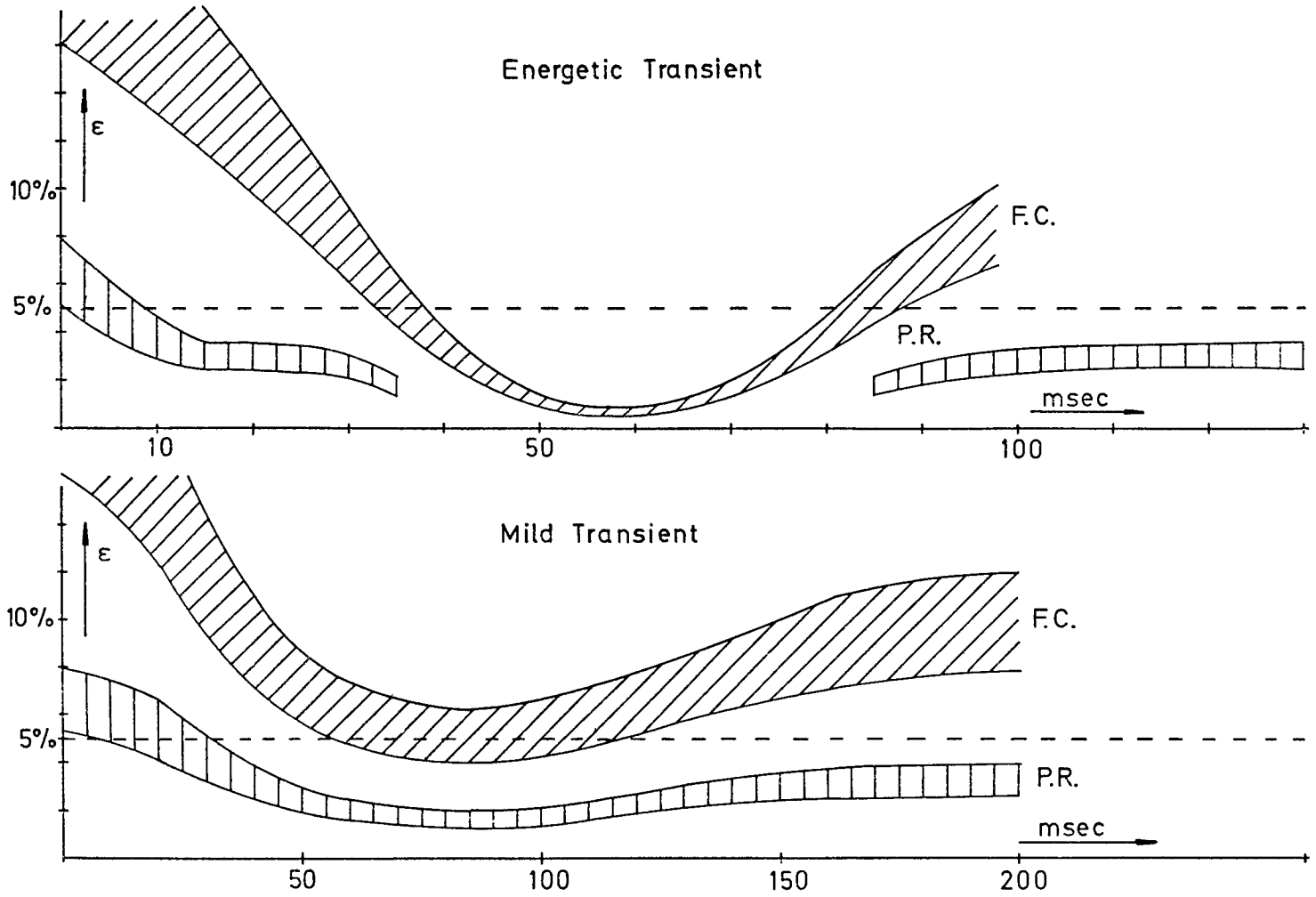

Figure 10. Time dependent hodoscope sensitivity for two extreme experimental situations.
Energetic transient: 50 $/sec, final reactivity inserted 3.5$. 12 msec f w h m
Mild transient: 30 $/sec, final reactivity inserted 1.1$. 85 msec f w h m

Results of 5 rows have been added and integrated over 5 msec. P. r. sensitivity is only drawn when p. r. counting rate less than 10^6/sec.

Hodoscope Collimator for 122-cm Viewing Height at TREAT*

by

A. De Volpi, J. J. English, L. E. Garrison, A. R. Jamrog,
W. J. Kann, R. W. Kush, C. V. Pearson, R. J. Pecina,
D. C. Rardin, and D. J. Travis

Argonne National Laboratory
Argonne, Illinois 60439

*This work supported by the U. S. Energy Research and Development Administration.

Hodoscope Collimator for 122-cm Viewing Height at TREAT

The fast neutron hodoscope at TREAT contains major subsystems for collimation, detection, pulse processing, data storage, and support facilities. The collimator was designed to measure fuel motion in experiments containing typically 34-cm EBR-II fuel pins. Now, transient tests with active fuel length of 91 cm are beginning to be performed. A new collimator system has been designed, fabricated, and -- at this time -- partially installed at TREAT to satisfy requirements for extended fuel surveillance.

Functional Requirements

Functional goals for the new design were formulated with two major constraints: existing detectors and electronics were to be reused, and modification of the reactor was to be minimized. In order to provide coverage of fuel dispersal above and below active zones of FTR fuel, the total height viewed was set at about 122 cm. The viewing width was expanded to 6.6 cm, corresponding to a 61-pin FTR bundle.

Based on the above functional requirements, it was necessary to modify the viewing matrix at the object plane. The existing collimator views a height of 51 cm and width of 5.7 cm with a 23 x 15 array of detectors viewing 0.38 x 2.25 cm rectangles at the object plane. (Actual "resolution" for fuel motion is about an order of magnitude better than inter-detector spacing.) The new collimator has spacings of 0.66 by 3.45 cm. Although there are 360 slots slots in the 36 x 10 array collimator, instrumentation is restricted to the 334 detectors available from the original system.

Design Features

The new collimator design is similar in principle to the original collimator, yet incorporates many improvements intended to increase its usefulness as a research tool and facilitate the preparation process prior to the performance of experiments.

The seven major components of the collimator subsystem are as follows:

(1) Front Collimator: high-density material to minimize background and cross-over neutrons.

(2) Rear Collimator: primary-fast-neutron channeling component, including 20 slotted steel plates 181 cm in length.

(3) Rear Collimator Base and Shielding: to provide adjustments for alignment and shielding to minimize hazard during operations.

(4) Lead Filter Assembly: to have capability of inserting up to six lead plates in front of neutron detectors in order to reduce perturbations from gamma rays.

(5) Detector Plate: mounting for 360 neutron detectors.

(6) Detector Enclosure: light- and dust-tight enclosure around the detectors.

(7) Source Locator: remote positioning of higher intensity (30 Ci Pu-Be) neutron calibration source for greater reproducibility and reduced personnel hazard.

In addition to the major components of the collimator, reactor facility modifications are required:

(1) Existing Collimator: disassembly, removal, modification, and relocation to opposite end of TREAT slot. Also, addition of a shield and beam shutter.

(2) Slotted Elements: fabrication of unfueled elements to provide a clear viewing path for full-length pins.

(3) Cable Trenches and Cables: extension of existing trench and routing of a new trench to the relocated collimator and new cables to both collimators.

(4) Front Collimator Installation: Support plate installation at the North face reactor cavity.

The old collimator is to be placed on a standby basis for possible use primarily in single-pin experiments for which the better resolution may be needed.

In order to accomplish the requisite expansion of viewing region and still meet physical constraints, the collimator channels are "cross-focussed," that is, the image is inverted with respect to both vertical and horizontal axes of symmetry in the object plane. The crucial parameter which was maximized in design was the minimum path length through steel for radiation from one channel crossing over to an adjacent channel; this was held to a minimum of 100 cm, although the present collimator has a 150 cm path.

Specific Features

The seven major components are illustrated in Fig. 1. The front collimator is open horizontally but restricts vertical entry of neutrons not focussed directly upon target detectors. The aperture pieces, made of a tungsten alloy, are separated by 1 cm.

The 21 plates of the rear collimator are stacked, doweled, and bolted together. An outline of one type of plate is shown in Fig. 2, along with an indication of the method of stacking.

A scanning apparatus for manually adjusting (panning) the collimator has been included in the base of the collimator, along with an dial indicator.

Up to 7.5 cm of lead are included in the gamma filter assembly in the form of six plates each of 1.25 cm thickness. Any number of plates may be positioned manually.

The aluminum detector plate supports each detector at the proper angle of beam emergence. This detector plate is mounted within the neutron detector enclosure.

A remotely controlled motorized drive has been designed for positioning the calibration source in front of each detector. The source may be positioned in 0.025 mm increments with positioning reproducibility of ±0.0125 mm vertically or horizontally. The locator is interfaced to a microprocessor which operates under paper tape or operator control.

Fabrication

Fixturing and machining of the rear collimator lamination assembly represented the largest task in fabrication of the collimator. Nineteen carbon steel plates (1.90 x 137.79 x 182.24 cm) were first rough cut to profile and heat treated. Then another rough cut was made, this time to taper on a horizontal mill. Next, the plates were finished on a surface grinder using a vacuum chuck mounted on a sine table. The plates were ground to one of two sizes.

Each plate was then slotted on the horizontal mill by mounting the vacuum chuck and sine table vertically; an indexing fixture was used to rotate the plate together with the chuck and table, in order to provide the angles required for each of the slots. The outside surface of each side plate was stepped using the horizontal mill; these steps correspond to positions for collimator shielding blocks which reduce leakage radiation.

The plates were then stacked and aligned on a fixture, starting with the unslotted side plate followed by the 19 tapered plates, alternating the two types of plates. The slotted side plate finished the stack, which was then clamped and dimensionally inspected. The inspection was used to verify the dimensions required to machine the instrument hole locations in the detector plate so as to assure alignment of the detectors with the stack slots.

After inspection, the lamination stack was transferred to the vertical position and drilled and reamed for bolts and dowel holes, as shown in Fig. 3. Next, the stack was disassembled for cleanup and deburring of holes in each plate. The plates were coated with a thin

layer of silicon grease and restacked. The assembly was bolted together with side brackets in place.

Quality Control Provisions

Project practices were in accordance with Argonne Quality Assurance Division (QAD) policies and procedures. A plan was prepared which established specific QA requirements for design, procurement, and fabrication. These measures were particularly important with respect to the rear collimator and its relationship to the detectors.

Inspections of the slotted plates by QAD were made at the completion of each of the fabrication steps indicated in the previous section. The tapered plate surfaces were checked for flatness while held in the vacuum chuck mounted on the bed of the surface grinder. The plates were then released and inspected for thickness and taper.

The indexing fixture used to establish the angle of the slots on each plate was inspected for angular conformance while mounted on the horizontal milling machine. After each slot was cut it was checked for depth, width, and surface finish. The lamination stack was inspected after assembly to establish final dimensional requirements for the detector plate.

Lead sheets for the gamma filter were radiographed and inspected for voids.

Discussion

Because the new collimator design represents an extension of the previous multi-channel collimator, no significant problems in design or fabrication were encountered. The use of cross-focussing accommodates some limitations caused by the requirement that reactor modifications be minimized. In this case, no cutting of concrete from the biological shield area was needed, and only a cable trench was extended on the reactor floor. Had the design not been limited in this fashion, the cross-focussing feature could have been applied to reducing the width of the slot through the reactor which was retained at a nominal width of 10 cm. It was necessary to compromise on the amount of material in the minimal neutron cross-over path between detectors, but close to 100 cm of steel is probably conservative in terms of preventing neutron cross-talk.

By filling all gaps between the front collimator, rear collimator, and biological shield with stepped concrete blocks, a significant reduction in ambient background is expected. This reduction is primarily needed during steady-state experiments when personnel are allowed on the reactor floor. Because calibration of the hodoscope detectors will be based on a 30 Ci Pu-Be source, it may be necessary to add portable shielding to minimize inadvertent exposure.

Present status of the project is as follows: All major components have been fabricated and assembled. Slotted fuel elements have already

been used in the reactor. Modifications of the TREAT facility necessary to accommodate the new collimator have been completed. The front collimator has been installed and aligned with minimal difficulty during an allocated reactor shutdown in October. The next major phase of installation is scheduled to start in December for the primary purpose of installing the rear collimator and alignment of the two collimator sections with the core centerline. Then the detector system will be reconnected to the electronics, and testing of the entire system will take place.

Related activities still to be performed include fixtures and enclosures for the fission and gamma detectors and the reinstallation of the 51-cm collimator. A flat fission plate to simulate a uniform plane source of neutrons at the center of the reactor is currently being designed. This will be used to provide a more precise calibration of the detection systems.

A RAS project was formed for the fabrication and installation of the collimator. Scheduling, cost control, and adherence to standards were managed by project personnel linking engineering, machine shop, vendor, operator, and user requirements. Use was made of the network processor program PMS-IV and of EZPERT project graphics.

The design, fabrication, installation, and project experience gained from this larger collimator will provide another steppingstone for scaling hodoscope techniques to other safety test facilities.

Acknowledgements

We are indebted to N. Kramer for supervising installation at TREAT, G. Lobell for fabrication planning and supervision, J. Kotura for procurement assistance, and C. Miller and E. Hill for scheduling assistance.

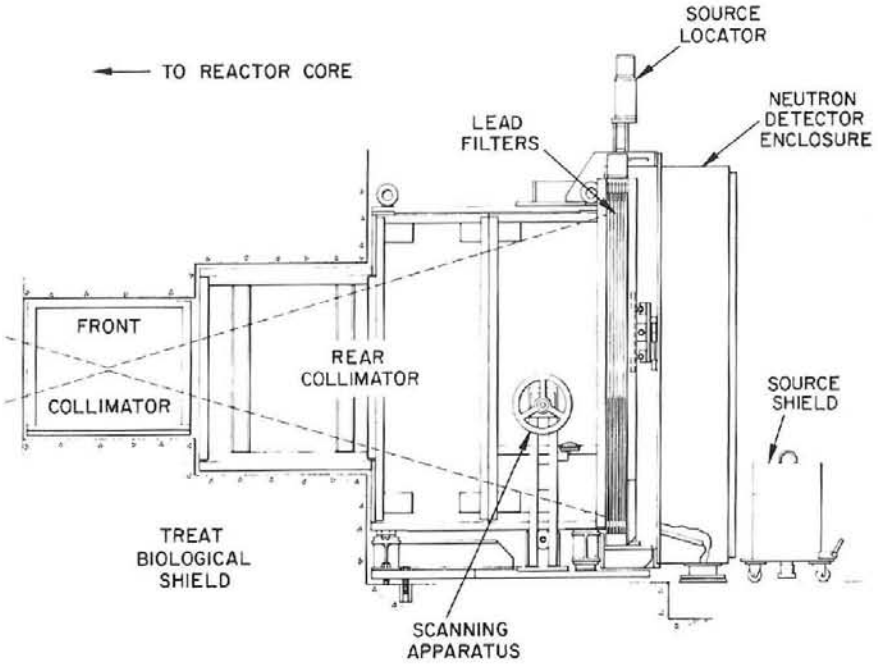

Figure 1. Schematic Assembly Drawing of New Collimator Positioned at Reactor Face

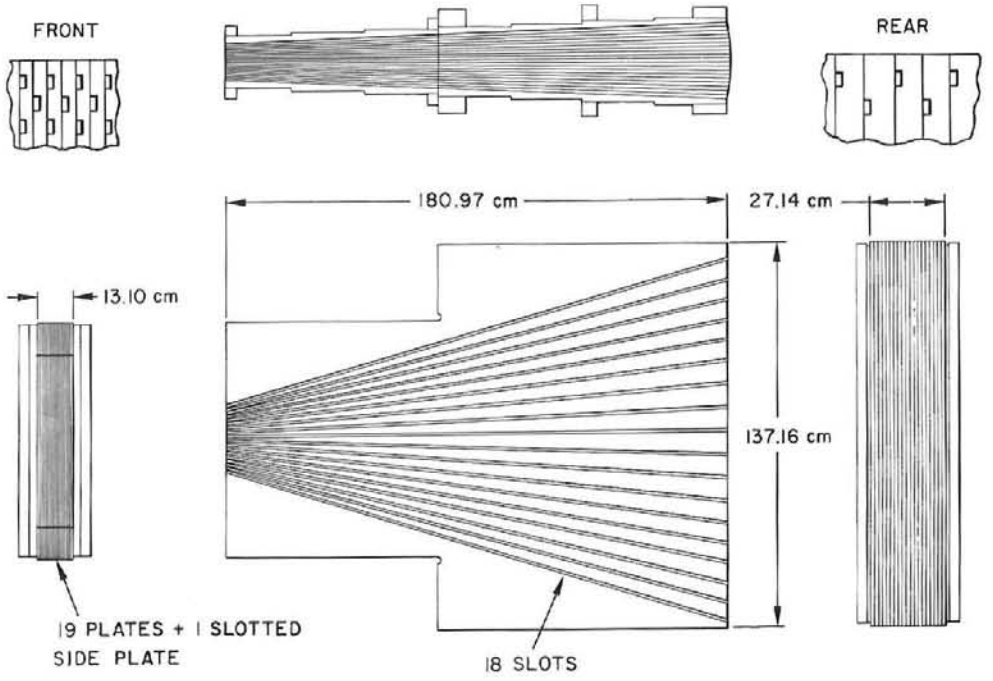

Figure 2. Design Details of New Collimator Plates

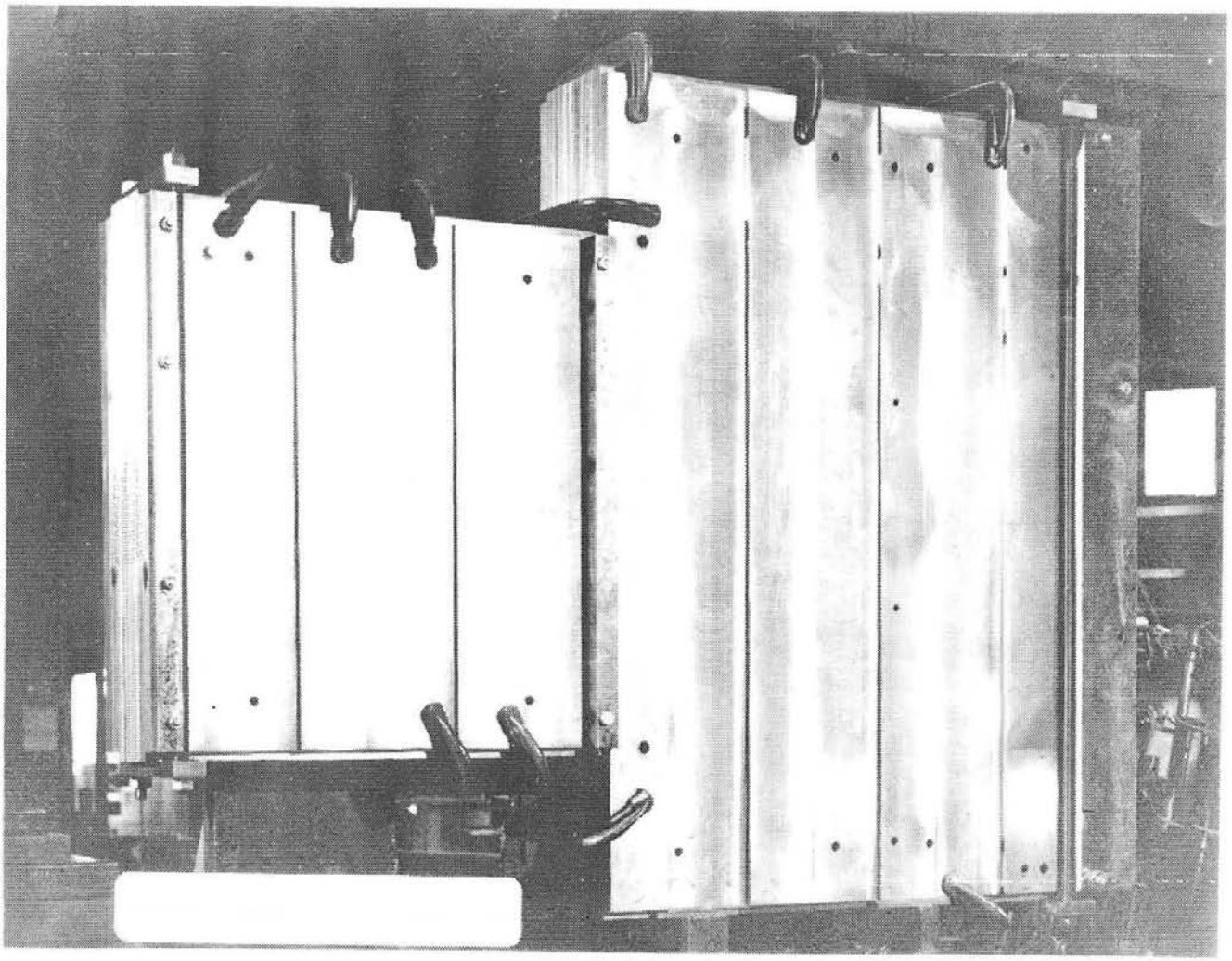

Figure 3. Collimator Plates Stacked and Clamped Temporarily Together

Dielectric Track Detector*
Fuel Motion Monitor System

by

S. R. Dolce
Field Experiments Division
Sandia Laboratories
Albuquerque, New Mexico 87115

*This work supported by the U. S. Energy Research and Development Administration

Introduction

The fuel motion monitor system to be described is one of the systems being developed for use in the upgraded Sandia ACPR. Like the Hodoscope, this system will image fast neutrons from the test fuel element--but there the similarity to the Hodoscope ends, because this system will use Dielectric Track Detectors (DTD's) for both neutron detection and recording.

Kimfoil[1] is a commercial polycarbonate film that is used as a capacitor dielectric. It is just one example of a Dielectric Track Detector. When a DTD is struck by an energetic and heavy ion, the ion produces damage along its path. If the dielectric is then etched, the damaged track enlarges to form a crater. These craters are then easily visible with an optical microscope.

These dielectrics have several properties that make them ideal for use in a reactor environment. First of all, they are completely insensitive to any of the background radiations to which they can be exposed in that environment. In particular, gamma-rays are incapable of producing sufficient damage to produce tracks. Thus a problem with a gamma-ray background will be non-existent. As an illustration of their insensitivity to backgrounds it might be pointed out that, in an application conceived by the author for use at the Nevada Test Site, they are used to measure neutron spectra (by registering fission fragments) of underground nuclear detonations.[2] With all of the

backgrounds in that environment, the DTD's see only what they are intended to see. A second advantage of the DTD's is that they are inexpensive. The Kimfoil used in this work cost less than $200 for 25 pounds of ½-mil-thick film. Another advantage of a system using these dielectrics is that no active instrumentation is required. Data recording is done in the detectors themselves. The tracks they bear are permanent. They can be exposed during a reactor pulse, and can be read anytime afterwards. Finally, their response will remain linear for two orders of magnitude greater neutron fluence than will be encountered in ACPR experiments.

Figure 1 shows a conceptual version of a system being developed for ACPR. The central portion of the figure is a view looking down on the ACPR core with a test fuel element at its center. The system consists of a moderating collimator with ^{238}U, or some other nuclide with a suitable fission threshold, at the exit of the collimator, and a tape transport. Since the dielectric is insensitive to the reactor radiations, the collimator does not have to be an absorber. It need only be a moderator to insure that the neutrons that reach the collimator exits have either not scattered, and so still remember where they came from, or else they have scattered below the fission threshold of ^{238}U. This means that a simple and inexpensive collimator of the sort shown at the top of this figure can be utilized. In this sketch, grooves are cut in polyethylene plates and then the plates are

stacked to form the collimator. The sketch at the bottom of this figure shows an enlargement of the dielectric region. Dielectric track detector material in the form of ¼ inch wide tape is drawn past the collimator exits in the zig zag fashion shown. Between the tape and the collimator exits is a relatively thick layer of ^{238}U. The ^{238}U is there to convert fast neutrons to fission fragments, and it is the fission fragments that are recorded on the track detectors as they move past the collimator. The uranium is to be thick so that there need be no calibration between channels. The same number of fission fragments with the same energy spectrum will emerge from a 6 mgm/cm^2 slab as from one a quarter inch thick.

The tape will be started before the shot and will move at a speed so that during the reactor pulse a portion that starts out at one collimator exit will not have moved to the next. At 60 inches per sec, the rewind speed of a typical home tape recorder, better than 1 msec time resolution is expected. On analysis, the number of tracks per unit area as a function of position along the dielectrics will give the number of unscattered neutrons coming through each channel as a function of time.

Development of this system is now underway. The next immediate step will be to demonstrate the imaging properties of such a system and to look into parameters for a collimator design. These investigations will be done with neutrons from a motionless californium 252 source. After that, a one channel

transport will be built, and we will test a moving system. This will be followed by fabrication of a complete multichannel system.

As far as the hardware of this system is concerned, no major problems are foreseen. For example, requirements on the collimator are very minor when compared with any system that requires that neutrons and gamma-rays be absorbed, and systems that actively detect neutrons require this. There is no need for pulse shaping, descriminating, and signal conditioning electronics that are required for an active detector system. There is also no need for a high data rate data storage system. As far as the tape transport system is concerned, whether the zig-zag system shown in Figure 1 is used or other designs being considered, at 60 inches per second that problem is within the state of the art.

The one problem that caused concern was how to handle the data. A typical experiment will produce yards of tape which will have to be quickly and accurately read. To be useful, the reading system must be automatic and inexpensive--or else on hand. There were two methods available to read track detectors. The tapes could either be read optically or with a spark gap reader. Without going into the details of these methods or their drawbacks, neither was found suitable for this system.

A method developed by the author as a result of this concern is listed by title in the November 1975 Nuclear Science Symposium.[3] This method reads the track density by measuring

the energy spectrum of alpha particles transmitted through the dielectric--or of other particles with a well defined range. The basic features of this method will be described, but not the arithmetic involved in extracting the track density from the measured spectra--that detail is in the NSS paper.[3]

Figure 2 illustrates how the technique works. Consider alpha particles of energy E_o incident upon a track detector that has craters of the nature shown. Those that are incident in the region away from craters will lose an amount of energy ΔE that corresponds to the full thickness of the dielectric. Those that are incident at $r < r_2$ lose no energy whatever and emerge at their full energy E_o. Those that are incident with $r_2 < r < r_1$ lose some energy between none and ΔE depending upon the amount of material they encounter. The energy spectrum of alpha particles transmitted through a crater-bearing DTD will then depend upon the numbered craters per unit area. Figure 3 shows the simulated energy spectrum of alphas transmitted through a dielectric track detector with 10^6 craters/cm^2. The ordinate is the log of the fraction transmitted with a given energy, and the abscissa is energy in MeV. The simulation first calculated the number of alphas incident on each region and the thickness through which they pass, and their residual energy after passing through. The simulated spectrum was then dispersed to make it resemble an experimental spectrum. The simulation is broken into two components for clarity. The dots represent alphas that were transmitted through the undamaged bulk material, and the circled dots represent alphas that were

transmitted through craters. The peak at right is due to alphas transmitted through holes in the craters, and the broad region between the two peaks is due to alphas passing through the sloping walls of the craters. An actual measured spectrum would be the sum of these two components.

To demonstrate this technique experimentally, samples of Kimfoil were placed behind a mask in which there were three rectangular openings, and the samples were exposed to known numbers of the fission fragments from ^{252}Cf. Track densities ranging from less than $10^3/cm^2$ to greater than $10^6/cm^2$ were produced in this manner. The samples were then etched and were returned to the exposure chamber for reading with the alphas from ^{244}Cm.

Figure 4 shows the log of the spectrum measured through a sample in which there were 1×10^6 craters/cm^2. In it, one can see the three regions. At right is the peak due to alphas coming through the holes in the craters; at left are the alphas coming through the undamaged bulk material, and between are the alphas coming through the sloping walls of the craters.

Figure 5 shows the spectrum of unattenuated 5.8 MeV alphas taken right into the solid state detector without the Kimfoil in place. It is shown to explain the difference in slope between the two peaks in the simulation, and in the experimental spectrum. Symmetric dispersion was assumed in the simulation; and as can be seen here, there is in fact a large low energy tail.

Figure 6 shows the spectrum of alphas transmitted through a control sample--one that was etched, but was not exposed to fission fragments. There are two things to see here. First, the energy is downshifted from 5.8 MeV to 4.7 MeV. Secondly, and more importantly, there are no counts above the peak. Alphas that transmit with greater energy, as in Figure 4, had to have come through craters.

Figure 7 shows the last three spectra in one photo. In it, one can see first of all that the peak attributed to alphas coming through holes is in fact at the incident energy of 5.8 MeV and that the peaks of alphas transmitted through the bulk material do in fact line up also.

How these spectra may be used to obtain the number of craters per unit area in a DTD that has been exposed in an experiment may be seen by considering the spectrum of Figure 4. This spectrum is due to transmission through the whole DTD sample, and the region to the right of the large peak is due to transmission through craters. The ratio of these crater counts to the total number of counts is equal to the fraction of the total sample area that is occupied by craters. If one knows the average area per crater, then one has the number of craters per unit area. How the average area per crater and the number of crater counts can be determined in spite of the overlap caused by experimental dispersion is treated in the NSS paper.[3]

It might be noted in passing that this spectrum not only contains information about the crater numbers, but also contains information about the detailed shape of the craters. The size of the crater peak depends upon the number of craters per unit area, but it also depends upon the radii of the holes through those craters. The separation between the peaks determines the thickness of the dielectric, and the slope or yield of the region between peaks can be used to determine the cone angle of the craters.

Returning to the subject of fuel motion detection, to automate the process of reading tapes produced in an experiment, one needs only a simple slow moving transport to pass the tapes between an alpha source and a solid state detector. To obtain position resolution, one could use an aperture, but more reasonably a position sensitive detector[4] will be used and the data recorded in 2 - parameter mode. This is the next step in our experimental program with these detectors.

It might be pointed out finally that this technique should be useful for reading track densities at least as high as $10^7/cm^2$, with essentially no lower limit. To measure a low track density, one simply lets the dielectric sit in front of the alpha source longer. There are no background counts to worry about. Counts that appear in the crater region are there because there are craters.

Footnotes/References

1. KIMFOIL is the registered trademark for a high molecular weight polycarbonate film made by the Peter J. Schweitzer Division, Kimberly-Clark Corp.

2. R. I. Ewing, Trans ANS 17, 92 (1973).

3. S. R. Dolce, "Reading Dielectric Track Detectors Using Transmitted Partices", to be published in February 1976 issue of IEEE Transactions on Nuclear Science.

4. S. R. Dolce, Rev. Sci. Instrum. 45, 499 (1974).

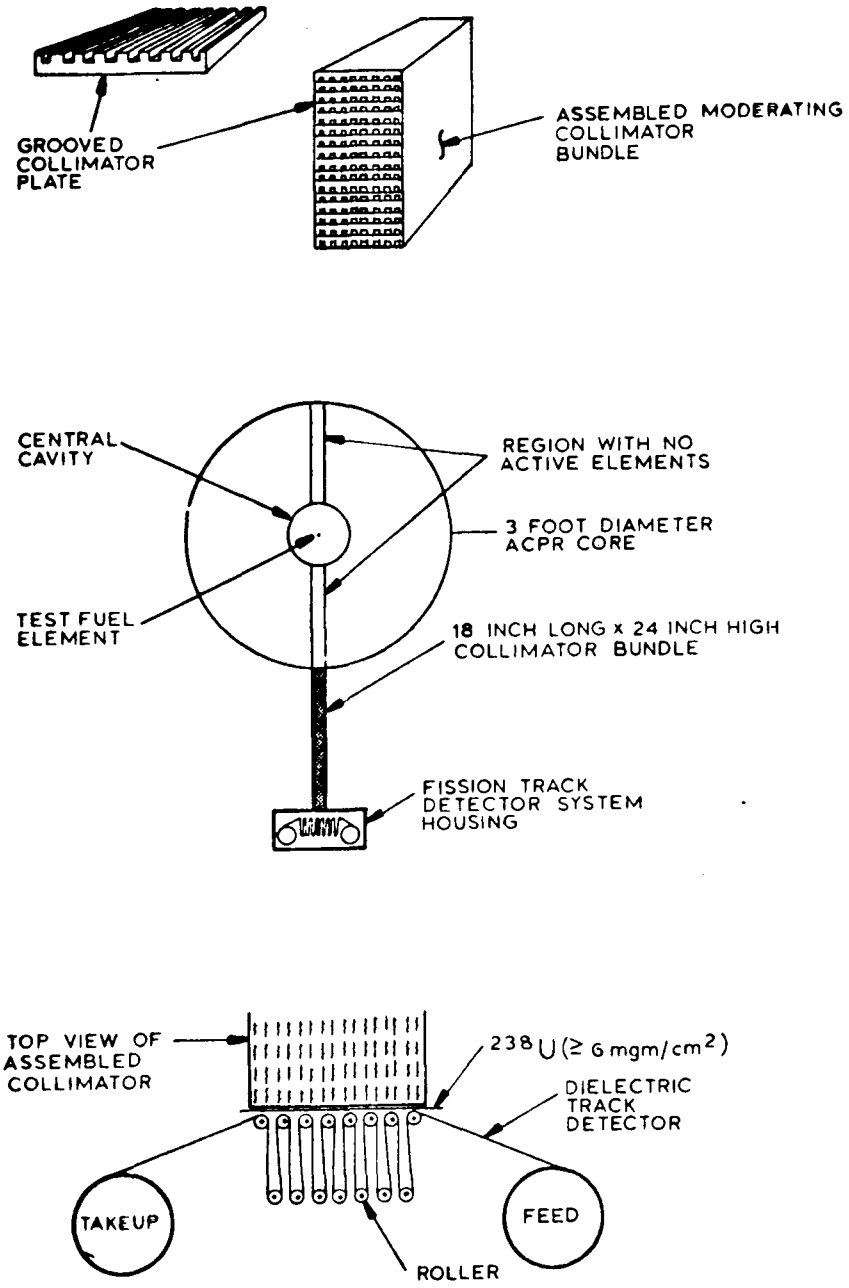

Figure 1. Conceptual version of a moving-DTD fuel motion monitor system for ACPR. The central portion views ACPR from above, and shows the collimator and DTD system. The upper portion shows how the collimator may be constructed, and the lower portion shows an enlargement of the DTD transport system.

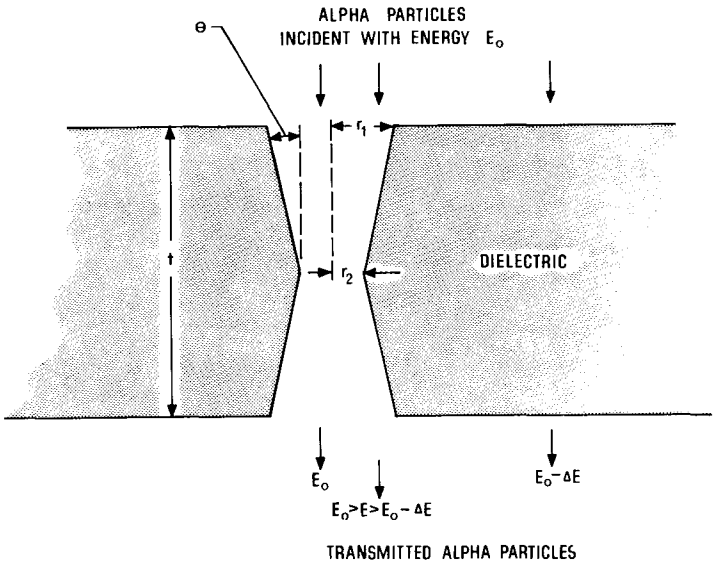

Figure 2. Cross section through a DTD showing doubly open conical crater, and the angle and radii that characterize crater shape. Also shown are the energies with which alpha particles incident on various regions of the DTD would be transmitted.

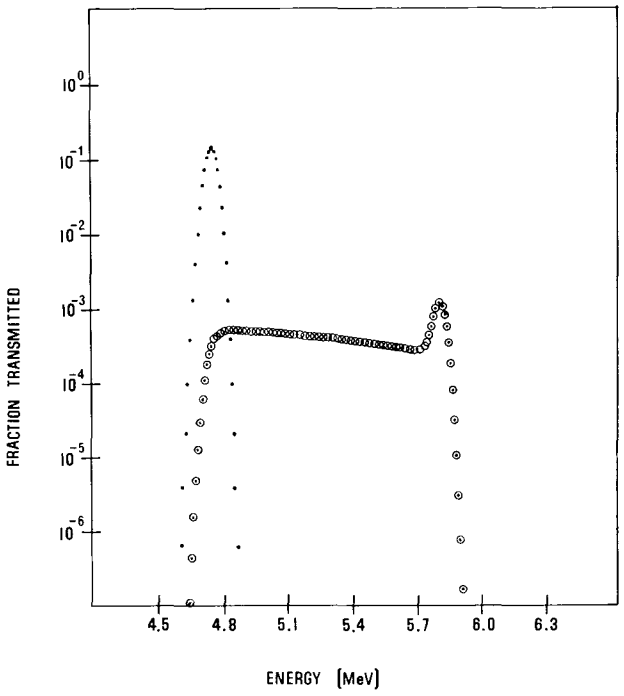

Figure 3. Simulated spectra of 5-8 MeV alpha particles after transmission through 1.42 mgm/cm^2 Kimfoil DTD with 1.02 x 10^6 craters/cm^2---each with r_1 = 1.28 μm, r_2 = 0.54 μm, and θ = 5.19°. Ordinate is log of the fraction of alpha particles transmitted with energy E, and abscissa is E in MeV. Dots represent transmission through undamaged bulk material, and circled dots represent transmission through craters.

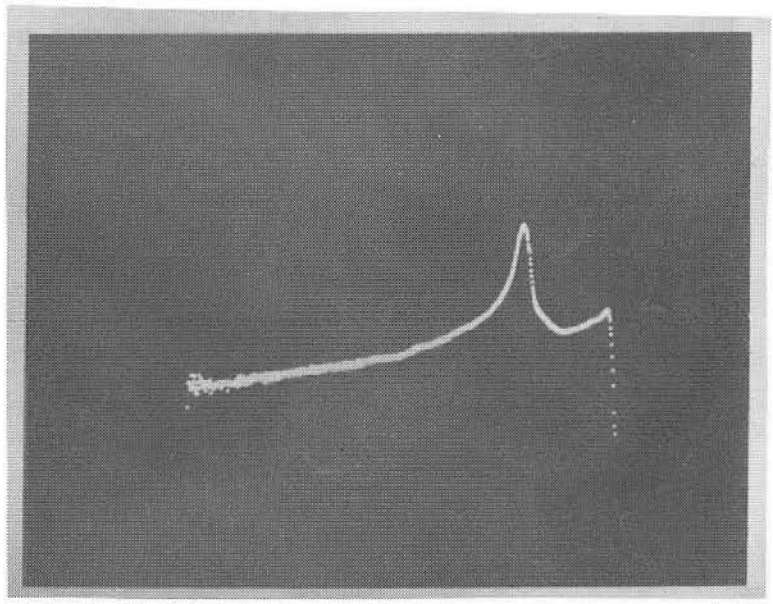

Figure 4. Log display of spectrum of alpha particles transmitted through the DTD with 1.02×10^6 craters/cm^2.

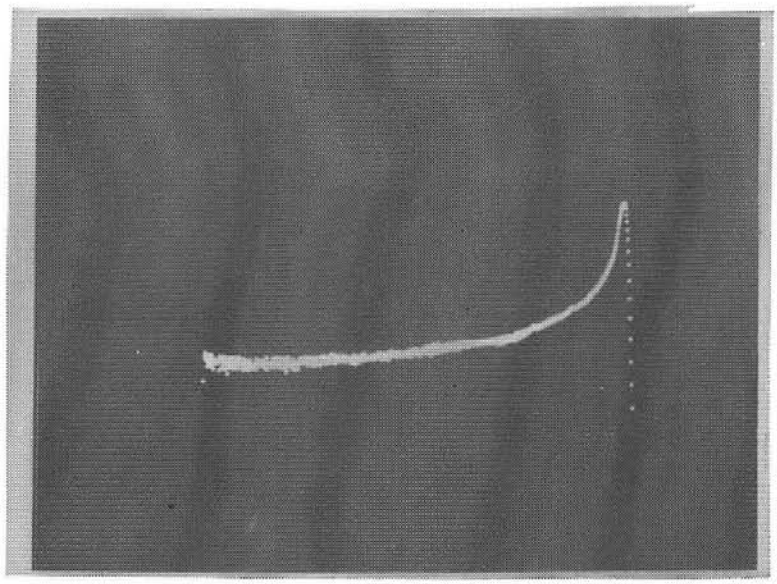

Figure 5. Log spectrum of unattenuated 5.8 MeV alpha particles.

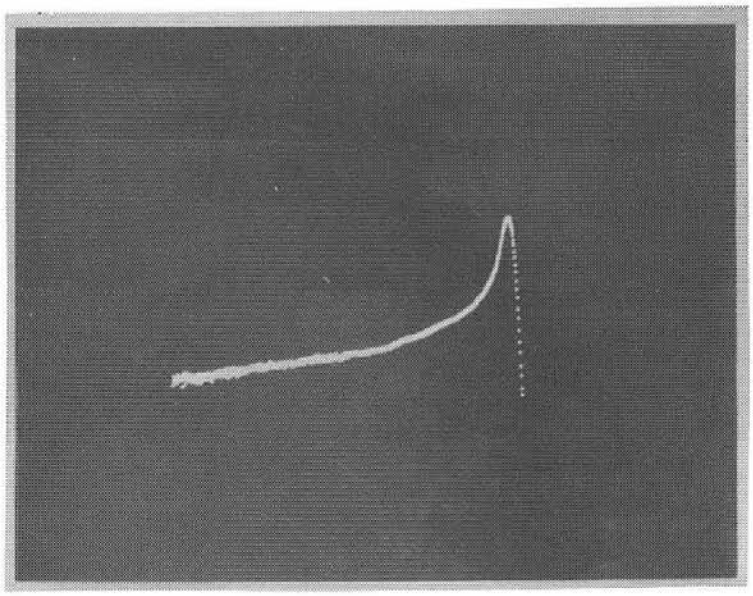

Figure 6. Log display of alpha particles transmitted through a DTD that was etched, but which had not been exposed to fission fragments.

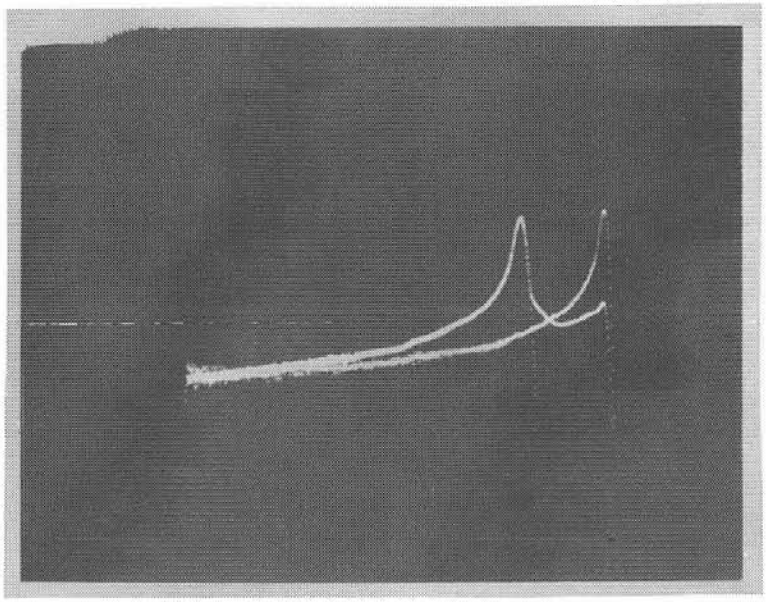

Figure 7. Spectra of Figures 4, 5, and 6 in one display.

Flash X-Ray Cinematography*

by

William E. Stein

Los Alamos Scientific Laboratory
Los Alamos, New Mexico 87544

*This work supported by the U. S. Energy Research and Development Administration.

I. INTRODUCTION

Flash x-ray cinematography is presently being evaluated as a possible diagnostic technique for use in a Fast Reactor Safety Test Facility (STF). As currently conceived, the system will consist of an external pulsed x-ray source and an external imaging detector located at a corresponding position in the opposite side of the reactor. A diametrical slot through the reactor driver core would be provided to allow a reasonably clear view of the material in the central test region. Extraneous radiation at the detector would be avoided by careful design of the collimation and shielding associated with the transverse viewing slot. Unavoidable material such as the reactor containment vessels would necessarily be in the x-ray path but other structural components which would attenuate and scatter the x-rays would be minimized.

Experiments are in progress using existing LASL facilities and available equipment to determine the feasibility of observing the motion of fuel and clad during and after a core disruptive, reactor power transient. These studies are intended to be exploratory and are being undertaken primarily to outline the general characteristics of a system which would satisfy the experimental needs and measurement requirements given in earlier papers of this meeting.

Radiographs taken previously with photographic film indicate that x-rays transmitted by various fuel pin configurations and steel plates simulating the containment vessels possess sufficient information to allow radiography with the desired spatial definition and contrast.[1] The required 1-mm radial spatial resolution and nearly linear density variation are adequately satisfied for a test array consisting of a limited number of fuel pins. For bundles of fuel pins approaching a full subassembly the desired radial resolution has been relaxed to about 5 mm. This requirement could also be satisfied by

observing the motion of fuel into the coolant channels between rows of fuel pins. X-ray scattering however limits the range of density variation attainable in the large arrays. It appears that the dynamic range of the imaging system need not be larger than about 10 to 1 to be compatible with the observed density variations in radiographs of large arrays.

In addition to the above spatial resolution, there is a temporal resolution requirement which the overall diagnostic system must satisfy. It is desired to observe fuel motion with a minimum time resolution of about one millisecond. Thus the x-ray source and imaging system must be capable of providing a maximum repetition rate of one thousand pictures per second. The use of photographic film in this application for a large number of pictures appears extremely doubtful. It would be quite difficult if not impossible to attain sufficiently rapid shutter speed and frame motion to prevent fogging of the film by radiation from either the reactor or previous and subsequent x-ray pulses. Therefore alternate imaging methods such as electro-optical systems will be necessary to satisfy simultaneously the temporal and spatial resolution requirements.

The first measurements in the present experimental program were undertaken to evaluate an available state-of-the-art electro-optical imaging system. Of primary interest was the determination of the sensitivity of this system to the primary radiation from the x-ray source relative to its response to the background radiation from the fuel pins under study. From these initial results an estimate has been made of the minimum x-ray source intensity required to obtain an adequate signal-to-noise ratio. The maximum allowable pulse duration consistent with an adequate signal-to-background ratio

was also determined. The latter was specified for the imaging system in the presence of the background radiation from a full subassembly of fuel pins operating at the maximum expected instantaneous power of 10^6 W/g.

The present report contains a description of the x-ray radiographic studies pertinent to STF applications performed to date. Previous work is reviewed briefly. The present experimental program is described and the results obtained so far are presented. Specification of a viable x-ray source compatible with existing imaging systems and expected reactor conditions is made based on these preliminary results. Finally a demonstration of x-ray cinematography of simulated fuel pins is presented.

II. PREVIOUS MEASUREMENTS

Results of initial measurements of the radiographic capability and the effects of background radiation have been reported previously.[1] PHERMEX and Godiva with the characteristics given in Fig. 1 were used in these studies. Radiographs were obtained at PHERMEX with the arrangement shown in Fig. 2 and the effects of the background radiation were assessed at Godiva with a similar experimental set up. These radiographs recorded on x-ray photographic film demonstrated that 30-MeV bremsstrahlung penetrating at least 100-mm thick steel and various numbers of uranium-oxide fuel pins still retains the necessary spatial resolution and contrast to satisfy the diagnostic requirements of the proposed facility. As an example of the exceptional picture quality, a radiograph of an array of 19 Pressurized Water Reactor fuel elements (10.8 mm outside diameter) with a total of 102-mm thick steel absorber is shown in Fig. 3. Furthermore the reactor measurements indicate that the background radiation from a full subassembly (217 fuel pins) operating at the maximum instantaneous power of 10^6 watts per gram expected at the peak of the reactor power transient would not seriously affect the images recorded on photographic film for a 0.2-μs exposure.

III. PRESENT EXPERIMENTAL PROGRAM

A. General

The previous static radiographs recorded on film indicate that the desired spatial resolution can be obtained from the transmitted x-rays for a variety of core configurations. The present series of measurements were designed to determine the general characteristics of the x-ray source and imaging detector which will satisfy not only the desired spatial resolution but also the temporal requirements. In extreme cases a time resolution of about one millisecond will be necessary to observe adequately the motion of core material. In addition, the radiation emanating from the core material under study imposes a further temporal constraint. The exposure time of the imaging system (shutter open time) and therefore the duration of the x-ray pulse will be limited by the allowable recorded background in comparison with the desired x-ray image. For a given reactor configuration the intensity of the x-ray pulse and therefore the size of the machine required for its production will be determined primarily by the sensitivity of the imaging system. (In rare cases the lower limit may be established by the allowable statistical uncertainty for each resolution element of the image.)

Electro-optical imaging systems are being used in the present evaluation. A plastic scintillator (decay time of a few ns) converts the x-ray radiograph to an optical picture which is viewed by an image intensifier coupled to a vidicon. The characteristics of this electro-optical device are listed in Fig. 4. These systems were developed for and used quite successfully in other LASL activities.[2] The gate duration or shutter open time of the image intensifier is adjustable from a few ns to many μs. In addition to this feature, the 30-Hz frame repetition rate and the proper sensitivity make this device a reasonable state-of-the-art choice for these initial evaluations.

B. Objectives

The specific objectives of these experiments are:

1. Determine the x-ray source intensity required to obtain distinct radiographs in a simulated reactor configuration.
2. Determine the response of this system to simulated reactor background radiation equivalent to a full subassembly (217 pins) operating at 10^6 watts per gram.
3. Determine the signal-to-noise and the signal-to-background ratios to be expected for various x-ray source intensities and pulse durations.
4. Outline general characteristics of an adequate x-ray machine.
5. Demonstrate capability of x-ray cinematography.

C. Measurements

The image intensifier-vidicon imaging system has been used at PHERMEX and Godiva to determine representative video signal levels and the effects of reactor background, respectively. An array of plastic scintillators backed by lead converter foils and a synchronized pulsed light source was viewed via a mirror by the imaging system. Scintillators of various thicknesses (0.5 mm to 2 mm) were used to allow a small dynamic range and lead foils of 0.5 mm and 0.9 mm were used to enhance the scintillator response. For these measurements only the video signal level of the light flasher and each scintillator-lead foil combination was determined, no attempt was made in these preliminary experiments to obtain resolved images. The pulsed light source was included in the field of view of the imaging system to facilitate adjustment of the apparatus and to provide a standard reference signal for ease of data comparison.

The experimental arrangement for the signal intensity measurements at PHERMEX is shown in Fig. 5. With the exceptions of the test object and the imaging method, the configuration is similar to that used in the previous radiographic measurements described briefly in Section II. The distance between the x-ray source and the scintillator array was again 6 m and steel plates with total thickness of about 100 mm were positioned to simulate the inner and outer reactor containment vessels. Most of the data were obtained with this configuration but for some measurements an additional 10-mm thick plate of depleted uranium was placed as shown in the center of the steel to simulate the attenuation of the x-rays by a small array of fuel pins. Although the pulse from PHERMEX is considerably shorter (0.2 μs), a 10-μs image intensifier gate was used in these measurements to assure complete response to the longer (few μs) light flasher signal. The video signal was observed livetime on a television monitor and recorded on video tape for later analysis. The radiation intensity from PHERMEX was determined by a Compton diode for each recorded pulse. Typically the x-ray yield per pulse was $\sim$ 100 roentgen at one meter on the beam axis.

A similar experimental arrangement was used at Godiva for the determination of the background signal level. As shown in Fig. 6 the distance between the pulsed reactor and the scintillator array was 3 m and steel plates simulating the containment vessels were placed approximately 1 m from Godiva. Data acquisition was similar to that described above except that the image intensifier gate was extended to 50 μs in accord with the longer reactor pulse. Information necessary to determine the total fission energy produced in the reactor during the gate interval was obtained from the already existing Godiva diagnostic instrumentation.

D. Data Analysis

The data to be analyzed consist of composite video signals recorded on magnetic tape. A separate record exists for each selected PHERMEX x-ray flash or Godiva burst. Since the exposure was momentary, the most distinct image for each experimental event is contained in the first television frame immediately following the radiation flash. The desired results are the relative light intensities from the scintillators in the form of video signal voltage levels for the variety of experimental conditions.

Processing of the video signals to obtain the desired information was accomplished by the use of additional electronic equipment. The television frame of interest was selected and displayed momentarily by stop motion of the magnetic tape. This frame was then transcribed onto a video magnetic disc for indefinite repetitive playback. The video voltage level associated with a selected horizontal line of the television raster was displayed in the form of an oscilloscope trace by means of a television waveform monitor. An example of such a display is shown in Fig. 7 where the particular horizontal line selected passed through the images of the pulsed light source on the left and the two top scintillators of the array near the center of the trace. The vertical deflections above the pedestal when properly calibrated provided the desired video signal levels. In a similar manner the video level for any arbitrary region of the raster could be determined by merely selecting the appropriate horizontal line for display.

E. Results

With the equipment available for these measurements the maximum recorded video signal level was slightly above one volt and the inherent noise level of the imaging system was approximately 0.01 volt. Therefore this system was

limited to a dynamic range of about 100 to 1. The intensity of the pulsed light source was adjusted to provide a near maximum response of one volt and was used for intercomparison of data taken at the two radiation facilities.

The results obtained at PHERMEX with the experimental arrangement shown in Fig. 5 with a total steel thickness of ~ 100 mm and without the uranium plate were 0.31 V and 0.33 V for the 1-mm thick scintillators backed by 0.89-mm and 0.51-mm thick lead foils, respectively. Corresponding results were obtained for the other scintillator-lead combinations. For the purpose of the remainder of this discussion the slight variations observed for the two lead thicknesses will be ignored and an average of the two results (0.32V) will be used in subsequent data comparisons. Signals from the existing Compton diode detector indicated that the x-ray intensity was 107 roentgen at one meter on the beam axis. Thus the response of the imaging system for a 1-mm thick plastic scintillator and the 6-meter geometry with ~ 100-mm total steel thickness is

$$\text{Signal} = 0.32\text{V}/107\text{R} \text{ @ } 1\text{m} = 3 \times 10^{-3} \text{ V/R @ } 1\text{m}$$

In the following it will be convenient to express the response in terms of the total charge per pulse of ~ 30-MeV electrons incident on the tungsten target. The conversion factor is about 10 roentgen at one meter per microcoulomb.[3] With this substitution the response becomes

$$\text{Signal} = 3 \times 10^{-2} \text{ V/}\mu\text{C for 30-MeV electrons.}$$

The result obtained from the Godiva measurement with the experimental arrangement shown in Fig. 6 with comparable geometry and steel thickness was

0.05 V for a 1-mm thick plastic scintillator and 1.15×10^5 J of fission energy produced in the reactor during the 50-μs image intensifier gate. The background video signal for the particular experimental arrangement is then

$$\text{Background} = 0.05 \text{ V}/1.15 \times 10^5 \text{ J}$$
$$= 4.3 \times 10^{-7} \text{ V/J of fission energy.}$$

A full subassembly of 217 fuel pins containing 36 kg of fuel operating at the assumed maximum instantaneous power of 10^6 W/g produces 3.6×10^{10} J/sec. Thus the background signal level is time dependent and for these extreme conditions is given by

$$\text{Background} = (4.3 \times 10^{-7} \text{ V/J}) (3.6 \times 10^{10} \text{ J/sec})$$
$$= 1.5 \times 10^{-2} \text{ V/μsec for a full subassembly operating at } 10^6 \text{ W/g.}$$

The signal-to-noise and signal-to-background ratios derived from these measurements are shown in Fig. 8 for the itemized conditions and for various assumed x-ray pulse lengths.

These results indicate that reasonable (10 to 1) signal-to-noise and signal-to-background ratios could be obtained even at the extreme instantaneous reactor power levels by a less powerful and therefore less expensive x-ray source than PHERMEX. A modern 30-MeV electron linac operating with a peak current of a few amperes and a pulse duration of a few microseconds could not only satisfy the intensity requirement but also at the same time provide the desired pulse repetition rate.

IV. X-RAY CINEMATOGRAPHY

An electron linac developed and built at LASL for other research purposes is coincidentally an ideal prototype of the required accelerator. As shown in Fig. 9 the linac is of a new design based on the side-coupled, standing-wave accelerator principles developed for the LAMPF proton accelerator. Performance tests indicate that this single section is capable of greater than one ampere peak current and pulse durations of at least one microsecond at 5-MeV nominal electron energy. The very high shunt impedance ($\sim$ 70 MΩ/m) and high beam loading ($\sim$ 80%) contribute to extremely efficient accelerating structures and therefore a low cost accelerator. To attain the desired 30-MeV electron energy for the STF, six of the 0.6-m long accelerating tanks and associated radio-frequency sources would be requried.

The present 5-MeV electron accelerator was used to demonstrate the x-ray cinematographic capabilities of the x-ray source and imaging system. The experimental arrangement is shown in Fig. 10. To compensate for the lower intensity of the x-ray pulses because of the lower electron energy a 0.3-m separation between the source and scintillator was used. The accelerator was operated at 5-MeV electron energy with approximately 0.5 ampere peak current and 1-μsec pulse duration. The focused beam was confined to 2-mm diameter by a graphite collimator and the transmitted beam ($\sim$ 0.1 A) was incident on a 1-mm thick tantalum target. Depleted uranium rods were positioned as shown approximately 10-mm from the plastic scintillator to simulate reactor fuel pins. A Palmer video recording camera[4] was used to photograph the monitor image and record the pictures on 16-mm motion picture film. For this demonstration the accelerator pulse, monitor unblanking and motion picture

camera were all synchronized to the video sync signals from the vidicon and the x-ray flash was produced during the vertical retrace period of the vidicon. Mechanical inertia in the motion picture camera limited the repetition rate to 20 pictures per second. A portion of the film strip taken at this maximum rate is shown in Fig. 11. A malfunction of the television monitor caused the squiggles in the radiographs of the simulated fuel pins. Nevertheless these crude pictures demonstrate that the spatial resolution required of the STF diagnostic system is easily within reach. In this case the spacing between the rods was about 3 mm whereas the desired resolution is 1 mm at the fuel pin array which corresponds to 2 mm at the scintillator because of the factor of two magnification expected in the STF arrangement.

V. SUMMARY

Experiments intended to provide an over view of the potential capabilities and limitations of flash x-ray cinematography as a diagnostic technique for a Fast Reactor Safety Test Facility have been performed. The results provide estimates of the x-ray pulse intensity required to obtain adequate radiographs of an array of fuel pins in a typical reactor configuration. An estimate of the upper limit on the pulse duration imposed by the reactor background radiation was also determined. X-ray cinematography has been demonstrated at a repetition rate limited only by the recording equipment on hand at the time of these measurements.

These preliminary results indicate that flash x-ray cinematography of the motion of fuel in a Fast Reactor Test Facility is technically feasible. State-of-the-art imaging systems and modern electron accelerators appear capable of providing the required spatial and temporal resolution as well as contrast within the limits imposed by x-ray scattering which has been

discussed previously.[1] Based on these initial results, the cost of this diagnostic system (x-ray source, imaging systems and data recording equipment) would be only a small fraction (a few percent) of the cost of the overall STF.

Work is in progress to improve the quality and accuracy of these results. The measurements will be repeated with improved apparatus and conditions. Radiographs of simulated LMFBR fuel pin will be obtained with the electro-optical system for direct comparison with those taken on photographic film. An effort will be made by experiment and calculation to determine more accurately the effects of the reactor background radiation.

REFERENCES

1. G. I. Bell, et al., Study of Fast Reactor Safety Test Facilities, Los Alamos Scientific Laboratory Preliminary Report LA-5978-MS (1975) Page VIII - 8.

2. Group J-12, Los Alamos Scientific Laboratory, private communication from George Berzins.

3. D. Venable, et al., PHERMEX, A Pulsed High-Energy Radiographic Machine Emitting X-Rays, LA-3241, p. 109.

4. Model SW-3 Video Recording Camera, W. A. Palmer Films, Inc., San Francisco, California.

PHERMEX

~30 MeV Tungsten Bremsstrahlung
100 Roentgen at 1m/pulse
Pulse Duration = 0.2 μs
Charge/Pulse ~10 μC
Radiation Source Size = 1mm Dia
Maximum Pulse Repetition Rate = 0.1 pps

GODIVA IV

Unreflected Enriched Uranium Fast-Burst Assembly
Typical Peak Power ~ 9 x 10^3 MW
Pulse Duration ~ 50 μs FWHM

Fig. 1. Characteristics of PHERMEX and Godiva.

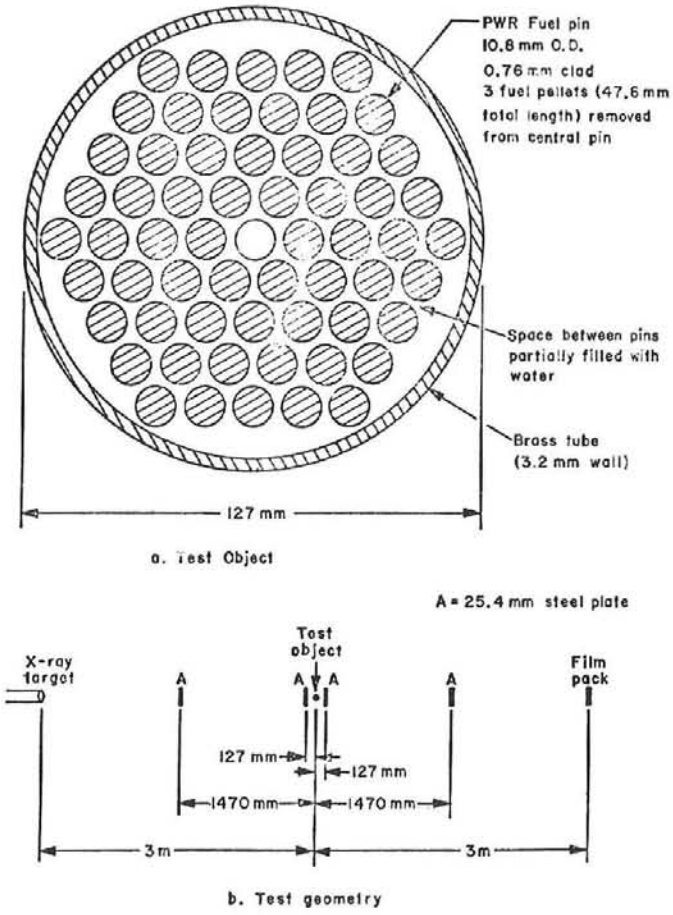

Fig. 2. (a) Test array of Pressurized Water Reactor fuel elements.
(b) Experimental arranbement used previously to radiograph the above array at PHERMEX.

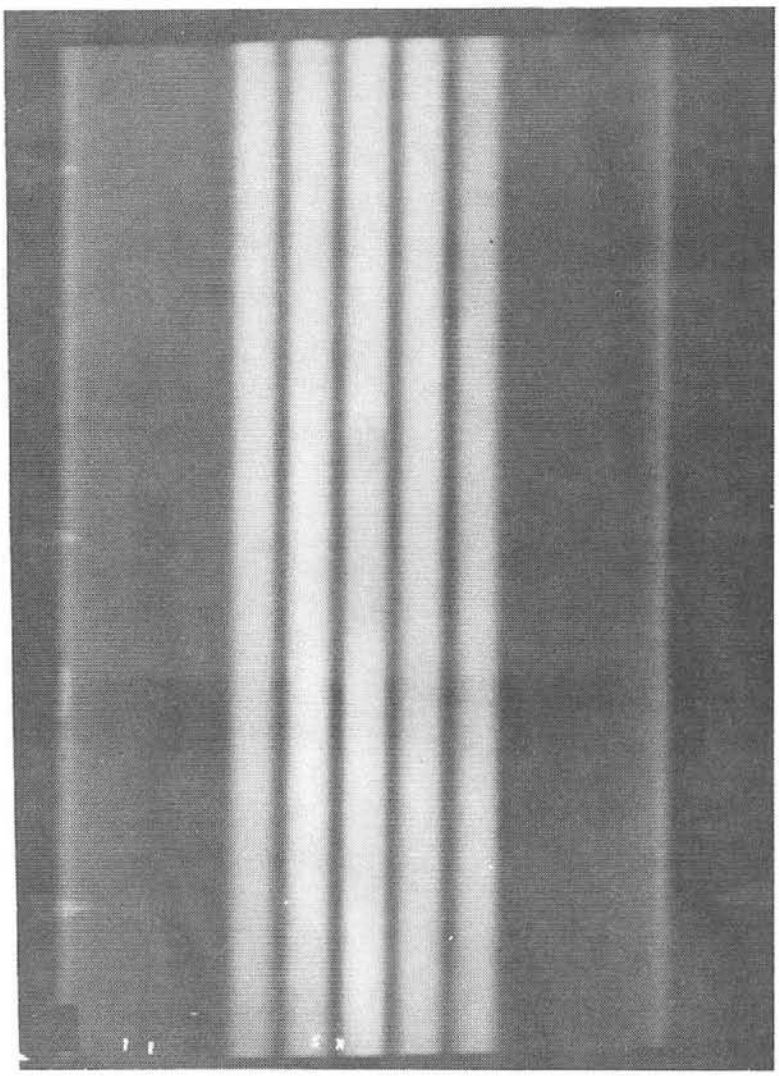

Fig. 3

Radiograph of 19 PWR pins, looking at apex of hexagon. Magnification = 2, 102-mm steel absorber.

ELECTRO-OPTICAL IMAGING SYSTEM

- IMAGE INTENSIFIER
  - ITT 18MM PROXIMITY FOCUSED
  - GATED
  - GAIN ~ 10^4
- VIDICON
  - MTI VC24
  - SCAN RATE: 1029 LINES/FRAME (8 MS/FIELD)
- LENS: 50MM F/1.2

PHERMEX

- ~30 MEV TUNGSTEN BREMSSTRAHLUNG
- 100 ROENTGEN AT 1M/PULSE
- PULSE DURATION = 0.2 μS
- CHARGE/PULSE ~10 μC
- RADIATION SOURCE SIZE = 1MM DIA
- MAXIMUM PULSE REPETITION RATE = 0.1 PPS

GODIVA IV

- UNREFLECTED ENRICHED URANIUM FAST-BURST ASSEMBLY
- TYPICAL PEAK POWER ~ 9×10^3 MW
- PULSE DURATION ~50 μS FWHM

ELECTRON LINAC

- 5 MEV TANTALUM BREMSSTRAHLUNG
- 10^{-2} ROENTGEN AT 1M/PULSE
- PULSE DURATION = 1 μS
- CHARGE/PULSE = 0.1 μC
- RADIATION SOURCE SIZE = 2MM DIA
- MAXIMUM PULSE REPETITION RATE = 10^3 PPS

Fig. 4

Characteristics of imaging system and LASL facilities used in the present series of measurements.

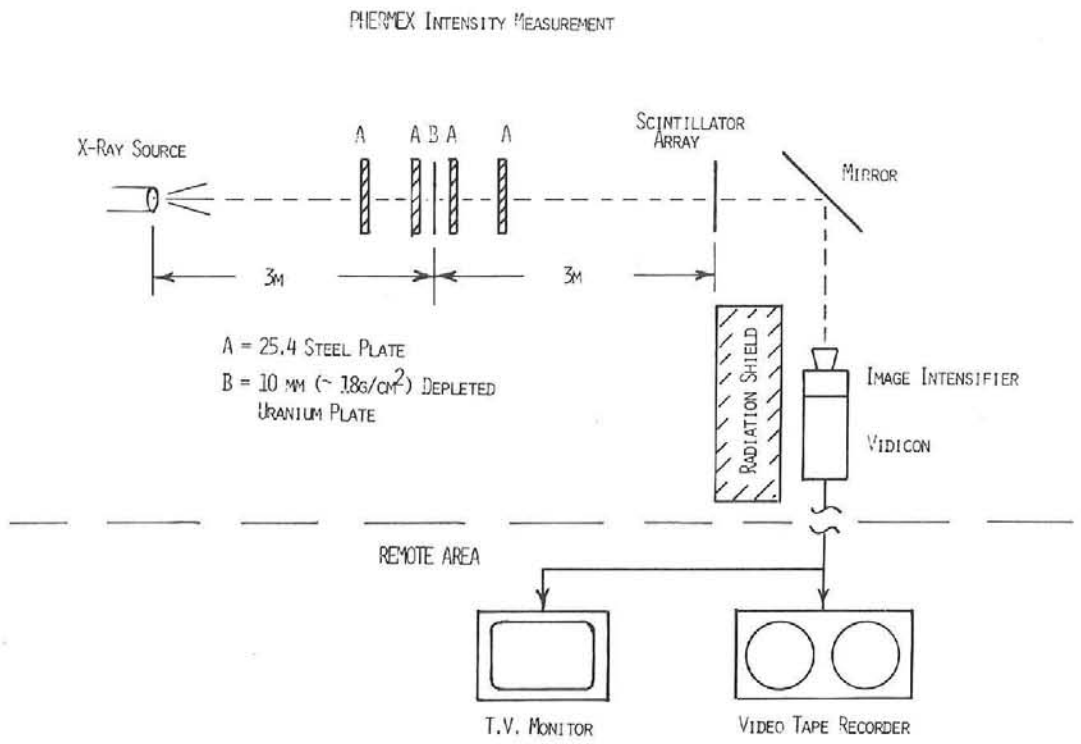

Fig. 5. Experimental arrangement for PHERMEX intensity measurement.

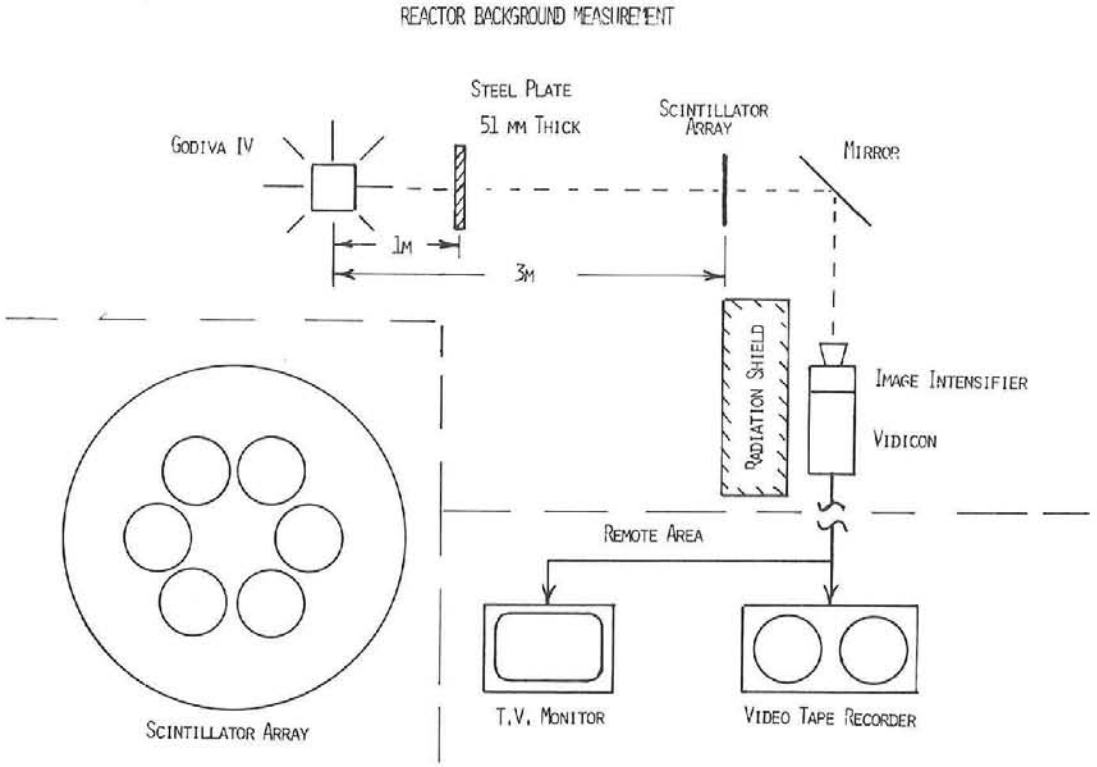

Fig. 6. Experimental arrangement for Godiva reactor background measurement. Insert indicates the scintillator array.

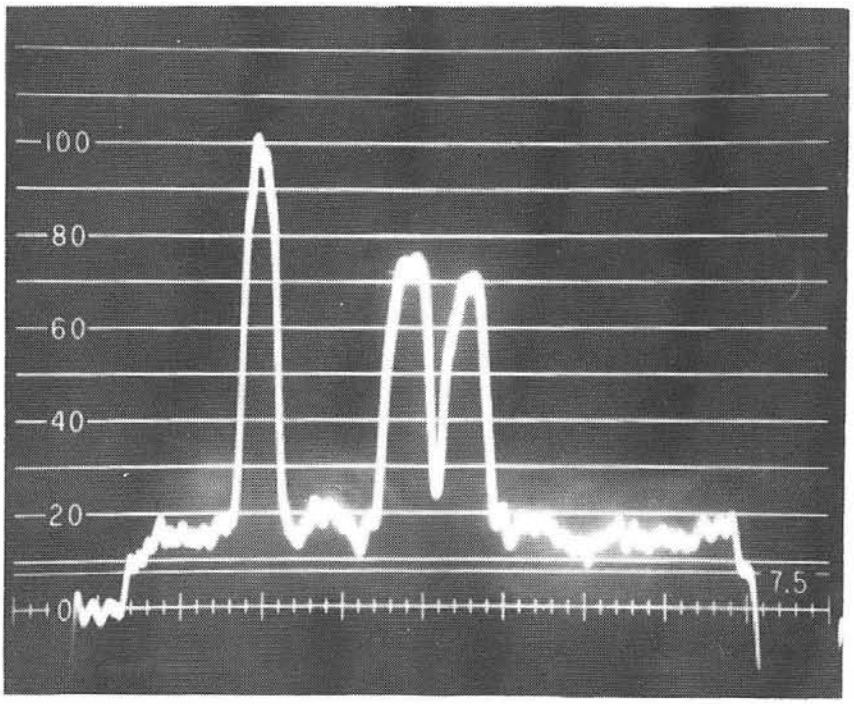

Fig. 7

Video signal associated with the horizontal television line through the image of the pulsed light source on the left and two scintillators near the center of the oscilloscope trace.

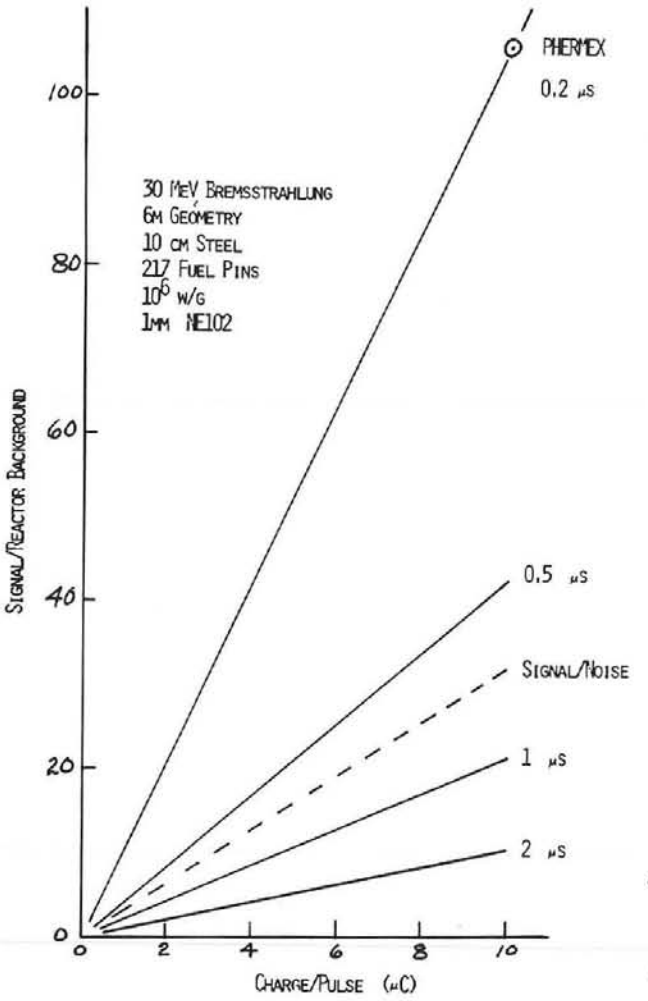

Fig. 8

Expected signal-to-background and signal-to-noise ratios for various x-ray pulse intensities and durations based on the results of the present measurements.

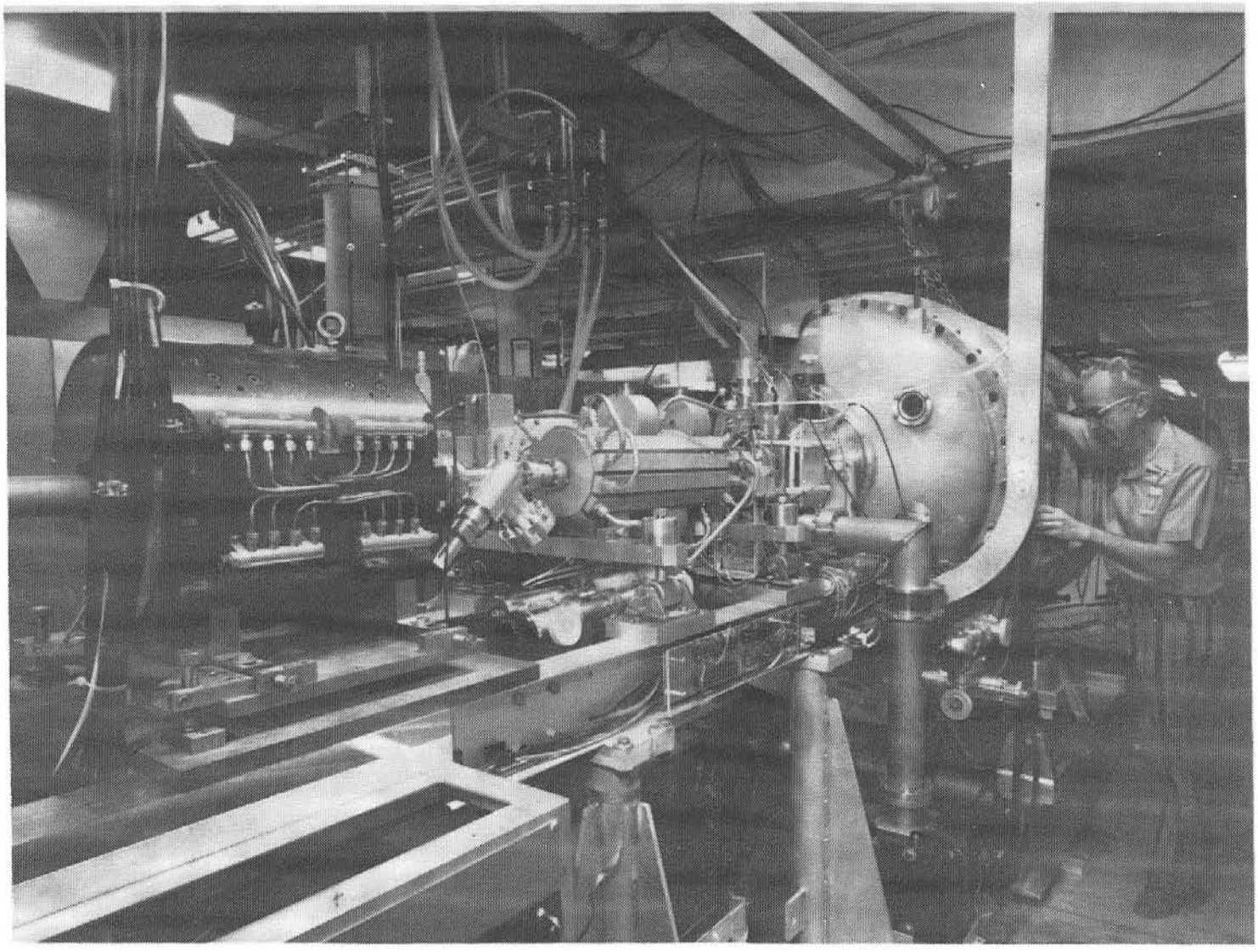

Fig. 9. Side-coupled, standing-wave electron linear accelerator used as an x-ray source for cinematography.

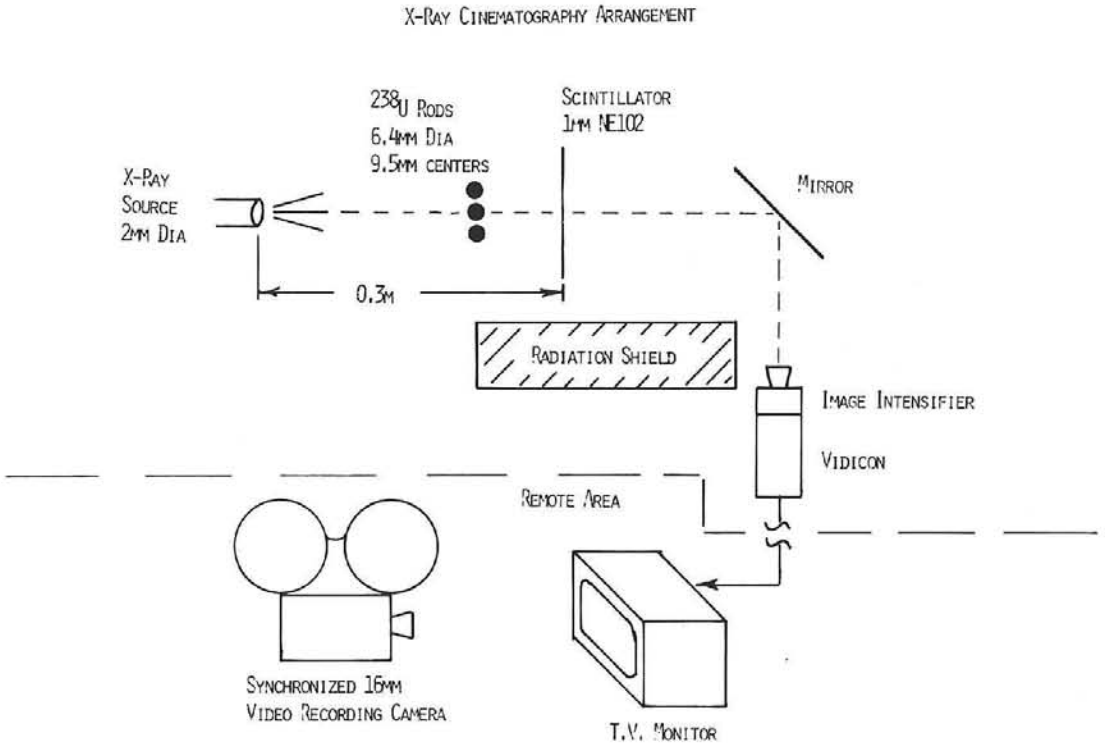

Fig. 10. Experimental arrangement for the x-ray cinematographic demonstration.

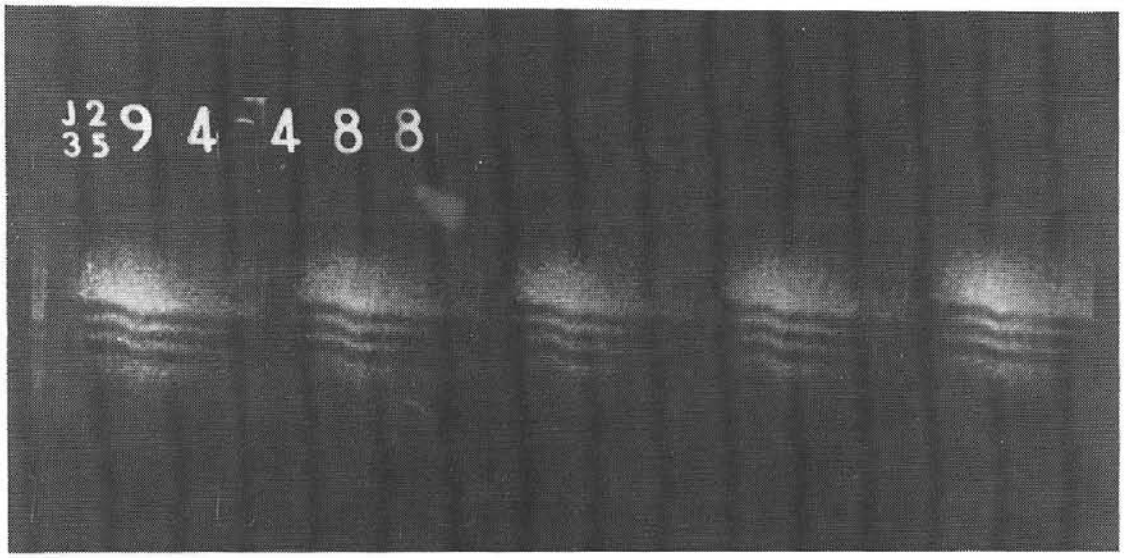

Fig. 11. Portion of the 16-mm film strip demonstrating x-ray cinematography of three simulated fuel pins.

X-ray Cinematography of Fuel Pin Motion*

by

J. A. Halbleib, Sr.

Theoretical Division
Sandia Laboratories
Albuquerque, New Mexico 87115

I would first like to discuss the procedure we have used to estimate imaging fluxes and imaging detector deposition rates in our study of the feasibility of employing x-radiography for observing fuel motion. I will then discuss the results of applying these methods to:

1. An in-tank configuration for an upgraded version of Sandia's Annular Core Pulsed Reactor for looking at one- and seven-pin test assemblies.
2. A potential SAREF configuration with experiments ranging from single pin to multiple subassemblies.

Finally, based primarily upon this work and the work documented in Reference 1, I would like to make a few general comments on the feasibility of x-ray cinematography of fuel pin motion.

In order to arrive at predictions for the imaging signals, it was first necessary to generate the continuous bremsstrahlung environments. This was accomplished using the one-dimensional, coupled electron/photon Monte Carlo transport code, TIGER.[2] Calculations were performed for mono-energetic, normally incident source electrons with energies from half an MeV up to 30.0 MeV. The converter configuration consisted of a foil of tantalum, the thickness of which was about three tenths of the continuous-slowing-down-approximation (CSDA) range, followed by a layer of graphite, the thickness of which was about seven tenths of the CSDA range. Each calculation yielded the coupled energy and angular distribution of the forward

* This work supported by the U.S. Energy Research and Development Administration

directed continuous bremsstrahlung. About 6 to 7 times 10^5 bremsstrahlung histories were followed leading to one sigma statistical error of less than 5 percent over most of the range of distributions.

The forward 2π energy spectrum at 1.0 MeV is shown in Figure 1a. The contribution from Ta characteristic x-rays has been subtracted out before plotting. The Ta absorption edge is clearly visible for source energies up to 5.0 MeV. As can be seen in Figure 1b which shows the 30-MeV spectrum, a peak containing the annihilation radiation appears at the three highest energies. Note that having used the same ordinate in Figures 1a and 1b, the increase in bremsstrahlung efficiency with increasing source energy is quite evident. These environments were then used as input into models for predicting imaging fluxes and detector deposition rates.

As a first example of the application of these data, we consider the suitability of three specific sources for permitting the detection of the motion of relatively simple test-pin configurations in response to the environment of an upgraded version of Sandia's Annular Core Pulsed Reactor. Details of this study may be found in Reference 3.

From operational as well as economic considerations, it would be desirable to locate both the flash x-ray source and imaging detector within the existing inner tank of the ACPR facility. Consequently, we postulated source and image locations in which the source-object distance was 140 cm and the object-image distances was 60 cm. We also used the flux spectra averaged over the forward 0 to 10-degree half-angle.

The predicted fluxes for this configuration are shown in Table I. The predicted flux at the imaging detector from a 1.0-MeV, 100-kA high intensity field emission electron source with no pin attenuation is 3.81×10^{17} photons/cm^2-sec, which we use as our unit of flux, α. Maximum attenuation for a one-pin experiment should be about 0.5 cm of UO_2, and maximum attenuation for a seven-pin experiment should be about 1.5 cm -- i.e., three pin diameters for a configuration consisting of a single pin surrounded by a ring of six pins. Using the uncollided attenuation factors for these

object thicknesses we obtain predicted imaging signals of 0.0837α and 0.0164α for 1- and 7-pin experiments, respectively. Following the same procedure, we predict imaging fluxes for a 20-MeV, 20-A LINAC-type facility which are about 1/40 that of the 1-MeV, 100-kA field emission source for zero thickness of UO_2, about 1/6 for 0.5 cm and about 1/2 for 1.5 cm. On the other hand, results for a 5-MeV, 100-kA field emission source range from one to two orders of magnitude higher than those from the 1.0-MeV source.

The quantity, n, is the power of the source electron kinetic energy by which the flux for the two higher energy sources scales relative to the 1.0-MeV source for the same beam current.

We have also attempted to estimate some of the background contributions. Background A is the estimated gamma flux at the image position due to fission within the test pins. It was obtained from a transport calculation in which the cylindrical geometry, coupled electron/photon Monte Carlo code, CYLTRAN[4], was employed to obtain the coupled energy and angular distribution of photons escaping from a fuel pin, using a uniform, isotropic fission-gamma spectrum due to Maienschein et al. as the source. For seven pins this background is only about 1/4 the signal flux for the 1.0-MeV, 100-kA flash x-ray source. Background B is an estimate of the gamma flux at the imaging position due to pin scattering of the uncollided fission gammas from the ACPR (upgrade) core. The method of estimating the uncollided core fission gamma flux at the test pin involved the triple integration of a spatially uniform isotropic Maienschein fission gamma spectrum over the ACPR (upgrade) core volume and included core-attenuation of the source photons for a homogeneous mixture of core materials. This flux was then multiplied by the scatter-escape fraction, as determined from a CYLTRAN Monte Carlo calculation, since only those photons which both scatter in and escape from the pin can reach the imaging detector if collimation prevents the detector from viewing anything but the pin. Further multiplication by the pin cross section (length times diameter) and the solid-angle factor for the pin-image distance gave the

result shown here. Background C is a crude upper bound for the direct core fission gamma flux which assumes no shielding between detector and reactor core and ignores any self shielding of the core itself.

Due to the substantial impact which installation of a radiographic diagnostics system would have had upon existing and planned ACPR experiments, this application was not pursued any further. On the other hand, diagnostics for observing dynamic fuel motion are an integral part of the design of the proposed SAREF facility.

Table II shows the resulting predictions of scalable imaging fluxes and imaging detector deposition rates for potential SAREF applications. They are again based upon the bremsstrahlung flux spectra averaged over the 0 to 10-degree forward half-angle. The source-object and object-image distances were both assumed to be 2.5m[5]. The UO_2 thicknesses of 0.5, 1.5, 10.0 and 18.0 cm correspond to the estimated maximum UO_2 thickness for a single-pin experiment, a seven-pin experiment, an experiment involving a full LMFBR subassembly (271 pins) and an experiment involving a single subassembly surrounded by six partial subassemblies. The fluxes themselves should only be considered as qualitative measures of the relative effectiveness of various x-ray sources. The spectral sensitivity of a particular imaging detector system may significantly alter the conclusions based upon flux alone. Our choice of detectors was somewhat arbitrary, though it does demonstrate the relative importance of atomic number for various source energies and UO_2 thickness, since the average atomic number of the NE316 scintillator[6] is substantially lower than that of the photographic emulsion.

It is quite evident that the signal fluxes for such a broad range of experiments span several orders of magnitude. This is shown graphically in Figure 2. This plot may be used to estimate the imaging fluxes for other source energies and object thicknesses which fall within the range of the present calculations.

Figure 3 is a similar plot of the predicted NE316 deposition rates. If one knew the uncollided x-ray energy deposition per pulse needed for a given detection system, in order to satisfy the requirements for the kind of fuel motion to be observed in a particular SAREF experiment, one could use these data to determine the μC/pulse required of a given x-ray source. At present this does not appear to be a credible exercise for two reasons:

1. First of all, there appears to be no clear consensus as yet as to the diagnostics requirements of various proposed experiments.
2. Secondly, we must also know a great deal more about the expected background and noise environments before signal requirements can be established.

In order to demonstrate the procedure, however, let us simply postulate a required x-ray deposition of .01 rads in the NE316 scintillator. From these data it is a simple matter then to determine the μC/pulse required to obtain this deposition for various source energies and object thicknesses, and this is shown in Figure 4.

Consider, then, where existing sources would appear on this plot. Typical of the best available, off-the-shelf commercial LINAC's would be a 20.0-MeV source with an output of 1.25 μC. There is now in operation at the Boeing Aircraft Company a 16.0 MeV LINAC with an output of about 22 μC per pulse. In Russia there is a linear induction accelerator which operates at 30.0 MeV and delivers approximately 125 μC per pulse. Finally, the Hermes II[7] source--an example of a high-intensity, field emission accelerator--is capable of delivering 10^4 μC of electrons per pulse with a mean energy of almost 10.0 MeV. The pulse lengths of all these sources are less than 10 μsec, and so should permit 0.1-cm resolution for material velocities up to 10^4 cm/sec, which have been predicted by the SAS code[8] for severe prompt burst situations.[9] Source requirements and availability will be discussed in more detail in the following paper by Larry Posey.

It is also important to consider the vertical dimension of the object in the SAREF geometry. It would be desirable to observe the motion of a

2.0-m section (length) of an LMFBR pin. A source-object distance of 2.5 m and an object image distance of 2.5 m then result in a magnification of 2 and a viewing half-angle of 22^{o}. Thus, the vertical dimension of the radiographic slot would reach a maximum 4.0 m at the image position. This viewing half-angle is more than twice the value used in the calculations (10^{o}). Furthermore, the average flux over a 10^{o} half-angle was employed in the calculations; whereas the angular distribution of the bremsstrahlung from a monodirectional 30.0-MeV electron source is strongly peaked in the forward direction. Calculations with the TIGER code predict that the average flux (photons/str) within the 17.5^{o}-20.0^{o} angular interval, measured with respect to the beam direction, is a factor of six less than that within the 0.0^{o}-2.5^{o} interval.

The stainless steel containment vessels for SAREF are not yet well defined. One suggestion for reducing the total amount of stainless between source and image was to have a relatively thin spherical bubble at the source position, located in an otherwise thick containment wall. In any case, the effect of the stainless must also be included--perhaps as some equivalent thickness of UO_2.

What we have done then is develop models for predicting imaging signals for the radiographic diagnostics of fuel motion. It is only these uncollided signals which contain any imaging information. On the other hand, direct and scattered radiation from both the driver reactor and test assembly, as well as scattered x-rays from the radiographic source, may severely reduce the signal-to-noise ratio. Once these backgrounds are better defined, along with the specific diagnostics requirements of various test configurations, it should then be possible to assess the feasibility of x-ray cinematography for observing fuel motion in fast reactor safety experiments.

References

1. G. I. Bell, J. E. Boudreau, T. McLaughlin, R. G. Palmer, V. Starkovich, W. E. Stein, M. G. Stevenson and J. L. Yarnell, Study of Fast Reactor Safety Test Facilities (Preliminary Report), LA-5978-MS, Los Alamos Scientific Laboratory, May 1975.

2. J. A. Halbleib, Sr. and W. H. Vandevender, Nucl. Sci. Engr. 57 (1), 94 (1975).

3. J. A. Halbleib and A. R. Phillips, Theoretical Studies of Flash X-ray Diagnostics for Fuel Motion Experiments, SAND75-0223, Sandia Laboratories, September 1975.

4. J. A. Halbleib, Sr. and W. H. Vandevender, CYLTRAN: A Cylindrical-Geometry Multimaterial Electron/Photon Monte Carlo Transport Code, SAND74-0030, Sandia Laboratories, March 1975.

5. R. G. Matlock, Argonne National Laboratory, private communication.

6. Nuclear Enterprises, Ltd., San Carlos, California 94070.

7. T. H. Martin, IEEE Trans. Nucl. Sci., NS-16, No. 3, 59 (1969).

8. M. G. Stevenson, W. R. Bohl, F. E. Dunn, T. J. Heames, G. Hoppner and L. L. Smith, "Current Status and Experimental Basis of the SAS LMFBR Accident Analysis Code System," Proc. ANS Conf. Fast Reactor Safety, Beverly Hills, California, USAEC-CONF 740401 (1974).

9. R. Henninger, Argonne National Laboratory, private communication.

TABLE I

Predicted flux signals and backgrounds at imaging position for one- and seven-pin (UO_2) assemblies, for three electron sources and for a source-image distance of 200 cm--ACPR

Signals

UO_2 Thickness (cm)	1-MeV, 100-kA	20-MeV, 20-A		5-MeV, 100-kA	
	Flux (α)	Flux (α)	n	Flux (α)	n
0.0	1.00	0.0248	1.61	13.8	1.63
0.5	0.0837	0.0155	2.28	5.83	2.63
1.5	0.0164	0.00866	2.63	2.67	3.16

Backgrounds

	A* Flux (α)	B* Flux (α)	C* Flux (α)
1-Pin	0.000592	0.000104	1.74
7-Pin	0.00414	0.000729	

*Description of backgrounds:

A - Gamma flux from pin fission.

B - Gamma flux due to pin scattering of the uncollided portion of fission gammas from ACPR (upgrade) core.

C - Gamma flux due to direct fission gammas from ACPR (upgrade) core.

TABLE II

Mean bremsstrahlung flux at imaging detector and mean energy deposition rate in two imaging detectors for various source electron energies and UO_2 object thicknesses and a source-image distance of 5.0 m--SAREF

UO_2 Thickness (cm)		Electron Energy (MeV) 1.0	2.0	5.0	10.0	20.0	30.0
0.0	α*	6.114×10^{14}	1.774×10^{15}	8.388×10^{15}	2.661×10^{16}	7.588×10^{16}	1.274×10^{17}
	β**	1.663×10^{5}	4.874×10^{5}	3.566×10^{6}	1.772×10^{7}	8.194×10^{7}	1.858×10^{8}
	γ***	9.956×10^{5}	1.650×10^{6}	5.963×10^{6}	2.423×10^{7}	1.210×10^{8}	3.002×10^{8}
0.5	α	5.119×10^{13}	3.843×10^{14}	3.563×10^{15}	1.453×10^{16}	4.728×10^{16}	8.331×10^{16}
	β	1.398×10^{4}	1.439×10^{5}	2.118×10^{6}	1.256×10^{7}	6.159×10^{7}	1.404×10^{8}
	γ	1.538×10^{4}	1.436×10^{5}	2.096×10^{6}	1.398×10^{7}	8.306×10^{7}	2.137×10^{8}
1.5	α	1.006×10^{13}	1.231×10^{14}	1.633×10^{15}	7.594×10^{15}	2.646×10^{16}	4.756×10^{16}
	β	3.263×10^{3}	5.636×10^{4}	1.149×10^{6}	7.513×10^{6}	3.755×10^{7}	8.419×10^{7}
	γ	3.278×10^{3}	5.331×10^{4}	1.130×10^{6}	8.419×10^{6}	5.071×10^{7}	1.270×10^{8}
10.0	α	1.914×10^{9}	4.268×10^{11}	2.021×10^{13}	1.286×10^{14}	4.768×10^{14}	8.450×10^{14}
	β	7.900×10^{-1}	2.667×10^{2}	1.914×10^{4}	1.591×10^{5}	7.306×10^{5}	1.417×10^{6}
	γ	7.469×10^{-1}	2.454×10^{2}	1.936×10^{4}	1.833×10^{5}	9.544×10^{5}	1.956×10^{6}
18.0	α	2.081×10^{6}	5.163×10^{9}	5.338×10^{11}	3.747×10^{12}	1.363×10^{13}	2.374×10^{13}
	β	8.944×10^{-4}	3.450×10^{0}	5.463×10^{2}	4.856×10^{3}	2.041×10^{4}	3.721×10^{4}
	γ	8.406×10^{-4}	3.178×10^{0}	5.616×10^{2}	5.623×10^{3}	2.581×10^{4}	4.838×10^{4}

* Flux at imaging detector (photons/cm^2-sec-kA).

** Mean energy deposition rate in 1.0-cm thick NE316 imaging detector (rads/sec-kA).

*** Mean energy deposition rate in 0.0025-cm thick Kodak Type A emulsion (rads/sec-kA).

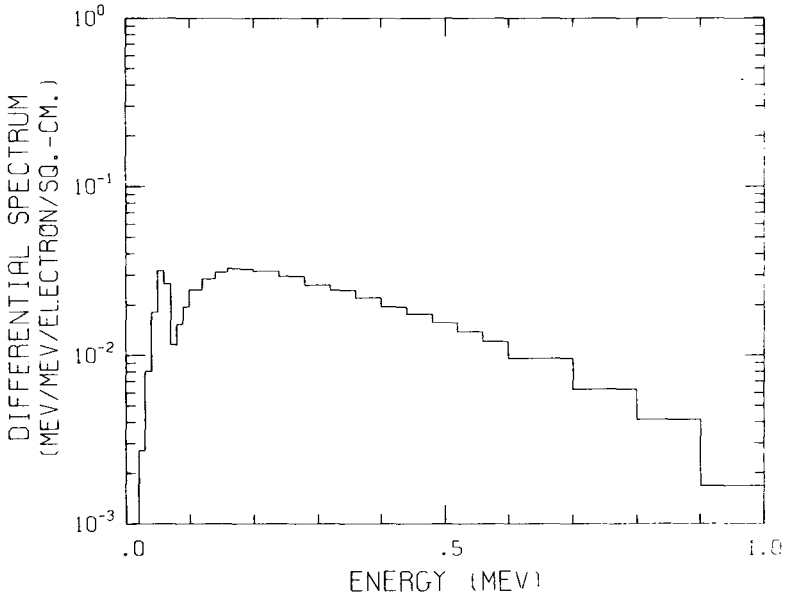

(a) 1.0 MeV

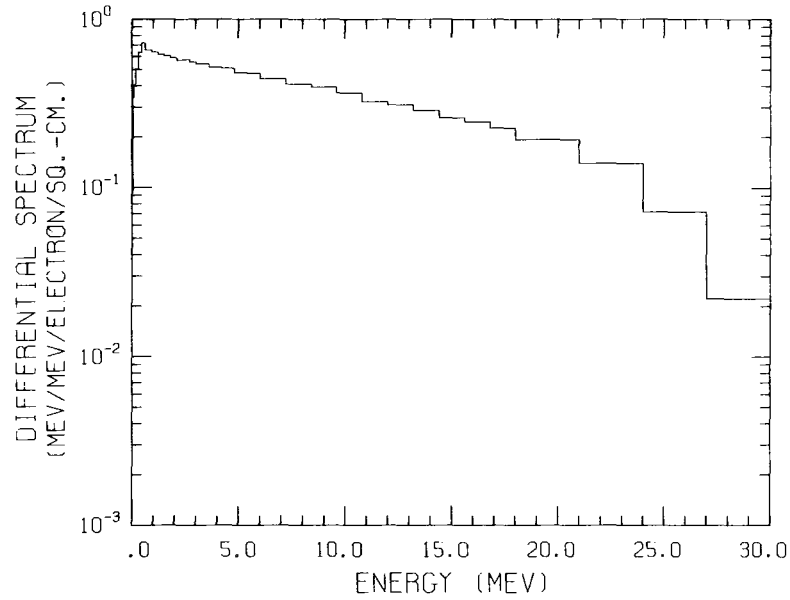

(b) 30.0 MeV

Figure 1. The forward directed bremsstrahlung energy spectra per source electron for source electron kinetic energies of (a) 1.0 MeV and (b) 30.0 MeV.

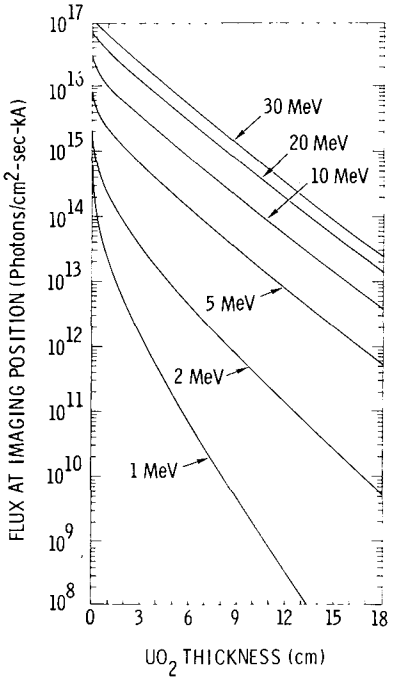

Figure 2. Mean bremsstrahlung flux at imaging position as a function of UO_2 thickness for various source electron kinetic energies and for a source-image distance of 5.0 m

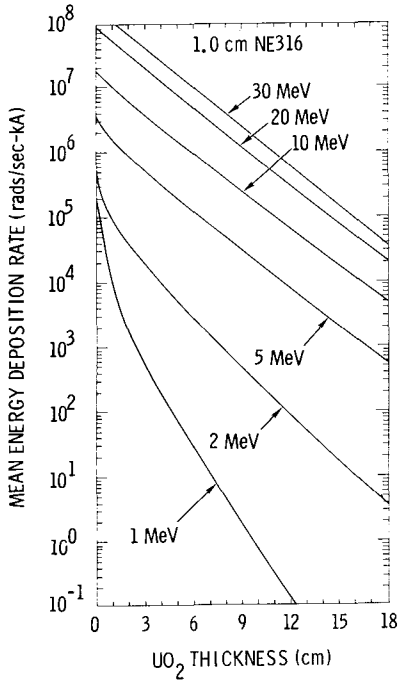

Figure 3. Mean energy deposition rate in a 1.0-cm thick NE316 scintillator at the imaging position as a function of UO_2 thickness for various source electron kinetic energies and for a source-image distance of 5.0 m

Figure 4. Source electron charge per pulse required for a deposition of 0.01 rads in NE316 as a function of source electron kinetic energy for various thicknesses of UO_2 and for a source-image distance of 5.0 m

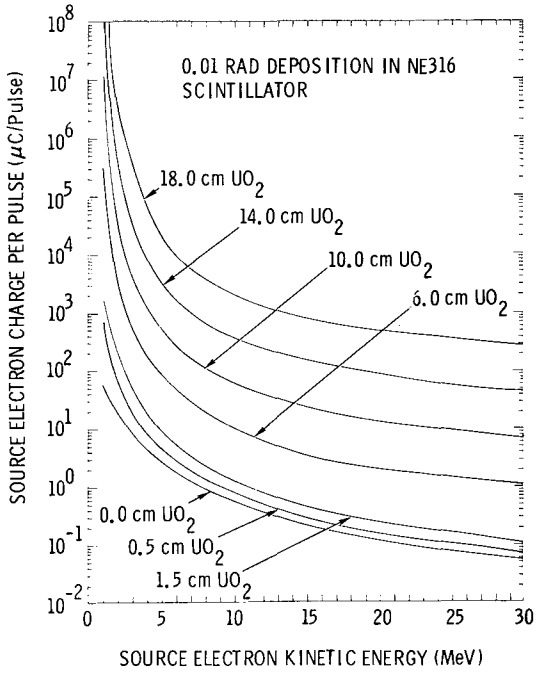

Source Requirements for Flash* X-Radiography Diagnostics

by

L. D. Posey

Beam Source Application Division
Sandia Laboratories
Albuquerque, New Mexico 87115

*This work supported by the U. S. Energy Research and Development Administration

ABSTRACT

Electron beam sources capable of being used for x-ray cinematography were evaluated with respect to their applicability for the detection of fuel motion. In the study each source type was coupled with a common detector system in order to determine source requirements. The basis for this determination was the proposed experiment matrix for the ANL SAREF program. The experimental situations considered corresponded to partial, single, and multiple subassemblies and operating power densities of 250 watts/gm to 10^6 watts/gm. The electron beam source types considered were LINAC, Linear Induction Accelerator, and Relativistic Electron Beam Accelerator.

The background (neutron and gamma) from the driver reactor core and the test assembly itself were found to be a very important factor in sizing the electron beam sources. It is possible, however, that through the use of selective filtering techniques, differentiation between signal and background may be enhanced.

The results of this work indicate that the Linear Induction Accelerator should be able to satisfy most experimental requirements up to and including full subassembly test configurations. Reasonable resolution should be attained for these configurations although it will be determined to a substantial degree by the effects of photon buildup and scattering. It does not appear that acceptable resolution will be possible for multisubassembly exposures or single subassembly exposures at 10^6 watts/gm. Improved detector performance might make the latter possible but it is felt that as a result of buildup and scattering the former would remain impossible. The Relativistic Electron Beam Accelerators presently do not possess adequate multiple pulsing capabilities. Indeed, even the Linear Induction Accelerator would be hard pressed to achieve the 10^3 pps for the high intensity operating conditions required. Only a modest LINAC could easily satisfy this repetitive pulsing requirement but such a source would be limited to yielding shadowgraph information only.

SOURCE REQUIREMENTS FOR FLASH X-RADIOGRAPHY DIAGNOSTICS

I. Introduction

An important part of experiments dealing with the behavior of prototypic LMFBR fuel pin bundles under mild to severe nuclear transients is that of the observation of fuel/cladding/coolant motion. At present the neutron hodoscope[1] is used for this purpose although this instrument is only able to distinguish fuel material undergoing fission via detection of the emitted neutrons. Thus pre- and post-test fuel disposition cannot be determined using this device.

Coded aperture techniques have also been proposed for fuel motion diagnostics[2]. These techniques can be used to observe γ-rays emitted from the fuel/cladding/coolant which, as with the neutron hodoscope, is most useful during the nuclear transient but should also yield some useful data immediately after termination of the transient as a result of the finite time for decay of the fission product γ-activity. They can also be used in conjunction with a large area pulsed X-ray radiographic source to form a coded image for diagnostic purposes. Since an external source is utilized in this case, pre- and post-transient data can also be obtained.

More conventional multiple pulse X-ray radiography (X-ray Cinematography) techniques have the potential of being applicable to fuel motion diagnostics. The Phermex Facility at LASL has been used for some initial feasibility experiments[3] and more recently a LINAC and active detector system have been used to evaluate X-ray cinematography techniques by Stein, et.al.[4]. When X-ray cinematography is used to obtain shadowgraph information, the experimental quantity of interest is spatial resolution. If photon buildup and/or scattering do not seriously perturb the transmitted beam and the sensitivity limits of the detector system are not exceeded it should be possible to obtain information concerning changes in areal density as well as position. Areal density changes are indeed of major importance in order to observe fuel/cladding/coolant motion. In general X-ray cinematography techniques cannot be used to distinguish between the motion of the fuel, cladding, and coolant but rather to observe changes in areal density averaged over these constituents. Since fuel is the dominant component of the system, both in terms of mass and attenuation contribution,

the technique is essentially a fuel motion monitor. The effects of photon buildup and scattering will be very important in determining the ultimate applicability of this technique. The work reported upon here did not include effects of this type but rather assumed that that the unattenuated transmitted beam alone contained information. This assumes that the scattered beam can be discriminated against or does not overwhelm the uncollided beam. If the scattered beam does possess useful information content the source requirements presented later in this report could be relaxed. In Section II of this report the basis used to arrive at these source requirements is discussed. In Section III the source requirements are presented as well as details of the detector system. Finally, Section IV presents existing and projected capabilities with conclusions to be found in Section V.

II. SAREF Experimental Program

The operating characteristics of an electron beam source to be used as a conventional radiographic source for the observation of fuel motion is strongly dependent upon the details of a given experimental test (i.e., test assembly configuration and power level temporal profile). An entire experimental test matrix has been proposed for the Argonne SAREF Facility[5]. The experiment categories are listed in Table I where more than one test assembly configuration may be used in each category. The full experimental test matrix is presented in Table II where the projected number of individual tests are presented when data was available. Associated with each experiment category, was a projected power density temporal profile. There was not time to analyze each element of this experimental matrix. As a result, a limited number of tests were considered and these were chosen so as to span the range of test assembly configurations and power densities contained in the matrix. These elements are indicated by the intensified boxes in Table II.

For each experiment category it was necessary to estimate background dose levels arising from the test assemblies due to direct emissions or through the scattering of driver core radiations. Experimental data obtained on Godiva IV[3] and calculations performed by J. A. Halbleib[6], which were found to be in good agreement, provided the basis for the γ background estimates which are presented in Table III.

TABLE I

EXPERIMENT CATEGORIES

- Subassembly-to-Subassembly Failure Propagation
- Prototypic Fuel Failure Thresholds
- Large Bundle Overpower Transients, including effects of subassembly incoherence
- Large Bundle Loss-of-flow Transients, including effects of subassembly incoherence
- Large Bundle Power Transients Under Loss-of-Flow Conditions
- Transition Phase
- Effects of Bundle Size and Period on Fuel-Coolant Interactions
- Fission-Gas Effects on Fuel Dispersal

TABLE II

KEY EXPERIMENTS IN SAREF

	Single Pin (1)	Small Bundle (37)	Partial S/A (127)	Single S/A (271)	Multi S/A (271 + 6x126)
S/A to S/A Failure Propagation			1	1	3
Prototypic Fuel Failure Thresh.	X	20-30			
Large Bundle OPT			10-20	1-2	
Large Bundle LOFT			10-20	2	
Transition Phase			2-5	4	1
FCI		X	3	1	
Fission-gas Effects	X	3-5			
Totals	X	23-35	26-49	9-10	4

TABLE III

	Peak Pin Power	Total Back-ground	Acceptable spatial resolution		Max UO_2 Thickness
	(W/g)	D_γ(r/s)	radial (mm)	axial (mm)	(cm)
S/A to S/A Failure Propagation	2.5×10^2	1.7×10^3	~25	~120	$\lesssim$18
Prototypic Fuel Failure Thresh.	1.7×10^3	6.6×10^2	0.5-1	1-5	$\lesssim$ 4
Large Bundle OPT	6×10^2	1.3×10^3	5-25	60-120	$\lesssim$10
Large Bundle LOFT	1.1×10^4	2.3×10^4	5-25	60-120	$\lesssim$10
Large Bundle PT & LOF	1.1×10^4	2.3×10^4	5-25	60-120	($\lesssim$10)
Transition Phase	2.1×10^4	1.5×10^5	5-25	60-120	$\lesssim$18
FCI	1.8×10^5	3.9×10^5	1-5	5-60	$\lesssim$10
Fission Gas Effects	6.7×10^4	2.6×10^4	0.5-1	1-5	$\lesssim$ 4

These background estimates were based upon gammas alone due to the fact that it was assumed that the detector system could be made relatively insensitive to neutrons. Also presented in this table is the maximum thickness of UO_2 to be penetrated for each experiment category. Correction factors of 1.25 for a multi-subassembly, 1.5 for a full subassembly, 1.75 for a partial subassembly, and 2 for a small bundle were assumed in order to account for pin scattering of core radiation plus collimator scattered radiation. The acceptable spatial resolution values presented in Table III were obtained from data presented at previous SAREF review meetings.

III. Source Requirements

In addition to estimates of the radiation background as discussed in the last section, it was necessary to identify detector system sensitivity limits in order to calculate electron beam source operating characteristics. The detector system proposed in reference 3 was chosen for this purpose, in which case the minimum measurable energy deposition, with acceptable precision error, was .01 rad (fluor). Improvements in detector system performance are certainly possible. Thus, the source requirements to be presented later in this section could be relaxed providing that detector sensitivity, and not radiation background, is the limiting factor.

Transmitted beam intensities, and associated fluor dose, were obtained from the calculations of J. A. Halbleib[7] for source-to-object and object-to-image distances of 2.5 meters. These calculations do not include the effects of photon buildup or scattering and correspond to the uncollided fluence only. As mentioned in the introduction this may place too stringent requirements upon the operating characteristics of the sources. A minimum signal-to-background ratio of 4:1 was chosen as a basis for the determination of transmitted fluence. This was done, in part, to compensate for uncertainties in background estimates (e.g., neutron contribution). As mentioned earlier, sometimes it was the background which determined source operating characteristics while at other times it was the minimum detection system sensitivity. Indeed the maximum signal-to-background ratios were encountered for those cases where the minimum detector system sensitivity established source requirements.

Minimum pulse durations were assumed to be 1 μsec for the LINAC and Linear Induction Accelerator (LIA) and .025 μsec for the Relativistic Electron Beam Accelerator (REB). Bunching techniques, although quite expensive, can be employed on the linear accelerators in order to reduce pulse duration and therefore improve signal-to-background in high background situations.

A pulsing rate of 10^3 pulses per second for a total of 20 seconds was assumed to be required. This is consistent with the vast majority of requirements for the SAREF experimental program. Programmed pulsing could reduce the total number of pulses, and therefore the total energy requirement, but this case was not considered in the analysis since a detailed knowledge of the temporal behavior of pin failure and fuel motion was not available for the test areas delineated earlier.

The results of this analysis are presented in Tables IV, V and VI for LINAC, LIA, and REB respectively. As shown in these tables the calculations were performed for two operating energies. LINAC's are inherently capable of producing the smallest beam size, and therefore the highest spatial resolution for conventional radiographic techniques. They are also more easily able to meet the repetitive pulsing requirements mentioned earlier. They are, however, severely limited in current capability as compared to the LIA and, in light of this fact, a LINAC was only considered for use prior to and subsequent to the power transient. The sample power level maximum during these two periods of a test and the associated operating characteristic are found in Table IV. As can be seen from this table the only entries which appear realistic in terms projected LINAC technology are those at 25 MeV operating voltage for the Large Bundle LOFT and FCI experiment categories. Although the existing and projected pulse durations are longer than specified the available charge is adequate to satisfy fluence requirements in order to meet the minimum sensitivity of the detector system. Longer pulse width would be acceptable since the background is so low for these cases.

In Table V the operating characteristics of a LIA for operation during the power transient are presented. Also included for comparison with the three selected experiment categories is the "maximum postulated excursion;" i.e., a full subassembly reaching a maximum power density of 10^6 watts/gm. In all cases, except the "maximum

TABLE IV

LINAC's

	S/A to S/A Failure Propagation		Large Bundle Loft		FCI		Typical LINAC's		
Pre/Post Test Power Den. (w/g)	25		16		∿0		existing large	off the shelf	projected
Test Sample (# pins)	Multi S/A (1028)		S/A (271)		Partial S/A (127)		Boeing (163)	Varian	--
E(MgV)	25	10	25	10	25	10	16	20	30
I(A)	330	$2x10^3$	10	60	3	20	2.7	0.25	1
Pulse Width (μs)	1	1	1	1	1	1	8	5	10
Pulsing Rate, pps	10^3	10^3	10^3	10^3	10^3	10^3	$\sim 10^2$	10^3	250/ 1000
$\overline{D}_{(\gamma)}$	.01	.01	.01	.01	.01	.01	.03*	0.003*	.05*
E(kJ)	8	20	0.25	0.6	.07	0.2	0.35	.025	0.3
Source Size, mm	S	S	S	S	S	S	--	few	few

*Based upon a partial S/A (127 pins)

TABLE V

LINEAR INDUCTION ACCELERATORS

	S/A to S/A Failure Propagation		Large Bundle LOFT		FCI		Maximum Postulated	Typical Machines	
Peak Power Density (w/g)	2.5×10^2		1.1×10^4		1.8×10^5		10^6	Existing	Projected
Test Configuration (# pins)	Multi-S/A (1029)		S/A (271)		Partial S/A (127)		S/A (271)	USSR	--
E(MeV)	25	10	25	10	25	10	50	30	10
I(A)	330	2×10^3	80	560	200	1.4×10^3	3000	250	$1\text{-}2 \times 10^3$
Pulse Width (μs)	1	1	1	1	1	1	1	0.5	1
Pulsing Rate (pps)	10^3	10^3	10^3	10^3	10^3	10^3	10^3	50	$5\text{-}10 \times 10^2$
D (r)	.01	.01	.09	.09	0.7	0.7	4.0	--	.15-.30*
E(kJ)	8	2	2	5.6	5	14	75†	3.8	10-20
Sources Size, mm	M	M	M	M	M	M	M	--	25 to 50 D

* Based upon penetration of a full S/A

† 20,000 pulses at 75 kJ each would mean 1500 MJ of total beam energy

TABLE VI

RELATIVISTIC ELECTRON BEAM ACCELERATOR

	S/A to S/A Failure Propagation		Large Bundle LOFT		FCI		Maximum Postulated		Typical Machines	
Peak Power Density (w/g)	2.5×10^2		1.1×10^4		1.8×10^5		10^6		Existing	Projected
Test Configuration (# pins)	Multi-S/A (1029)		S/A (271)		Partial S/A (127)		S/A (271)		Hermes II @ Sandia	--
E(MeV)	10	5	10	5	10	5	10	5	10	5
I(kA)	20	180	0.6	5	1.5	13	50	400	100	800
Pulse Width (μs)	0.1	0.1	0.1	0.1	.025	.025	.025	.025	0.1	.025
Pulsing Rate (pps)	10^3	10^3	10^3	10^3	10^3	10^3	10^3	10^3	10^{-3}	∿250
D (r)	.01	.01	.01	.01	.02	.02	0.2	0.2	.05 (4)	0.4 (1)
E(kJ)	13	56	0.4	1.6	0.3	4	7.5	30	65	65 (2)
Source Size	L	S (3)	L	L	L	L	L	S (3)	L	S (3)

(1) Based upon penetration of a full S/A
(2) 25 pulses at 65 kJ each would mean ∿1.5 MJ of total beam energy
(3) Axial magnetic field control of the beam could be used to provide a large area source as opposed to a 5 to 10 mm source diameter.
(4) Based upon penetration of a Multi-S/A.

postulated excursion," a 10 MeV LIA operating at 2 kA should prove satisfactory. Spatial resolution will be limited by source size which is on the order of 5 to 10 mm for this source type and the pulsing repetition ratio will likely fall short of the 10^3 pps. Although a LIA of this size has not been built to date it is felt that such a project is technically feasible[8] as can be seen from the projections presented in the table. It is obvious that for most of the experiment categories considered here the source operating conditions were determined based upon background considerations. Worthy of notice also is the rather sizable amount of energy contained in each pulse. These results prompted the earlier comment concerning the temporal programming of pulses in order to conserve total energy.

In Table VI the operating characteristics for REB's operating during the power transient are presented. Again the "maximum postulated excursion" is included for comparison. As can be seen from this table the background and therefore the required detector signal produced by the source is, in most cases, substantially reduced over that of the LIA. This results from the short pulse duration of this type of source. For a REB the two maximum energies considered have implications concerning the radiographic mode of operation; i.e., conventional point source radiography as opposed to coded aperture X-radiography as discussed in Section I. A machine with lower voltage and higher current operating characteristics has the potential of producing small source diameters, $\sim$ 5-10 mm, through the process of beam self pinching in the diode [9]. A large area beam of suitable geometrical shape can be produced by a source with the higher voltage and lower current. A small area converter could be used with this latter source to produce a small area Bremsstrahlung spot but only at the expense of the effective utilization of beam energy. The results presented in Table VI show that this type of source should be able to satisfy detector system dose requirements for all the experimental categories. However, large REB's of this type are not presently able to provide multiple pulsing capability at a high repetition rate. Work is presently being carried out to develop multiple pulsing REB's as laser drivers[10]. This work is aimed at producing $\sim$ 25,000 pulses of 800 J each at a rate of 1 pps. It is evident from this table that present and projected sources of this type produce pulsed beams of sizable energy. Even if an energy source were available to provide the energy

needed for a train of 20,000 pulses, the inherent characteristics of these large machines is to limit the number of reproducible and reliable pulses to 25 to 100 and at a much reduced pulsing rate over that required. As a result it appears that a source of this type could only be used during the power transient in a programmed manner.

V. Summary and Conclusions

Based upon the results of this study it appears that a linear induction accelerator should be able to satisfy most of the experimental category requirements up to full subassembly test assemblies with acceptable spatial or areal density resolution. The actual resolution attained will be strongly dependent upon photon buildup and scattering. For this single subassembly test configuration, resolution is likely to be marginal at 10^6 watt/gm power density. X-ray cinematography should not be capable of achieving acceptable spatial or areal density resolution for multi-subassembly test configurations as a direct consequence of photon buildup.

It should be possible to use a modest LINAC to obtain shadowgraph information for full subassemblies or less. The relativistic electron-beam accelerators are not presently capable of repetitive pulsing at the required rate and with sufficient beam intensity, especially when this type of source is used in the conventional point radiography mode of operation. Indeed as pointed out by J. G. Kelly[11] this type of accelerator would be much better adapted to the use of coded aperture X-radiography.

It should be emphasized once more that this analysis was based upon the assumption that only the uncollided photon beam contained information relative to spatial and areal density resolution. If there is some information content in the scattered photons which reach the detector system the requirements presented above could be relaxed. This would also be the situation for a more sensitive detector system (this appears to be technically feasible) when background was not the limiting factor or for one which could effectively discriminate background from signal (improvements should also be possible in this area). As a result it might be possible to reduce source requirements by as much as an order of magnitude. In this case it would be possible to lower the operating voltage of an LIA which is dominate in determining the cost[8]. This may also be

advantageous for reducing the effects of buildup. The modest LINAC mentioned earlier should still only be capable of obtaining shadowgraph information. Beam energy requirements could be reduced for a REB by either decreasing the operating current or voltage, or both, depending upon the radiography mode; i.e., conventional point source or coded aperture. Such a decrease would improve the probability of achieving a useful multiple pulsing capability for this source type. A programmed series of pulses might satisfy the experimental requirements or alternatively it might be possible to combine a LINAC - to observe fuel motion pre- and post- power transient - with a REB to observe fuel motion during the power transient. In this way it might be possible to realize better coverage for all possible power densities more economically than for a LIA.

Important areas of study which require further attention are as follows:

1. The identification and evaluation of improved detector systems and signal-to-background discrimination techniques.
2. Evaluation of the importance of photon buildup and scattering upon spatial and areal density resolution capabilities.
3. Pursue the development of high repetition rate multiple pulsed REB's operating at moderate-to-high beam intensity.

REFERENCES

1. A. DeVolpi, et. al; Nucl. Tech. 27, 449 (1975).

2. D. A. McArthur and J. G. Kelly, these proceedings, (A Coded Aperture Material Motion Detection System for the ACPR).

3. G. I. Bell, et. al; Los Alamos Scientific Laboratory Report, LA-5978-MS (May 1975), Section VIII.B.

4. W. E. Stein, these proceedings, (Flash X-Ray Cinematography)

5. Information obtained from vugraph material used in presentations at the SAREF Review Meeting of September 1975 and prior meetings.

6. J. A. Halbleib and A. R. Phillips; Sandia Laboratories Report, SAND 75-0223 (September 1975).

7. J. A. Halbleib, these proceedings, (X-Ray Cinematography of Fuel Pin Motion).

8. D. Penner (National Bureau of Standards), private communication

9. G. Yonas, et. al; Nuclear Fusion 14, 731 (1974).

10. K. R. Prestwich (Sandia Laboratories), private communication.

11. J. G. Kelly, D. A. McArthur, and H. H. Barrett; these proceedings, (Coded Aperture X-Radiography).

Qualitative Diagnostics of Coolant and Cladding Motion* During LMFBR Safety Experiments Using Intrinsic-Junction Thermocouples

by

B. W. Spencer, R. E. Holtz, and F. J. Testa

Argonne National Laboratory
Argonne, Illinois 60439

*This work supported by the U. S. Energy Research and Development Administration.

Qualitative Diagnostics of Coolant and Cladding Motion During LMFBR Safety Experiments Using Intrinsic-Junction Thermocouples

The R-series is an on-going program of LMFBR safety experiments performed in the Transient Reactor Test (TREAT) facility. The purpose of the program is to provide experimental confirmation of modeling in accident analysis codes such as SAS.[1] The R-series test apparatus provides a flowing-sodium system with hydraulic and thermal features characteristic of current LMFBR design, in which multi-pin bundles of full-size LMFBR fuel pins may be subjected to simulated LMFBR accident conditions. The initial mission of the program has been to perform tests related to the hypothetical unprotected loss-of-flow (LOF) accident for FFTF safety studies.[2,3]

Instrumentation systems are relied upon to diagnose events occuring as a result of the transient undercooling, including a) coolant boiling and voiding; b) cladding melting, molten cladding motion, and blockage formations; and c) fuel behavior. Coolant behavior is typically assessed during the tests using acoustic detection,[4] apparatus flowmeters, and test section thermocouples. Fuel motion is monitored using the neutron hodoscope which is a part of the TREAT facility.[5] The motion of molten cladding and structure material would desirably be monitored in a similar manner, except that this capability does not presently exist. In the absence of such a capability, experimenters have succeeded in obtaining qualitative information about cladding motion by using fast-response thermocouples located on the outside of the test fuel holder. In addition to the TC's normal response to bundle heatup, coolant

voiding, film dryout, and structure heatup, the TC's also show a distinctive response to the transient wall heating associated with molten cladding moving coherently within the test bundle and bridging to the adjacent wall. The TC's have been effective in establishing the time during the test sequence when cladding motion begins, the location of initial cladding motion, and the progression of motion. This paper describes the thermocouple techniques and test data which have provided experimental information about molten cladding behavior during the R-series LMFBR safety tests.

The components and general layout of the TREAT/R-series test apparatus[6] are illustrated in Fig. 1. Two sodium tanks, located atop the TREAT reactor, are used to flow sodium through a piping system which penetrates the reactor core. The test section, containing the test fuel bundle, is located within the reactor core in the return leg of the pipe (upward-flowing sodium). An enlarged piping section above the test section represents the LMFBR upper plenum. The flowrate through the system is controlled by the pressure difference between the two tanks.

Figure 2 illustrates schematically the features of the test train. The inlet orifice, the multi-pin bundle of full-length fuel elements, and the upper plenum provide hydraulic simulation of current LMFBR design. The cross section of the 7-pin bundle used in the FTR-LOF tests is illustrated in Fig. 3. The test section was designed to give a uniform radial temperature distribution which is representative of the central 7-pin region of an FTR subassembly. This was accomplished by varying the pin enrichments to give radially uniform power generation (14% edge pin enrichments vs. 20% center pin enrichment) and by minimizing the overcooling at the outer edge of the pin bundle. In the latter regard, it may be noted in Fig. 3 that the wire wraps on the outer pins are of reduced diameter, that filler wires displace coolant at the inside flats of the

fuel holder, and that the fuel holder is thin-walled (20 mil) to minimize wall heat capacity effects. Radial temperature coherency is important to the rational of detecting coolant and cladding motion using thermocouples because it suggests the possibility of placing the TC's on the outside surface of the thin-walled fuel holder to monitor the coherent thermal conditions within the bundle. This is advantageous because it permits the use of a large number of TC's which do not involve penetrations through the sodium containment system. Accordingly, up to eighteen TC's are typically used on the fuel holder at various axial locations. The locations are selected on the basis of a) monitoring the overall axial temperature distributions during the course of a transient, and b) monitoring the local temperature conditions in a particular region, such as where initial cladding melting and motion are expected to take place.

The thermocouple design selected for this application is shown in Fig. 4. The thermocouple wires are individually spot-welded to the fuel holder wall. The fuel holder thereby becomes an integral part of the thermocouple junction which adds negligible thermal inertia at the heated surface. The time response of the circuit is limited principally by the internal resistance of the thin-walled fuel holder. The thermocouple assemblies are comprised of 0.040-in. O.D. 316 SS sheaths, chromel/alumel TC wire (nominal 6-mil diameter), and MgO insulation. Lengths vary from 50 to 100 inches where, at the cold end, there occurs a transition to 16-ga extension wire. Weld tabs are affixed to the sheath near the junction-end of the assemblies. During installation, the tabs are spot welded to the fuel holder, firmly attaching the sheath to the wall at its junction end. The remainder of the sheath is loosely banded to the fuel holder, such that differential thermal expansion is permitted. The bare TC wires, about 1/4-inch long, are flattened in a vise and are individually spot-welded to the wall at a separation of about 1/32-in. The bare, hot end of the sheath

is potted with Aremco Cerama-Dip 538 which serves both as a sealant and as a protection against the wires shorting either to the sheath or to one another away from the wall.

The 63% time constant for this surface temperature measurement is estimated to be about 40 msec based upon internal resistance to heat flow within the 20 mil flowtube wall (Biot Modulus $\simeq$ 70). Transient test data generally verify that the TC's respond adequately fast for the time scale of events during a LOF-type test. As an illustration, test data in Fig. 5 show the relation between inlet sodium flowrate and wall temperature (at the inlet plane of the test fuel column) during a 7-pin LOF experiment. At about 14.8 sec in this transient, the coolant reverses flow direction at the inlet and thereafter becomes oscillatory with alternating inward and outward flow. The flowtube thermocouple at the fuel inlet plane responds as expected to these changes in direction of the coolant motion. Prior to flow reversal the temperature is a steady 600°F; upon reversal, the temperature is seen to rapidly rise as the heated sodium is expelled back into the inlet plenum. The wall heating thereafter becomes cyclic, in response to the cyclic coolant flow. The time lag for this measurement is determined to be about 50 msec.

While data from the inlet region of the test bundle is useful for assessing the time response of the flowtube thermocouples, data from the outlet region of the bundle is important for understanding the test sequence itself. Figure 6 shows a typical temperature trace from near the top of the fuel column during a simulated unprotected LOF transient. Prior to fission heating of the test fuel, the system temperature is uniform at 600°F. Upon initiation of the power transient (point a), the outlet temperature reaches a quasi-steady plateau at about 840°F (240°F bundle temperature rise). The temperature oscillation during this preheat interval reveals that the test

pins move within the fuel holder as permitted by the assembly tolerances; this is consistent with neutron hodoscope indications that the test fuel generally shows coherent, oscillatory motion during the predistruption stage of the transient. The flow coastdown, initiated at point b in Fig. 6, results in a progressively worsening undercooling situation. The coolant temperature increases until the sodium saturation temperature of about 1700°F is reached (point c), at which point coolant boiling and voiding ensue. The wall temperature remains approximately constant after voiding, due to the presence of a sodium film left on the structure. Upon film dryout (point d), the stainless steel structure resumes heatup, leading to eventual melting at about 2500°F and loss of thermocouple signal (point e).

From this type of thermocouple data, obtained at various locations along the fuel bundle, it is possible to construct event profiles as illustrated in Fig. 7. Plotted on this figure are the times at which a) sodium saturation temperature is reached, b) flowtube dryout is indicated, and c) TC failures occur. These events are representative of, respectively, a) the progression of coolant voiding (with confirmatory data from inlet and outlet flowrate integration), b) structure dryout, and c) structure melting. It should be recognized that the assumption of temperature coherency, which permits bundle temperature conditions to be inferred from wall temperature measurement, is valid only up to the time of sodium voiding. After this, the wall dryout and temperature rise will necessarily lag behind the cladding dryout and heatup within the bundle. As indicated in Fig. 7, cladding failures, cladding melting, and upper blockage formation all occur well before melting of the fuel holder. This is the time domain of interest in attempting to detect molten cladding behavior from the still-functioning wall thermocouples.

Figure 8 illustrates test data from the R4 LOF experiment during the interval of cladding melting and motion.[7] Two aspects of the thermocouple data are of special interest insofar as their implications about bundle events. First, with the onset of sodium voiding at about 14.4 sec, sodium vapor streaming becomes an important phenomenon within the bundle. Sodium vapor, produced in the lower region of the bundle, streams upward toward condensation sites in the pin plenum region. The estimated vapor velocity of up to 300 fps exceeds the flooding threshold for liquid sodium (wall film) or for molten stainless steel (cladding) by an appreciable margin.[8] The vapor flow is oscillatory in nature due to the chugging behavior exhibited by the lower sodium slug (Fig. 8). As a consequence of the cyclic nature of the associated film motion and vapor condensation, the vapor streaming phenomenon is detectable by the wall thermocouples as a characteristic temperature oscillation. Hence, the occurrence of sodium vapor streaming is an event which is qualitatively detectable from the fast-response wall thermocouple. Secondly, at a time in the test sequence when SAS calculates the onset of cladding motion (about 1 sec after the cladding solidus temperature is reached), thermocouple TCTS-7, located 3 inches below the top of the fuel column, indicates a rapid transient heating event. This is interpreted as being caused by the motion of molten cladding material which accumulaes and bridges to the flow-tube wall. Additionally, thermocouple TCTS-5, at the top plane of the fuel column (not shown in Fig. 8), shows a similar heating event about 0.1 sec after the lower TC, suggesting a net upward motion of the molten material. However, thermocouple TCTS-4, located one inch above the heated zone in the colder insulator pellet region (Fig. 8), does not show such an event, suggesting that the molten material stopped its upward motion between these two measurement locations. This upper thermocouple indicates that at about

this same time in the test sequence the cyclic wall temperature behavior is interrupted, suggesting that a cutoff of the vapor streaming has taken place. Hence, the thermocouple data has provided indications of important bundle events including a) the time of molten cladding motion (first indication at 17.3 sec for R4 data), b) the initial progression of motion under the influence of sodium vapor streaming (upward in direction from initially 3 to 4 inches below the top of the fuel column to less than 1 inch above the fuel column), and c) the influence of cladding relocation upon the bundle configuration (formation of a steel blockage at the top of the fuel).

It should be mentioned that this evaluation of test data, and corresponding interpretations about the test sequence, were carried out and reported[7] prior to obtaining any physical evidence of the cladding blockage. The subsequent posttest cutup and examination did indeed reveal that steel had been swept up into the reflector region of the pins. Its posttest disposition was as a complete blockage of the channel cross-section, although there is no way to ascertain its complete history between its formation stage during the test and the later cooldown stage. Figure 9 shows a photograph of the blockage looking upward from the former fuel region toward the bottoms of the insulator pellets. As is evident in the photograph, the blockage is located only slightly downstream from the former fuel pellet/insulator pellet interfaces. What cannot be assessed from the photographs is that the planar blockage is very thin, only about 1/8 to 3/16 inch in thickness.[9]

In conclusion, it is regarded that test train thermocouples have proven successful at qualitative diagnostics of coolant and cladding motion. This is particularly significant in the case of molten cladding behavior because of the current unavailability of other diagnostics capabilities for real time steel-motion surveillance. The thermocouple techniques described have

yielded information about the time and location of initial cladding motion, its early progression under the influence of vapor streaming, and the formation of an upper blockage. However, the technique also involves inherent limitations insofar as there is no way to obtain details of the material behavior, to quantify the axial extent of materials involved, or to assess the thicknesses or radial coherency of blockages. Hence, the incomplete picture provided by test data of this important aspect of material motion is prompting development at ANL of a facility-type capability for steel-motion detection similar in approach to the fuel motion detection provided by the TREAT neutron hodoscope.[10]

References

1. F. E. Dunn, et. al., "The SAS2A LMFBR Accident Analysis Computer Code," Argonne National Laboratory ANL/RAS 73-39 (Dec., 1973).

2. M. G. Stevenson, et. al., "Report on the Analysis of the Initiating Phase of a Loss-of-Flow (Without Scram) Accident in the FTR," Argonne National Laboratory ANL/RAS 74-24 (Sept., 1974).

3. M. A. Grolmes, R. E. Holtz, B. W. Spencer, C. E. Miller, and N. A. Kramer, "R-series Loss-of-Flow Safety Experiments in TREAT," Proc. ANS Conf. Fast Reactor Safety, USAEC CONF-740401, Beverly Hills, CA (April, 1974).

4. B. W. Spencer, T. T. Anderson, R. E. Holtz, and A. P. Gavin, "Acoustic Surveillance in LMFBR Safety Experiments," Trans. Am. Nucl. Soc., 21, 377 (1975).

5. A. De Volpi, et. al., "Fast-neutron Hodoscope at TREAT: Development and Operation," Argonne National Laboratory ANL/RAS 74-31 (Dec., 1974).

6. R. E. Holtz, M. A. Grolmes, B. W. Spencer, C. E. Miller, and N. A. Kramer, "The R-series In-TREAT Test Apparatus," Trans. Am. Nucl. Soc., 19, 238 (1974).

7. B. W. Spencer, M. A. Grolmes, R. E. Holtz, and C. E. Miller, "Cladding Motion and Blockages in R-series Safety Experiments," Trans. Am. Nucl. Soc., 19, 238 (1974).

8. H. K. Fauske, M. A. Grolmes, and R. E. Henry, "An Assessment of Voiding Dynamics in Sodium-cooled Fast Reactors," Argonne National Laboratory ANL/RAS 74-20 (August, 1974).

9. F. J. Testa, Posttest Examination of R3, R4, and R5," ANL-RDP-36 (Jan., 1975).

10. A. De Volpi, C. L. Fink, and R. R. Stewart, "Monitoring Clad Blockages," (following paper).

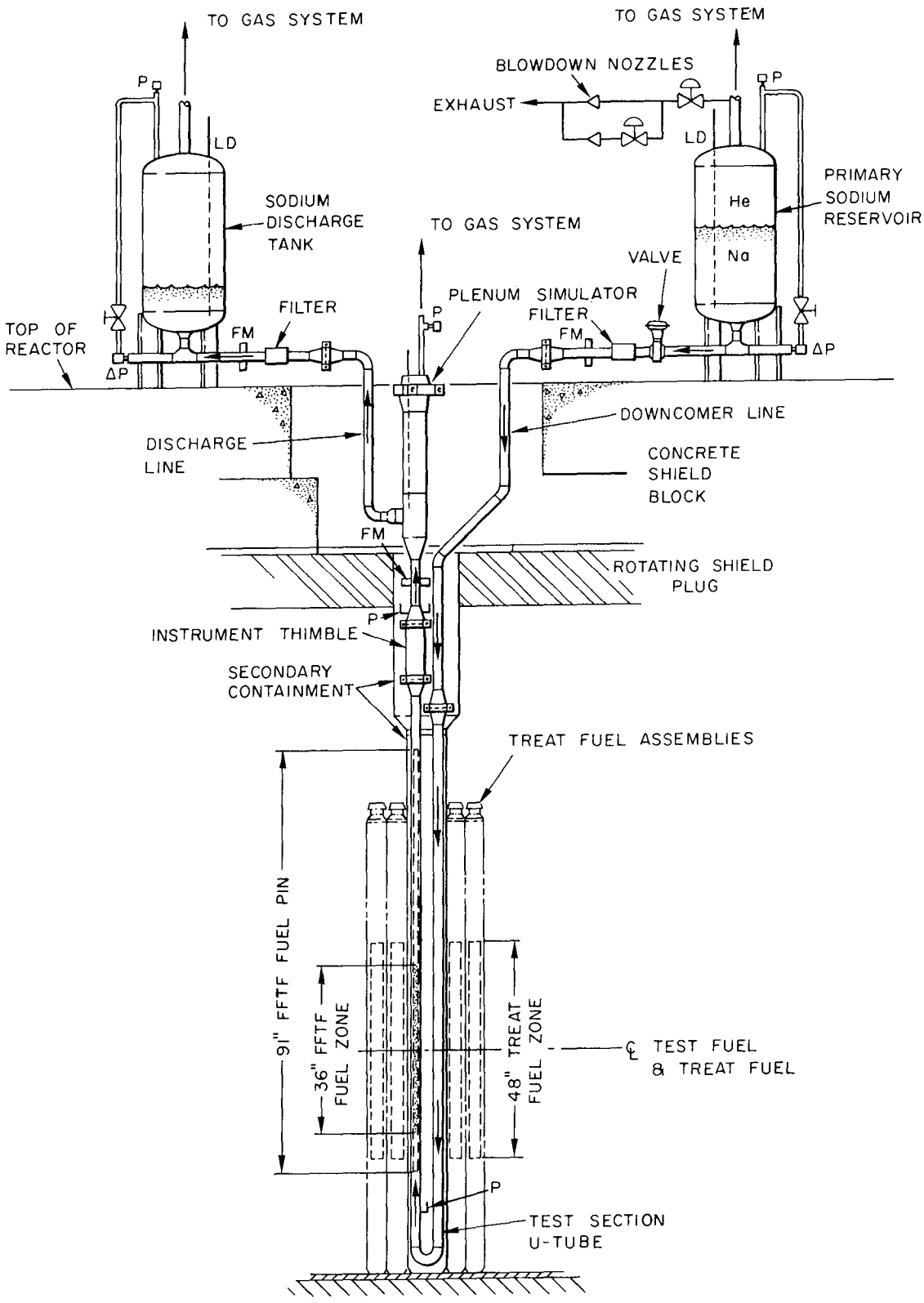

Figure 1. R-series/TREAT Apparatus for Performing LMFER Safety Tests

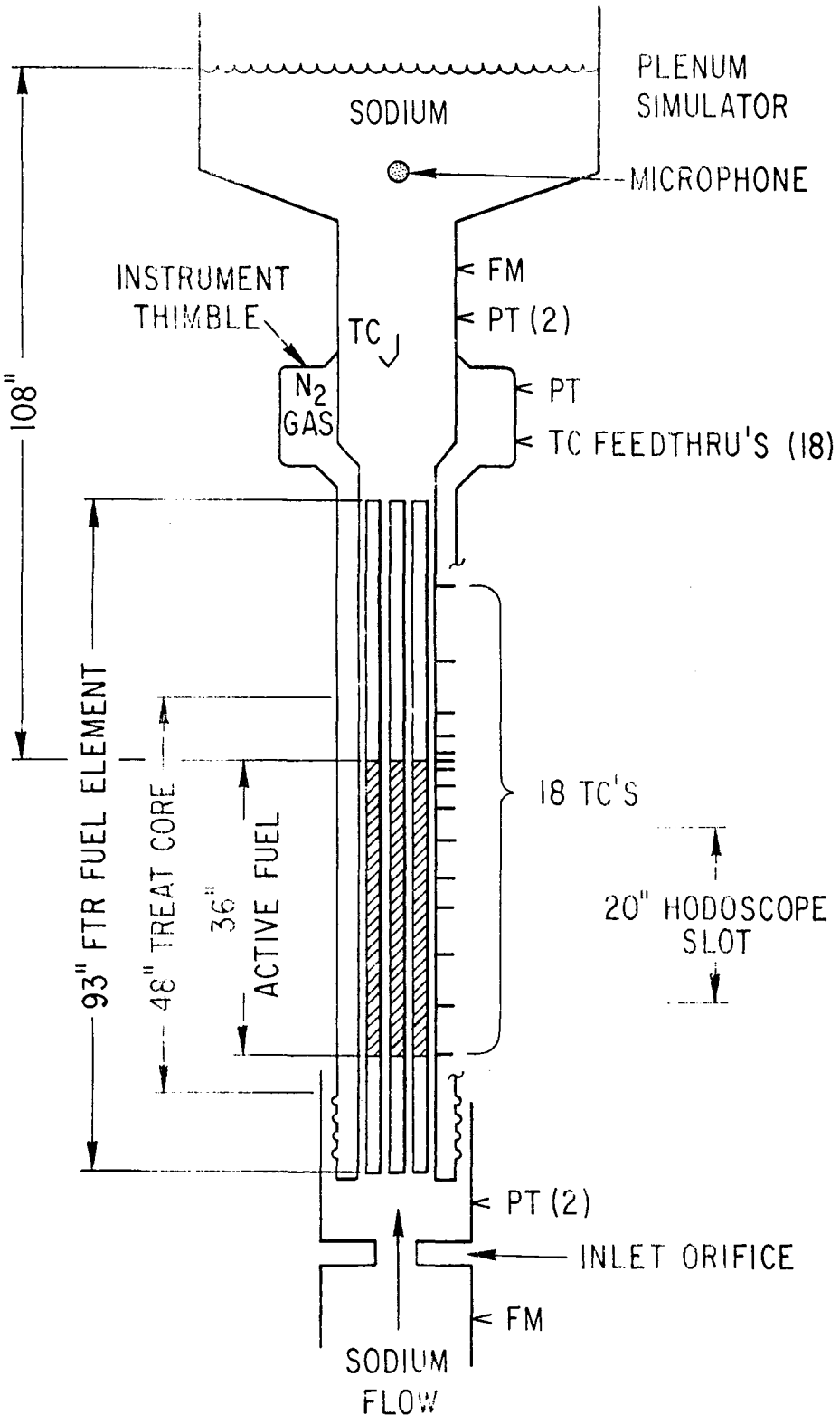

Figure 2. Test Train Components for R-series 7-pin Loss-of Flow Tests

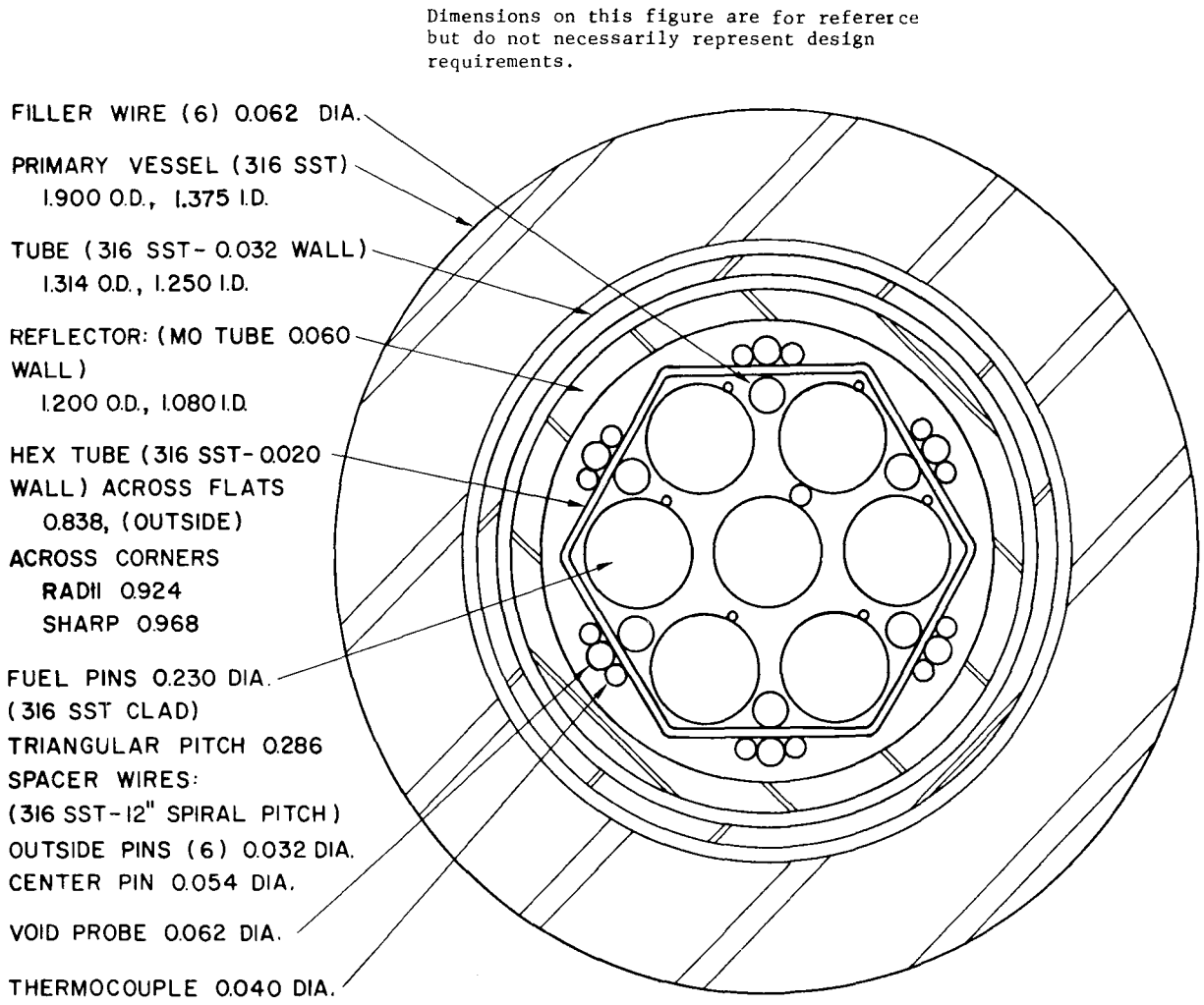

Figure 3. Cross-sectional View of 7-pin Used for Loss-of-Flow Tests

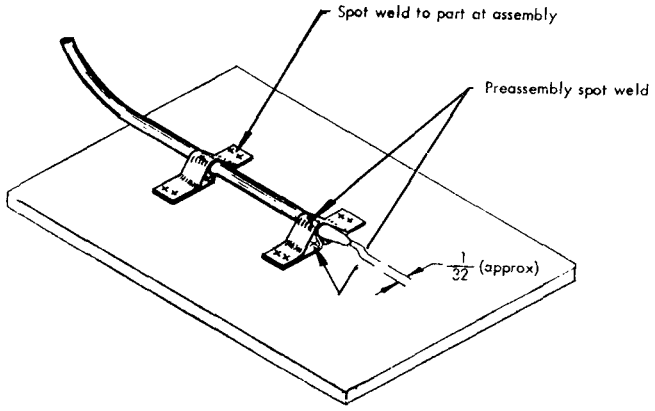

Figure 4. Typical Intrinsic-junction Thermocouple Used on Outside Surface of Hex-Tube (Fig. 3)

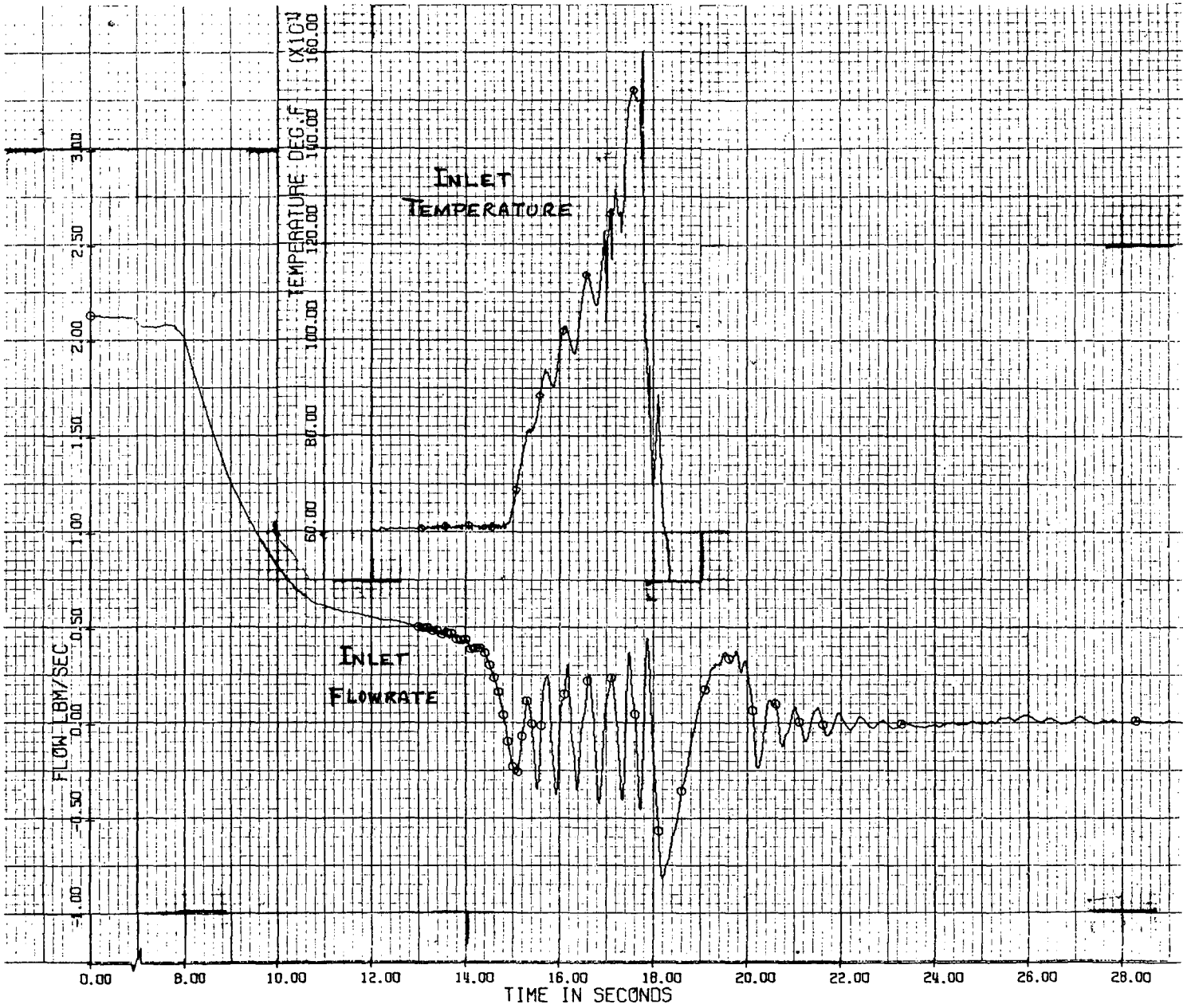

Figure 5. Wall Temperature Measured by Intrinsic-junction TC at Inlet to Fuel Zone during Flow Reversal and Coolant "Chugging"; from Test R4

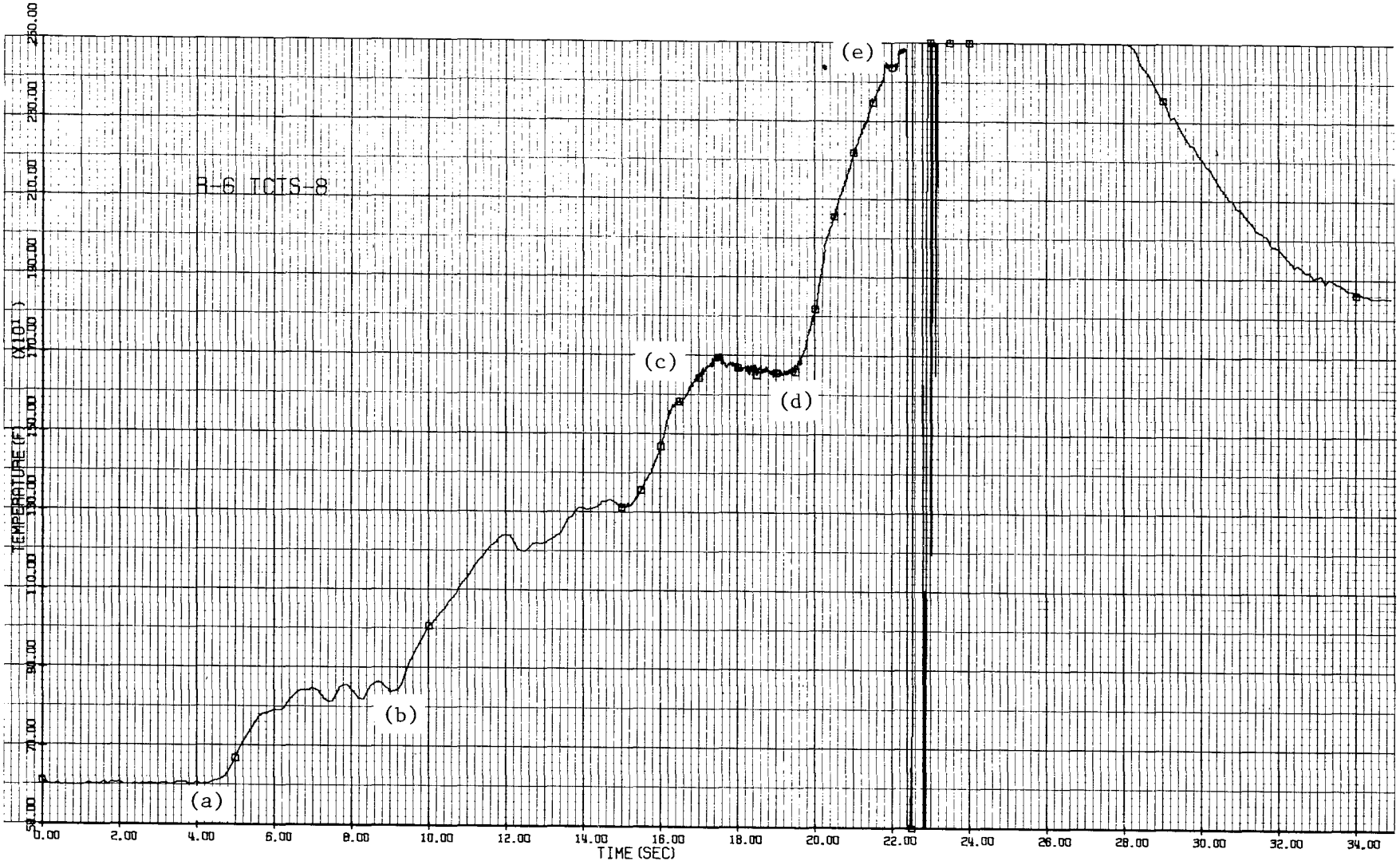

Figure 6. Wall Temperature Measured by Intrinsic-junction TC at Outlet of Fuel Zone During R6 Loss-of-Flow Test; (2) start of power transient, (b) start of flow coast-down, (c) sodium boiling temperature, (d) film dryout, (e) structure melting

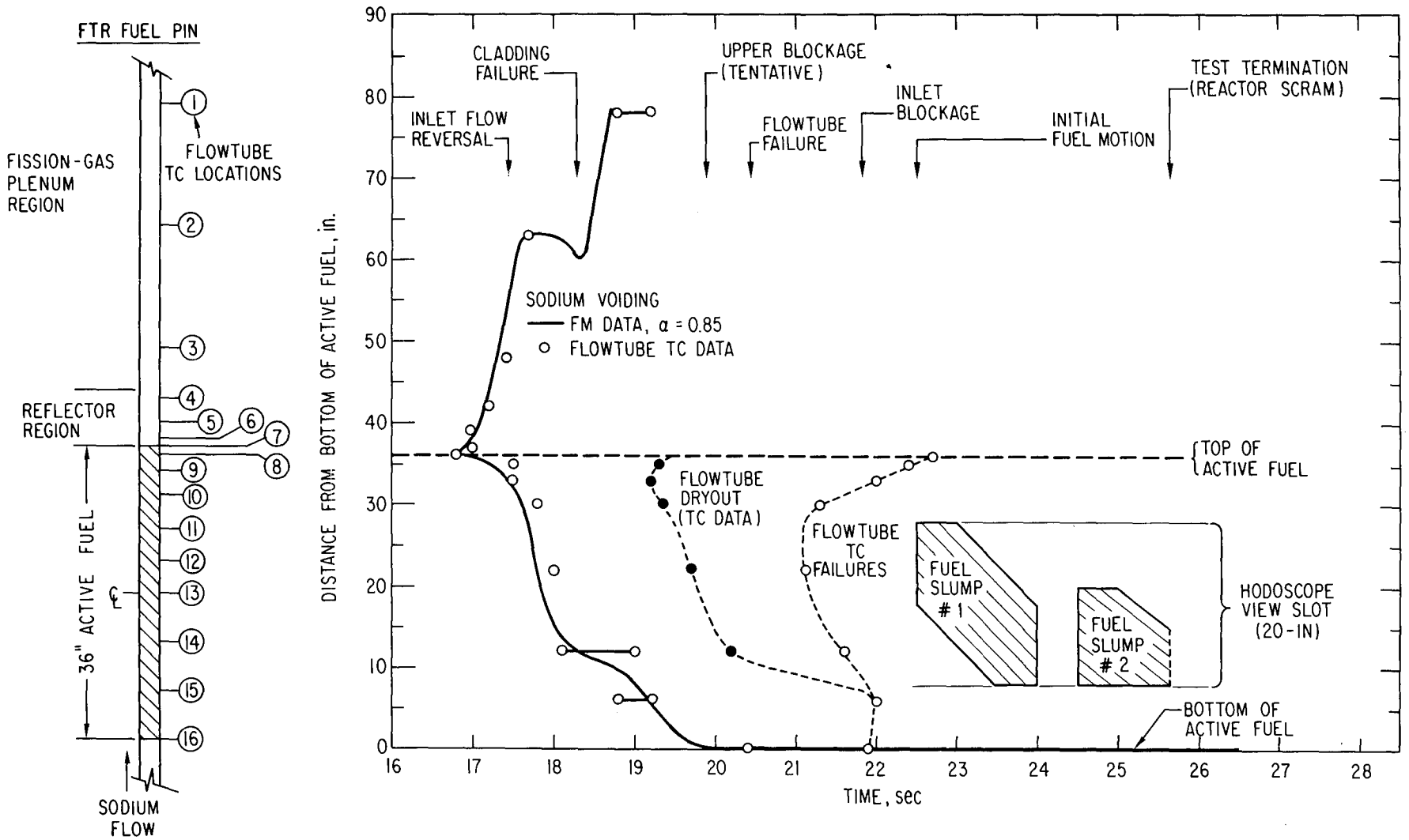

Figure 7. Event Profiles Constructed from Flowtube TC Data for Loss-of-Flow Test R6

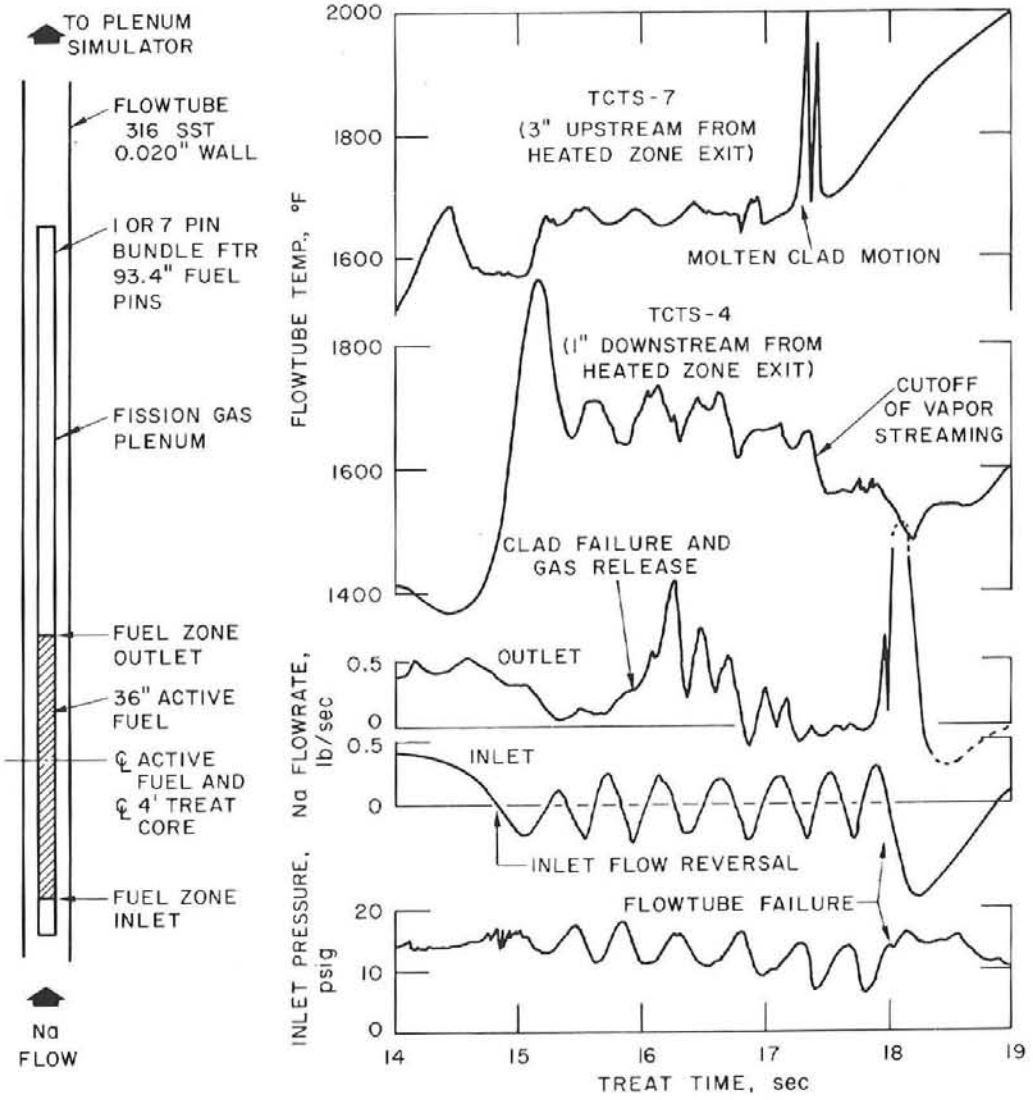

Figure 8. Test Data from Loss-of Flow Experiment R4 Showing Evidence of Molten Cladding Motion and Blockage Formations (Ref. 7)

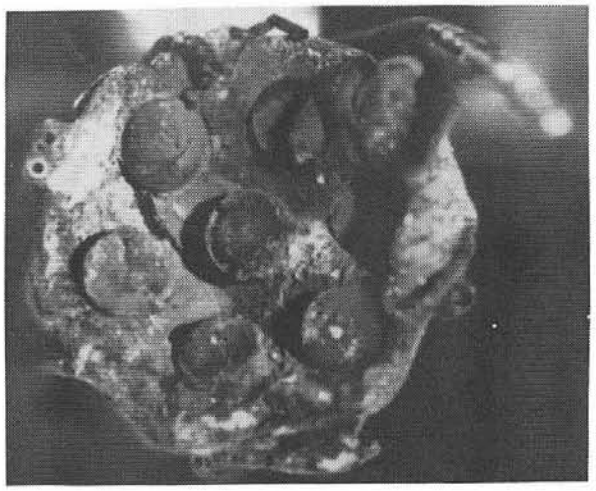

Figure 9. Photograph of Upper Cladding blockage formed in Region of Insulator Pellets during Loss-of-Flow Test R4; blockage thickness is about 3/16-inch average (Ref. 9)

Monitoring Clad Blockages*

by

A. De Volpi, C. L. Fink, and R. R. Stewart

Reactor Analysis and Safety Division
Argonne National Laboratory
Argonne, Illinois 60439

Abstract

In the coolant channels of fuel rod subassemblies, melting and accumulation of clad material may cause flow blockage. No method of detecting these effects during radiation transients has been implemented to date; however, studies indicate that the fast neutron hodoscope at TREAT can be modified to accomplish unambiguous clad blockage detection. The procedure, which has been tested for several years, consists of adding a gamma detection array in tandem with the hodoscope neutron detectors. The array would be biased at energies high enough to favor detection of capture gamma rays from the various components of steel in contrast to gamma rays from fission and other competing processes. Estimated volume sensitivity, under reasonable conditions, is about 0.2 cm^3 of steel.

*Work performed under the auspices of the U.S. Energy Research and Development Administration

Monitoring Clad Blockages

During destructive tests of the type performed on fuel pins at TREAT, cladding motion can be a significant passive or active factor. In a passive role, clad may fail because of internal gas pressure or molten fuel contact, or the cladding may simply melt; and the molten clad may drain or be swept away. In the more active sense, clad may be vaporized causing dispersal of fuel; furthermore, blockages resulting from accumulations of melted steel can prevent cooling of test sections and dispersal of disrupted fuel.

Consequently, the time history of the cladding and structural materials in a test section are of significance, both as cause and effect, in analysis and understanding of such transient experiments and their relationship to future LMFBR design and acceptance.

No method of detecting these effects during radiation transients has been implemented to date, although the motion of fuel itself is monitored by the fast neutron hodoscope, which intentionally is not sensitive to steel effects. Recent studies at TREAT indicate that, by adding a gamma detection array to the hodoscope, detectability specific to clad blockage is feasible.

Difficulties in Detecting Steel

Instrumentation could be inserted within a test section for the purpose of measuring some properties (temperature, physical state) of steel; however, these devices appear to be of limited value. More important, devices installed within the test section by their presence tend to perturb the experiment itself.

The primary problems that make clad detection difficult from outside the test section relate to competitive effects. Neutrons from the reactor produce gamma rays in fuel, the test section, and provide a general background of gammas and neutrons which interfere with detection. The cladding surrounding fuel constitutes only a few percent of the total steel in a test

section. Identification of a distinct cladding signature has been stymied by both the general wealth of background radiation and the presence of an overwhelming amount of material similar to that being observed.

Ex-core techniques using externally generated neutrons or gamma photons depend upon differences in transmission. The fuel and steel in an initial undisturbed test configuration may have sufficiently dissimilar density or transmission characteristics to provide some means of discrimination. But once the movement and mixing of fuel, clad, and coolant takes place, variations in grey level will no longer specifically identify material components.

Method Being Tested

One technique, which does appear promising, identifies steel by detecting its prominent capture gamma ray emission above 6 MeV. This method has been investigated at TREAT for several years. The primary components of steel -- iron, nickel and chromium -- all yield high energy capture gamma rays. On the other hand, other gamma rays from the reactor tend to be produced at lower energies. The primary sources in fuel are fission and capture processes. The reactor acts as a diffuse source of gamma rays from fission and capture in structure, such gamma rays being scattered by material in the test section. In addition, there are direct gamma rays caused by capture in the structural material and coolant of the test section.

The problem of detection may be divided into two parts: how to distinguish steel signal from that of fuel and then how to sense the cladding signal amidst the parallel background from other steel. The first part of the problem must be resolved because fuel is expected to move during most transients; thus any method which fails to distinguish between fuel and clad is of very limited utility. The second part of the problem may be categorized as one of detecting a small change in signal, where we may consider the primary sources of structural steel (such as test section containment) to be fixed during the transient.

A steel signature may be achieved satisfactorily by biasing a photon detector so that lower energy gamma rays characteristic of fuel are excluded. Some calculations will be described later. Capture gamma rays from sodium can be ignored because of their low intensity above several MeV.

The problem of measuring small signal differences is a classic issue in statistics of nuclear counting. In principal, signal changes of only a few percent may be determined with adequate confidence if the count rates are sufficient. In practice, a delicate balance must be achieved between various limitations resulting from real and spurious effects.

Detection System

The gamma-ray hodoscope technique has been tested by placing small sodium iodide crystals directly behind the collimator slots in tandem with the fast neutron detectors of the hodoscope. This is shown in Fig. 1, where the gamma detector bay is mounted behind the neutron bay. In this manner, it has been possible to utilize existing spare signal processing, data collection, and data processing facilities of the hodoscope.

Experiments have been conducted in several stages to select the most viable options. Early tests were focused on gamma spectrum measurements using both NaI(Tl) and Ge(Li) detectors. We also investigated requirements for instrumentation; background effects due to fuel, sodium, and structure; the use of lead filters; optimization of bias level, efficiency and count rates; size of crystal; and transient response. The results led to setting up a temporary 24-channel array, containing 3/4 x 1-in. (1.9 x 2.5-cm) NaI(Tl) crystals, which has been operational for over 2-1/2 years. There was no apparent advantage to having energy resolution any better than that obtainable from sodium iodide; this conclusion also results in considerable savings in detector and pulse processing costs. In fact, after reducing phototube high voltage, the sodium iodide signals could be properly processed by the existing electronic chain designed for Hornyak button fast neutron detection using a single threshold.

The original experiments conducted in 1972 were made in the context of sodium void detection; the results indicated that unique definition of sodium by means of characteristic capture radiation is marginal and would require further investigation. At the same time, however, it was evident that the steel capture radiation was quite prominent.

Recent Experiments

Some analysis of our sodium iodide transient data has been accomplished, but results are not conclusive in terms of clad blockage detectability. We have been unable to devote an adequate effort level to analyze remaining transient data, nor have there been many transients well suited for this purpose. The lack of enough gamma detector channels has also hampered definitive results. One conclusion regarding instrumental effects is that bias levels were not initially chosen high enough to provide a dominant steel over fuel signal ratio, and count rates were allowed to be too high, resulting in saturation for high power experiments.

Calculations have been performed of the expected steel/fuel signal ratio for a seven-pin test assembly[1] and the results are displayed in Fig. 2. In earlier measurements we apparently used bias levels around a few MeV, whereas the calculations indicate that the threshold should probably be set about 6 MeV. One problem we have not yet resolved is that of ultimately achieving a reproducible and simple technique for calibration of detectors in the field.

Experiments were recently conducted at TREAT to evaluate response to certain known source conditions. Data were obtained by "scanning" the hodoscope collimator across the field of view at the center of the reactor in the same manner that similar profiles are obtained of the neutron distribution from fuel.

The "source" was a 14% enriched fuel pin, with stainless steel cladding, offset within a stainless vessel of 65 mil (1.65 mm) wall thickness. As seen in Fig. 3, the 65 mil steel tube is clearly detectable amidst the back-

ground of reactor and fuel pin. In fact, by scaling from the relative thickness of steel or clad vs. tube, it is evident that some portion of the peak amplitude and width are attributable to the cladding. It should be kept in mind that the steel/fuel ratio was not yet optimized. In this test, calculations indicate that the detector threshold was ∿4 MeV. If the threshold had been set at 6 MeV, a single-pin steel-to-fuel ratio of 20 would have been possible.

A further test was made to simulate conditions more typical of transient experiments: a 1-in. (2.54 cm) steel plate was inserted in front of the source. The results are shown in Fig. 4; again, the detector (which differs from the detector used in Fig. 3) was not optimized (estimated threshold ∿3 MeV). Despite the very thick "source" and attenuation effects caused by the 1-in. steel plate, there is a statistically significant signal from the steel tube and fuel and, by inference, marginally from the cladding. Statistical errors are within the plotted symbol size. The signal from the steel vessel amounts to 8% of the total count. Such evidence clearly points to a detection capability for massive blockages of steel and, in fact, suggests a marginal possibility of detecting the original clad melting under appropriate conditions. One factor to keep in mind is that the geometry used in Fig. 4 permits a larger clad plus tube signal than if the 1-in. steel attenuator were to surround the source.

Predictions for Time-Resolved Steel Motion

Stainless steel cladding on LMFBR fuel pins has a typical thickness of about 15 mils (0.4 mm) with pin diameters of 230 mils (5.8 mm) or larger. Moreover, a total of 1/2 to 1 in. (1.26 to 2.54 cm) of steel usually surrounds the TREAT test assembly. The results shown above indicate that accumulations of steel which represent at least 50% of the test vehicle cross section for a few mm height should be time resolvable. Such accumulations are adequate to detect total flow blockage.

In situations where steel blockage occurs well before fuel motion, then a higher level of sensitivity should be achievable. Our estimated volume sensitivity under favorable conditions is 0.2 cm^3 of steel, which is comparable to existing fuel motion capability of the hodoscope fast neutron detectors at TREAT.

We plan when the budget permits to expand the gamma array up to 100 or so detectors for both the 21-in. (51 cm) and 48-in. (122 cm) collimators. Additional work in characterizing the optimal size, adjustment, calibration, and bias setting of the channels is underway.

Experiment and reactor designers can improve prospects for clad blockage detection by minimizing the amount of construction steel or by substituting fabrication materials, such as tungsten, tantalum, niobium, titanium, or even zircaloy, which provide fewer capture gammas above 6 MeV.

Radiography

In-situ radiography is an informative procedure. It would be useful to have radiographs of separated fuel and steel (and coolant) dispositions following a transient. Furthermore, in view of the real possibility of mechanical disturbance caused by removal of the test section from the reactor, such radiographs obtained in-situ would be most valuable, especially if provided to the experimenter not long after a test.

The hodoscope provides a means for both neutron and gamma-ray in-situ radiography. A paper being provided for the IEEE Nuclear Science Symposium[2] explains the proposed method for fast neutron radiography. Similar techniques would be applicable for gamma radiography by using the characteristic capture gamma radiation from steel as described earlier for time-resolved clad blockage detection. The primary difference is that radiographs of stationary configurations are easier to achieve than the time-resolved data.

For time resolution, we are statistically limited, whereas a post-transient radiograph may be generated taking advantage of several hours of low-

power reactor operation. To effect the type of radiograph that the hodoscope produces, the hodoscope collimator is moved horizontally and vertically. This contrasts with time-resolved operation where the material being observed moves and the collimator is stationary. When the material is stationary and the collimator is scanned, then a type of digital radiography ensues. A series of profiles of fuel and clad response can be built up (as shown in Figs. 3 and 4), and ultimately a pseudo-radiograph can be constructed depicting the relative 2-dimensional disposition of steel as distinct from fuel. Since radiographs are frequently digitized in order to yield quantitative data, having digital data to start with is not an inherent limitation but, in fact, may be a significant advantage.

In Fig. 3 data points were taken laterally at intervals of about 50 mils (1.3 mm); in principle, lateral resolution in the order of 10 mils (0.25 mm) and vertical resolution of about 100 mils (2.5 mm) should be achievable with the 48-in. (122-cm) collimator adapted to radiographic scanning.

Summary

It is difficult is isolate some characteristic signature of steel in a realistic transient reactor background. Tests have been performed at TREAT on the possibility of measuring steel by detecting capture gamma radiation above 6 MeV, making use of a simple modification to the hodoscope. Steady-state experiments indicate that the large amounts of steel are resolvable, which would satisfy requirements for detection of blockages caused by accumulated steel. It is likely that this can be accomplished on a time-resolved basis. Whether actual melting of clad or accumulations of amounts smaller than full blockages can be detected cannot be reliably predicted from the existing data. There are indications that such detailed steel motion resolution is possible, but confirmatory evidence is presently lacking. In any event, it should be possible to achieve high resolution digital radiographs comparing the pre- and posttest stationary disposition of steel.

References

1. Susan Cheng, "Detection of Steel Clad Motion in the TREAT Reactor," Undergraduate Research Participation Report, Argonne National Laboratory, unpublished (Summer, 1975).

2. A. De Volpi, "High-Resolution Fast-Neutron and Gamma Digital Radiography," Proceedings of IEEE Symposium on Nuclear Science, San Francisco, California, November 19-21, 1975 (to be published).

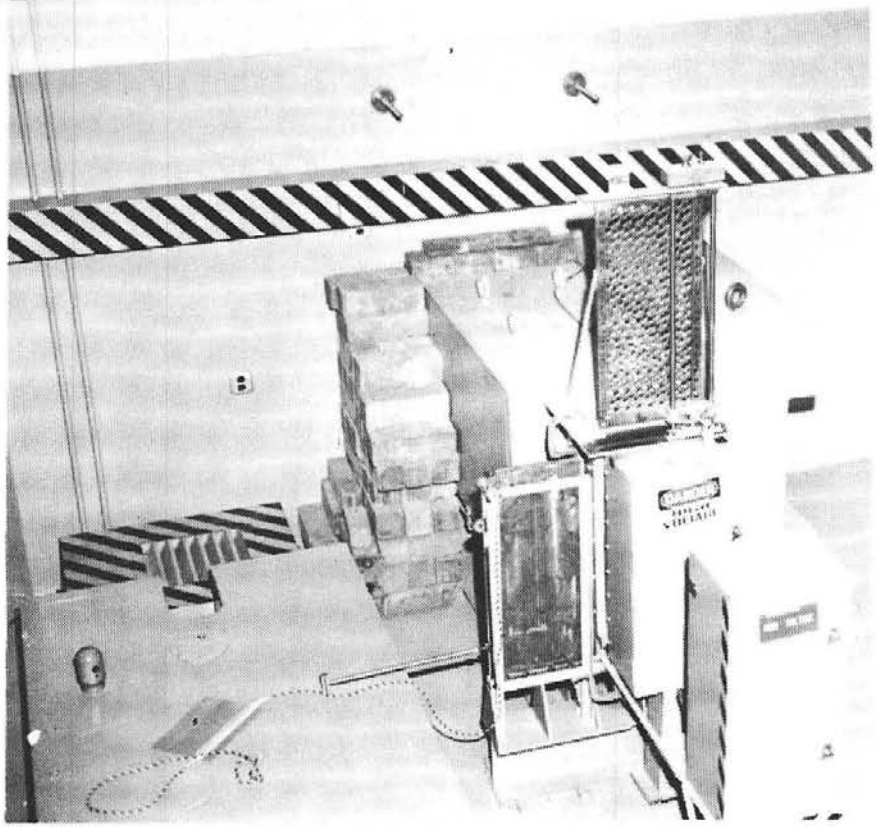

Figure 1. Gamma Array in Tandem Inside Enclosure (Marked "High Voltage") Behind Neutron Enclosure (Marked "Danger, High Voltage") at TREAT Hodoscope

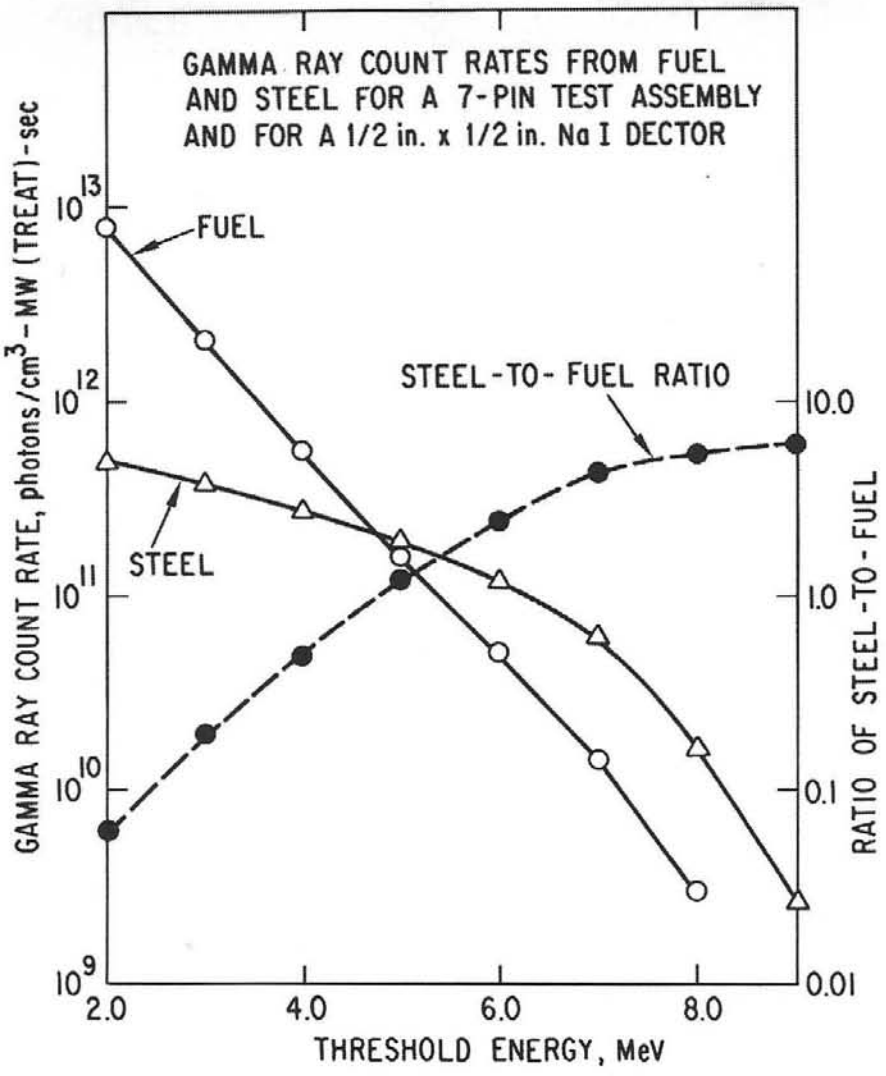

Figure 2. Calculated Count Rate and Ratio Trends for Detection of Fuel and Steel Using Small NaI Crystals

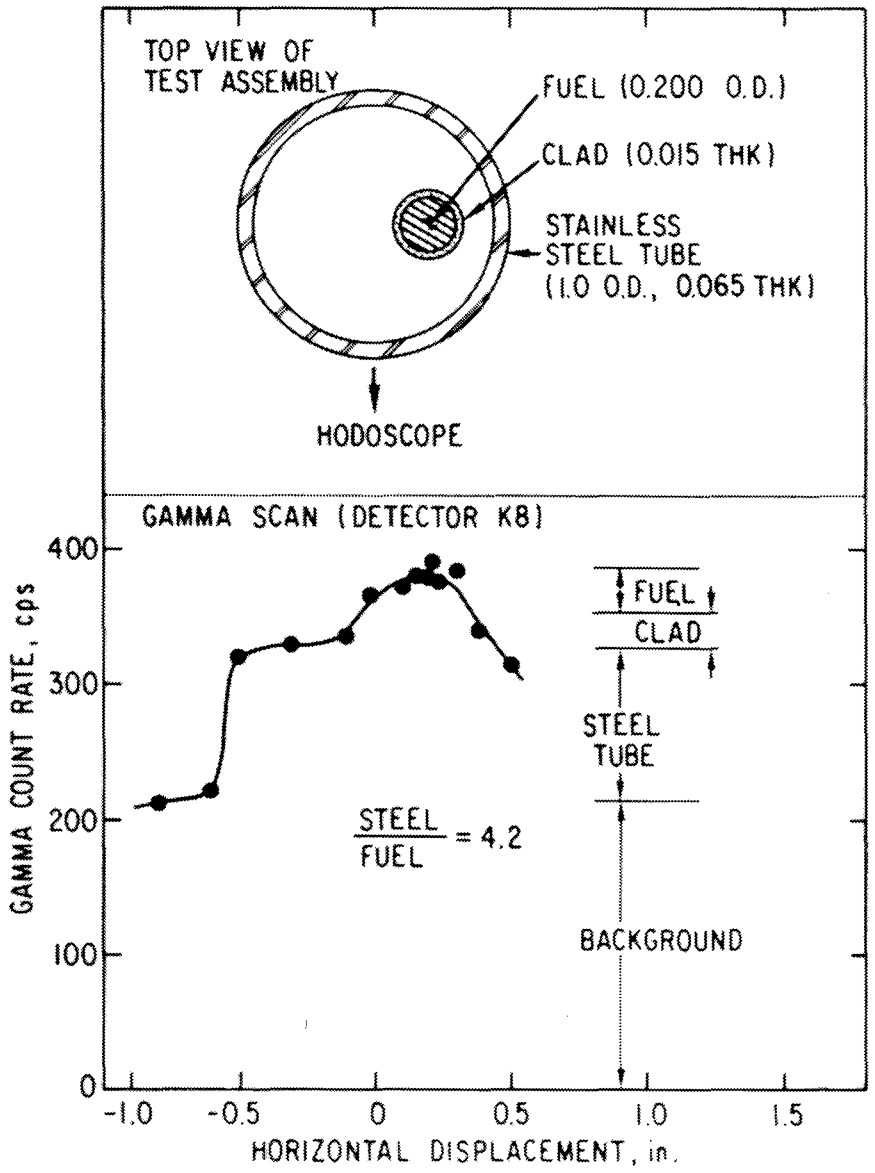

Figure 3. Gamma Scan of Single-Pin within Steel Tube with TREAT Reactor at 80 kW

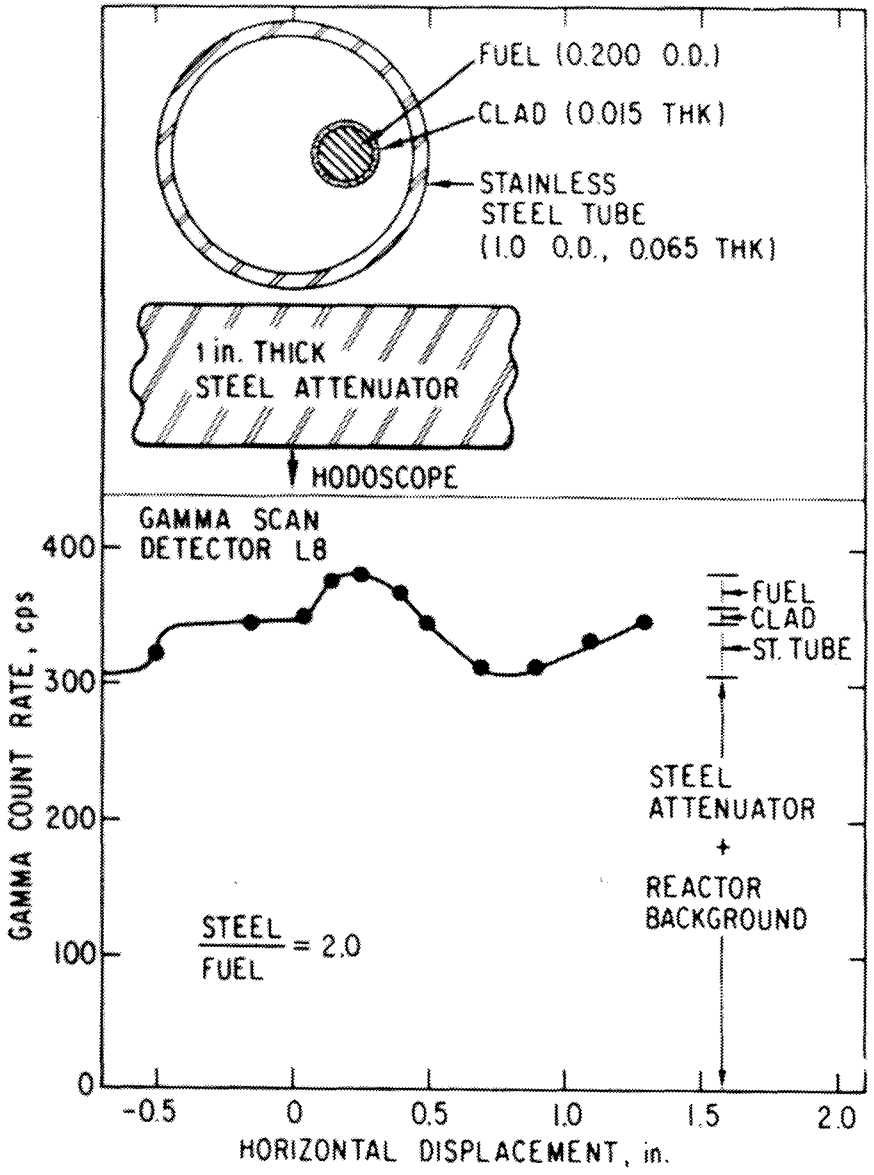

Figure 4. Gamma Scan of Single-Pin within Steel Tube thru 2.54 cm Steel Plate

A Survey of Coded Aperture Imaging

BY

H. H. Barrett
Optical Sciences Center
University of Arizona
Tucson, Arizona

I. Introduction

There are a number of important applications, particularly in nuclear medicine and astronomy, where it is necessary to form an image of a source emitting x-rays or gamma rays. Since this radiation is not appreciably refracted or reflected by matter, the image cannot be produced by ordinary focusing optics. Instead, the conventional approach has been to use a pinhole aperture or multihole collimator as shown in Fig. 1 to form an image of the source on a scintillation camera, film, or other image detector.

This type of imaging has made possible the field of diagnostic nuclear medicine. With a modern scintillation camera, acceptable images with 1 to 2 cm resolution can be obtained with a radiation dose to the patient that is one to three orders of magnitude below the dangerous level. The information gained in this manner is valuable in delineating the physiological function of an organ, e.g., which parts of the organ absorb a given pharmaceutical and how rapidly. However, the resolution is inadequate to give the kind of detailed, morphological information contained in a radiograph. Improved resolution in nuclear medicine would offer many new diagnostic possibilities, such as the early detection of small focal lesions and metastases, or more precise differentiation between benign and malignant tumors.

But increasing resolution with a pinhole or collimator is a very difficult task. Because of the low collection efficiency of the apertures (typically 0.01%), the scintillation camera must have high detection efficiency

in order to "make every photon count." The high efficiency is obtained by using a relatively thick scintillation crystal and sensitive photomultipliers to detect the resulting light. Economic constraints limit the number of photomultipliers and hence the intrinsic spatial resolution of the camera. But even if that problem were solved, the resolution would still be severely limited by the collimator itself. For example, suppose it is desired to increase the system resolution from 12 mm to 6 mm and that a fictitious camera with perfect intrinsic resolution is available. Then the resolution can be increased a factor of two simply by using a finer collimator or smaller pinhole. With all other factors remaining constant, the result is a four-fold reduction in gamma ray flux. However, in order to keep the same signal-to-noise ratio, the number of detected gamma ray quanta per resolution element must remain constant, or the total number of quanta should increase by a factor of four. The net result is that a factor of two increase in resolution must be accompanied by a factor of sixteen increase in patient dose or exposure time.

A similar result is obtained for a scintillation scanner used with a focused collimator. The scanner has an efficiency of 1 to 5%, but it views only one resolution element of the object at a time. Again large doses or exposure times, which can be reduced only at the expense of spatial resolution, are required. For example, a typical whole-body skeletal scan now takes about an hour.

Thus, whether a camera or scanner is used, an apparently inevitable tradeoff between radiation flux and resolution is required. Very similar tradeoff situations occur also in other fields such as radar technology,[1] x-ray astronomy,[2-4] and infrared spectroscopy.[5-8] But in these areas sophisticated signal processing techniques have been devised to avoid the tradeoff, to obtain high flux, and after the processing, high resolution as well.

These ideas have recently been carried over into nuclear medicine,[9-11] where they have come to be called "coded aperture imaging" techniques. The key feature that sets coded aperture imaging apart from conventional imaging

techniques is that the initial image is not immediately recognizable. Instead it is a coded or scrambled representation of the object. The processing step is not merely to enhance the image, but is essential to obtain any useful image at all.

The most successful coded aperture to date is the Fresnel zone plate.[2, 3, 9-11] In this case the coded image is closely analogous to a hologram and can be reconstructed with a coherent optical data processing system.

The zone plate aperture can be a factor of 1000 more efficient than a pinhole or parallel-hole collimator. For a point source, this means that an image with a given signal-to-noise ratio can, in theory, be formed with a factor of 1000 smaller exposure time or dose.[12, 13] For larger sources, the advantage is considerably less, but it should still be as much as a factor of 10 for many practical clinical situations.[13]

However, in most of the work we have performed to date, this large advantage is not realized, primarily because x-ray film, rather than a scintillation camera, is used as the detector.[11, 14] The resulting camera is an extremely simple one that is lightweight, portable and inexpensive, and gives high-resolution, tomographic[15] images. Clinical trials of this camera are now under way.[16] Excellent results have been obtained in studies of the thyroid, bone lesions, myocardium, lungs, liver, and spleen. Examples are shown in Figs. 2 and 3.

Although this camera definitely seems to be a useful diagnostic device, it requires substantially larger doses or exposure times than conventional systems. Until recently, it had seemed that it might not be possible to realize the full theoretical advantage of coded apertures because an off-axis zone plate[11, 14, 15] seemed to be necessary to eliminate undiffracted background light. The off-axis zone plate has very closely spaced zones and is not, therefore, compatible with a low-resolution, high sensitivity, detector such as the Anger camera. Thus an impasse had developed: To utilize

the high sensitivity of the zone plate it was necessary to use a low-sensitivity detector like x-ray film, so the overall sensitivity was no better, and usually substantially worse, than with conventional systems.

Recent work, however, has shown that this impasse may be surmounted in several ways. As discussed below, several apertures including the on-axis zone plate, annulus and non-redundant pinhole arrays can be used with an Anger camera.

II. Basic Principles of Zone Plate Imaging

The operation of the zone plate aperture can best be understood by first considering a point source of gamma rays. The probability distribution of the gamma rays on the image plane is just a geometric shadow of the zone plate (see Fig. 4). This shadow contains the full three-dimensional information about the location of the point; the lateral position of the shadow depends linearly on the lateral position of the point, and the scale of the shadow depends on the distance of the point from the zone plate.

Thus the imaging operation is a transformation of each point in the object into a zone plate. Exactly this transformation occurs in optical holography where the zone plate is the interference pattern between the light scattered from an object point and the reference beam. Therefore, once the coded image has been recorded, it no longer matters how the zone plates were formed. Whether it was by geometric shadowing of gamma rays or interference of light waves, a hologram is obtained.

The reconstruction step uses the fact that a zone plate transparency behaves as a lens, but with diffraction rather than refraction deviating the light. Thus, if the zone plate shadow is recorded as a transparency of suitable scale and inserted into a laser beam, part of the light is diffracted into a bright local spot that is the reconstructed image of the gamma ray point source. If two adjacent points sources were present (Fig. 4), the

hologram would consist of overlapping zone plate shadows, but the reconstruction would be two non-overlapping focal spots. Two sources at different distances from the zone plate would produce foci in two different planes.

Then, to the extent that linear superposition holds, any extended object can be considered to be composed of points and should be properly imaged. However, in practice this seldom occurs except for small objects. The difficulty is the undiffracted light (or "dc light" in optical jargon) that is present since both the gamma ray source intensity and the zone plate transparency are non-negative functions. For a point source, this undiffracted light overlaps the focal spot, but it is much less intense and therefore not troublesome. When a second point source is added, the two focal spots may be well resolved, but the undiffracted light patterns are not. Therefore the presence of a second point reduces the contrast of the first. For large, extended sources, the image contrast becomes so small that the image can no longer be seen.

A spatial filtering technique to alleviate this problem has been described.[9] In this approach, a Schlieren stop is used to block low-spatial frequency components of the image, thereby suppressing the undiffracted light. However, the usefulness of this technique is limited because a large object itself has low frequency components. Therefore, a stop large enough to block the undiffracted light will also block much of the desired object information.

A better approach is to use an off-axis section of a zone plate with a halftone screen plate, the undiffracted light pattern does not overlap the local spot and is therefore not a problem. The halftone screen is necessary because the off-axis zone plate will not properly code low spatial frequencies. The screen serves to spatially heterodyne the object spatial frequency spectrum into the passband of the zone plate. When the zone plate and halftone frequencies are properly matched there is a strong Moire fringe pattern formed on the image plane as shown in Fig. 5. Diffraction from these fringes forms the reconstruction.

The only major drawback to the off-axis zone plate is that its rings are very closely spaced. Therefore, a high-resolution image detector must be used. Alternatively, for a given detector resolution, the resolution of the final image will be much worse with an off-axis plate than an on-axis one. As a useful rule of thumb,[12] the final image resolution with an off-axis zone plate will be about a factor of three worse than the intrinsic detector resolution. Therefore, an Anger camera is not very attractive, and we turned to x-ray film as the detector.

An experimental camera consisting simply of an off-axis zone plate, a halftone screen, and an x-ray film cassette was built several years ago. The zone plate and halftone were prepared either by casting lead onto tinned aluminum plates and machining them into the desired pattern, or by electroforming gold.

The output of the camera is a low-density coded picture on x-ray film, usually 10 x 12 in. This film is placed in a copy camera and copied at reduced scale onto a photographic plate, which is then developed and bleached so that the original density differences are translated into optical phase differences.

The reconstruction or decoding system, shown in Fig. 6, uses a helium-neon laser, a lens-pinhole spatial filter, a collimating lens, and an iris to select the correct diffraction order of the hologram. The reconstructed image first appears at a very small scale and is magnified by a subsidiary lens onto a fine ground glass. The ground glass may be viewed visually, or with a silicon vidicon TV camera.

An important part of the reconstruction system is the iris that separates the correct diffraction order from the undiffracted light and the other orders. The open diameter of the iris determines the bandwidth of the system. Image smoothing is therefore easily accomplished if desired.

The point at which the reconstruction occurs along the axis of the optical system depends on the focal length of the reduced coded image, which

in turn depends on the distance of the object from the zone plate. Thus, the image may be examined plane by plane by moving the magnifying lens in the reconstruction system. All planes of the object are thus contained in a single coded image.

Examples of the clinical images obtained with this system are shown in Figs. 2 and 3.

III. Background Suppression Techniques

The main problem in coded-aperture imaging is that the apertures always have a positive-definite transmission. In zone plate imaging with optical processing this leads to the undiffracted or "dc" light background in the reconstructed image. For point objects, this undiffracted component is relatively unimportant since it is weak compared to the desired diffracted light. However, for large continuous objects it completely obscures the reconstructed image.

Two solutions to this problem have already been mentioned. Some improvement can be obtained by spatial filtering[9] with a dc stop in the Fourier plane, but, in general, high quality imagery cannot be obtained this way. A stop large enough to block all of the dc term will frequently also block most of the signal. Another solution is to use an off-axis section of a zone plate, for which the dc and signal components are spatially separated. Here it is necessary to also use a halftone screen as a spatial carrier. The drawback to this approach is that the off-axis zone plate has very fine rings, placing stringent requirements of the spatial resolution of the image detector.

Still another approach, suggested by Tipton,[30] is to choose the zone plate in such a way that the phase of the light in the reconstructed image is opposite to that of the background. The result if a dark image on a bright field. The drawbacks to this method are that it works only for a

restricted range of object sizes and that the inevitable nonuniformities in the background can be misinterpreted as nonuniformities in the object.

It has long been recognized[18-20] that an effective dc suppression could be obtained if two coded images were formed, one with a positive zone plate and one with its negative, and these coded images were subtracted before reconstruction. Let the transmission of the positive zone plate, treated as sinusoidal, be denoted by

$$g_+(\vec{r}) = \frac{1}{2} + \frac{1}{2}\,\mathrm{sinar}^2, \quad (r \le R)$$

and that of the negative one be

$$g_-(\vec{r}) = \frac{1}{2} - \frac{1}{2}\,\mathrm{sinar}^2, \quad (r \le R)$$

where $\vec{r}$ is a two-dimensional position vector, $r = |\vec{r}|$,

$$\alpha = \pi/r_1^2,$$

and r_1 is the radius of the first zone.

The coded image is basically a convolution[12] of the aperture transmission with the object distribution $f(\vec{r})$. Let the individual coded images, obtained with the positive and negative zone plates, be given by $h_+(\vec{r})$ and $h_-(\vec{r})$, respectively, where

$$h_\pm(\vec{r}) = f(\vec{r}) \; * g_\pm(\vec{r})$$

The asterisk denotes a convolution with suitable scale factors as discussed in Ref. 12. The difference image, $h(\vec{r})$, is

$$h(\vec{r}) \equiv h_+(\vec{r}) - h_-(\vec{r})$$

$$= \frac{1}{2}\, f(\vec{r}) * \mathrm{sinar}^2$$

Thus the net effect is a convolution with a bipolar (positive and negative valued) zone plate, even though negative transmissions have no physical meaning. A bipolar zone plate has no constant or dc term in its transmission and therefore does not give rise to a dc background term in the reconstruction.

This approach has recently been implemented with computer processing by MacDonald et. al.[18] and with optical processing by Stoner, Wilson and Barrett.[21, 22] In the latter case, the subtraction was performed by means of a grid coding technique originally proposed by Pennington et. al.[23]

The basic arrangement for grid-coded subtraction with positive and negative zone plates uses a standard Anger camera without any modification except for a grid (Ronchi ruling) which is placed adjacent to the film in the oscilloscope camera. A coded image is first recorded with a positive zone plate in place. Then the negative zone plate is substituted, the grid is shifted by half its period and a second coded image is recorded. Since the film in the oscilloscope camera is not moved between exposures, the two coded images are interleaved on the film. A reduced-scale copy of this film is inserted into the optical system shown in Fig. 6. When a single diffraction order is selected with the iris, it can easily be shown that the dc components cancel while the signal components add.

The first attempt to experimentally demonstrate this technique with an Anger camera gave very encouraging results. Subsequent experiments, however, soon showed that one problem remained. Although the dc component was effectively cancelled, there was still an out-of-focus twin image term that substantially degraded the image for large objects. The solution to this problem was found in the literature on optical holography. Adapting an idea of Burckhardt and Doherty,[24] we went to a succession of three or four zone plates (e.g., positive and negative sine and cosine plates). Then it could be shown[22] that both dc and twin image terms cancelled and that the result was mathematically equivalent to using an off-axis zone plate and halftone screen. This result was fully verified by optical simulation experiments; Anger camera experiments are in progress.

It rapidly became apparent that the grid-coded subtraction technique opened up a great variety of new possibilities for coded apertures. To date, we have demonstrated, by optical simulation, the feasibility of using an annular aperture, an inverted zone plate, a spiral zone plate, a step-wise spiral zone plate, and the Girard grill.[22]

IV. Quantum Noise in Coded Aperture Systems

Although a coded-aperture can have up to a thousand times the collection efficiency of a pinhole or collimator, it has been recognized from the beginning that this did not imply that dose or exposure time could be reduced by such a factor. The difficulty is that although coded aperture techniques collect more quanta, they also require more quanta to get the same signal-to-noise ratio.

Very detailed analyses of quantum noise have been presented, both for coded aperture imaging per se[12, 23, 25-27] and for the analogous area of multiplex spectroscopy.[28, 29] A full account of the mathematical details is beyond the scope of this review, but the basic results can be stated fairly simply. Consider an assembly of m point sources of equal strength and assume that each point is well resolved from all the others, but that the whole assembly is sufficiently compact[50] that all of the individual zone plate shadows almost completely overlap. Then it is fairly easy to show[12, 13] that the signal-to-noise ratio (SNR) for the quantum-limited zone plate camera is given by

$$(\mathrm{SNR})_{zp} = \frac{\alpha\sqrt{N_t}}{m}$$

where N_t is the total number of detected quanta and α is a factor somewhat less than unity whose precise value depends on the details of the data processing. For comparison, the SNR for an equivalent pinhole is given by

$$(\mathrm{SNR})_{ph} = \sqrt{N_t/m}.$$

Since N_t increases linearly with exposure time T in both cases, it is easy to see that the ratio of exposure times for constant SNR in the two cases is

$$\frac{T_{ph}}{T_{zp}} = \frac{\alpha^2}{m}\,\frac{(N_t)_{zp}}{(N_t)_{ph}} = \frac{\alpha^2}{m}\,\frac{\eta_{zp}}{\eta_{ph}}$$

where η denotes geometric efficiency. This equation shows that for a single point source (m = 1) almost the full efficiency advantage of the zone plate

can be translated into an exposure time or dose advantage. As the object becomes larger and m increases, the advantage progressively decreases. For very large objects, such that the individual shadows no longer completely overlap, Eq. (3) must be modified, but the exact theory[13] still shows that there can be a net disadvantage to the zone plate for large objects. Similarly, the zone plate can be a disadvantage in imaging weak sources adjacent to strong ones. In general terms, the zone plate should have an advantage when imaging areas of the object that are substantially stronger than the average, taken over the field of view of the camera. Thus, thyroid, kidneys, brain, bone, and myocardium should all be "good" objects for zone plate imaging; lungs, liver, and placenta are "bad."

These quantum noise considerations constitute an inherent limitation to coded aperture techniques. If it were the only limitation, coded apertures could still be used to reduce patient dose or exposure time in most nuclear medicine imaging procedures. However, in practice, other factors creep in to reduce the sensitivity drastically, especially if film is used as the detector. These factors include film grain noise, scattered radiation,[16] incomplete absorption of the gamma rays, the absorption of the half-tone screen[25] and inefficient data processing.[13] However by using an Anger camera as the detector, computer processing and any of several apertures that do not require a half-tone screen, it is now possible to obtain the full theoretical advantage of coded apertures.

V. Current Research

Three trends can be discerned in current research in coded-aperture imaging. These are: (1) Use of time-varying apertures; (2) Use of "dilute" apertures with transmission much less than 50%; and (3) Attempts to derive transverse tomographic sections, unblurred by other planes, from coded images. Each of these pursuits has met with some degree of success, as we will now discuss.

We have already seen an example of temporally modulated coded apertures in the multiple zone plate system described in sec. III. In addition, Macovsky[30] has proposed a pinhole array in which each pinhole is opened and closed with a different temporal frequency. Spectral analysis serves to unravel the resulting image.

Workers at the University of Michigan[31] have used time-modulated "stochastic" apertures. Basically this approach employs a one-dimensional code whose cross-correlation with a cyclically repeated replica of itself has a uniform background level. A two-dimensional pinhole array is then temporally modulated by this code, so that each pinhole executes the code with a different phase. Digital decoding is used. The main advantage of this approach seems to be that out-of-focus planes blur smoothly without generating the coherent artifacts that can be troublesome with zone plates.

Two examples of dilute apertures have been discussed in the literature--the annular aperture and the non-redundant[32] pinhole array. The annulus was first proposed by Walton[33] who also suggested a clever video processing scheme. Mathematically, his processing method amounts to correlating the coded image with a very thin annulus of appropriate scale. This works well for point objects but fails for larger objects[34] because the point spread function falls off only as $1/r$, where r is the radial distance from the true location of the point. The reconstructed intensity at any point is therefore dependent on the object intensity at very distant points. Recent work by Simpson et. al.[34] shows that this problem may be avoided by suitable filtering.

The non-redundant pinhole apertures[32] are arrays in which the vector distance between any two pinholes is not repeated. They have superior autocorrelation properties to the completely random pinhole arrays proposed by Dicke.[4] Both digital and optical decoding has been employed.

Dilute apertures, in general, are attractive because they do not impose stringent requirements on the count rate capability, dynamic range or spatial

resolution of the detector. They collect fewer counts than a filled aperture such as a Fresnel zone plate, but also require less for the same signal-to-noise ratio.[34]

Attempts to derive transverse section data from coded images have been inspired by the recent success for the EMI-scanner. Work in this area is underway at the Universities of Michigan and Arizona and the Lawrence Berkeley Laboratory.[35] The latter group in particular, has demonstrated that an image of a single isolated plane can be obtained with a pinhole array looking down on the plane. There is no significant degradation due to other planes.

REFERENCES

1. J. R. Klauder, A. C. Price, S. Darlington, and W. J. Albersheim, Bell System Tech. J. 39, 745 (1960).

2. L. Mertz and N. O. Young in Proc. Internat. Conf. on Optical Instruments, (Chapman and Hall, London, 1961) p. 305.

3. N. O. Young, Sky and Telescope 25, 8 (1963).

4. R. H. Dicke, Astrophys. J. 153, L101 (1968).

5. L. Mertz, Transformations in Optics (Wiley, New York, 1965) p. 88.

6. A. Girard, Appl. Opt. 2, 79 (1963).

7. M. J. E. Golay, J. Opt. Soc. Am. 39, 437 (1949); 41, 468 (1951).

8. M. Harwit, Appl. Opt. 10, 1415 (1971).

9. H. H. Barrett, J. Nucl. Med. 13, 382 (1972).

10. W. L. Rogers, K. S. Han, L. W. Jones, and W. H. Beierwaltes, J. Nucl. Med. 13, 612 (1972).

11. H. H. Barrett, G. D. DeMeester, D. T. Wilson, and M. H. Farmelant in Medical Radioisotope Scintigraphy 1972 (Vienna, IAEA, 1973) Vol. I, pp. 269-284.

12. H. H. Barrett and F. A. Horrigan, Appl. Opt. 12, 2686-2702 (1973).

13. H. H. Barrett and G. D. DeMeester, Appl. Opt. 13, 1100 (1974).

14. H. H. Barrett, D. T. Wilson, G. D. DeMeester, and H. Scharfman, Opt. Eng. 12, 8 (1973).

15. H. H. Barrett, G. D. DeMeester, D. T. Wilson, and M. H. Farmelant in Tomographic Imaging in Nuclear Medicine, G. S. Freedman, Ed. (New York, Soc. Nucl. Med., 1973) p. 120.

16. M. H. Farmelant, G. D. DeMeester, D. T. Wilson, and H. H. Barrett, J. Nucl. Med., to be published.

17. M. Tipton, F. Bonte, and H. J. Caulfield, Opt. Eng. 12, (1973).

18. B. MacDonald, IEEE Nuclear Science Symposium, San Francisco (1974).

19. L. Mertz, Proc. IRIS 5, 157 (1960).

20. L. Mertz, Advertisement, J. Opt. Soc. Am. Feb. 1960.

21. W. W. Stoner, D. T. Wilson, and H. H. Barrett, Opt. Comm., to be published.

22. H. H. Barrett, W. W. Stoner, D. T. Wilson, and G. D. DeMeester, SPIE Annual Meeting, San Diego (1974) and Opt. Eng. 13, 539 (1974).

23. K. S. Pennington et. al, Opt. Comm. 2, 113 (1970).

24. C. B. Burckhardt and E. T. Doherty, Appl. Opt. 7, 1191 (1968).

25. A. Lindgren et. al., International Symposium on Optical Computing (Zurich, 1974).

26. G. Levy, J. Nuc. Med. 15, 214 (1975).

27. H. H. Barrett, J. Nuc. Med. 15, 215 (1974).

28. C. J. Oliver and E. R. Pike, Appl. Opt. 13, 158 (1974).

29. V. I. Tsoi and T. N. Sokolova, Opt. Spec. 36, 240 (1974).

30. A. Macovsky, Phys. Med. Biol., to be published.

31. R. May, et. al., Appl. Opt. 13, 2589 (1974).

32. L. T. Chang et. al., to be published.

33. P. Walton, J. Nucl. Med. 14, 861 (1973).

34. R. G. Simpson, H. H. Barrett and H. D. Fisher, Int. Opt. Computing Conf. (Washington D. C.).

35. B. MacDonald et. al., Int. Opt. Computing Conf. (Washington D. C.), 1975.

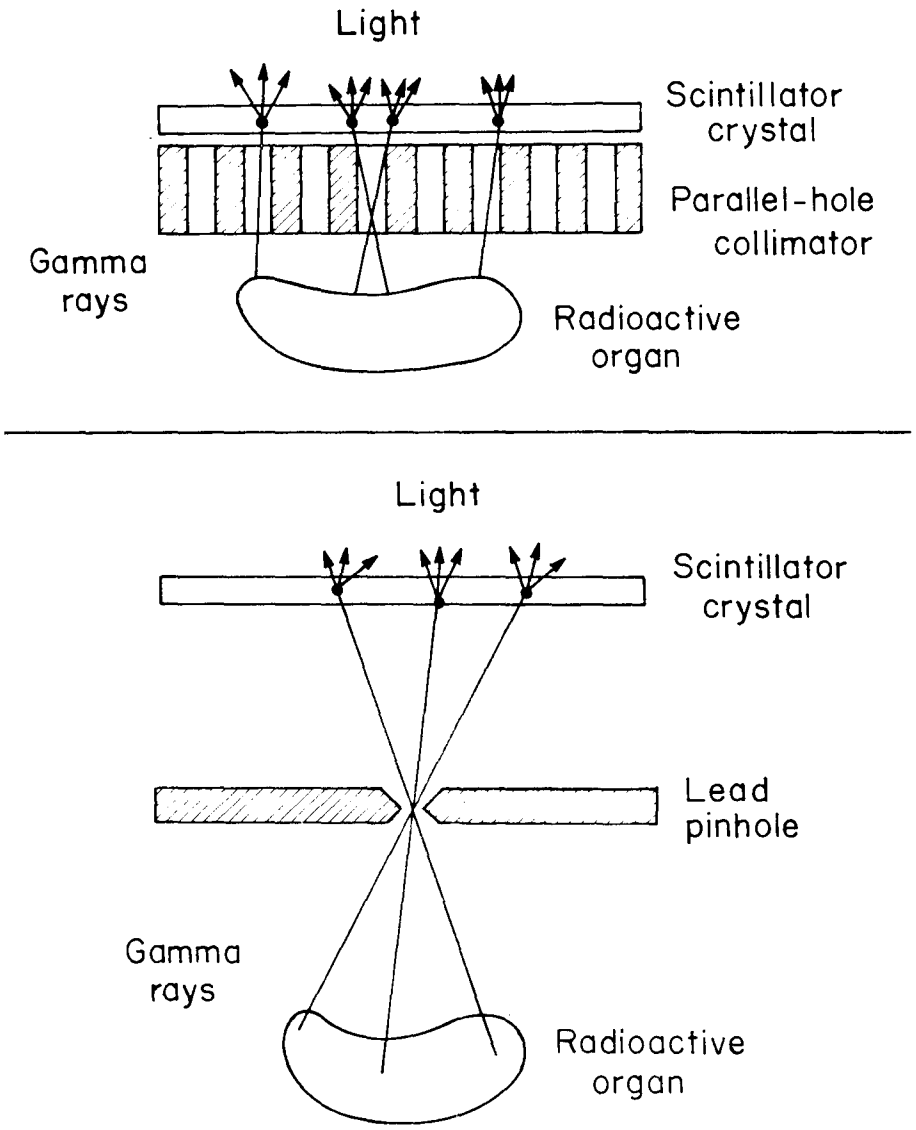

Figure 1. Conventional methods of gamma-ray image formation in Nuclear Medicine.

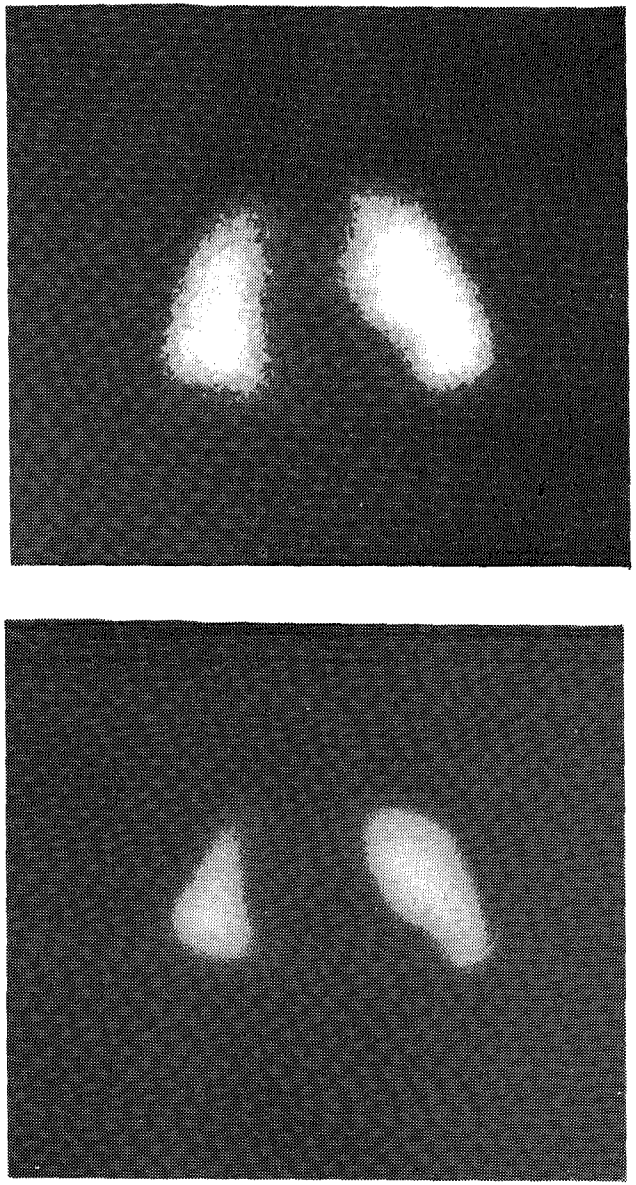

Figure 2. Normal lung perfusion images obtained with a conventional scintillation camera and collimator (left) and with the zone plate/film cassette camera (right).

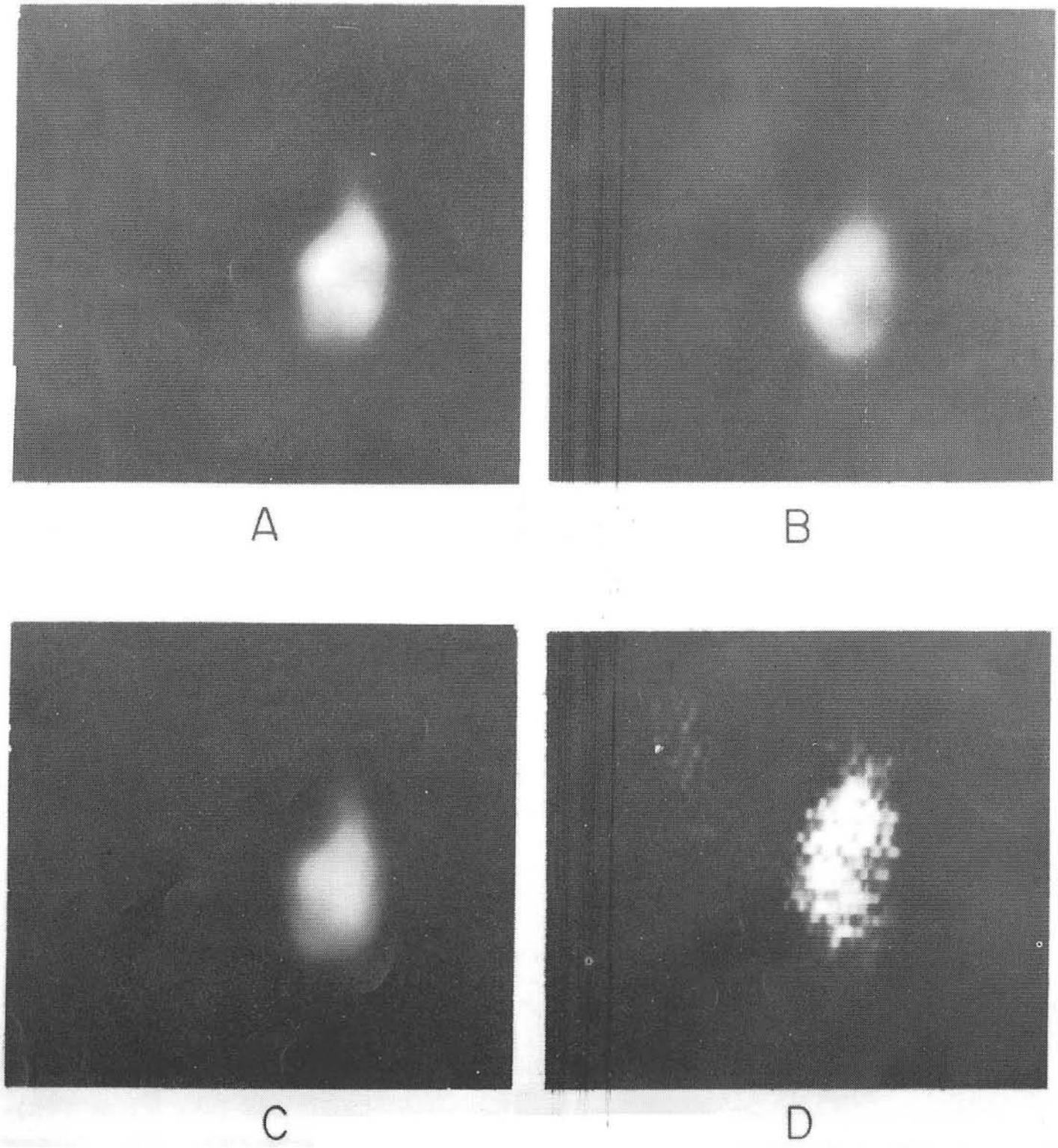

Figure 3. Images of the thyroid gland of a patient who had undergone a partial thyroidectomy. A-C are three different tomographic levels, separated by 6 mm, as imaged with the zone plate camera. D was taken with a rectilinear scanner.

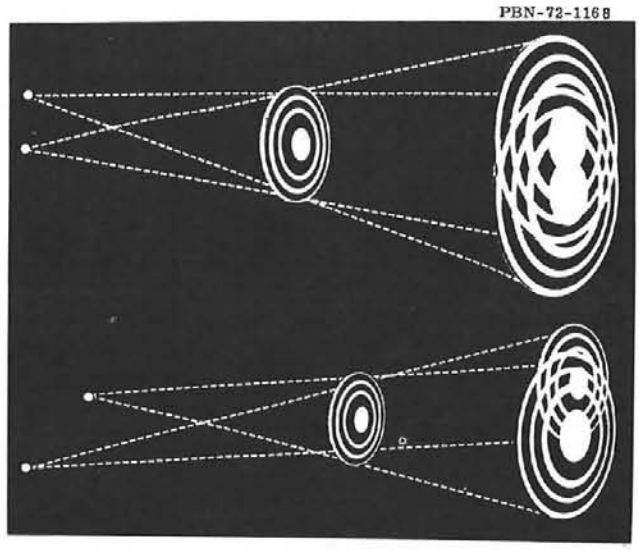

Figure 4. Basic principle of the Mertz and Young reticle camera.

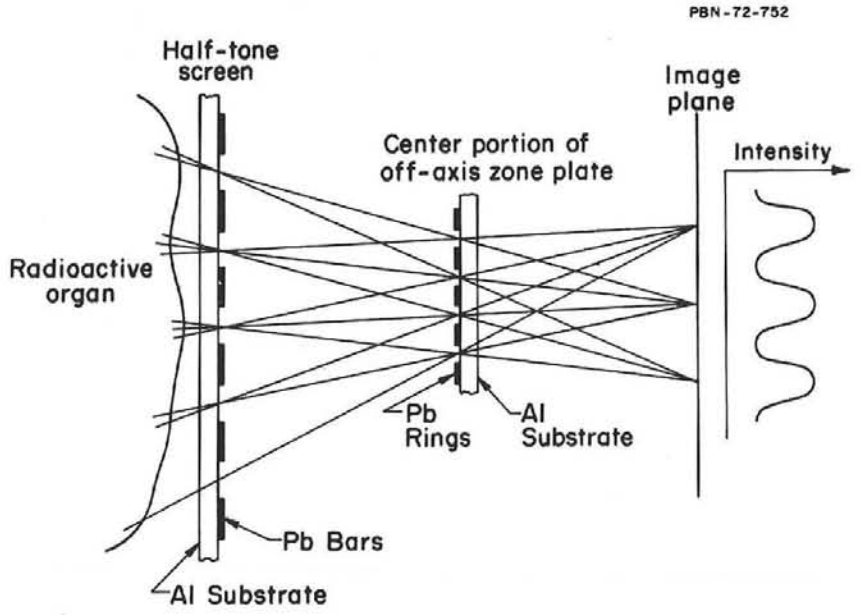

Figure 5. Illustration of the formation of Moire fringes by a zone plate and half-tone screen.

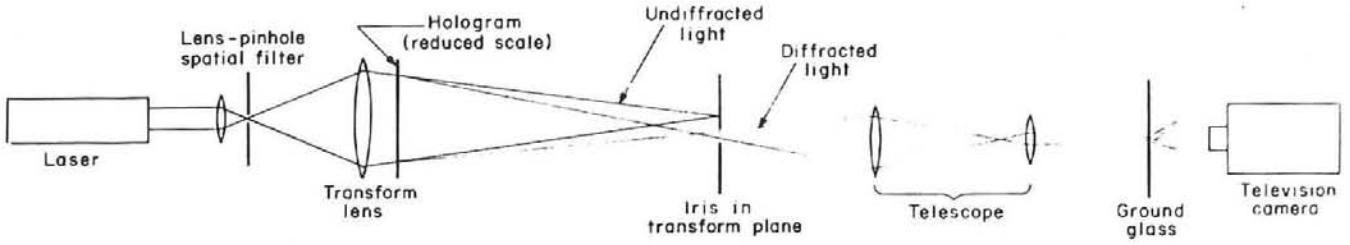

Figure 6. Optical reconstruction system

A Coded Aperture Material Motion Detection System for the ACPR*

by

D. A. McArthur and J. G. Kelly
Radiation Physics Division
Sandia Laboratories
Albuquerque, New Mexico 87115

The Nuclear Regulatory Commission (NRC) is currently funding Sandia Laboratories to irradiate single LMFBR fuel pins in Sandia's Annular Core Pulsed Reactor (ACPR). In these experiments single fuel pins have been driven well into the melt and vaporization regions in transients with pulse widths of about 5 ms. NRC and the Energy Research and Development Administration (ERDA) are also funding Sandia Laboratories to upgrade the ACPR so that it can be used to irradiate bundles of seven LMFBR fuel pins. The coded aperture material motion detection system described here is being developed for this upgraded ACPR, and has for its design goals 1 mm transverse resolution (i.e., in the axial and radial directions), depth resolution of a few cm, and time resolution of 0.1 ms. The target date for development of this system is Fall, 1977.

In this paper we shall briefly review the properties of coded aperture imaging, describe one possible system for the ACPR upgrade, discuss experiments which have been performed to investigate the feasibility of such a system, and finally describe briefly the further work required to develop such a system. The type of coded aperture to be used has not yet been fixed, but a one-dimensional section of a Fresnel zone plate appears at this time to have significant advantages.

*This work was supported by the U.S. Nuclear Regulatory Commission and the U.S. Energy Research and Development Administration

In this paper only Fresnel zone plate coded apertures are discussed because they proved to be well suited to most of the initial experimental work, and the images can be reconstructed with a fairly simple apparatus.

Figure 1 shows the method of obtaining a three-dimensional image of a distributed fission gamma ray source, using the Fresnel zone plate.[1] The zone plate is a plane structure made of alternating concentric rings of a dense gamma ray absorber and a light or thin material which readily transmits gamma rays. The plate is placed between the fission gamma ray source and a plane of gamma ray detector material such as a phosphor or x-ray film (Figure 1a). Each point of the radiation source casts a geometrical shadow of the zone plate onto the detector plane. The center location of the shadow and the geometrical shape of the shadow contain all the information required to reconstruct the location of the radiation source point. The pattern of overlapping shadows in effect forms a "pseudohologram" of the radiation source distribution. To reconstruct the radiation source image, the developed pseudohologram is illuminated with a parallel beam of coherent light, as shown in Figure 1b. Each zone plate shadow diffracts some of the incident light into a point image, the point image position and brightness corresponding to the location, size, and intensity of the original zone plate shadow. The collection of image points thus forms the desired reconstructed image of the radiation source. For a simple Fresnel zone plate, much of the undiffracted laser light also passes through the area of the reconstructed image and forms a troublesome background illumination, which will be referred to later.

Table I summarizes some of the advantages of coded aperture imaging, compared to simple pinhole imaging (Δr_N is the width of the outermost, smallest zone plate ring).

I. The coded aperture provides high transverse spatial resolution combined with high sensitivity, since the sensitivity is determined by the total zone plate area, but the transverse resolution δ is determined by the smallest structure in the zone plate pattern.

TABLE I

Potential Advantages of Coded Apertures
for Fuel Motion Detection

I. Large Aperture with High Spatial Resolution

$$\delta = 1.22\left(\frac{S_1 + S_2}{S_2}\right)\Delta r_N \qquad \text{Fresnel Zone Plate}$$

II. Tomographic

$$\Delta S_1 = \frac{3S_1}{8N}\left(\frac{S_1 + S_2}{S_2}\right) \qquad \text{Fresnel Zone Plate}$$

III. Small Modulation Sufficient for Reconstruction

(a) γ Ray Imaging Through Thick, Dense Materials

(b) Wide Field of View

IV. Analog and Digital Reconstruction

V. Decreased Sensitivity to Quantum Noise and Random Imperfections

II. The technique is tomographic, because in the reconstructed image of a thick radiation source, only one source plane of thickness ΔS_1 is in focus at a time. This allows one to image various planes in a thick source, or alternatively to focus on a thin test region and place the reactor radiation background out of focus to minimize interference with the test region image.

III. Since the image is formed by scattering of coherent light, only a small modulation (typically $\sim$ 10 percent) of the total intensity is required to form an image. This allows one to use relatively thin, high-resolution zone plates to image hard gamma radiations, even if the radiation can only be modulated to a small extent. This is a significant advantage in imaging the harder, image-bearing radiation which penetrates unscattered through thick, dense walls. Such thin zone plates will also have a wider field of view than a pinhole. Finally, the image quality is not greatly impaired by a substantial background exposure, so long as the background does not vary rapidly in space at the detector plane.

IV. The image can either be reconstructed by using a laser (analog reconstruction), or by digitizing the pseudohologram data and using a computer to calculate the reconstructed image to obtain directly a quantitative linear representation of the source distribution.[2]

V. Since the image information for each source point is spread over a large area of the detector plane, the resulting image is less sensitive to quantum noise and random imperfections in the imaging system.

Figure 2 shows a cutaway view of the ACPR at Sandia Laboratories. The reactor core is located at the bottom of a 9-meter-deep tank of water. Experiments are placed in the center of the annular core through a vertical experiment tube. The material motion detection system is to be placed just outside the reactor core, immersed in the shielding water. The system will be serviced and the data retrieved by raising it along guide rails to the top of the shield tank.

Figure 3 shows a schematic drawing of a proposed imaging system. Two rows of fuel elements will be removed from the ACPR core to make a half-slot 7.5 cm wide from the outer edge to the central cavity containing the test fuel pin. The shield water will be excluded from the slot by a thin-walled tank. The system will consist of a shielded enclosure containing a collimator system with coded apertures (two shown), a phosphor detector, a mirror, a lens system, an image intensifier and a fast framing camera. The shield and collimator are designed to attenuate greatly all radiation from the ACPR core except that part of the core immediately behind the test fuel pins. The system field of view is 5 cm wide by 33 cm high at the test fuel pin. The test fuel pin casts shadows onto the phosphor, which converts the image information to light. This light is reflected out of the main radiation path by a mirror system and into a shielded side chamber which contains the image intensifier and camera. Estimates of the fission gamma intensity show that the test fuel pin brightness will be much greater than that of the ACPR reactor fuel elements, and that good framing camera film exposure should be obtainable with commercial image intensifiers for fission rates corresponding to the main pulse of actual ACPR tests.

Feasibility Experiments

The most important initial feasibility question was whether one could image broad, hard fission gamma ray spectra with high spatial resolution using thin zone plates (i.e., ≤ 0.5 mm thick). Most of the earlier medical

imaging using coded apertures had been performed with isotopes which emitted narrow-line gamma ray spectra having peak energies of $\leqslant$ 300 keV.[3] On the other hand, the fission gamma ray spectra of Cf^{252}, Pu^{239} and U^{235} (which are all very similar) are continuous spectra extending up to 8 MeV, with average photon energies of about 1 MeV.[4] Therefore special zone plates about 6 cm in diameter were constructed of dense, high-Z materials such as gold and tantalum. Figure 4 shows a zone plate with 1 mm transverse resolution (at $S_1 = S_2$), made of 0.25 mm thick gold electroplated onto both sides of a 0.05 mm thick fiberglass sheet. This zone plate is shown surrounded by a thin lead shield. Figure 5 shows a zone plate with 2.5 mm transverse resolution (at $S_1 = S_2$), made of tantalum rings varying in thickness from 0.6 cm at the center to 0.3 cm at the outer edge. These rings are cemented onto a phenolic backing plate.

Figure 6 shows a typical experimental arrangement used for imaging of the fission gamma rays from a doubly encapsulated spontaneous fission source of Cf^{252}. The detector used was Kodak AA x-ray film, and the distances S_1 and S_2 ranged from 8 to 100 cm. The Cf^{252} source was either imaged directly through its encapsulation, or through thicknesses of various dense materials such as stainless steel placed either between the source and the zone plate or the zone plate and the film. These intervening materials were chosen to simulate the thicknesses of stainless steel, sodium, and moderator which would be encountered in an actual LMFBR fuel pin test. For $\sim$ 2 mg and 12 mg Cf^{252} sources, exposure times ranged from 5 to 60 minutes, depending on the source size and the amount of intervening material.

It should also be noted from Figure 6 that a significant fraction of the total film exposure comes from scattered Compton electrons and gamma rays which do not contain image information. These scattered backgrounds become more intense when thick slabs of material are placed between the source and the zone plate, and when S_1 and S_2 are small. There are several means which can be used to reduce these backgrounds, but even with

them present, very good images of the Cf^{252} source have been obtained, making use of only ~ 10 percent exposure modulation on the film.

Coupled electron-photon Monte Carlo calculations of the film energy deposition have been performed for the geometries of Figure 6. For imaging of only the encapsulated Cf^{252} source, the calculated and measured film exposure variation of 10% (as mentioned above) agree within experimental uncertainty.[5] The calculation is much more difficult when thick materials are interposed between the source and the zone plate, because many initial photon histories are required to calculate the scattered background contributions accurately. These calculations are continuing at the present time.

Figure 7 shows the reconstructed image of a 12 mg Cf^{252} source which was imaged with ~ 1 mm transverse resolution using the gold zone plate of Figure 4. In the reconstructed image no attempt has been made to reduce the undiffracted laser light (the DC term), which causes an approximately uniform background. The Cf^{252} source is visible as a "bean shaped" bright spot about 1 mm x 3 mm in size, a little above the center of the picture. If the pseudohologram is moved within the reconstruction apparatus, only the bean-shaped spot moves, demonstrating that the background is unrelated to the source image, and that broad, hard fission gamma ray sources can be imaged with high spatial resolution even with zone plates ~ 0.5 mm thick. Experiments were also performed to demonstrate the depth resolution capability of the zone plate, as described in the paper by Hessel and Stalker.[2]

Figure 8 shows the reconstruction of the same Cf^{252} source imaged through 5 cm of stainless steel, using the zone plate of Figure 5. In this case the undiffracted background laser light was greatly reduced by placing a stop in the reconstruction apparatus. A thin sheet of tungsten was also placed directly over the x-ray film, to reduce soft scattered backgrounds and enhance the film exposure by converting some of the fission gamma rays to Compton electrons which then expose the film. The resolution is

limited by the zone plate resolution of about 2.5 mm, but the oblong source size can still be discerned. Thus Figure 8 demonstrates clearly that even the scattering and absorption caused by 5 cm thick stainless steel walls do not seriously degrade the resolution of the reconstructed source image.

The Fresnel zone plate coded aperture is best suited for the imaging of small-area source distributions[6] (i.e., distributions with total areas $\leq 100\ \delta^2$ for typical zone plates discussed here). For large-area disc-shaped distributions the noise begins to increase because zone plate shadows from different parts of the distribution overlap excessively. However, the linear nature of a typical fuel pin means that a Fresnel zone plate should retain a significant signal to noise advantage compared to a pinhole aperture even for very long fuel pins. Calculations indicate that an even more suitable coded aperture for fuel pin imaging could be a one-dimensional section of a Fresnel zone plate.

To investigate experimentally the problems of imaging long fuel-pin-like objects, the following preliminary experiments have been performed. To simulate the broad-area fission-gamma source, the bremsstrahlung radiation from a pulsed electron accelerator (a 2.0 MeV, 5 kA, 30 nsec Febetron 705) was used. Figure 9 shows Fresnel zone plate images of the "bare" x-ray source and the source masked with a 2 mm wide Pb slot collimator. To mock up a fuel pin, multiple exposures were also made, in which the film was moved a small distance between each shot. Figure 10 shows the reconstructed image of a linear source ≈ 2 cm long, which displays good signal-to-noise with an object having an area of $20\ \delta^2$. Further experiments of this type are continuing.

Finally, Figure 11 shows radiation dose measurements which have been made in the water outside the ACPR core, for typical ACPR pulse sizes. These experiments indicate that with only 5 to 13 cm of Pb and about 1 cm of Boral sheet, the background radiation from the ACPR core can be reduced to acceptable levels at the phosphor location. Further

collimator design and experiments will be required to minimize the amount of background radiation which enters the system shielding through the coded aperture collimator. However, preliminary experiments with crude collimator arrangements on the Sandia SPR-II reactor have given encouraging results.

In summary, experiments at Sandia have shown for the first time that coded apertures can be used to image fission gamma sources, even though thick walls, with transverse spatial resolutions ~ 1 mm, and depth resolutions of a few mm. It also appears that radiation noise backgrounds in a practical system can be reduced to acceptable levels, so that it appears feasible to develop a coded-aperture material motion system with high resolution and fast time response for the ACPR reactor.

Much work remains to be done to develop such a system. This includes final choice of the type of coded aperture, development of the collimator and shield box, choice of phosphor and image intensifier, measurement of radiation effects on the image intensifier, development of analog and digital reconstruction methods, and development of a wide dynamic sensitivity range for observation after the peak of the ACPR reactor pulse.

REFERENCES

1. H. H. Barrett and F. A. Horrigan, Appl. Optics 12, 2686 (1973).
2. K. R. Hessel and K. T. Stalker, "Computer Reconstruction of Pseudoholograms Obtained from a Fission Gamma Source," Sandia Laboratories, this conference.
3. H. H. Barrett, J. Nucl. Med., 13, 382 (1972).
4. V. V. Verbinski, H. Weber, and R. E. Sund, Phys. Rev. C, 7, pp 1173-1185 (March 1973).
5. J. A. Halbleib and D. A. McArthur, unpublished calculations with the CYLTRAN code.
6. H. H. Barrett and D. D. DeMeester, Appl. Optics 13, pp 1100-1109 (May 1974).

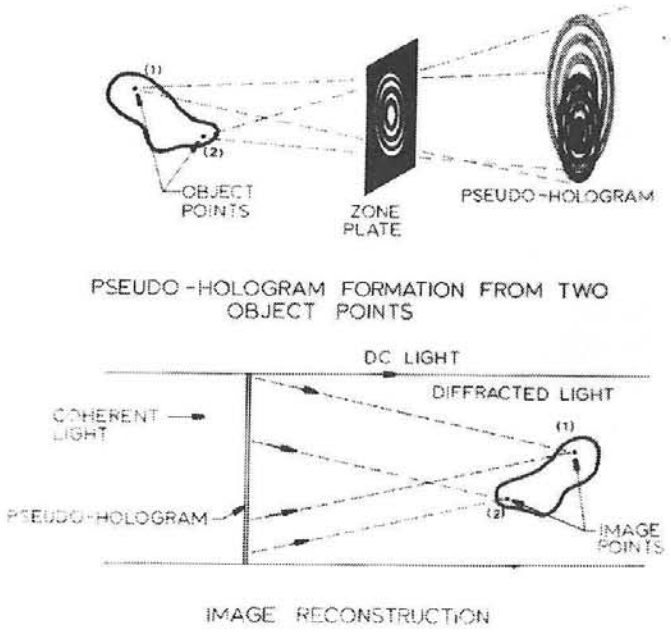

Figure 1. Method of Obtaining Three-Dimensional Image of a Distributed Fission Gamma Ray Source

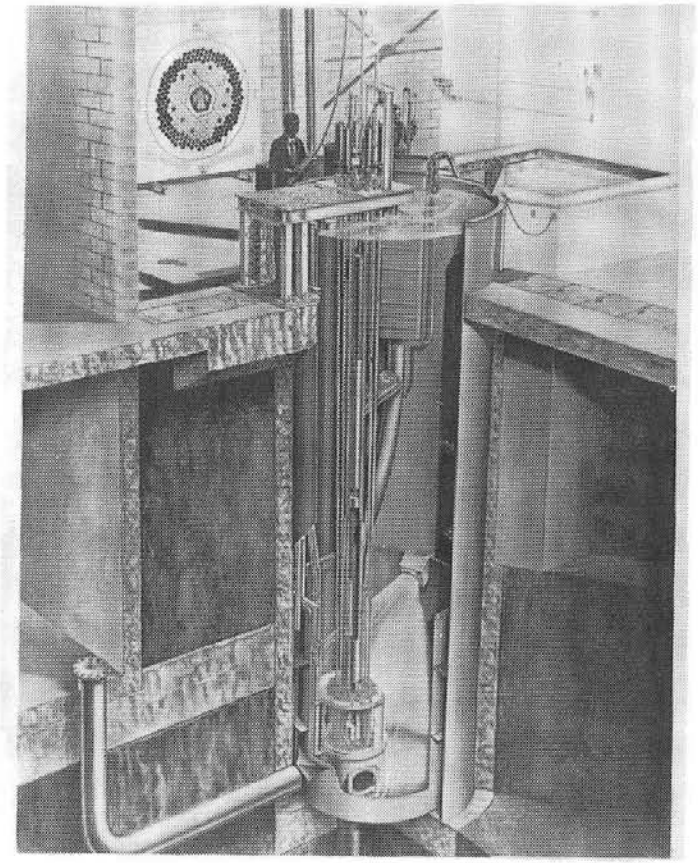

Figure 2. Cutaway View of Sandia Laboratories Annular Core Pulse Reactor

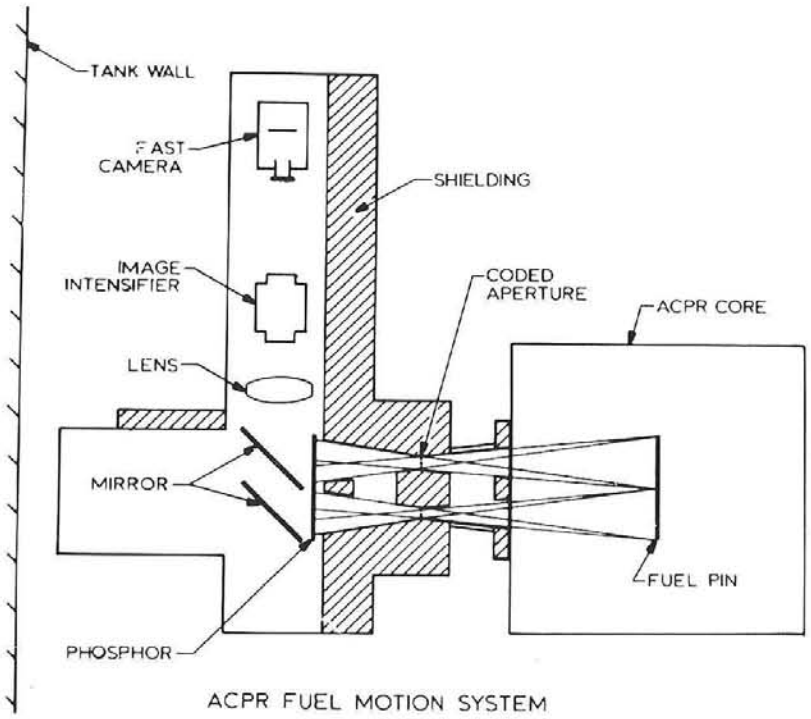

Figure 3. ACPR Fuel Motion System

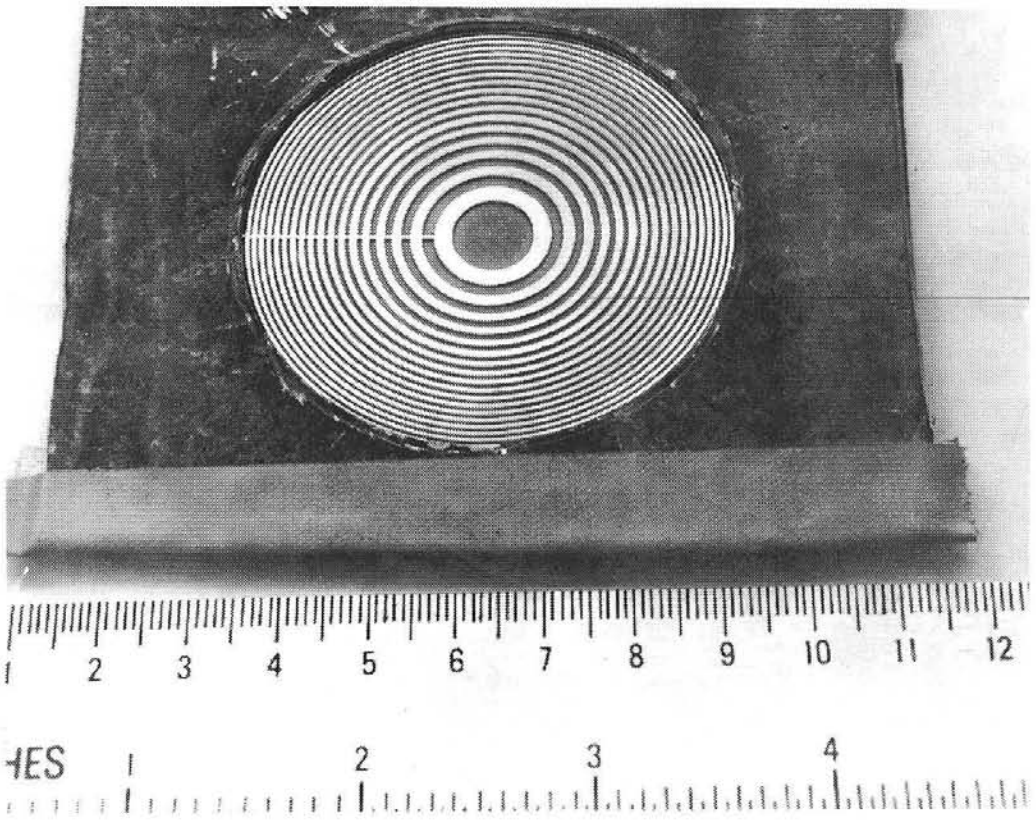

Figure 4. Zone Plate with 1 mm Transverse Resolution

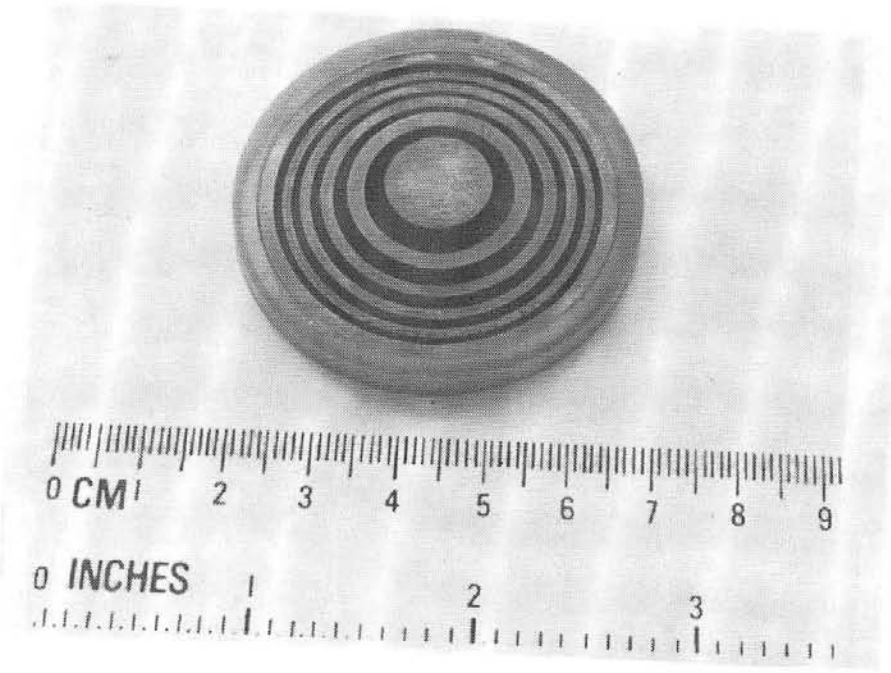

Figure 5. Zone Plate with 2.5 mm Transverse Resolution

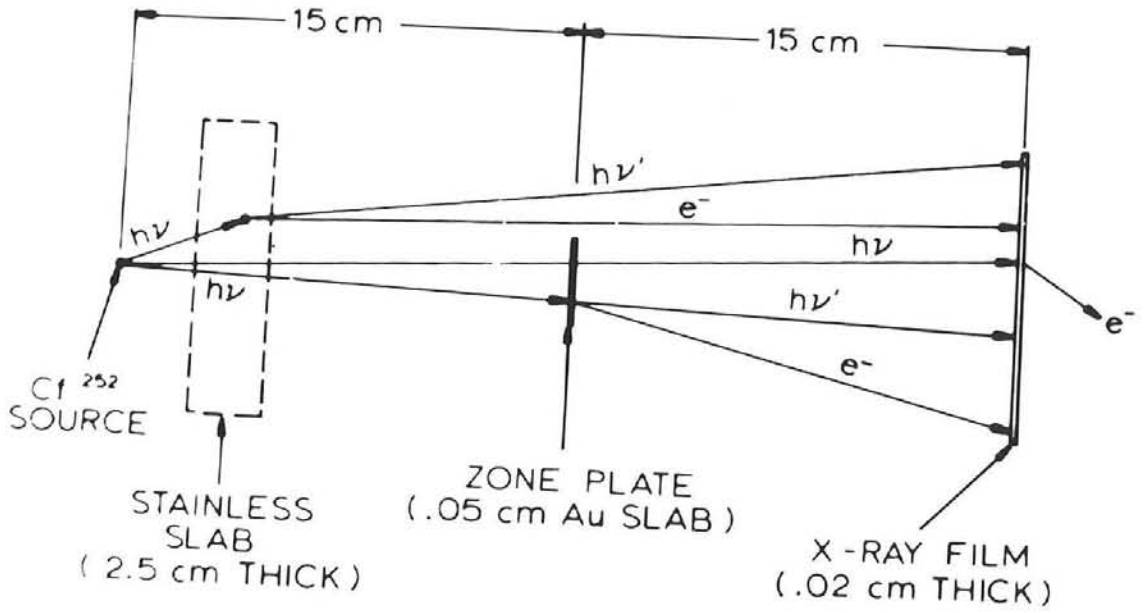

Figure 6. Typical Experimental Arrangement for Imaging of Fission Gamma Rays

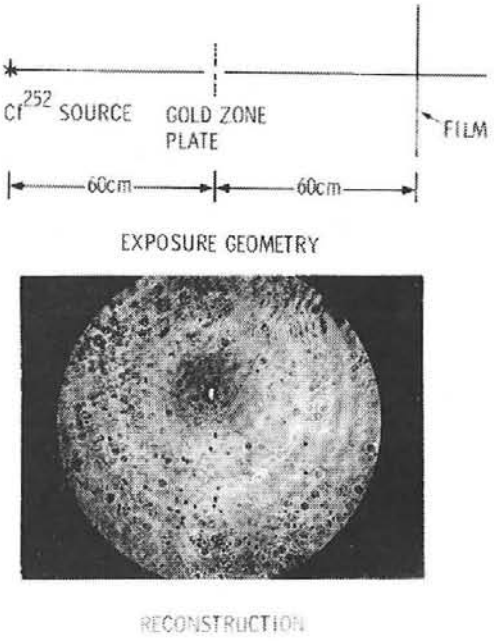

Figure 7. Reconstructed Image of a 12 mg Cf^{252} Source Which Was Imaged with ~ 1 mm Transverse Resolution

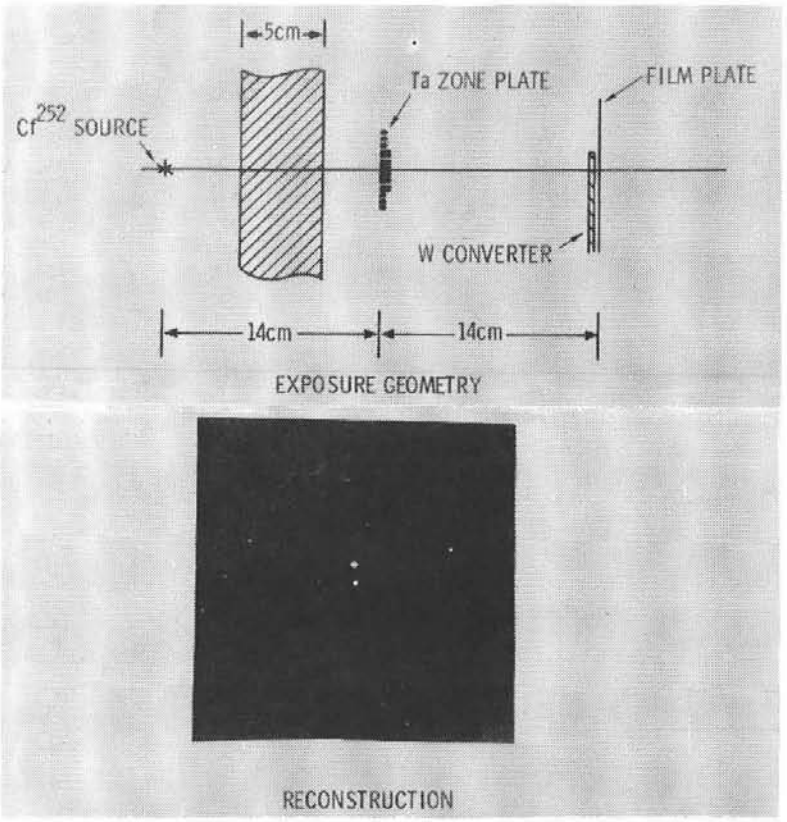

Figure 8. Reconstruction of the 12 mg Cf^{252} Source Shown in Figure 7 Imaged Through 5 cm Stainless Steel

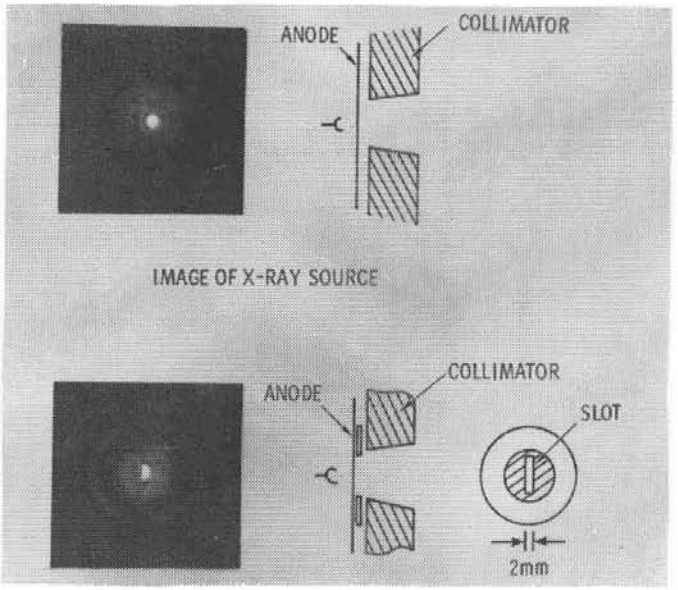

Figure 9. Image of Slot Masked X-ray Source

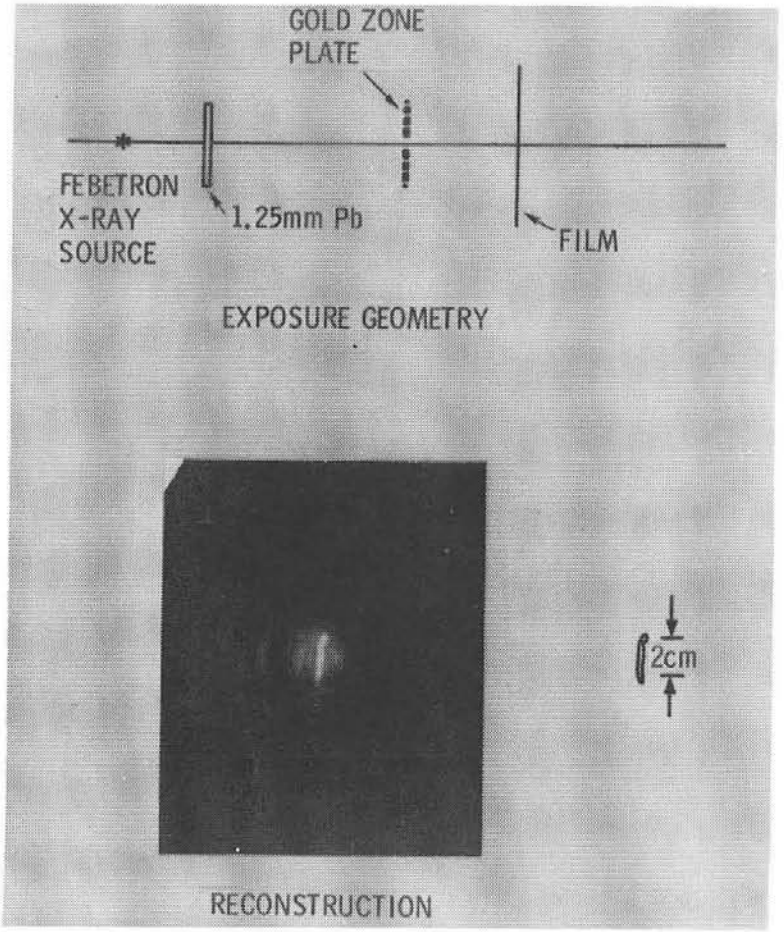

Figure 10. Reconstructed Image of a Linear Source ≈ 2 cm Long

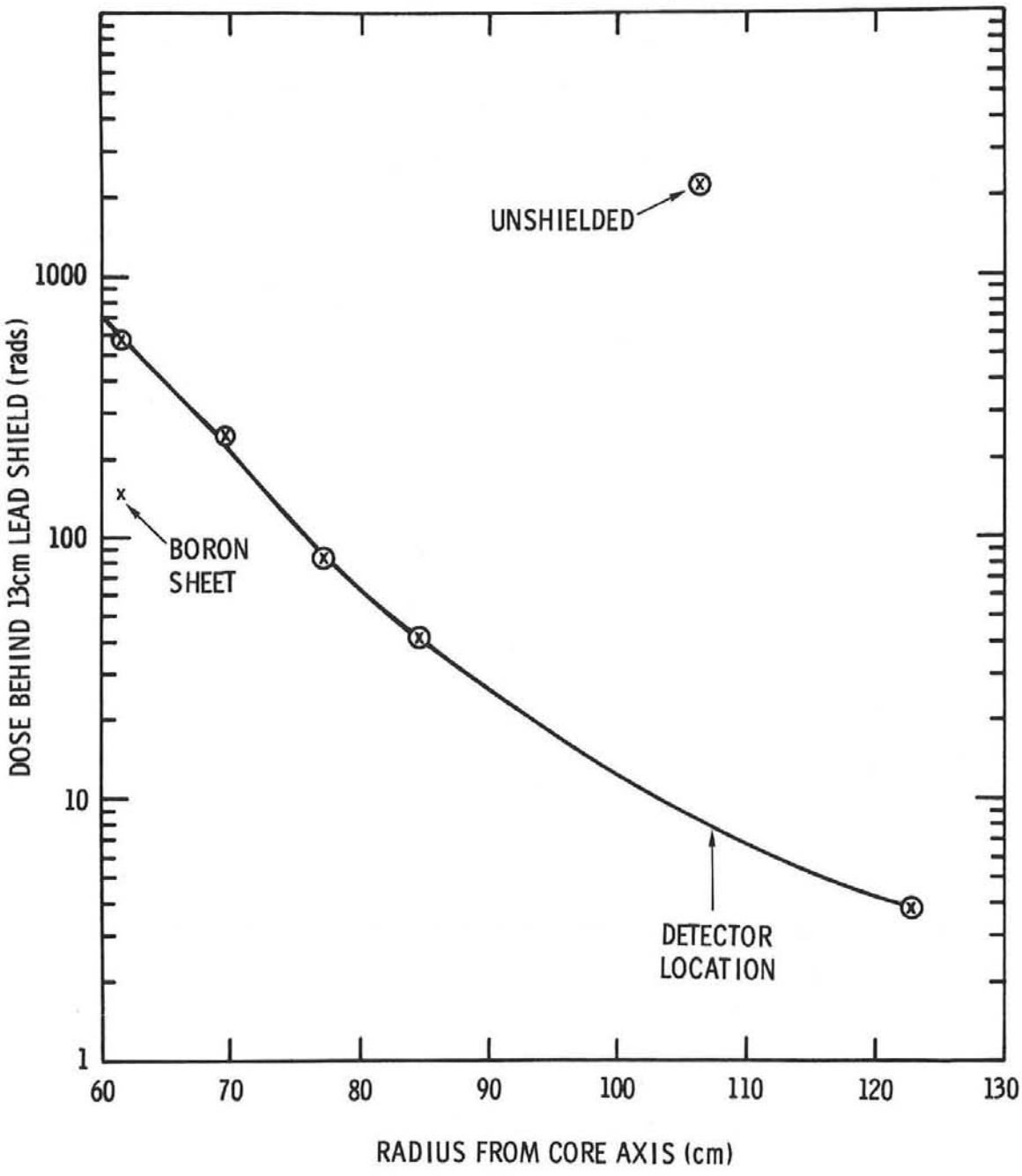

Figure 11. Radiation Dose Measurements Made in Water Outside ACPR Core

Two-Dimensional Nonredundant Arrays* for Coded Aperture Imaging

by

Ki S. Han and George J. Berzins

Los Alamos Scientific Laboratory
Los Alamos, New Mexico 87544

* This work supported by the U. S. Energy Research and Development Administration

I. INTRODUCTION

In recent years coded aperture imaging techniques[1] which are applicable to any radiation sources, have been employed where three-dimensional imaging capabilities are of utmost importance. These techniques increase imaging system efficiency without limiting spatial resolution--clearly an advantage over the classical single pinhole imaging system. The principal apertures used for the techniques have been Feresnel zone plates[2] (FZP) and nonredundant pinhole arrays[3] (NRPA). The techniques require two-step processing, i.e., (1) recording a coded image (pseudo-hologram) and, (2) reconstructing an image (deconvolution) from it.

II. NRPA IMAGING SYSTEMS

A NRPA is a multiple pinhole array in which pinholes are distributed in such a way that the vector distance between any two pinholes occurs only once. The array is characterized by its ideal autocorrelation function having a strong peak at the origin surrounded by uniform background. By definition, a NRPA is not unique for a given number of pinholes, resulting in a deviation of the autocorrelation function from an ideal case. There have been several array search programs written in the past.[4] The 27-pinhole array we used was developed by Klemperer.[5] The pinhole diameter used in our experiment was 0.3 mm.

Using a NRPA with an object that has n resolution elements in the longitudinal direction, a coded image i_{co} can be regarded

as the sum of convolution integrals (*),

$$i_{co} = \sum_{i,k=1}^{n} O_k * P_i \tag{1}$$

where O_k and P_i represent an object and a point response function of the aperture corresponding to the k^{th} plane.

The construction and reconstruction processes are schemetically represented in Figs. 1a and 1b, respectively. The image reconstruction process, an incoherent method, is exactly the reverse operation of taking a coded image. Thus the reconstructed image i_{re_j} corresponding to j^{th} plane is a convolution of i_{co} with the same array,

$$\begin{aligned} i_{re_j} &= i_{co} * P_j \\ &= O_j * P_j * P_j + \sum_{\substack{i,j,k=1 \\ i\neq j \\ k\neq j}}^{n} O_i * P_k * P_j \end{aligned} \tag{2}$$

But by definition of a NRPA

$$\begin{aligned} P_j * P_j &= \delta(x,y) \\ P_i * P_j &\neq \delta(x,y) \end{aligned} \tag{3}$$

Thus ideally the reconstructed image becomes

$$i_{re_j} = O_j(x,y,z=z_j) + \sum_{\substack{i,j,k=1 \\ j\neq i \\ j\neq k}}^{n} O_i * P_k * P_j \tag{4}$$

The second term in (4) corresponds to the collection of longitudinally defocused images appearing in the reconstructed image. By observing a basic theorem that a convolution integral in the spatial domain can be converted into a product in the frequency domain,[6] the Fourier transform of (1) can be written as

$$\mathcal{G}_{co} = \sum_{k,\ell=1}^{n} \mathcal{O}_k \mathcal{P}_\ell$$

$$\mathcal{G}_{co_j} = \mathcal{O}_j \mathcal{P}_j + \sum_{\substack{k,\ell=1 \\ k\neq j \\ \ell\neq j}}^{n} \mathcal{O}_k \mathcal{P}_\ell \tag{5}$$

or

$$\mathcal{O}_j = \frac{\mathcal{G}_{co_j}}{\mathcal{P}_j} - \left(\sum_{\substack{k,\ell=1 \\ k\neq j \\ \ell\neq j}}^{n} \mathcal{O}_k \mathcal{P}_\ell \right) \Big/ \mathcal{P}_j \tag{6}$$

Thus by transforming $\mathcal{O}_j$ back into the spatial domain one obtains the reconstructed image O_j. The coherent image reconstruction method described above can be achieved either digitally or optically. The optical Fourier transform system shown in Fig. 2 will give a reconstructed image with longitudinally defocused image if a spatial filter corresponding to $\mathcal{P}_j$ is used.

In Fig. 3, a block diagram of pseudo-real time imaging system using a NRPA is shown. Presently our work is in progress

to simulate a coded image of a well-defined object digitally with a NRPA. We are planning to develop deconvolution schemes in both spatial and frequency domains, which can be adapted later to STF experiments.

III. EXPERIMENTAL RESULTS AND DISCUSSIONS

We used back lighted letters S and L as objects, separated by 2 cm in the longitudinal direction. The coded image obtained with the 27 NRPA is shown in Fig. 4a. Employing the image reconstruction scheme shown in Fig. 1b, we reconstructed the objects S and L separately as shown in Figs. 4b and c, respectively. Note the defocused image L in b when S is in focus and similarly the defocused image S in c. As mentioned earlier for the coded aperture imaging techniques, it is crucial to remove or filter out longitudinally defocused images. For this end, we applied a subtraction method[7] in conjunction with a coherent optical processing system. We made a spatial filter using a defocused image L to be used when S is reconstructed. In Fig. 5a S is in focus and the defocused L is filtered out. We still observe background noise due to imperfect adjustments. Hopefully the results may be improved by applying digital processing methods or combined digital and optical ones.

We are grateful to R. Granfield for technical assistance.

REFERENCES

1. W. L. Rogers, K. S. Han, L. W. Jones, and W. H. Beierwaltes, "Application of Fresnel Zone Plates to Gamma-Ray Imaging," J. of Nucl. Med. 13, 612, (1972).

2. H. H. Barrett, "Fresnel Zone Plate Imaging in Nuclear Medicine," J. Nucl. Med. 13, 382 (1972).

3. Lee-Tzuu Chang, S. N. Kaplan, B. Macdonald, V. Perez-Mendez, and L. Shiraishi, "A Method of Tomographic Imaging Using a Multiple Pinhole-Coded Aperture," J. Nucl. Med. 15, 1063 (1974).

4. M. J. E. Golay, "Point Arrays Having Compact, Nonredundant Autocorrelations," J. Opt. Soc. Am. 61, 272 (1971).

5. W. K. Klemperer, "Non-Redundant Phased-Array Radar,", RADAR, Present and Future, London (1973).

6. G. Groh, G. S. Hayat, and G. W. Stroke, "X-Ray and γ-Ray Imaging with Multiple-Pinhole Cameras Using a Posteriori Image Synthesis," Appl. Optics 11, 931 (1972).

7. K. S. Han and G. J. Berzins, "Optical Data Processing of a Hologram Obtained with Coded Aperture Imaging," Los Alamos Scientific Laboratory Report LA-UR-74 1110 (1974).

Non-Redundant Pinhole Camera

(a) Recording

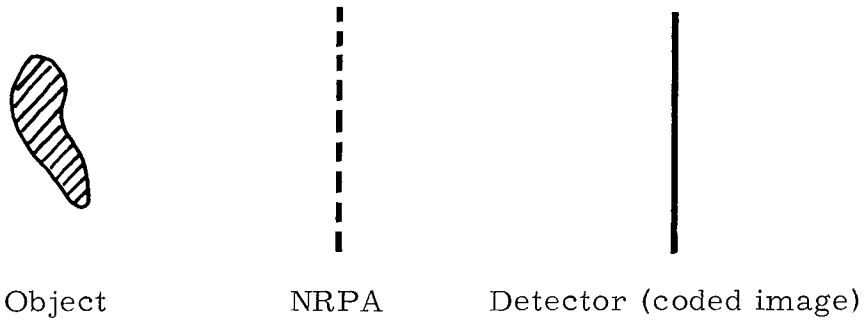

(b) Reconstruction

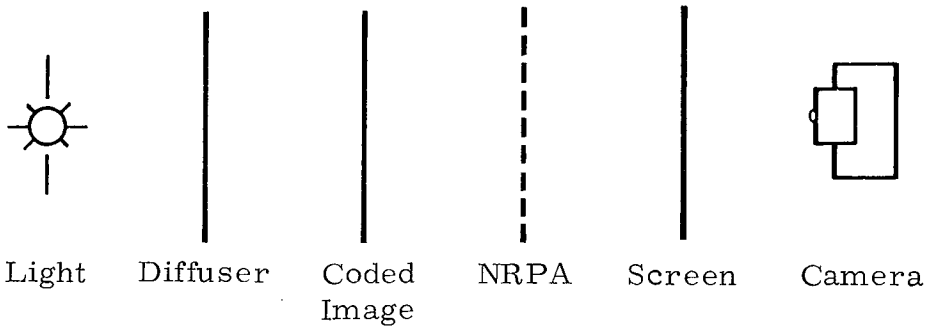

Figure 1. Schematic representation of the construction (a) and reconstruction (b) processes with a NRPA.

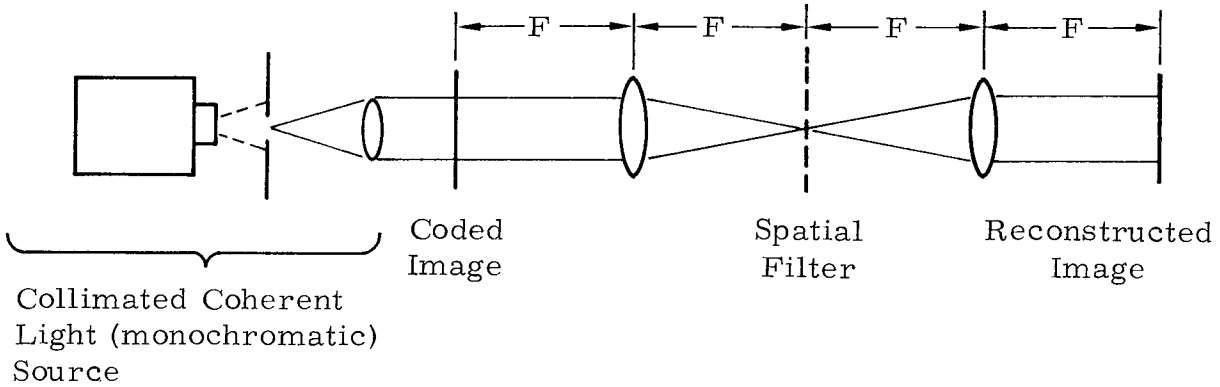

Figure 2. Coherent reconstruction scheme for a NRPA coded image.

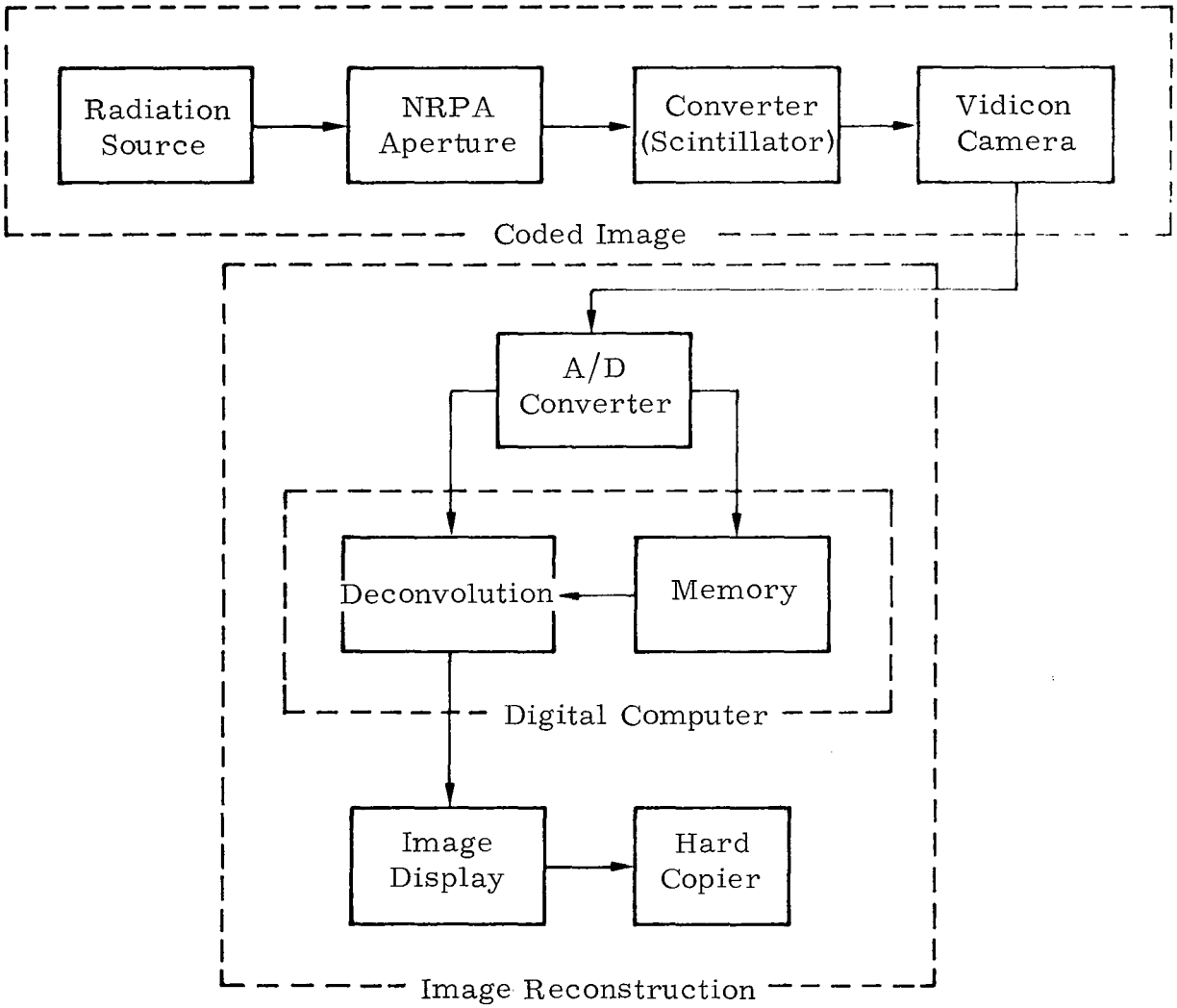

Figure 3. Diagram of our proposed on-line reconstruction and processing system.

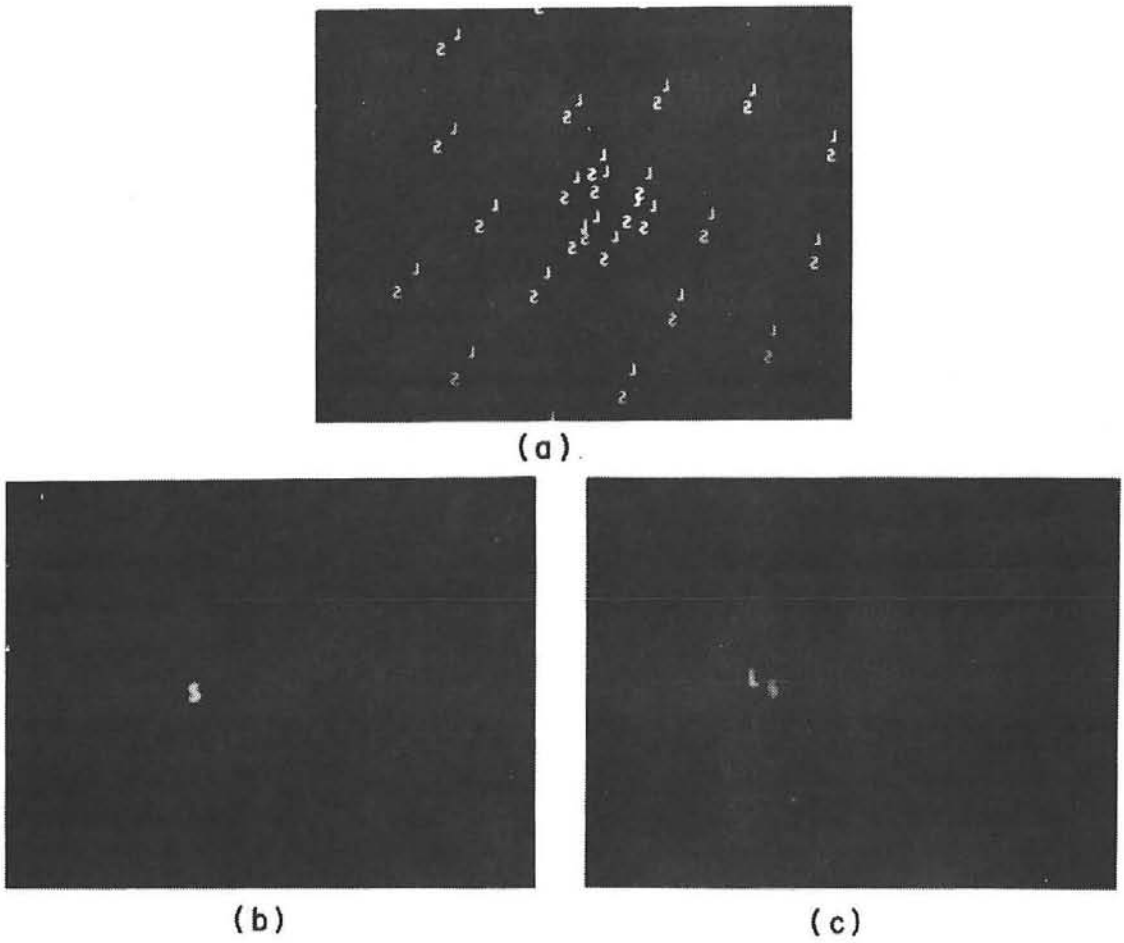

Figure 4. Coded image (a) and reconstructions (b and c) of longitudinally displaced sources L and S using a 27-hole NRPA.

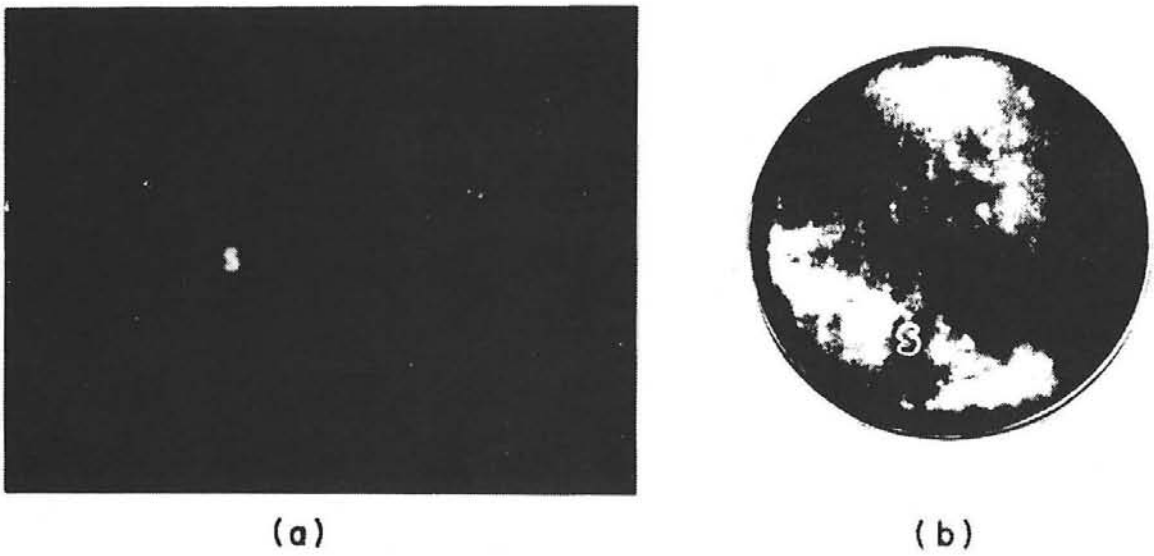

Figure 5. (a) Incoherent reconstruction of image of S with defocused L in background

(b) Coherent processing of (a) with defocused L removed. The background arises from imperfect optical adjustments in the coherent optical system.

Possible Application of Nonredundant* Pinhole Arrays to Fuel Pin Imaging

by

George J. Berzins and Ki S. Han

Los Alamos Scientific Laboratory
Los Alamos, New Mexico 87544

I. INTRODUCTION

Potential STF imaging experiments,[1] whether pinhole, hodoscope, Fresnel zone plate, or other coded aperture, rely on emission of radiation by the fuel pins. As such they appear to strongly complement radiographic techniques in that they are most employable during peak excursion--a time of least favorable radiographic signal-to-noise ratio. Radiography, on the other hand, can provide information long before or after the excursion--times of below threshold signal for direct imaging techniques.

An underlying premise of any imaging experiment is that, in addition to sufficient brightness, sufficient contrast exists in the scene. A further restriction is imposed by intervening materials, such as the wall of a containment vessel, that not only absorb but also scatter the radiation.

We are approaching these questions by examining the properties of potential recording instrumentation, of pinhole apertures, and of the necessary radiation sources.

II. EXPERIMENTAL OBJECTIVES

We wish to examine the applicability of the nonredundant pinhole array (NRPA) techniques to reactor imaging with a scaled "miniexperiment" in the laboratory. In this manner we hope to identify unforeseen problems

* This work supported by the U.S. Energy Research and Development Administration

as well as characterize the data quality in terms of the imaging system parameters.

Our specific objectives include:

(1) Determination of the absolute sensitivity of the recording system,

(2) Determination of the experimental resolution as a function of various parameters,

(3) Demonstration of a three-dimensional capability,

(4) Examination of gray scale discernability,

(5) Examination of the effects of intervening materials between the source and the detector.

III. EXPERIMENTAL CONFIGURATION

The experiment, schematically shown in Figure 1, consists of a gamma-ray emitting source, an imaging aperture, and a detection system that includes a scintillator and a camera.

A. Gamma-Ray Sources

For preliminary work we are using a pulsed 600 keV electron beam to generate a bremsstrahlung spectrum plus characteristic x-rays from a tantalum target. A photograph of the experimental arrangement is shown in Figure 2. The target generally consists of 0.075-mm to 0.25-mm-thick by 1-mm to 6-mm-wide metal strips. This source has been useful for several preliminary experiments, but is limited by size and the intensity of the electron beam.

In a more flexible experiment we plan to neutron activate strips of palladium metal of comparable dimensions to the above. Several hours after activation[2] the dominant gamma ray in natural palladium is the 88-keV isomeric transition in ^{109}Ag, following 99.9+% of the decays of ^{109}Pd. The 88-keV gamma-ray energy is ideal for our scaled geometry. Other characteristics[3] (isotopic abundance 27% half life 13 h, cross-section 12 b) in addition to the favorable branching ratio and energy make ^{109}Pd one of the best suited beta-decaying isotopes for our experiment.

B. Imaging Apertures

In the early experiments we have used a single pinhole to determine system performance parameters such as sensitivity, resolution, and field of view. Furthermore, data from single pinhole experiments provide a convenient reference for evaluating NRPAs.

Of the two most favorable, known NRPA configurations[4] (15 hole and 27 hole) we have chosen the former because of a slightly better autocorrelation function and because of machining considerations. The 27-hole array would have, of course, somewhat better efficiency.

A photograph of our 15-hole NRPA is shown in Figure 3.

C. Scintillator

Currently we are using plastic scintillators (NE-102, 5- to 20-mm thick) to convert the x-ray image to an optical signal. We anticipate delivery of a 15-cm-diam x 3-mm-thick NaI (Tℓ) crystal shortly. The latter will provide more sensitivity, and will enable us to use single pulse counting techniques. The longer decay time of NaI (0.25 μs vs 2.5 ns for the plastic) will permit us to gate the camera "on" (see next section) to accept most of the light from the crystal. A similar experiment is described in Reference 5. In this way we can accumulate a sufficient number of events to produce a useful image without adverse dark current effects.

D. Recording Instrumentation

Pinhole imaging of 88-keV gamma rays or bremsstrahlung x-rays directly into film requires uncomfortably intense sources. To reduce this dose to more tolerable levels we are utilizing a channel plate image intensifier with a gain of 10^4 to increase system sensitivity.[6] The intensifier views the pinhole image on the scintillator and fiber-optically transmits the amplifier light signal to film. A photograph of the camera is shown in Figure 4.

In the flash x-ray experiments the camera is gated "on" for 2 μs, beginning $\sim$0.5 μs prior to the 3-ns x-ray flash. In the palladium strip

experiment we plan to gate the camers "on" for ~0.5 μs following detection of a gamma-ray event in the NaI crystal. The electronic transit time (photomultiplier, logic, and gate pulse generator) is ~ 50 ns. In this manner we anticipate accumulation of events for hours without adverse effects from dark current. Typically, integration of dark current on film limits dc operation to seconds, or a few minutes at best.

IV. PRELIMINARY RESULTS

We have found the sensitivity of our intensified camera system to be considerably greater than for our intensified TV systems.[6] We can image 300-rad (contact) sources with a 1-mm pinhole at 1 m. A typical result is shown in Figure 5. The immediate implication for reactor diagnostics is that pinhole (single or NRPA) imaging of a core region is feasible if the scene emits more than 10^{12} γ MeV/cm^2 into 4π. For a single pin this is equivalent[1] to only a few joules/g-frame.

The system resolution is limited by the pinhole--a fact we anticipated. The resolutions of the intensifier, the optics, and the converter, are several times superior. The resolution in the data of Figure 5 is affected by statistical limitations. We estimate ~200 gamma-ray interactions per pinhole resolution element on the scintillator. Translation of the image onto the camera results in fewer than 100 photoelectrons per pinhole resolution element at the intensifier photocathode. For increased source strengths (i.e., ~10-100 joules/g-pin) the resolution will improve accordingly from that in Figure 5.

Pinhole thickness and the associated field-of-view limitations are as bad as we had expected. The problems are surmountable for our scaled miniexperiment, but are more serious when we contemplate reactor experiments.

Because of high sensitivity, scattered radiation poses a real threat to our camera. The background speckle, visible in the data in Figure 5, arises from a dose less than 10^{-5} rads on the camera. Again, increasing

the source strength will permit reduction of camera gain, lessening the relative intensity of the background speckle.

The initial attempts at NRPA imaging with the flash x-ray source were only partially successful due to too much high-energy component in the spectrum. We are increasing the thickness of our NRPA mask to remedy this problem.

We are encouraged by the preliminary results from the flash x-ray work and look forward to experiments with the palladium sources.

We are grateful to C. Pickett and A. Widman for technical assistance, to G. Barber and H. Naveaux for machining, and to W. Roach, H. Helmick, and J. Orndoff for overall support.

REFERENCES

1. G. I. Bell, et al, "Study of Fast Reactor Safety Test Facilities," Los Alamos Scientific Laboratory (preliminary) Report LA-5978-MS (1975).

2. J. P. Balagna and S. B. Helmick, "An Atlas of Gamma-Ray Spectra," Los Alamos Scientific Laboratory Report LA-4312 (1970).

3. C. M. Lederer, J. M. Hollander, and I. Perlman, Table of Isotopes, Sixth Edition, John Wiley and Sons, New York (1968); C. A. Rohrmann, "Chart of the Nuclides," Batelle-Northwest, Richland, Washington (1969).

4. W. K. Klemperer, "Aberration Compensation with Two-Dimensional Nonredundant Arrays," Conference on Optical Information Processing, Sydney, Australia (1974).

5. W. L. Rogers, K. S. Han, L. W. Jones, and W. H. Beierwaltes, "Application of Fresnel Zone Plates to Gamma-Ray Imaging," J. of Nucl. Med. 13, 612, (1972).

6. A. J. Lieber, "Nanosecond Gating of Proximity Focused Channel Plate Intensifiers," Rev. Sci. Inst. 43, 104 (1972); G. J. Berzins, K. S. Han, A. J. Lieber, and J. S. McGurn, "Nanosecond Photography of Radiochromic Processes," Proc. Electrooptical System Design Conference, p. 167 (1973).

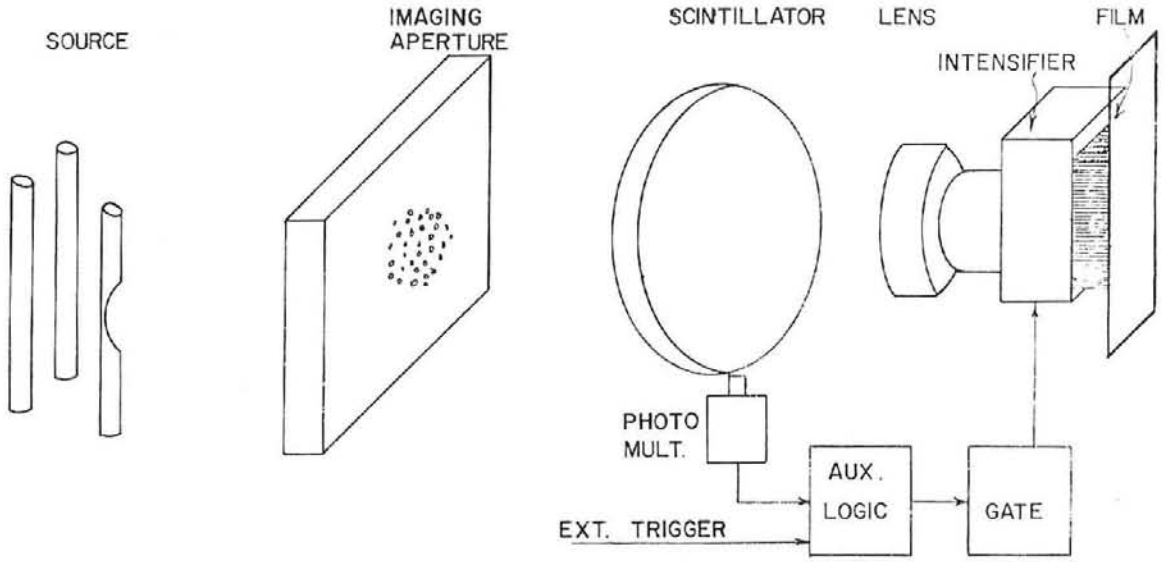

Figure 1. Schematic illustration of an NRPA imaging experiment with ionizing radiation. The photomultiplier identifies events from a continuously emitting source. In the bremsstrahlung flash experiment the gate is triggered from the electron accelerator.

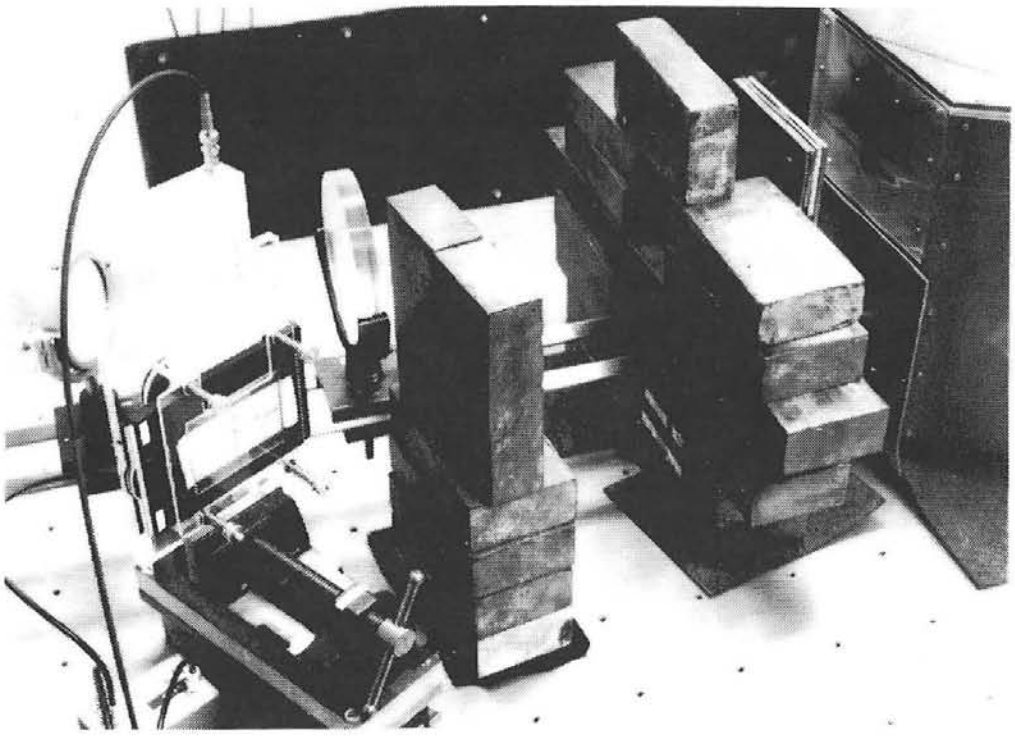

Figure 2a. Overall view of flash x-ray experiment. Components visible from the left include mirror, image intensifier camera, scintillator, lead shielding, pinhole packet, and canister in which bremsstrahlung is generated.

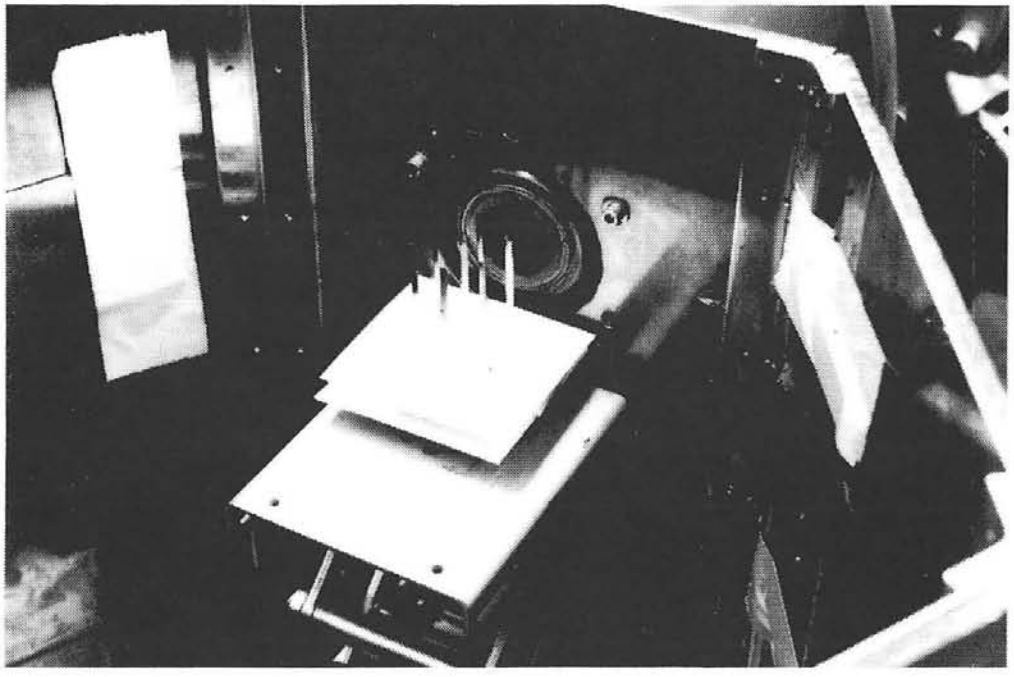

Figure 2b. Typical target of tantalum strips.

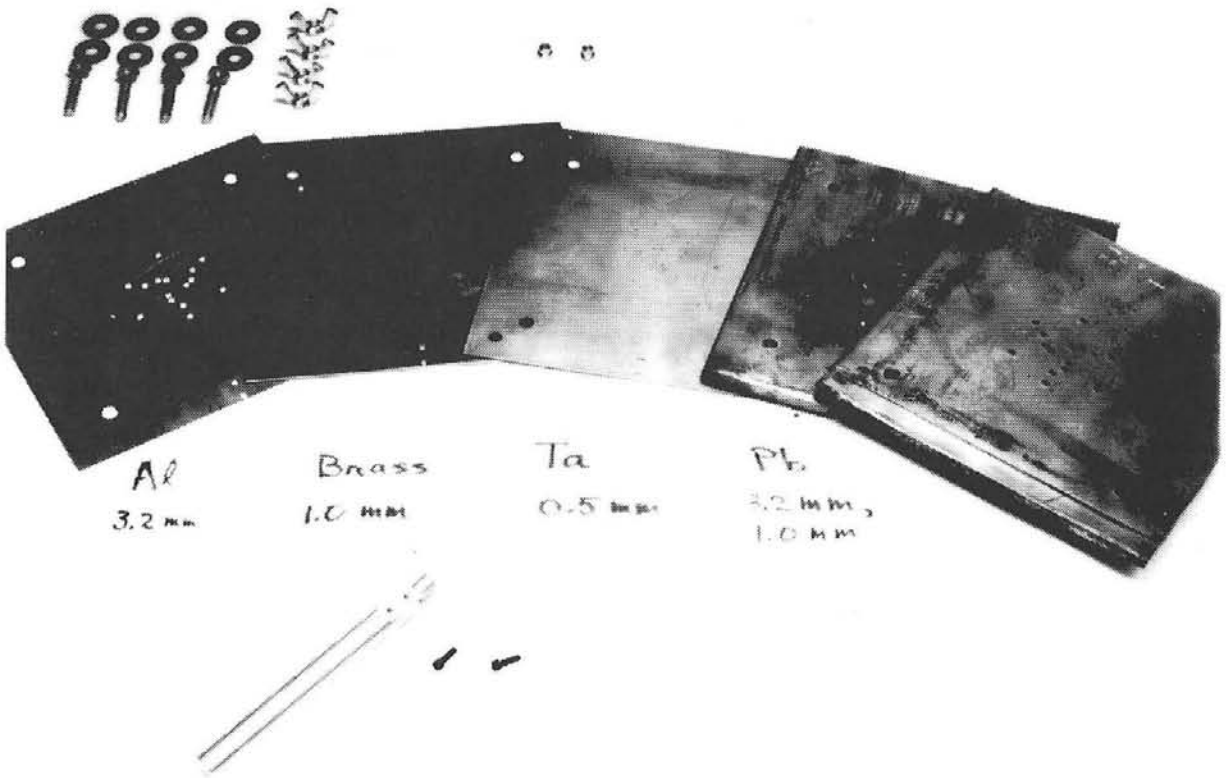

Figure 3. A 15-hole, graded-Z NRPA for use in the palladium strip experiment. Numbers below materials refer to pinhole diameters. The aluminum, brass, and tantalum sheets are each 1-mm thick; each of the lead sheets is 6-mm thick. This packet is too thin for 600-keV bremsstrahlung, producing poor, though identifiable coded images.

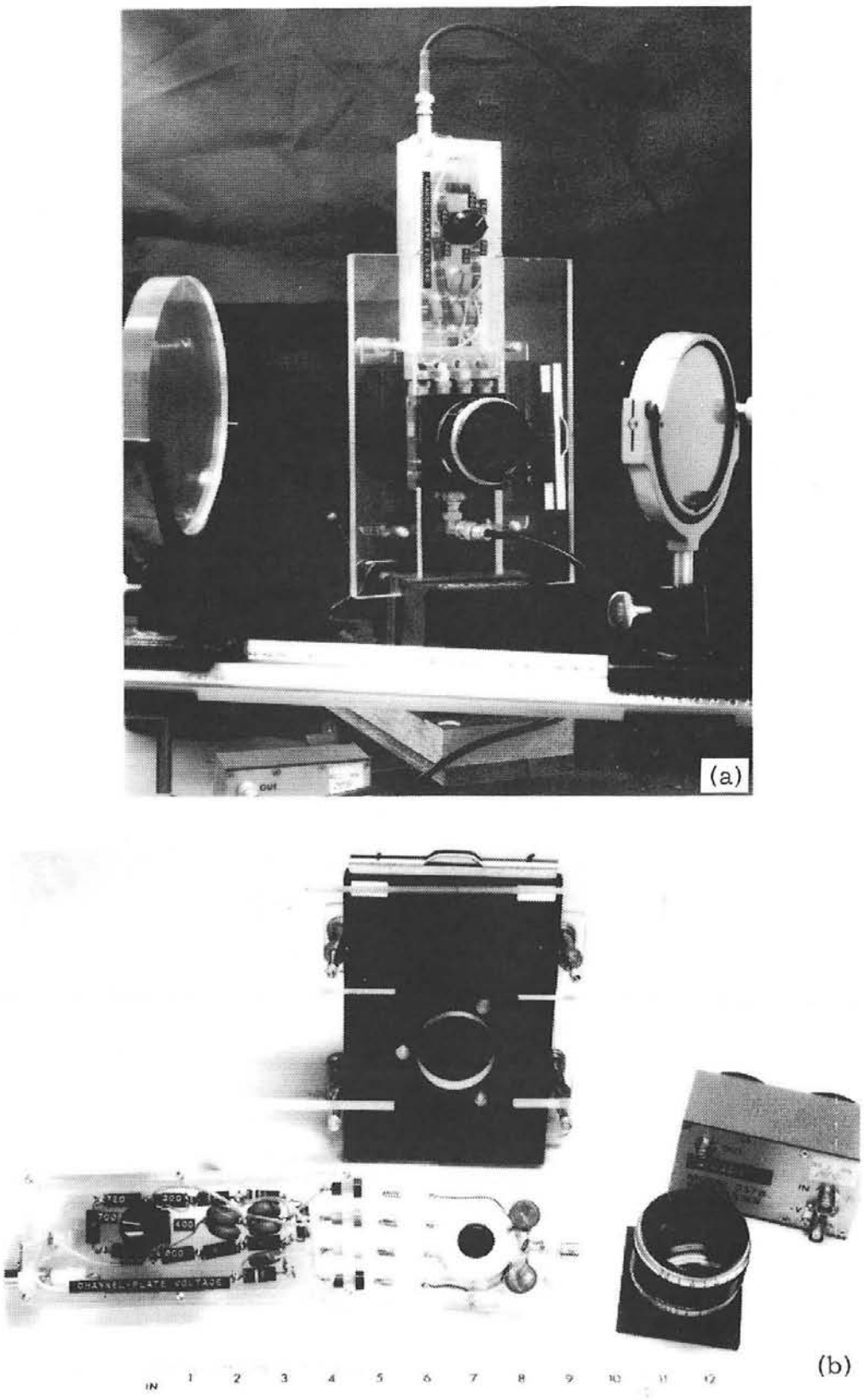

Figure 4. Operational (a) and dismantled (b) views of our gated image intensifier camera.

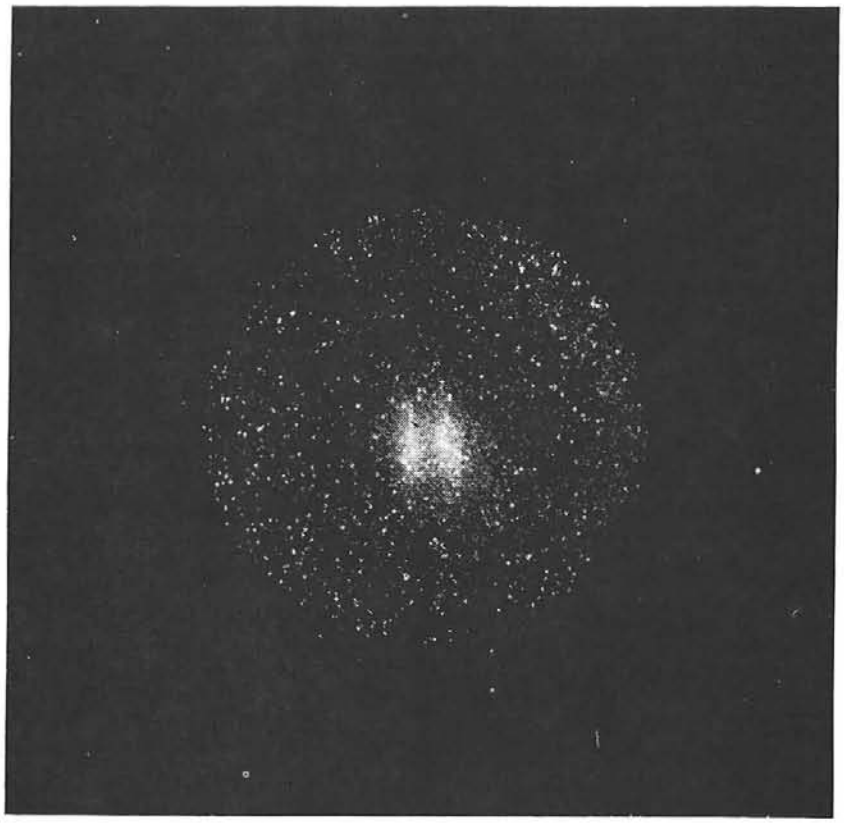

Figure 5. A single pinhole image of bremsstrahlung emitting 3-mm-wide tantalum strips. The tapered pinhole had a 0.5-mm diameter in the narrowest section, and had an overall thickness of 35 mm. The source intensity was ~300 rads at contact. The random bright spots in the field correspond to single gamma-ray interactions in the channel plate of the intensifier.

Coded Aperture X-Radiography*

by

J. G. Kelly and D. A. McArthur

Sandia Laboratories
Albuquerque, New Mexico 87115

and

H. H. Barrett

University of Arizona
Tucson, Arizona

Introduction

The detailed motion of fuel during an overpower transient in an LMFBR may determine the extent and the seriousness of the damage to the reactor and the environment. X-radiography could prove to be a useful tool for observing fuel motion during simulated accidents in safety test facilities if electron accelerators can be built to provide the msec frame rate x-ray flux required.

One study reported on at this conference[1] indicates that if adequate signal to noise is to be obtained during experiments on LMFBR subassemblies in which 10^6 watt/cm^3 of fission power is being generated in the fuel, and if a spatial resolution of approximately 1 cm is specified, then a multiple pulsed field emission electron accelerator (call this accelerator REB) may be the only feasible source. Therefore an experiment is being planned for the Hermes II at Sandia Laboratories to test the usefulness of this type of accelerator for radiography.

We believe that it will be extremely difficult to build a REB which will produce an x-ray beam of the required intensity over a small enough

* This work supported by the U. S. Energy Research and Development Administration

geometrical area to provide cm spatial resolution. This appears to be the case for the following reasons.

1. Although extensive research is being carried on with pinched relativistic electron beams for pellet fusion applications,[2-5] it has not been possible to produce pinches that are reliably positioned or highly reproducible in intensity or diameter in these diodes. (Positioning has been accomplished on a small accelerator.[6])
2. A more serious drawback of the very intense beams is that extensive damage is always done to the anode and usually to the cathode on each pulse. The diode is then filled with material debris and conducting plasmas which short the cathode and anode. Subsequent shots must wait until the diode is clear and then the damage areas will cause non-uniform beams to be generated.

However, very reliable broad area beams have been available for a number of years for the following reasons.

1. They can be generated with intensities which vary slowly over broad areas with high position reproducibility. Furthermore the positioning is not very important for the case where the source spatial variation is slow.
2. The energy may easily be deposited into an area which is 10^4 larger than in the pinched case and the power density is therefore lower by the same factor. Thus electrode damage can probably be avoided and multiple pulsing can be accomplished.

We propose to recover the spatial resolution for a broad x-ray source by using coded aperture imaging. The technique has been extensively developed for radiography in nuclear medicine. Although most of the work just mentioned has been carried out with line radiation sources in the 100 kV range, the imaging investigations which have been made at Sandia Laboratories[8, 9] of the fission gamma rays from Cf^{252} show that coded

aperture imaging of sources emitting high energy broad spectrum photons (0.3-8 MeV) can be carried out quite successfully. In the next section the planned Hermes II coded source X-radiography experiment will be described.

Description of the Hermes II Experiment

An artist's cutaway drawing of the Hermes II accelerator[10] is shown in Figure 1. It consists of a Marx capacitor bank which is charged in parallel and discharged in series to a pulse forming line and a field emission diode. A 10-MeV, 100-kA electron beam which lasts about 70 ns is generated and can be directed onto a Ta anode for bremsstrahlung x-ray production. The x-ray spectrum (measured with a Compton spectrometer[11]) as reproduced from the Hermes II experimenter's manual[12] is shown in Figure 2.

In normal operation of the accelerator the x-ray beam source size is more than 300 cm^2 in area. This means, of course, that a collimator at the anode small enough to provide cm resolution would use only 0.3 percent of the beam. The radial dose profile measured with passive dosimeter[12] is shown in Figure 3 where it is seen that the beam is in the shape of a shallow donut because of cathode shank emission.

The coded source experiment will be carried out in the configuration shown in Figure 4. Directly beyond the anode a Fresnel zone plate-coded aperture will be placed to modulate the x-ray beam. The zone plate is 20.3 cm in diameter and is made of lead rings 1-cm thick. The radial thickness of the outermost ring is $\Delta r_N = 2.5$ mm which in this geometry should allow 2.5-mm spatial resolution in the object plane. The object will be placed $S_1 \approx 5$ m from the zone plate and will consist of fuel pin size rods and/or small holes. In Figure 4 the transmission of one point of the object is represented by a small hole. The shadow on the detector plane caused by this hole at $S_2 \approx 5$ m will be a zone plate image which is the pseudohologram of a point source. When the film recorded pseudohologram

is illuminated with coherent light, a first order focus occurs (or in other words the point object is reconstructed) at the focal length (given by $f_p = r_1^2/\lambda$) of the recorded zone plate image. In this formula r_1 is the radius of the innermost image ring and λ is the wavelength of the coherent light. This formula exhibits another of the advantages of coded aperture imaging over a pinhole aperture - its ability to record three-dimensional information. The r_1 of the zone plate image is related to the r_1' of the actual zone plate by the formula $r_1' = r_1 S_1/S_2$ and therefore the longitudinal position of the reconstructed image depends on the longitudinal position of the object. Clearly since any object can be represented by a superposition of points, the complete image can be reproduced in three dimensions from a pseudohologram obtained in the configuration of Figure 4.

Some of the coherent light which passes through the pseudohologram will not be diffracted by the zone plate image. This light therefore will contribute a background illumination at the reconstruction plane, and is usually referred to as "dc". For broad objects, this dc can be very large and can severely degrade the signal-to-noise at the image plane. For this reason, different coded apertures such as off axis zone plates[7] have been developed to diffract the light which forms the image out of the area where the dc term exists. This requires that the original x-ray or γ-ray beam be modulated at frequencies much higher than that required for the desired spatial resolution. However this modulation can't be easily reached by practical gratings if resolution of less than 1 cm is required with γ rays in the MeV range. This is because insufficient modulation is obtained with apertures thin enough to avoid the venetian blind effect.

An alternative method which eliminates the need for high frequency modulation of the γ-ray beam but which requires multiple exposures has been developed by Burckardt and Doherty and has been described by Barrett, et. al.[13] Four separate pseudoholograms are obtained with a zone plate such as that shown in Figure 5. Between each exposure the film is changed and the zone plate is rotated 90 degrees. The reconstruction process then

involves two steps. In the first step shown in Figure 6, a new pseudohologram is formed as a combination of the four originals in which for each exposure the film is masked by a Ronchi ruling and moved between those exposures by 1/4 the ruling spatial frequency. In the second step of reconstruction process when the coherent light illuminates the pseudohologram, the image is diffracted out of the dc region by the grid spacing of the ruling.

This second method of image formation will also be tested in the Hermes II environment.

Discussion

We have described an experiment that will be conducted on the Hermes II flash x-ray facility to determine if coded source aperture techniques can be employed to make efficient use of a broad area, high power x-ray beam with a hard photon spectrum while concurrently maintaining good spatial resolution and tomographic capability. If this can in fact be demonstrated, then quality X-radiography may be possible with this type of field emission accelerator. Although the x-ray intensity provided by these accelerators is unequaled and may be needed during peak power levels of reactor pulses testing fuel motion, an extended program to develop multipulse capability would be required.

References

1. L. Posey, "Source Requirements for Flash X-Radiography Diagnostics," this Conference.

2. G. Yonas, K. R. Prestwich, J. W. Poukey, and J. R. Freeman, Phys. Rev. Lett. 30, 164 (1963).

3. J. G. Kelly and L. P. Mix, J. Appl. Phys. 46, 1084 (1975).

4. J. G. Kelly, S. A. Goldstein, and D. W. Swain, J. Appl. Phys. 46, 4726 (1975).

5. D. W. Swain, S. A. Goldstein, J. G. Kelly, G. R. Hadley, and L. P. Mix, submitted to J. Appl. Phys. in November 1975.

6. J. G. Kelly, Appl. Phys. Lett. 26, 665 (1975).

7. H. H. Barrett and F. A. Horrigan, Applied Optics 12, 2686 (1973).

8. D. A. McArthur and J. G. Kelly, "A Coded Aperture Material Motion Detection System for the ACPR," this Conference.

9. J. G. Kelly and D. A. McArthur, ANS Transactions, TANSAO 22 1-836 (1975), p. 394.

10. T. H. Martin, K. R. Prestwich and D. L. Johnson, SCPR 69-421, Sandia Laboratories, Albuquerque, NM (1969).

11. J. G. Kelly, L. D. Posey and J. A. Halbleib, IEEE Trans. Nucl. Sci., NS-18, 131 (1971).

12. A. M. Chodorow, "Hermes II Experimenter's Manual " SC-M-70-242, Sandia Laboratories, Albuquerque, NM (1970).

13. H. H. Barrett, W. W. Stoner, D. T. Wilson, and J. G. DeMeester, Optical Engineering 13, 539 (1974).

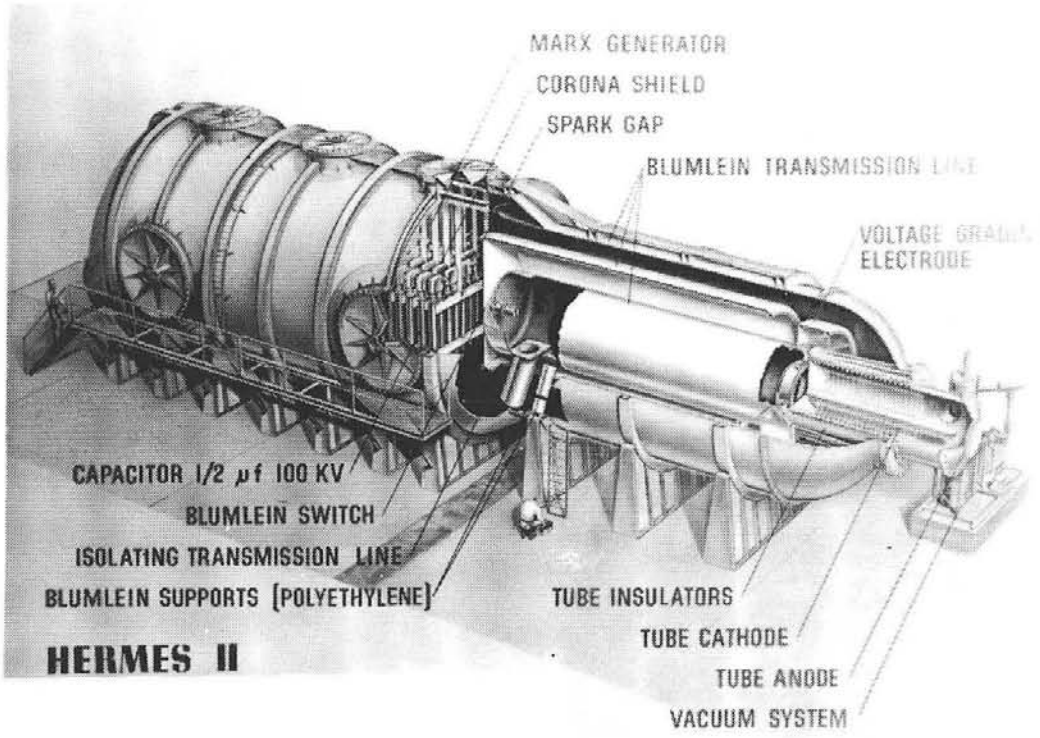

Figure 1. Hermes II Accelerator

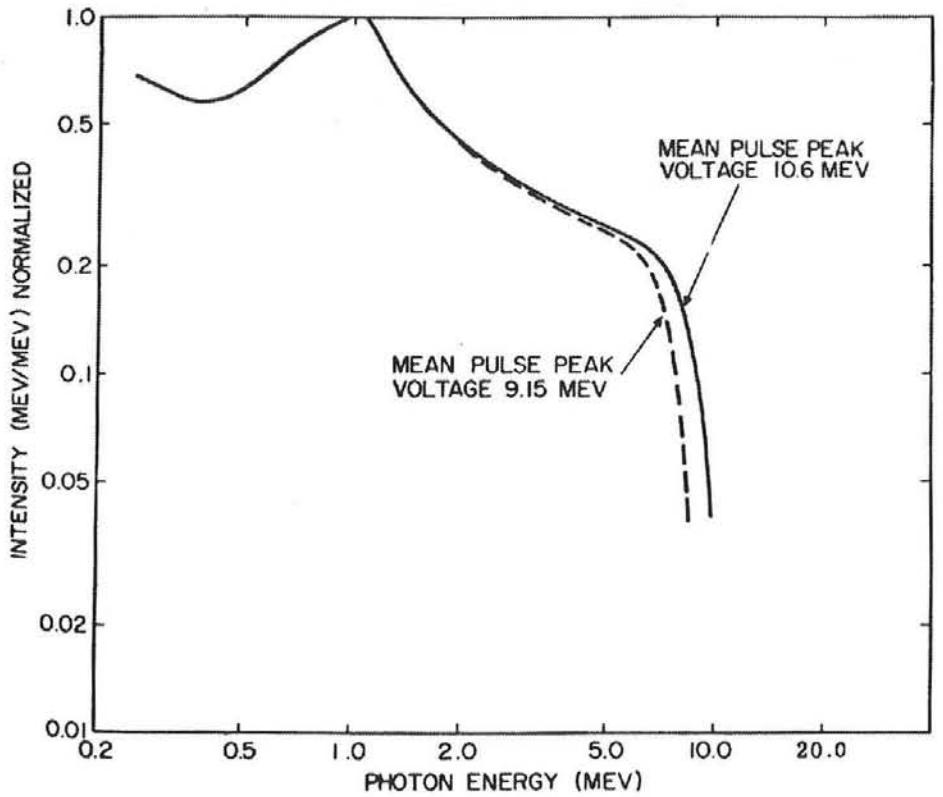

Figure 2. X-ray Spectrum as Reproduced from Hermes II Experimenter's Manual

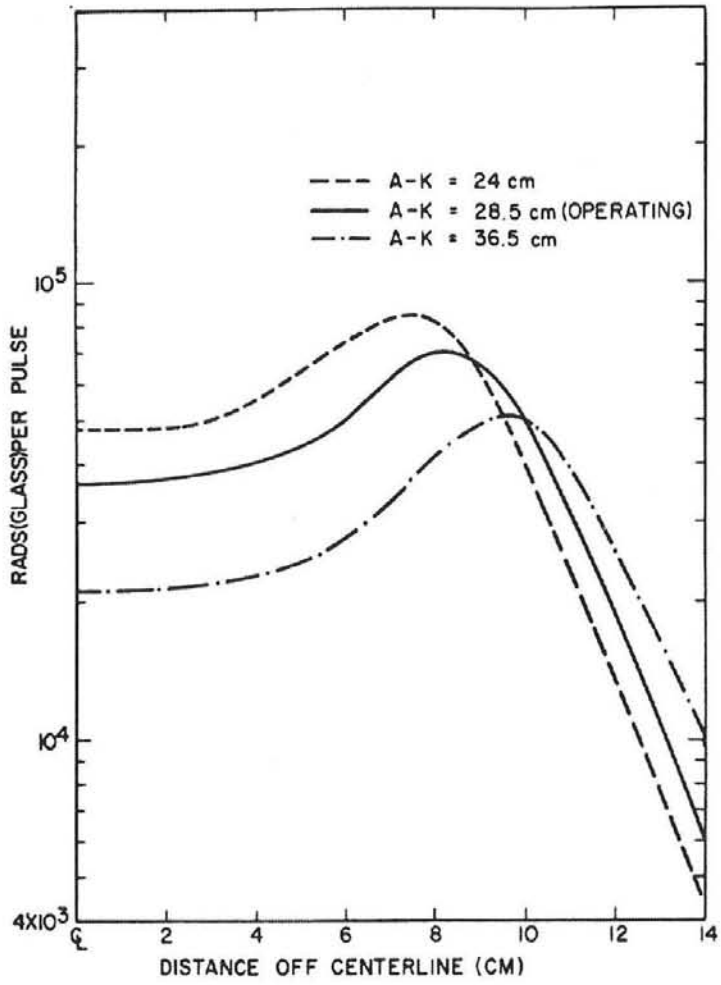

Figure 3. Radial Dose Profile Measured with Passive Dosimeters

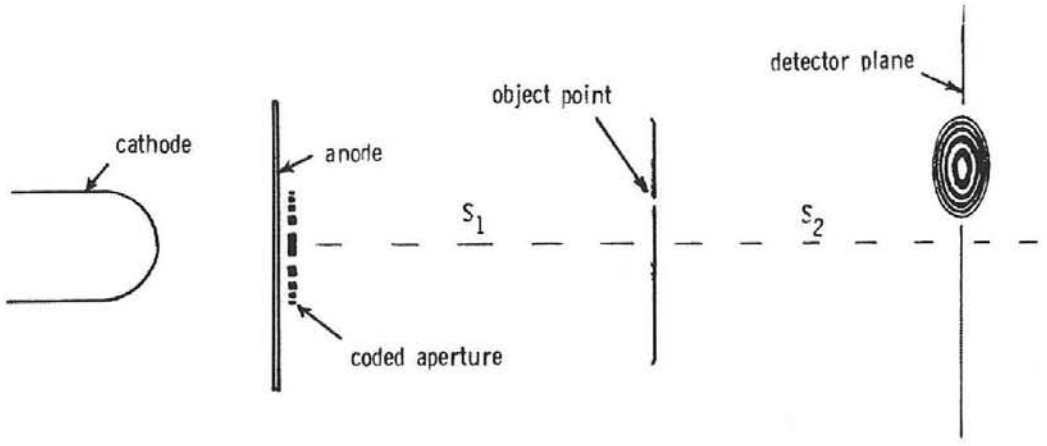

Figure 4. Configuration for Carrying Out Coded Source Experiment

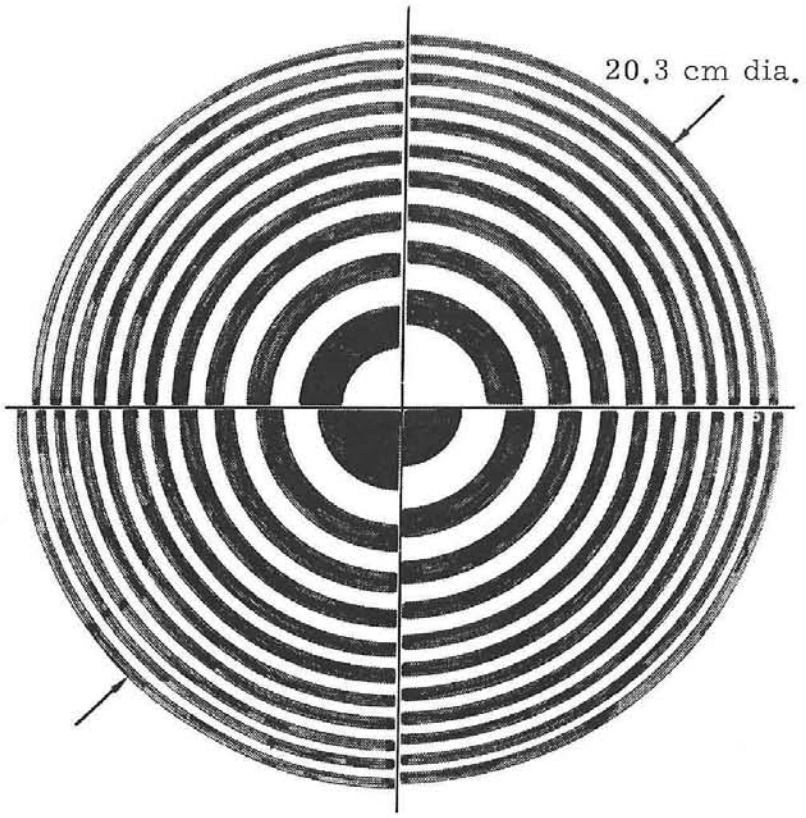

Figure 5. Zone Plate

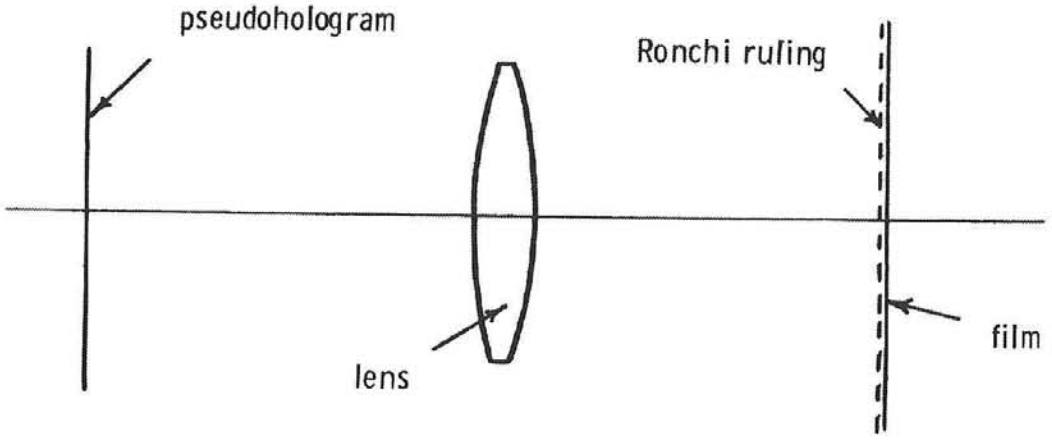

Figure 6. Pseudohologram

Computer Reconstruction of Pseudoholograms Obtained From a Fission Gamma Source*

K. R. Hessel and K. T. Stalker
Sandia Laboratories Optics Division
Albuquerque, New Mexico 87115

ABSTRACT

Pseudoholograms obtained with a Fresnel zone plate coded aperture have been reconstructed using digital computer techniques. The object was a Cf^{252} fission gamma source. The digital reconstruction procedure and its advantages relative to analog techniques is discussed. Image reconstructions indicate transverse and longitudinal resolutions on the order of millimeters. Several digital enhancement options are available. Our plans for improved results are discussed.

*This work supported by the U.S. Energy Research and Development Administration

Introduction

In coded aperture or coded source imaging of fission gamma sources an essential step is the reconstruction of the image from the recorded radiograph. Either analog or digital reconstruction techniques can be used. The analog reconstruction method typically requires a laser, collimator, and an associated optical system. Digital reconstruction systems perform equivalent operations on a computer.

In this paper the digital reconstruction procedure is discussed; the advantages and limitations of the digital method are pointed out, typical results are presented, and a brief description of the current objectives is given. Although results are presented for the Fresnel zone plate coded aperture much of the digital reconstruction procedure is applicable to other coded apertures as well.

Digital Reconstruction Procedure

The essential steps in the reconstruction of images from the recorded radiograph, for Fresnel zone plate coded apertures, are the following:

a. The pseudohologram is digitized, giving a density array. Typically a 200 x 200 array is used with a 10 cm x 10 cm radiograph although this will vary depending upon the zone plate parameters, object size, and required resolution.

b. The digitized points are raised to an exponential power to convert to transmittance. This is required since the Fourier transform reconstruction requires the use of transmittance rather than density values.

c. The DC transmittance is subtracted. This will remove background intensity in the reconstructed image. In analog reconstruction systems the DC light must be eliminated by more complex procedures.

d. The array is multiplied by a complex exponential to focus. This step is completely equivalent to focusing in an optical analog reconstruction system.

e. The array points are alternately multiplied by ± 1 to center. This is a simple but essential step in order to obtain recognizable images.

f. The array is Fourier transformed using a fast Fourier transform subroutine.

g. The array is conjugated to obtain an intensity array from the complex array.

h. The array is plotted.

Instead of a completely digital or completely analog reconstruction there are several hybrid alternatives:

a. The pseudo-hologram can be high-contrast copied and then digitized and computer reconstructed.

b. The pseudohologram can be digitized, converted to a high contrast pseudohologram with distortion and non-linearity removed, transferred to microfilm with size reduced and then analog reconstructed. This alternative has been used with excellent results.

c. The analog reconstruction can be digitized, computer enhanced and reprinted.

Merits of Digital Reconstruction

The disadvantages of the digital reconstruction method are fairly obvious: The digitization step, computing, and output interface require considerable time and cost. The advantages, however, are quite significant:

a. The DC transmittance can be subtracted before taking the transform, greatly reducing the image background. In analog systems elimination of the DC term is much more difficult.

b. It is simple to compensate for film nonlinearity, allowing a linear reconstruction. Analog reconstructions are, in general, nonlinear, which make image interpretation more difficult.

c. Distortion present in the pseudohologram can be eliminated. Distortion, particularly non-linear distortion, makes an analog reconstruction very difficult, if not impossible, to obtain.

d. With the Fresnel zone pseudohologram, conjugate and higher order images can be reduced or eliminated.

e. Various enhancement options are simple to implement.

Results

Figure 1 is the original radiograph of two Cf^{252} fission sources separated only transversely by 2.85 mm with S_1 = 61 mm and S_2 = 92.4 mm. S_1 is the distance from the zone plate to the object and S_2 is the distance from the zone plate to the film. The zone plate consisted of an aluminum base with lead-gold eutectic rings. The reconstruction is shown in Figure 2. In all the reconstructions broad intensity distributions are also evident in addition to the sources. These are from conjugate and higher order images which can be reduced or eliminated.

Figure 3 is also a reconstruction from Figure 1, only the focus has been changed so the two sources are now out of focus and only the center of the reconstruction, which is enlarged, is shown. Both digital magnifications and demagnifications are easily obtained options.

In Figure 4 the radiograph of two Cf^{252} sources separated transversely by 3.2 mm and longitudinally by 12.7 mm is shown. All the radiographs are fairly low contrast due to the low depth of modulation by the zone plate, but excellent reconstructions are still possible so long as noise does not dominate the radiograph. The image is shown in Figure 5 with the computer focused on the left source.

The original radiograph of two Cf^{252} sources separated only longitudinally is shown in Figure 6. The sources are 63.5 and 88.9 mm from the zone plate. Figures 7, 8, and 9 are the reconstructions with the computer focused for 63.5 mm, 74 mm (out of focus for both sources), and 88.9 mm respectively. The tomographic imaging capability of the Fresnel zone plate coded aperture is clearly evident.

Figures 10, 11, and 12 are color plots with the hue proportional to image intensity. Figure 10 is a reconstruction of two Cf^{252} sources separated only transversely by 2.85 mm. Figures 11 and 12 show the left and right images focused, respectively, for two Cf^{252} sources separated transversely by 3.2 mm and longitudinally by 12.7 mm. Figure 13 is a color contour plot of Figure 12 with the contour hue indicating the intensity level. These indicate some of the computer enhancements which can be obtained to aid in image interpretation.

Summary and Current Objectives

The procedure involved in digital reconstructions, the advantages and limitations, and typical results for Cf^{252} sources indicate that further work in the computer reconstruction of pseudoholograms is warranted.

Current efforts are directed toward reduction or elimination of conjugate and higher order images from the reconstruction, the direct deconvolution of pseudoholograms, and toward cross-correlation and deconvolution reconstruction of non-redundant and redundant pinhole array images.

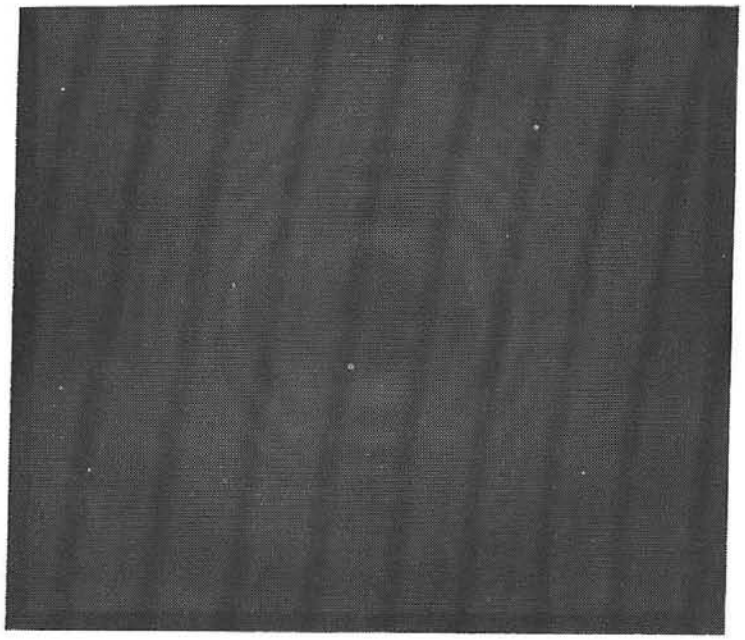

Fig. 1. Original Radiograph. Two fission sources separated only transversely by 2.85 mm. S_1 = 61 mm, S_2 = 92.4 mm.

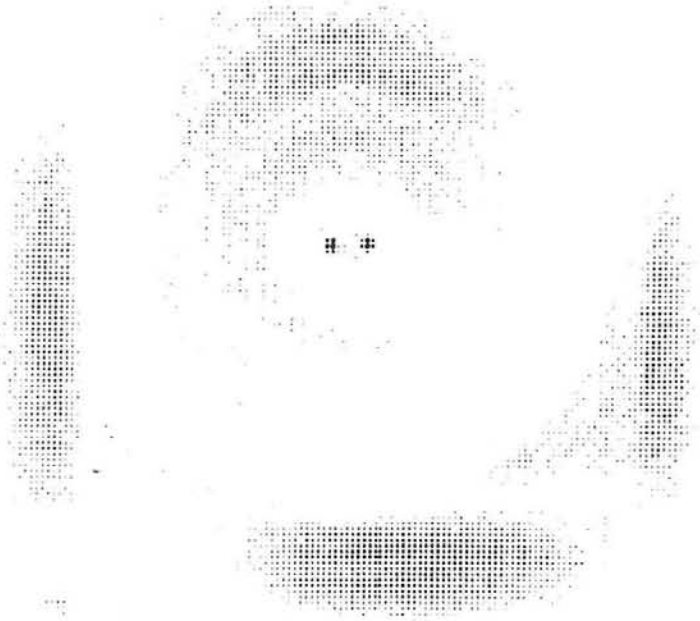

Fig. 2. Computer Reconstruction. Two fission sources separated only transversely by 2.85 mm. S_1 = 61 mm, S_2 = 91.4 mm. Computer is focused for sources 61 mm away.

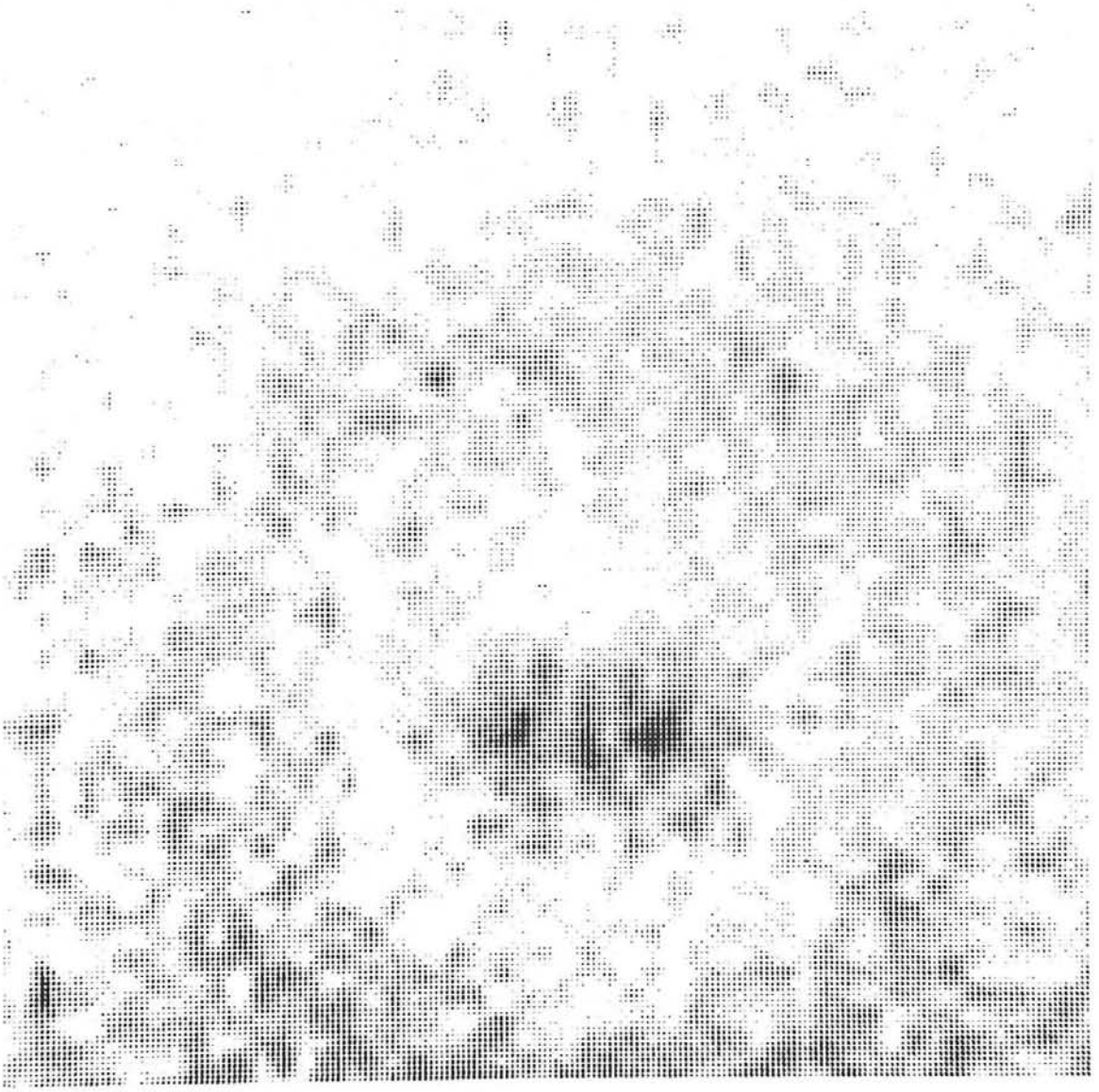

Fig. 3. Computer Enlargement. Central area of reconstruction has been enlarged.

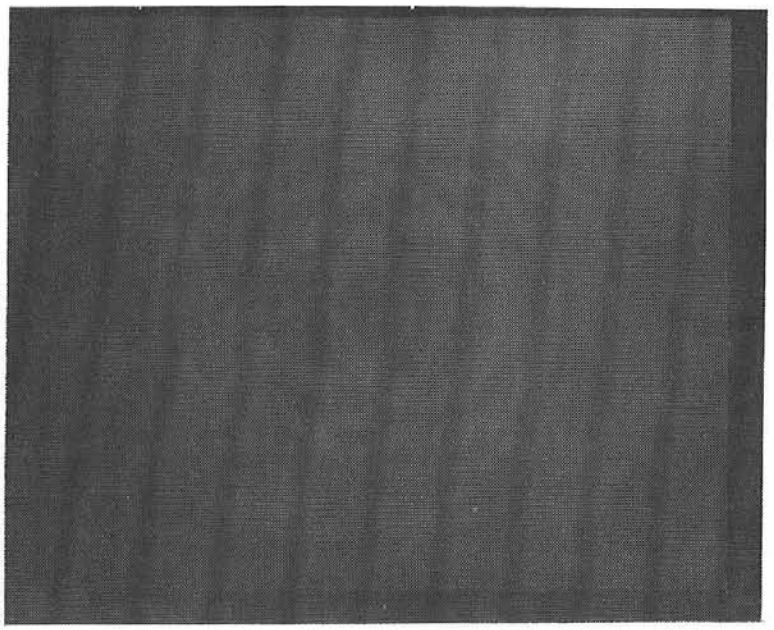

Fig. 4. Original Radiograph. Two fission sources separated transversely by 3.2 mm, longitudinally by 12.7 mm.

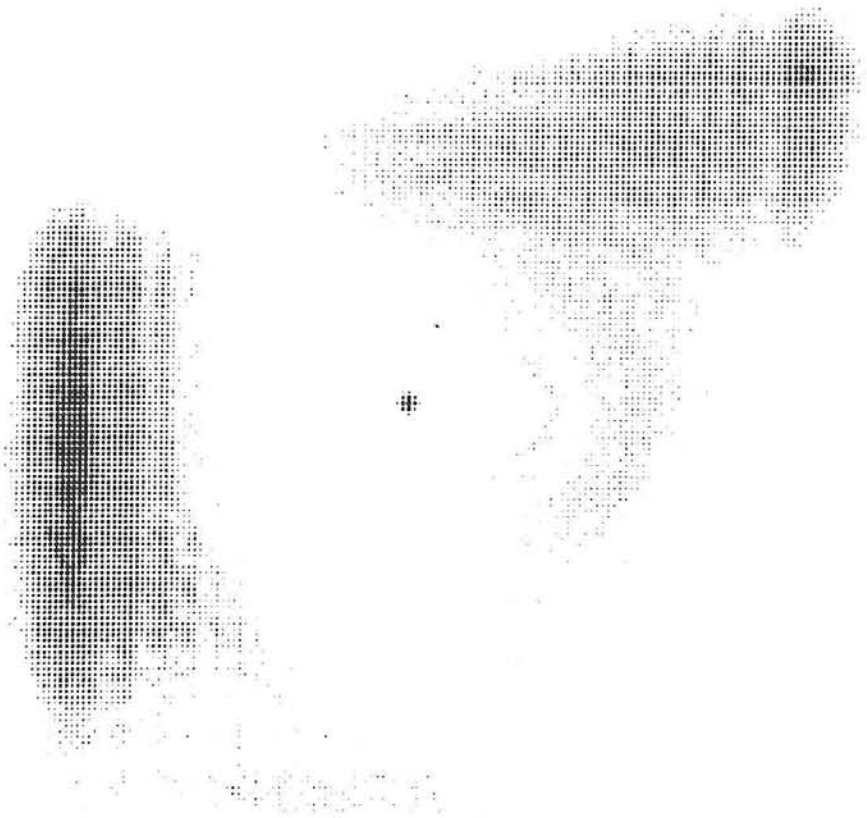

Fig. 5. Computer Reconstruction. Two fission sources separated transversely by 3.2 mm, longitudinally by 12.7 mm. Computer is focused on left source.

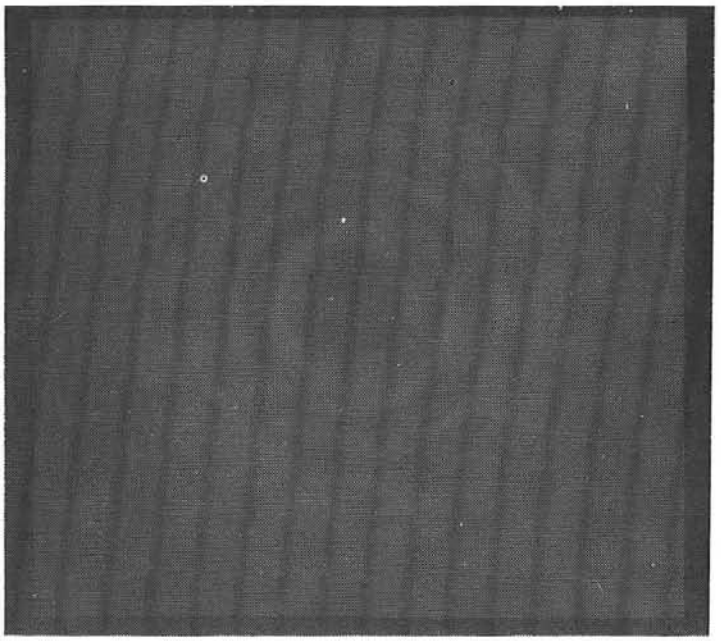

Fig. 6. Original Radiograph. Two fission sources separated only longitudinally. S_1 = 63.5 and 88.9 mm, S_2 = 88.9 mm.

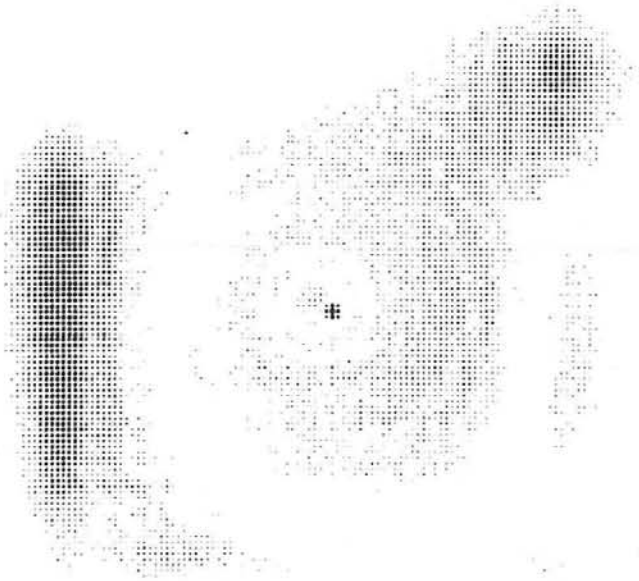

Fig. 7. Computer Reconstruction. Two fission sources separated only longitudinally. S_1 = 63.5 and 88.9 mm, S_2 = 88.9 mm. Computer focused for source 63.5 mm away.

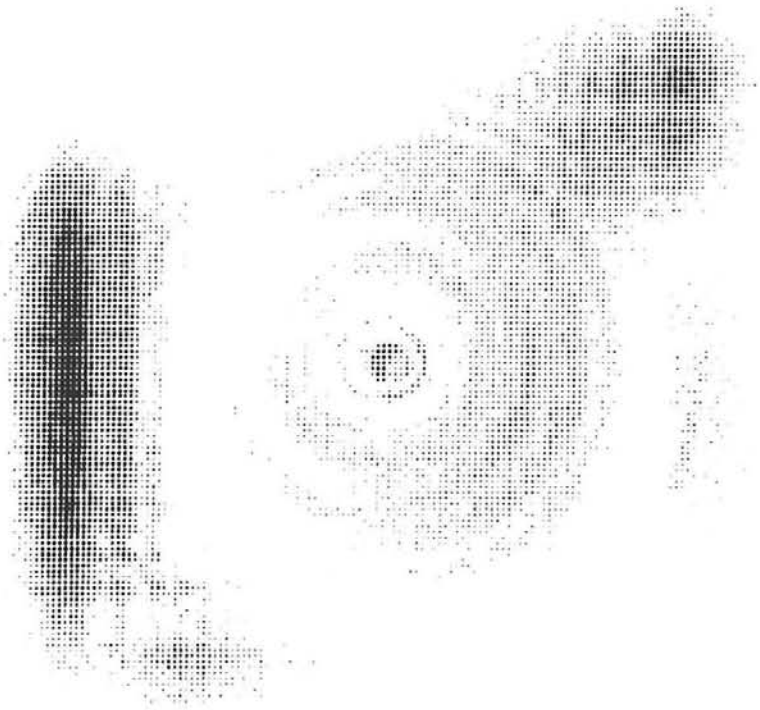

Figure 8. Computer Reconstructed. Two fission sources separated only longitudinally. S_1 = 63.5 and 88.9 mm, S_2 = 88.9 mm. Computer focused for source 74 mm away.

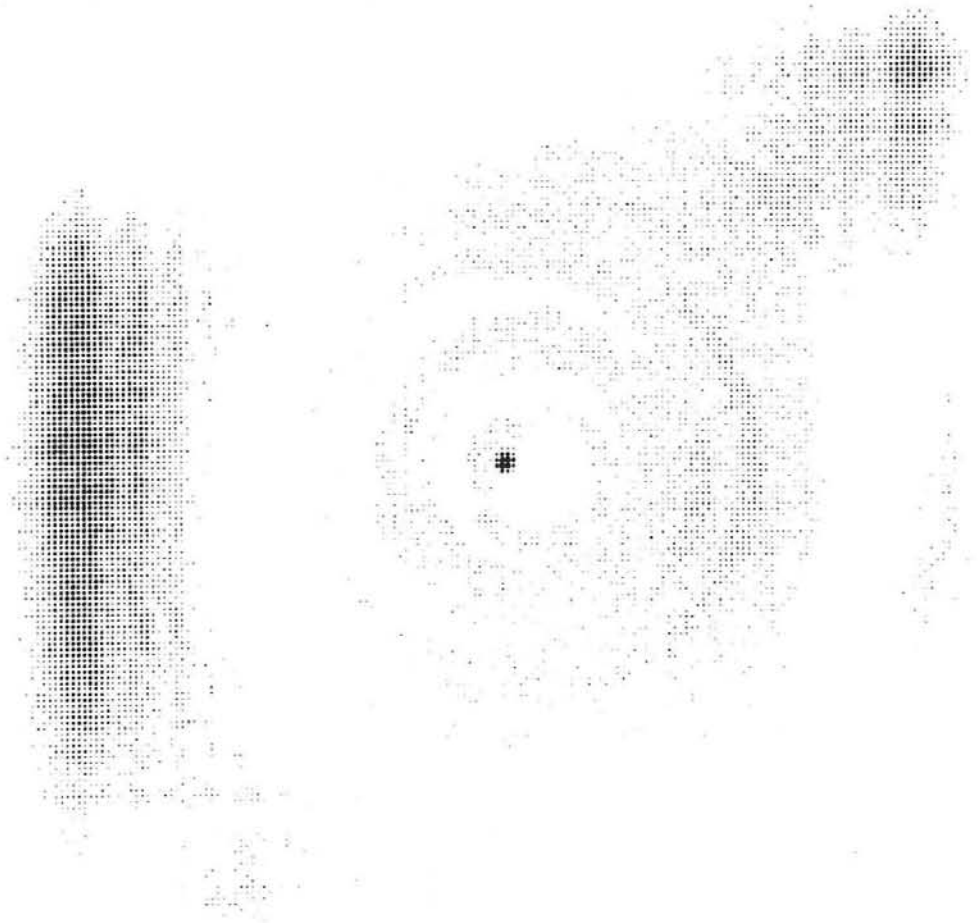

Fig. 9. Computer Reconstruction. Two fission sources separated only longitudinally. S_1 = 63.5 and 88.9 mm, S_2 = 88.9 mm. Computer focused for source 88.9 mm away.

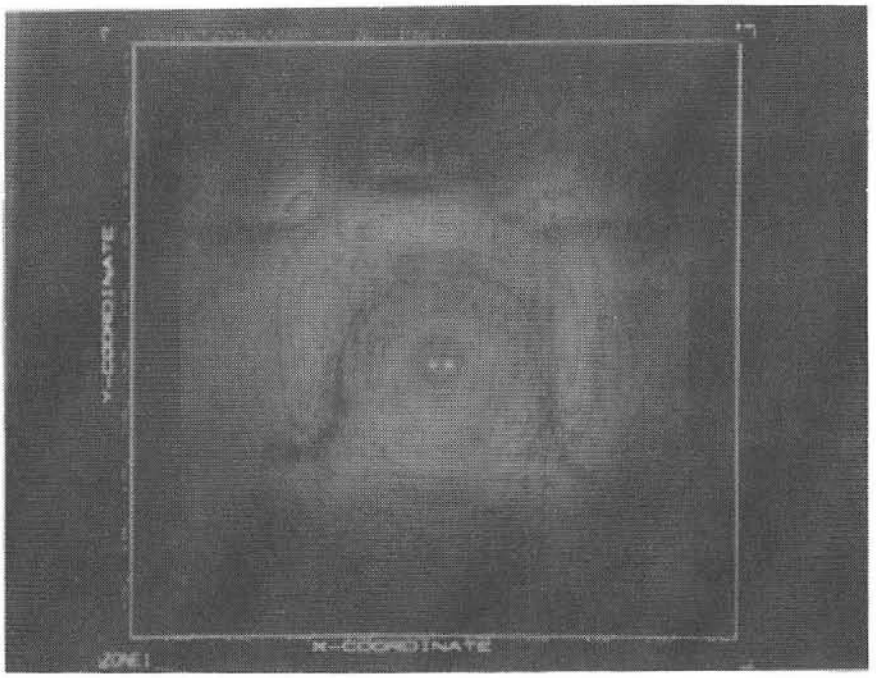

Fig. 10. Computer Reconstruction. The fission sources separated only transversely by 2.85 mm. S_1 = 61 mm, S_2 = 91.4 mm. Computer is focused for sources 61 mm away. The original plot is in color.

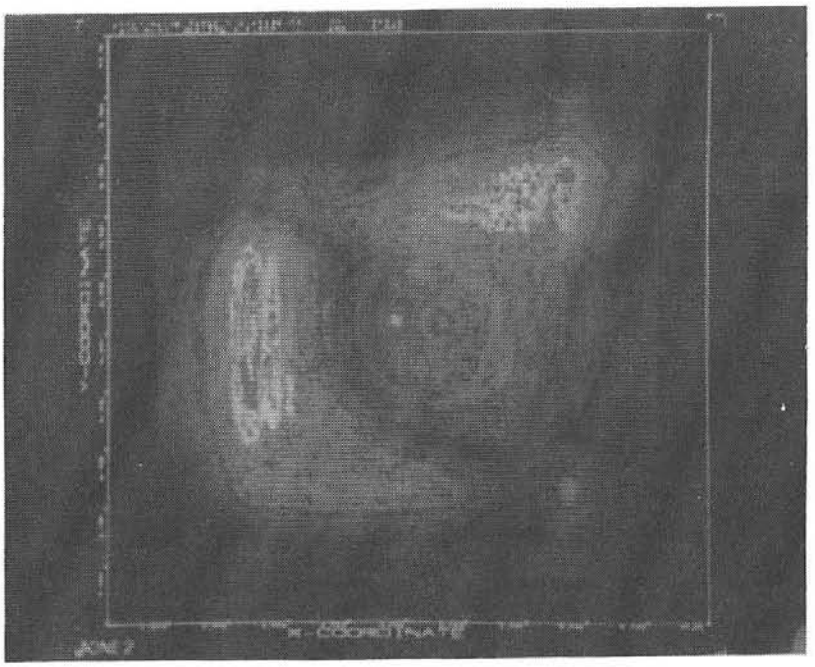

Figure 11. Computer Reconstruction. Two fission sources separated transversely by 3.2 mm, longitudinally by 12.7 mm. Computer is focused on left source. The original plot is in color.

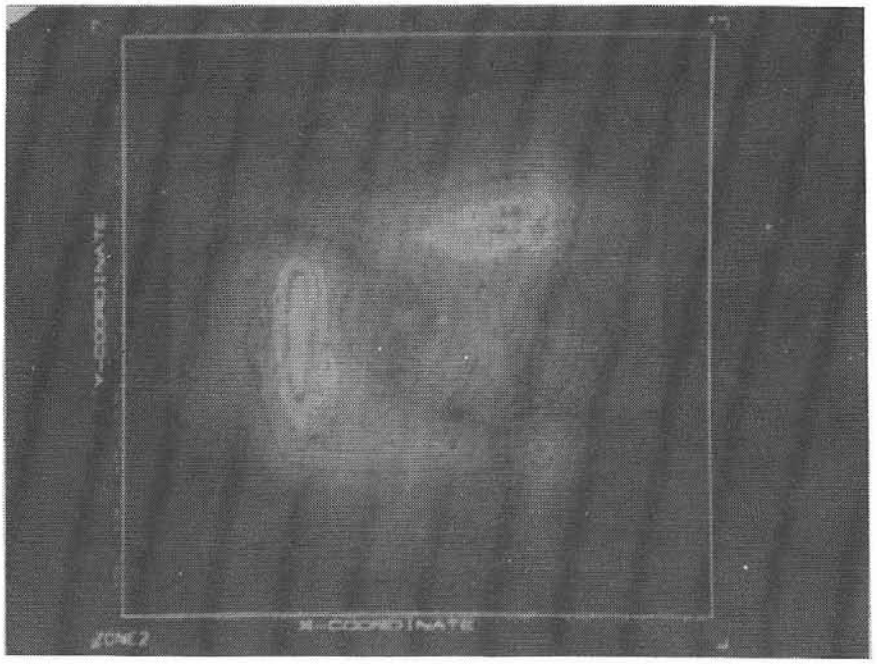

Fig. 12. Computer Reconstruction. Two fission sources separated transversely by 3.2 mm, longitudinally by 12.7 mm. Computer is focused on right source. The original plot is in color.

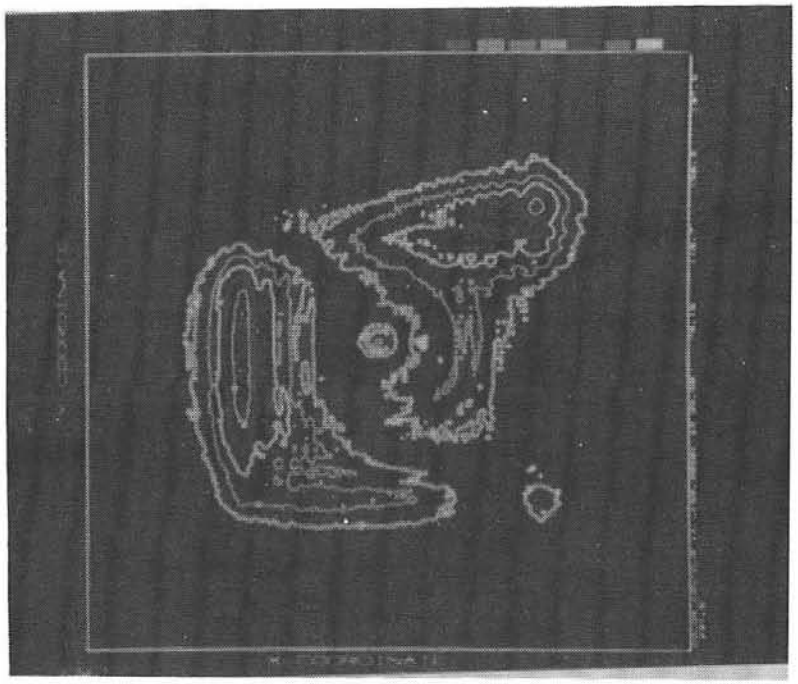

Figure 13. Computer Reconstruction. Intensity contour plot for two fission sources. The original plot is in color.

Simulation of LMFBR Test Facility Conditions With LASL Critical Assemblies*

by

John Orndoff

Los Alamos Scientific Laboratory
Los Alamos, New Mexico 87544

*This work supported by the U.S. Energy Research and Development Administration

I. GENERAL

The evaluation of certain instrumentation concepts for the LMFBR Safety Test Facility (STF) requires some means of simulating conditions in and around the test region. Proposed driver-reactor test cell geometries are so asymmetric and non-homogeneous that modeling for detailed calculations becomes an extremely questionable alternative. Fuel motion diagnostics for multi-pin test assemblies is a difficult task, and proposed techniques depend so strongly on the STF environment that they must be evaluated by simulation. What may appear promising under simplified laboratory conditions may not be adaptable to the STF.

Techniques that have demonstrated some promise of providing significant diagnostic information in the STF application include (1) flash x-ray cinematography, (2) the hodoscope neutron counting system and (3) gamma ray imaging with coded aperatures. Flash x-rays have demonstrated the capability of resolving single fuel pins in multiple pin arrays through two inches of steel containment, and with STF radiation conditions simulated crudely. The hodoscope, developed at Argonne, has been used in the TREAT facility with single pin and seven pin arrays.[2] Computations predict that this technique will be useful for larger arrays as well. Coded aperatures have been applied to medical diagnostics with low energy gamma rays. Gamma ray imaging experiments using fission gamma energies have thus far been confined to point sources where signal to background conditions are most favorable.[3]

Two critical assemblies at LASL are being adapted to simulate the STF conditions: (1) The PARKA critical assembly is being modified to

serve as a driver for fuel pin arrays at the center for scaled-down simulation of STF and (2) A moderator geometry adjacent to the Godiva IV prompt burst assembly provides the capability of driving a few fuel pins to instantaneous power levels higher than those expected in STF transients. These simulation facilities are discussed below.

II. STF DRIVER-REACTOR SIMULATION IN PARKA

The PARKA critical assembly is a Rover Project Kiwi reactor loaded with graphite-uranium fuel elements. These are one-hole bead loaded elements that were used for critical assembly studies for Rover reactor design. Four uranium loadings (93% ^{235}U) of 100, 200, 300, and 400 mg/cm^3 are distributed to give approximately flat fission density across the 35 in. fueled diameter. Figure 1 shows a cross sectional view of a 60 degree sector of the PARKA geometry with a test region at the center. Onetran transport calculations have been run to determine the effect of adding a 37 pin test assembly. For these calculations, fuel pins are assumed to be made of highly enriched uranium oxide. In three calculated cases it was assumed that the space between pins was void or filled with either water or sodium. Addition of the test section increased reactivity 3.2$ for the water filled cell and 0.9$ and 1.1$ respectively for void and sodium. Relative fission density as plotted in Figure 2 is the ratio of fission density in the modified PARKA core to that in the original core. In all three cases the fission density peaks strongly in the test fuel pins because of their high uranium loading. Perturbation introduced in the adjacent PARKA core is mild in all three calculations, consisting of a slight peaking with water and a depression with void and sodium.

A slot through the beryllium reflector and the PARKA fuel elements provides experimental access to the test region. The initial setup in an experimental program to evaluate various hodoscope geometries and

detector options is represented in Figure 3. The program will serve to verify parallel Monte Carlo calculations. Monte Carlo analyses should then be useful for more general evaluation and optimization of the hodoscope technique.

Present PARKA operating conditions, without special shielding, limit the PARKA transients to about twenty megawatt seconds per experiment, corresponding to about a 400^{o}C rise in temperature of the uranium oxide fuel pins in the water filled test cell. With sodium or void the temperature rise would be one half that value. Relocation of PARKA or some provision for local shielding could extend power levels by an order of magnitude.

Potential applications of the PARKA simulation are: (1) studies of STF radiation environment, (2) evaluation of flash x-ray diagnostics with realistic scattering and radiation environment, (3) investigation of in-core diagnostic methods, and (4) investigation of shielding requirements for instrumentation concepts. The advantages of the PARKA system are its flexibility and the ease with which geometry can be changed. An essential experiment will be to determine what changes in a multiple pin test array can be detected by the hodoscope. Fuel pins can easily be removed or fuel can be rearranged to simulate almost any proposed accident condition.

III. GODIVA DRIVER FOR SIMULATING FUEL PIN TRANSIENTS

High fission levels have been induced in mockup fast reactor fuel pins in moderator geometries external to the Godiva IV prompt burst assembly. A typical experimental arrangement is shown in Figure 4. In this arrangement, two fuel pins provide an intense three dimensional source for coded aperature imaging experiments. For fuel pins located

25 cm from the Godiva centerline, in an annular moderator segment as shown in the figure, the average fissions per gram of uranium in fuel pins is a factor four higher than the peak value in Godiva. In this experiment, fast reactor fuel pins were mocked up with an appropriate spiral of uranium foil inside a one-quarter inch o.d. aluminum tube. The moderator geometry contributes 0.4$ to Godiva reactivity and results in a fission pulse in the pins about one hundred microseconds wide. For this particular geometry at the 25 cm distance, the maximum Godiva IV pulse will give about 1000^{o}C rise in temperature in highly enriched uranium oxide fuel pins. Instantaneous power levels are greater than 10^{6} watts per gram but the transient length is much shorter than in contemplated STF transients. This demonstrated capability can probably be increased by a factor of two with a moderator geometry closer to Godiva.

The advantages of the Godiva driver system is that it provides the capability of conducting imaging experiments in a three dimensional geometry under realistic conditions. Intensities are high enough to permit realistic distances between source and detector and the effects of intervening materials and background radiation can readily be investigated.

References

1. G. I. Bell, et al, "Study of Fast Reactor Safety Test Facilities, "Los Alamos Scientific Laboratory (preliminary) Report LA-5978-MS (1975).

2. A. De. Volpi, et al, "Fast Neutron Hodoscope at TREAT: Data Processing Analysis, and Results," Argonne National Laboratory Report ANL/RAS 75-15 (June 1975).

3. "Experimental Fast Reactor Safety Research Program Quarterly Report," Sandia Laboratories Report SAND-75-0449 (April-June 1975).

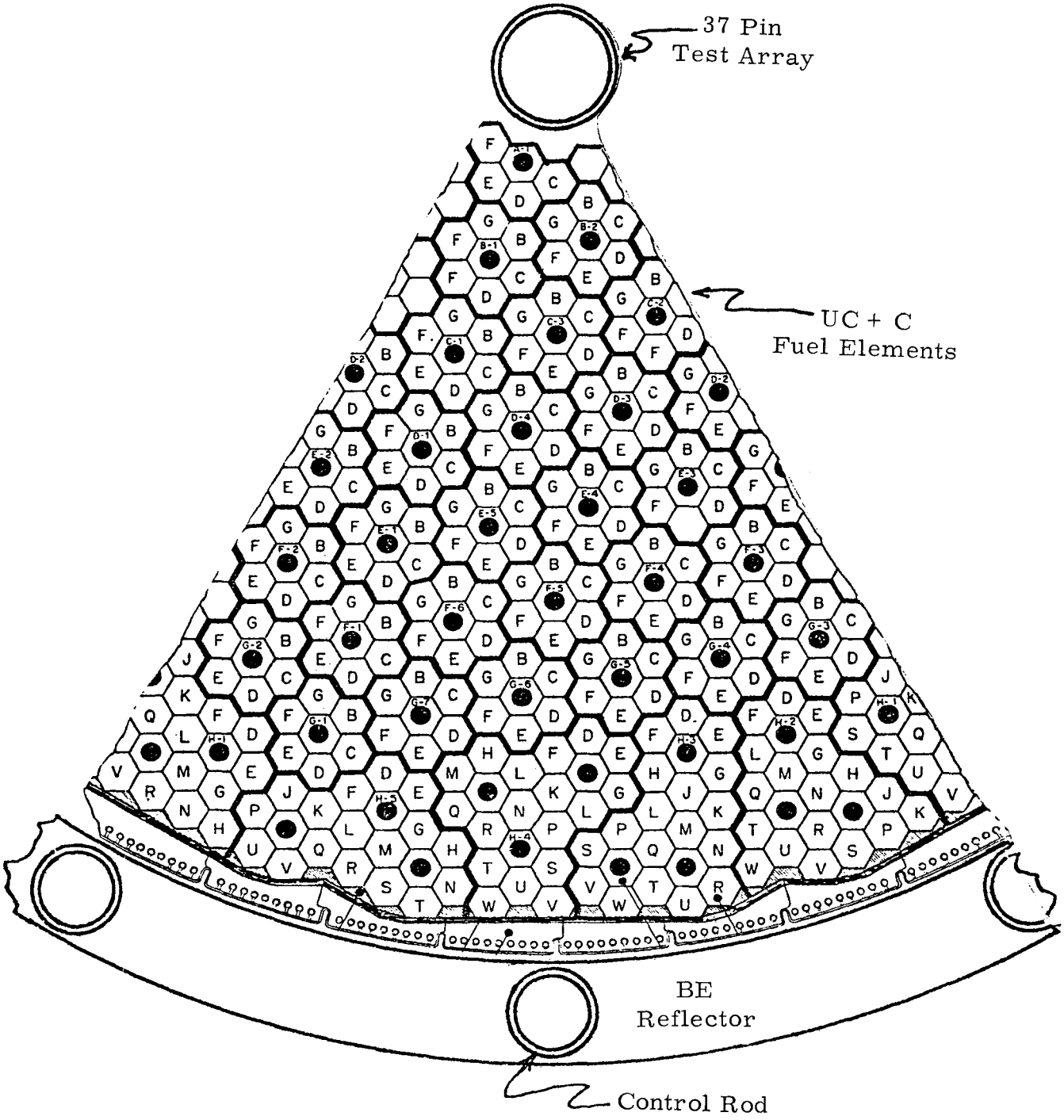

Fig. 1. PARKA Configuration

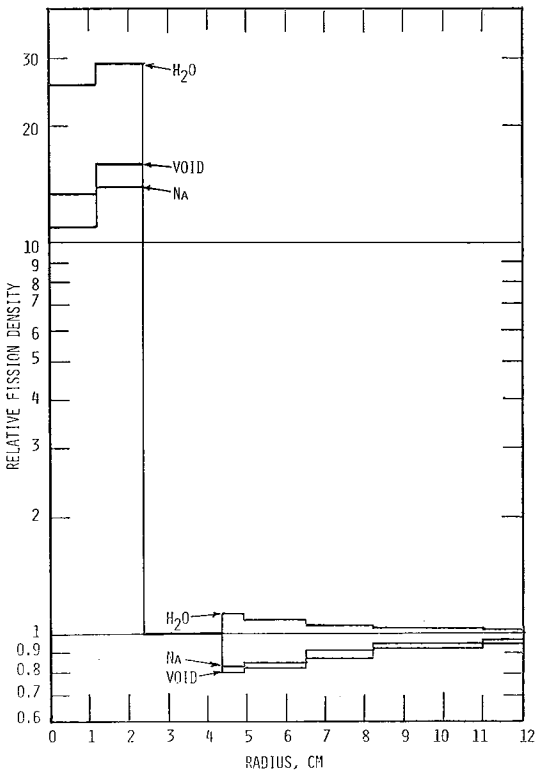

Fig. 2. Ratio of Modified to Unmodified Fission Density in PARKA

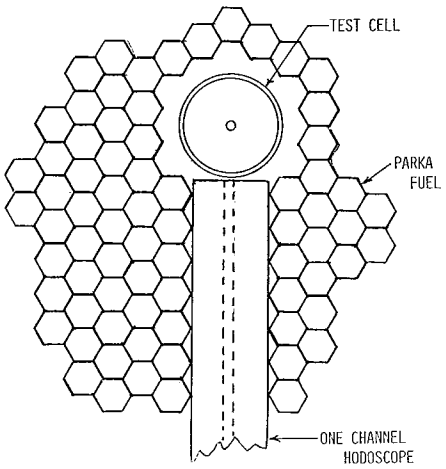

Fig. 3. Closeup of PARKA Modification at Central Plane

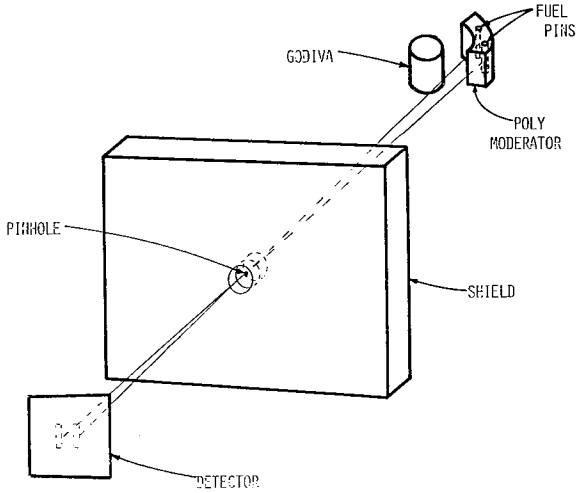

Fig. 4. Godiva Fuel Pin Driver Geometry

Evaluation of Instrumentation and the Development of Models by Pyrotechnic Methods*

by

P. W. Cooper, S. R. Kurowski, J. M. McKenzie
Sandia Laboratories
Albuquerque, New Mexico 87115

ABSTRACT

The simulation of fuel motion by pyrotechnic methods appears restricted to individual phenomena within an overall HCDA. But the possible range of experiments extends all the way from single fuel pins, through energetic disassembly of the core, to compaction of the core. We present our preliminary experiments to mimic the pressure pulse within the fuel resulting from a prompt critical power transient.

We also discuss:

1. The ease of instrumentation.
2. An iterative procedure for comparison and matching of explosive and neutronic fuel motion experiments to establish models and to check codes.
3. Investigation of neutronic fuel motion instrumentation without going to full scale neutronic experiments.
4. The cost advantages.

NOTE: Complete paper not available.

*This work supported by the U.S. Energy Research and Development Administration, ERDA.

A Possible Material Motion Simulation System

by

R. L. Brehm and D. A. Himes
University of Arizona
Tucson, Arizona

INTRODUCTION

Direct electrical heating (DEH) of oxide fuel has been used at several laboratories to simulate in-pile behavior of this material at high temperature under both steady-state and transient conditions. The DEH offers the advantages of being a relatively simple, inexpensive, non-radioactive means of investigating those aspects of the fuel behavior which are thermally rather than neutronically dominated. Because of the volumetric Joule heating, the radial temperature distribution can be made to approximate relatively closely the corresponding distribution obtained in-pile through fission heating. It is proposed here that this technique might be utilized to simulate fuel pin behavior during rapid transients and that these experiments might be of value in testing certain of the fuel motion diagnostic techniques proposed at this information exchange meeting.

A DEH apparatus is currently under construction at the University of Arizona for purposes of conducting UO_2 properties' measurements at temperatures up through and including the molten regime. As a possible future extension of this activity, we have examined the potential of modifying this apparatus in order to simulate fuel behavior under rapid transient conditions of the type being investigated in-pile at the Sandia Laboratory. The initial objective of this out-of-pile simulation would be to confirm that the simulation does, in fact, result in fuel behavior comparable to the in-pile behavior. If this turns out to be the case, then the simulation technique could be useful in expanding the scope of experimentation beyond that allowed technically or financially with the in-pile program. Perhaps

of more importance, these simulations could assist in the understanding of the in-pile experiments and in the analytical modeling of fuel behavior under rapid transient conditions. We should hasten to point out that at least two aspects of fuel behavior under rapid transient conditions do not presently appear capable of totally realistic simulation by the DEH method. First, those categories of experiments in which the steel cladding plays a significant role cannot be simulated without sacrificing some deviation from the geometry or materials of the actual fuel pins of interest. Use of quartz cladding or an electrically insulating coating on the inner surface of the steel cladding (e.g., boron nitride or alumina) are possible and have been used, but both of these can and do introduce differences from the actual pins which may be unacceptable for certain classes of experiments.

The second category of experimentation which the DEH technique is incapable of accurately simulating is somewhat more subtle and involves a knowledge of the behavior of the fission gas atoms generated within the UO_2 grains. Briefly, the gas effects can be only partially studied by DEH techniques since, under certain reactor conditions, the fission process itself may dominate the gas atom behavior (through the fission fragments). As a consequence of this, DEH experiments on pre-irradiated or gas-loaded pins should be viewed in the same context as DEH experiments in general: either confirmatory of in-pile behavior or as an aid to understanding and modeling.

The objective of this paper is to present a brief indication of the potential for simulating rapid transient experiments on a typical DEH apparatus. We have used, for this purpose, the specifications associated with our own equipment or equipment presently available to us, but this is

stoichiometry is used. No attempt has been made to consider fuel motion during the transient and, hence, the results presented here should be viewed only in the context of indicating the calculated power densities and temperature distributions prior to the loss of integrity of the specimen. For the millisecond time span of interest for oxide purposes, this is probably not a significant restriction, so that the calculated temperature rise rates and peak temperatures should be approximately correct.

As an example of these calculations, we have selected the results for a UO_2 specimen with nominal diameter of 0.635 cm (1/4 inch) and length of 3.81 cm (1-1/2 inch), O/M of 2.00, and 95% theoretical density. The initial radial temperature distribution was assumed (arbitrarily) equal to the steady-state value obtained from a constant 2 ampere current through the specimen.

Figure 2 shows the calculated average power density as a function of time for the discharge of a capacitance bank of 480 μf charged at the various voltage levels indicated. We note from these results that transient power profiles quite comparable to those anticipated in the in-pile tests can be obtained and that considerable flexibility in shaping the profile by initial voltage selection can be achieved. The dashed curves labeled 480 μf and 360 μf are simply connections of the points of peak power at the various voltages for the respective capacitance levels indicated and serve to demonstrate how the duration and magnitude of the power transient can be adjusted.

Figure 3 shows the transient power profiles for various levels of total capacitance at the fixed voltage of 4000 v. The 480 μf maximum capacitance and 60 μf increments shown correspond to the eight 60 μf

capacitors actually in our equipment inventory. These results indicate that the magnitude of the pulse can be conveniently incremented without changing significantly the duration of the pulse.

The largest energy transient considered was for the case of 480 μf capacitance at 6000 v (8.64 KJoules). The results for this case are shown in Figs. 4 through 6. Figure 4 shows the transient on a gross time scale covering 40 sec (even though the specimen would probably lose its integrity shortly after the power burst. An initial 2 amp current is applied at time zero with the specimen at a uniform temperature of 1000°K. Steady state is reached in about 7 sec. The capacitor switch is closed at 15 sec., and the center line temperature rises to over 5000°K in about 1.5 msec. The molten zone extends out to about half the fuel rod radius. Only surface and centerline temperatures are shown in Fig. 4.

Figure 5 shows an expansion of the time scale after the capacitor switch is closed. Volume averaged power density as well as temperatures at various radii are shown. The shape of the power curve is due to the slow-down in temperature rise (and, therefore, slowdown in increase of the total electrical conductivity) associated with onset of melting.

Figure 6 shows the time-varying temperature profile in the specimen. Times shown are after the capacitor switch is closed. Dashed lines are profiles during cooldown, again under the assumption that the physical integrity of the specimen has been maintained.

CONCLUSIONS

Calculations of the power and temperature transients obtainable on LMFBR prototypical diameter UO_2 fuel through capacitor discharge indicate that these transients can be tailored to simulate relatively closely the corresponding transients anticipated from in-pile rapid transient fission heating. The tailoring can be accomplished through a combination of the total discharge capacitance and the initial charging voltage.

This type of simulation could possibly provide a convenient means for checking out fuel motion or other fuel behavior diagnostics prior to their application to the in-pile situation. These possibilities have not yet been explored by us nor are we aware of any other DEH group working in this direction.

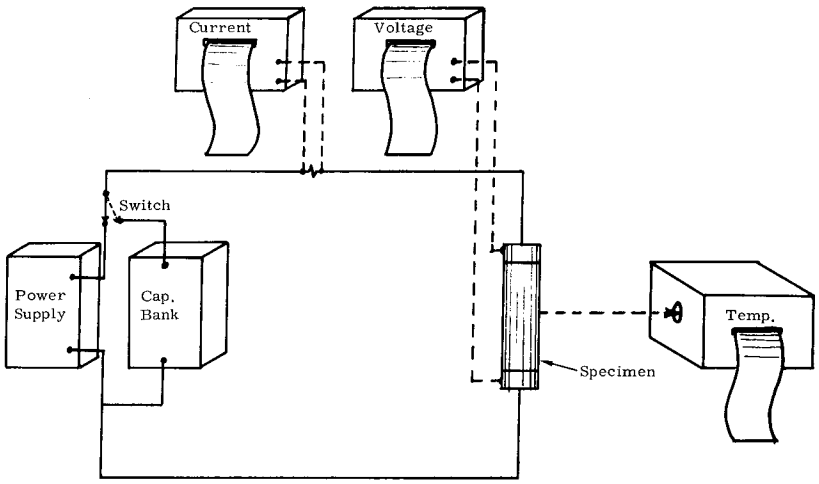

Fig. 1. General Experimental Arrangement

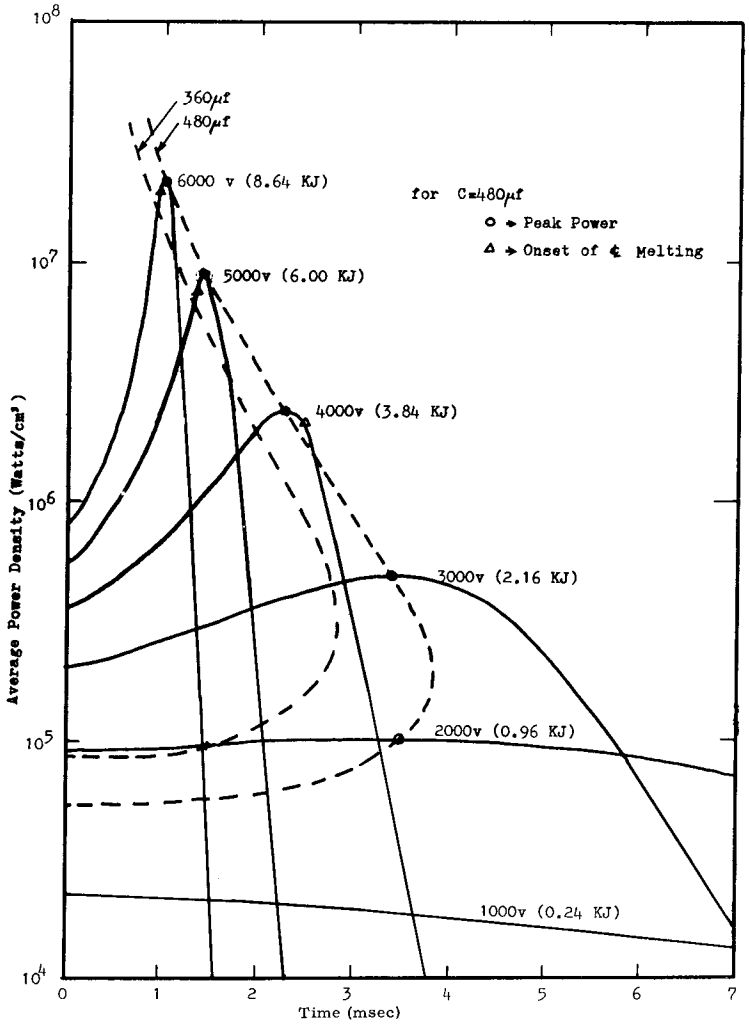

Fig. 2. Average Power Density vs Time

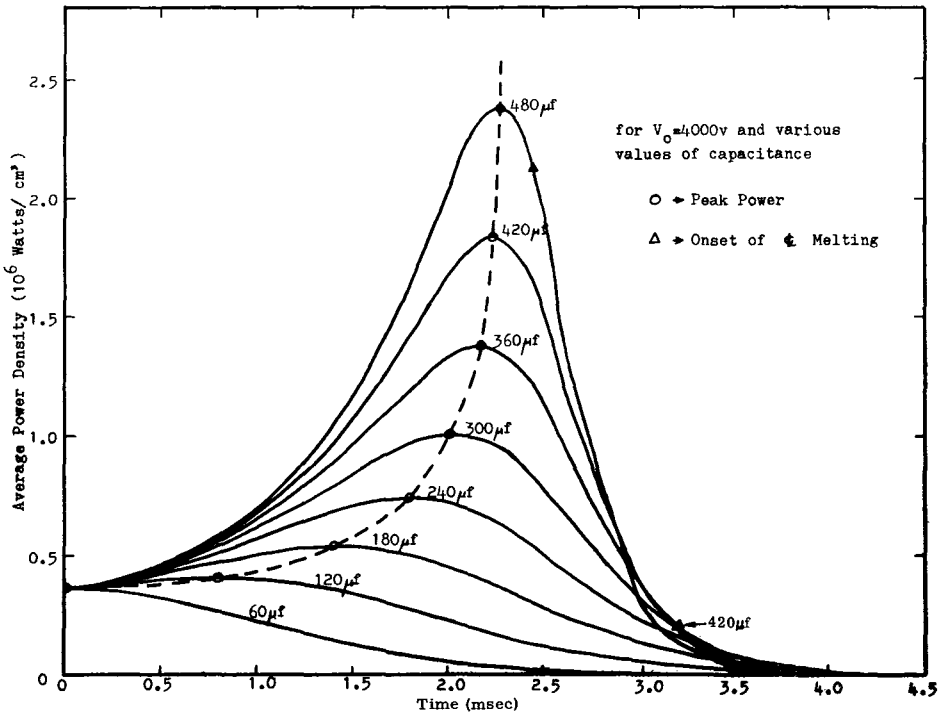

Fig. 3. Average Power Density vs Time

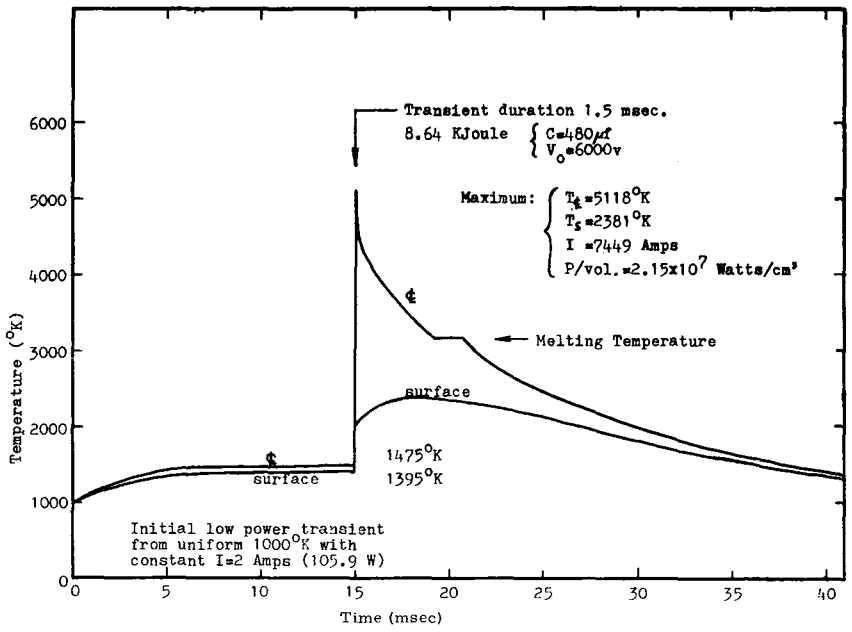

Figure 4. Centerline and Surface Temperature (T_s) vs Time

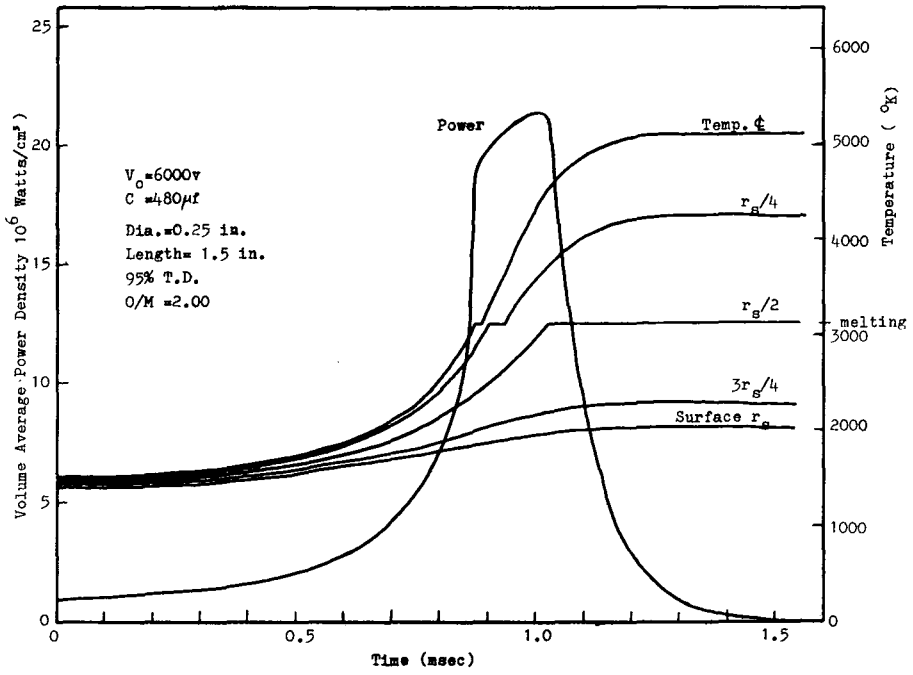

Fig. 5. Average Power Density and Temperature at Various Radii

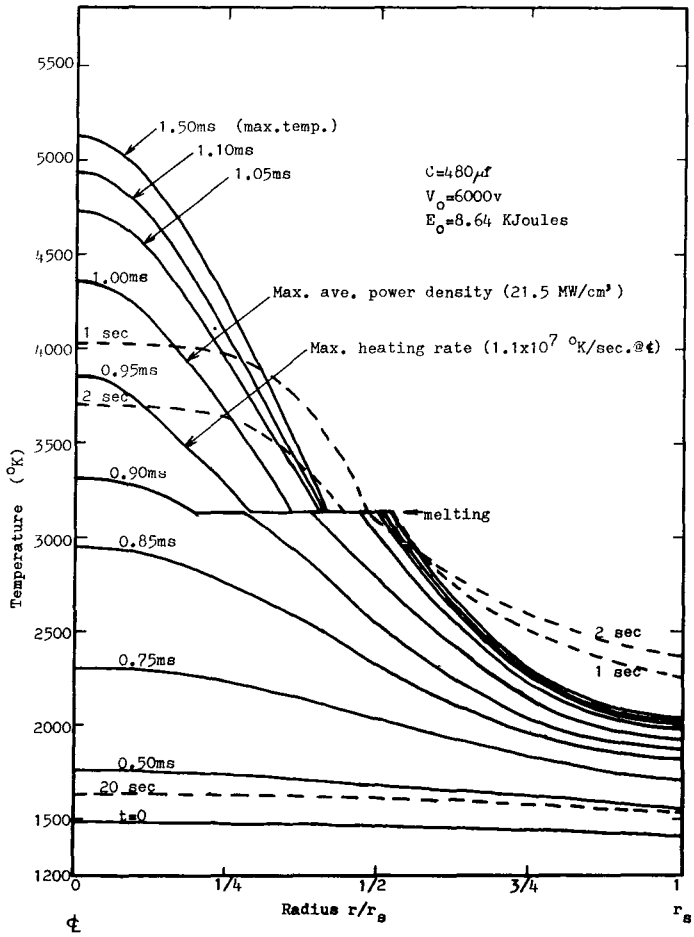

Fig. 6. Temperature Profiles vs Time

Analysis of In-Core Fuel Motion Detection*

by

F. Biggs and J. H. Renken

Sandia Laboratories
Albuquerque, New Mexico 87115

A plan has been devised for analyzing proposed experiments in which we hope to determine the motion of fuel rods in a reactor test cavity from measurements of neutron fluxes at points inside the cavity. The plan is organized into four phases that are successively more expensive in manpower and computer costs. A favorable result on any one of the first three phases justifies proceeding to the next phase.

Encouraging results from an analysis of small-fuel configurations of simple geometric design have led us to proceed to the second phase of the study. This phase is in progress and consists of detailed neutron transport calculations to determine if assumed fuel displacements of interest produce changes in the neutron fluxes at the detector locations that are significant compared to background levels. Preliminary results from this phase indicate that a detailed feasibility study in Phase 3 is justified for at least some of the experimental designs under consideration.

The third phase involves the use of adjoint transport calculations to obtain "importance" functions to be used in the error-analysis option of our UNFOLD[1] computer program so that the accuracy with which fuel motion can be unfolded from measurements during the initial part of the motion (near zero time) can be determined. An encouraging result from this effort would justify proceeding to the fourth phase which involves

*This work supported by the U. S. Energy Research and Development Administration.

numerical simulation studies. This last phase of the study would provide information on how long in time the data analysis can follow the fuel motion with satisfactory resolution. It is also an appropriate time to organize the analysis procedure for efficient use with the subsequent experiments. Let us now turn to a description of the Phase 3 analysis.

A neutron detector placed in the core of a reactor is more likely to be influenced by neutrons which are emitted close to the detector than by those emitted at some distant part of the core. The output signal $\hat{G}_i(t)$ of the i-th detector at time t is given by

$$\hat{G}_i(t) = \int \cdots \int \phi(\vec{r}, E, \vec{\Omega}, t) R_i(\vec{\Omega}, E)\, dP, \quad i = 1, \ldots, M , \qquad (1)$$

where ϕ is the neutron flux and R_i is the response of the i-th detector to neutrons of energy E that are moving in direction $\vec{\Omega}$. The differential dP denotes integration over the phase-space variables: position, energy, and direction. It is also possible to express $\hat{G}_i(t)$ as

$$\hat{G}_i(t) = \int \cdots \int I_i(\vec{r}, E, \vec{\Omega}, t)\, S(\vec{r}, E, t)\, dP, \quad i = 1, \ldots, M . \qquad (2)$$

Here S describes the variation of the neutron emission amplitude, and I is the importance, or sensitivity, function for the i-th detector. This function is a measure of the probability that a neutron emitted at a phase-space point denoted by the function's arguments will make its way to detector i and produce a response. It can be shown[2-4] by appropriate manipulation of the forward and adjoint transport equations that I_i is the adjoint flux which solves a well-defined adjoint transport problem. This fact provides a convenient method by which the necessary importance functions can be calculated.

The function S can be written as

$$S(\vec{r},\ E,\ t) = W(t)\psi(E)\rho(\vec{r},\ t)\ , \tag{3}$$

where W(t) gives the time dependence of the power excursion and is taken here to be the same at all positions in the reactor fuel. The neutron emission energy distribution $\psi(E)$ is assumed to be the same throughout the fuel; it is equal to the fission neutron spectrum. The function $\rho(r,\ t)$ gives the distribution of fuel mass at time t.

The time dependence here is assumed to be caused by the power excursion and the fuel motion versus time, and the time resolution of interest is ~milliseconds. The time-dependent processes involved in the neutron transport problem are much faster than this. Therefore, an adiabatic approximation in which the neutron transport is describable as a sequence of steady-state solutions is valid.

Now define

$$\Gamma_i(\vec{r},\ t) = \int \cdots \int I_i\ (\vec{r},\ E,\ \vec{\Omega},\ t)\psi\ (E)\ d\hat{P}\ ,\ i = 1,\ \ldots\ ,\ M \tag{4}$$

where the integration is carried out over all the phase space variables except the spatial ones to get

$$\hat{G}_i(t) = W(t)\iiint_V \Gamma_i(\vec{r},\ t)\rho(\vec{r},\ t)\ dx\ dy\ dz,\ i = 1,\ \ldots\ ,\ M \tag{5}$$

This remaining integration is over the volume V that contains the fuel.

The time dependence of the excursion W(t) is a dimensionless multiplier that has the value unity at t = 0, the start of the power excursion, and is expected to increase by more than two orders of magnitude during the excursion. There are several possibilities for determining W(t):

(1) Measure it from time-dependent quantities that are insensitive to test-specimen fuel motion, such as out-of-core neutron detectors,

(2) Calculate it from theory,

(3) Unfold it together with the fuel motion from the measurements,

(4) Some combination of (1) to (3).

It is convenient to rewrite Eq. (5) in a form suitable for any of these approaches.

$$G_i(t) = \iiint_V \Gamma_i(\vec{r}, t)\, Z(\vec{r}, t)\, dx\, dy\, dz, \quad i = 1, \ldots, M \ . \tag{6}$$

If W(t) is determined independently of the unfolding analysis, then we define

$$G_i(t) = \hat{G}_i(t)/W(t), \quad i = 1, \ldots, M \tag{7a}$$

and

$$Z(\vec{r}, t) = \rho(\vec{r}, t) \ . \tag{7b}$$

However, if W(t) is to be determined from the measurements, let

$$G_i(t) = \hat{G}_i(t), \quad i = 1, \ldots, M \tag{8a}$$

and

$$Z(\vec{r}, t) = \rho(\vec{r}, t)W(t) \ . \tag{8b}$$

We now focus our attention on Eq. (6). This is a Fredholm integral equation of the first kind in which the unknown fuel-mass distribution $Z(\vec{r}, t)$ is inside the integral. The $G_i(t)$ are provided by the measurements and the $\Gamma_i(\vec{r}, t)$ can be calculated from neutron transport theory. The phase-3 investigation includes, not only the method of solving Eq. (6) for the fuel-mass distribution $Z(\vec{r}, t)$, but also the analysis of what kind of resolution in space and in time that can be expected from the solution of the equation for the various proposed experiments.

We have available the computer programs for the study of this problem: the neutron transport codes for calculating the $\Gamma_i(\vec{r}, t)$ and updating it as fuel-motion changes the neutron emitting source configuration, and the data-analysis program UNFOLD[1] for doing the feasibility studies and for solving for the fuel-mass distribution $Z(\vec{r}, t)$ versus time. In terms of computer costs, the calculation of the $\Gamma_i(\vec{r}, t)$ is, by far, the most expensive. It also requires a significant effort in order to specify the changing geometric conditions.

We now turn to a brief description of the procedure used to analyze Eq. (6) with the UNFOLD program. In solving this integral equation, it is very important to include any "auxiliary" information that is available. This would include such a priori information as the fact that there can be no negative sources of neutrons or that the total fuel-mass in the volume V is constant. It could also include any information that becomes available

during the evolution of the fuel motion. For example, once a pattern of fuel motion develops an approximate extrapolation of the motion from one time interval to the next is useful. It may be desirable to constrain the fuel motion to a "smooth" pattern. Program UNFOLD has proven capability to solve the least squares problem (such as Eq. (11a)) subject to the condition that the "auxiliary" information be satisfied. It also calculates various statistical quantities that are useful in conducting feasibility studies.

One way to parameterize the distribution of fuel mass is to write

$$Z(\vec{r},\ t) = \sum_{j=1}^{N} C_j(t) D_j(\vec{r},\ t), \quad N \leq M \quad . \tag{9}$$

The basis functions $D_j(\vec{r},\ t)$ define spatial cells that are equal to the reciprocal of the volume of the cell if $\vec{r}$ falls inside the cell and equal to zero if $\vec{r}$ falls outside the j-th cell. The $C_j(t)$ is the mass of fuel in the j-th cell, so the product $C_j(t)\, D_j(\vec{r},\ t)$ is the mass of fuel per unit volume for the j-th cell. This is simply one representation out of many possibilities to describe the motion of the fuel. It will probably be necessary to change this form as the motion evolves. It may be convenient to use cells that move with the fuel, especially after some motion pattern develops or for "resolving" the problem after a tentative motion versus time has been obtained. These kinds of considerations would be addressed in Phase 4 of this study.

Substituting Eq. (9) into Eq. (6) gives

$$G_i(t) = \sum_{j=1}^{N} C_j(t) \iiint_V \Gamma_i(\vec{r},\ t)\, D_j(\vec{r},\ t)\, dx\, dy\, dz, \quad i = 1 \ldots, M \tag{10}$$

or

$$G_i(t) = \sum_{j=1}^{N} A_{ij}(t) C_j(t) , \quad i = 1, \ldots, M \tag{11a}$$

where

$$A_{ij}(t) = \iiint_V \Gamma_i(\vec{r}, t) D_j(\vec{r}, t)\, dx\, dy\, dz \quad . \tag{11b}$$

As stated here, the problem now is to solve Eq. (11a) for the solution vector $\vec{C}(t)$ (with elements $C_j(t)$) when the $G_i(t)$ are measured and the $A_{ij}(t)$ are calculated from Eq. (11b) using the $\Gamma_i(\vec{r}, t)$ as calculated by our neutron transport programs and the basis functions $D_j(\vec{r}, t)$. Whenever $N < M$ a least squares solution to the problem is used. Note that one run of the transport code to get a set of $\Gamma_i(\vec{r}, t)$ can be used for various sets of $D_j(\vec{r}, t)$. This will be an important consideration when we try various spatial cell sizes in the error-analysis operation of program UNFOLD to find a set that gives a satisfactory error tolerance.

In order to calculate the fuel motion during the first time step Δt, the values of $A_{ij}(0)$ are first used to calculate a set of $C_j(\Delta t)$ which specifies a new fuel distribution. This new fuel distribution is then used to determine new values of A_{ij} which apply to the average fuel configuration during this time step. This updated value of the matrix A is then used to calculate the second iteration of the solution vector $\vec{C}$. If this iterative procedure fails to converge, either the time interval Δt is decreased and/or the space-cell size is increased until convergence is obtained. A similar procedure is used in the subsequent time steps.

If the function W(t) is also being estimated from the measurements, the $C_j(\Delta t)$ are first set equal to $C_j(0)\omega$, and the best single multiplier ω

is determined. This value of ω then provides the first iteration to $W(\Delta t)/W(0)$. This time dependence is then divided out of the $G_i(\Delta t)$ and the procedure is continued as explained above.

Estimates of the errors ΔC_j in the C_j that correspond to the specified variances σ_i^2 of the measurement errors in G_i are provided by[1]

$$\Delta C_j = \sqrt{(Q^{-1})_{jj}} \tag{12a}$$

where

$$Q_{k\ell} = \sum_{i=1}^{M} \frac{A_{ik} A_{i\ell}}{\sigma_i^2} \tag{12b}$$

Note that the C_j depend on the parametrization $D_j(\vec{r}, t)$ and on the σ_i^2 but not on the $G_i(t)$. This permits us <u>a priori</u> to carry out feasibility studies on any specified experiment. For example, we can estimate the spatial resolution of a proposed experiment by determining the cell sizes that give acceptable values of ΔC_j. The resolution (cell sizes) may be different in different parts of V. In general, the ΔC_j decrease as the average size of the spatial cells increase.

REFERENCES

1. Frank Biggs and Don E. Amos, "Numerical Solutions of Integral Equations and Curve Fitting," SC-RR-71-0212, (Sept. 1971).

2. James H. Renken, "Use of Solutions to the Adjoint Transport Equation for the Evaluation of Radiation Shield Designs" SC-RR-70-98, (Jan. 1970).

3. B. Davison, Nuetron Transport Theory, Oxford (1957), Chapter III,

4. G. I. Bell and S. Glasstone, Nuclear Reactor Theory, Van Nostrand Reinhold Company, New York (1970), p. 252.

Accuracy of Fuel Motion Measurements Using In-Core Detectors*

by

S. A. Dupree

Theoretical Division
Sandia Laboratories
Albuquerque, New Mexico 87115

*This work supported by the U.S. Energy Research and Development Administration

Accuracy of Fuel Motion Measurements Using In-Core Detectors

An initial assessment has been made as to how accurately fuel motion can be measured with in-core detectors. A portion of this assessment has involved the calculation of the response of various detectors to fuel motion and the development of a formalism for correlating uncertainties in a neutron flux measurement to uncertainties in the fuel motion.

Initially, four idealized configurations were studied in one dimension. These configurations consisted of

1. A single fuel-pin test using ACPR
2. A seven fuel-pin test using ACPR
3. A full subassembly (271 pin) test using a Class I ANL-type SAREF
4. A full subassembly plus six partial subassemblies (~ 1000 pin) test using a Class III GE-type SAREF

It was assumed that melt would occur symmetrically at the center of the test fuel and that fuel would therefore disappear from the center of the geometry. For each case a series of calculations was performed in which detector responses were determined at several radial locations for the unperturbed core and for the core with various fractions of the fuel replaced with Na. This fuel loss was assumed to occur essentially instantaneously such that the power level in the remaining portion of the test fuel remained unchanged from that of the initial unperturbed condition.

Three types of detectors have been considered for the purpose of comparison:

1. An isotropic detector with a flat energy response
2. A 2π detector with a flat energy response, the active hemisphere being directed radially inward
3. An isotropic detector with a U^{238} fission cross section response

These responses are believed to be reasonable for representing a possible range of application for in-core detection.

Figure 1 shows the ratio of the detector response in the perturbed configuration to that in the unperturbed configuration, ϕ/ψ, vs the fraction of total test fuel mass which has disappeared, $\Delta m/m$, for the 1-pin experiment on the ACPR. Only isotropic U^{238} and flat-response detectors are shown. Radial positions vary from 0.56 to 4.5 cm from the center of the test pin. A steep negative slope indicates a sensitive response to fuel motion. Thus the detectors closest to the pin are the most sensitive to fuel motion. In addition, the U^{238} response detector is more sensitive to fuel motion than the flat response detector. This is due to the energy discrimination afforded by the U^{238} fission threshold. Note that at 20 percent fuel motion (i.e., 20 percent of the volume of the fuel in the pin has vaporized or otherwise disappeared from the calculation) the most sensitive detector signal has fallen about 6 percent below its unperturbed level.

Figure 2 shows the analogous results from the seven-pin ACPR experiment. Again, isotropic U^{238}-fission and flat-response detectors are assumed, and again the U^{238} detector is seen to be superior. Radial locations from 0.464 to 4.5 cm are shown, the 0.464 cm location being between the central pin and the surrounding six pins. Note that for the most sensitive detector in this 7-pin case, a 20 percent fuel loss results in a signal decrease slightly in excess of 10 percent.

For both of these hypothetical ACPR experiments it is apparent that all detectors shown will see a relatively high background neutron flux from

the driver core. This is inherent in a test such as this since the test fuel mass is necessarily small compared with the driver core, and its signal correspondingly so. Such a disparity between the signal and background can be minimized by placing the detectors close to the test fuel and by tailoring the experimental configuration in some way so as to shield the detector from the driver core. No attempt was made in the calculations performed here to minimize the background inside the test region and it is believed the present results can be improved without great expense.

The corresponding curves for a 2π flat-response detector have not been processed in time for this presentation. It is expected that such detectors will have responses similar to the isotropic U^{238} response shown here. Optimization of in-core detector schemes for use in an ACPR experiment of the present type will require additional studies on candidate detectors and on the tailoring of the geometry to reduce the background.

Figure 3 shows detector response curves for the full subassembly test in the Class I SAREF. Detector radial locations vary from 0.5 to 9.9 cm; i.e., from points deep within the pin matrix to points several cm outside the test hex. The value of placing detectors inside the fuel pin matrix is apparent from this figure. At 20 percent fuel loss the 0.5 cm U^{238} detector signal falls by over 30 percent while the signal for a U^{238} detector located outside the test hex falls by less than 3 percent at the same fuel loss. A 2π flat response detector located outside the test hex shows a signal decrease of about 4 percent under the same conditions.

Obviously the interpin U^{238} detector offers interesting possibilities for measuring fuel motion in large-scale tests. Conversely, in this full subassembly configuration, any detection system viewing the test core from the outside suffers from a severe lack of sensitivity to fuel motion.

Figure 4 shows a similar set of detector response curves for the Class III SAREF with a full test subassembly and six partial subassemblies. In this figure $\Delta m/m$ refers to the fraction of fuel lost from the central test hex only; no fuel loss is considered from the partial subassemblies.

As before, the interpin U^{238} detectors show far more sensitivity to fuel motion than do the others considered. The most sensitive detector shows about a 28 percent drop in signal for 20 percent fuel motion, which is very close to the result obtained for the Class I SAREF.

Having examined in-core detectors in one dimension, and having found somewhat favorable results, a series of two-dimensional calculations was undertaken to provide additional information. The two-dimensional analysis considered only the Class III SAREF with full test subassembly and six partial subassemblies in the test region. The unperturbed case and two perturbed configurations were examined. Normalization between configurations was based on the assumption that the power level in the test core remained unchanged.

Unlike the one-dimensional calculations, the two-dimensional studies require the use of an a priori model of the fuel motion. Without presuming to judge the merits of one model over another, a model which might be described as the "toothpaste tube" model was used for the present study. That is, the fuel was assumed to melt and vaporize at the center of the core, the vapor pressure rupturing the clad at the top of the active fuel region and forcing the molten fuel to squirt out at that point. Thus fuel is rapidly transported from the center to the top of the core and is distributed there within the coolant channels in some manner. For present purposes, fuel was assumed to be forced out of the inner seven layers of pins, to fill the coolant channels in the lower part of the upper axial blanket first and then begin

filling the upper part of the test core and the top of the upper axial blanket, depending on the amount of fuel being moved.

Detector responses to such fuel motion are included in Figure 5 which shows vertical transits at three different radii for U^{238} detectors when about 6.5 percent of the fuel mass of the central hex has moved. The initial and final fuel configurations assumed are shown diagramatically on the left; the detector responses are shown on the right. The maximum relative response occurs in the upper blanket region where the fuel is deposited. The meaning of the double peak in the detector responses in this region is unclear. It may not be physical but rather be the result of a numerical problem in the calculation.

Figure 6 shows the same data when about 12 percent of the core mass has moved. Again the largest proportional response occurs in the axial blanket with the most sensitive response being given by the detector located closest to the core axis. The profile of the displaced fuel is followed in general by the detectors; however, all sharp edges on the fuel density are blurred over, giving a greatly smoothed profile. One may conclude that pinpointing the location of the fuel motion and its density profile based on measurements such as these will be a difficult task; however, an axial resolution of about ±5 cm and a radial resolution of about ±0.5 cm should be possible.

These two-dimensional data can be put into a form similar to the one-dimensional results presented earlier. This has been done in Figure 7 in which the detector response vs $\Delta m/m$ is shown for various interpin detector locations. The abscissa here goes only to 12 percent but at this level the response of the most sensitive detector in the depletion region has dropped by about 40 percent from the unperturbed case. Correspondingly, the response of the most sensitive detector in the fuel deposition region has increased by about a factor of 5. Therefore the tentative conclusion that

in-core detection of fuel motion is a potentially viable scheme for multiple subassembly tests is supported by preliminary two-dimensional studies.

An approximate formalism has been developed for correlating detector response with fuel motion. It can be shown that a linear detector located at the center of the fuel depletion region in the two-dimensional model considered here, and measuring the neutron flux to an accuracy of ±10 percent, should be able to detect fuel losses on the order of 2 percent of the total central hex mass. At fuel-motion levels of 10 percent such a detector should be able to measure the motion quantitatively roughly to within a factor of 2. If n(independent) measurements of the flux in the vicinity of the fuel motion are correlated by an unfolding technique such as that described in the previous talk, this error should decrease as $1/\sqrt{n}$; i.e., 100 detectors should reduce the uncertainty in the measured mass of moving fuel from a factor of two to about ±20 percent. Larger fractional fuel motion should be measureable to correspondingly greater precision.

To summarize: accurate in-core detection of fuel motion in experiments involving a large number of pins appears at this state of the analysis to offer an improvement in sensitivity of fuel-motion detection compared with systems viewing the core from outside the test chamber, and thus to be viable from a theoretical point of view. The desirable attributes for such a detection scheme are:

1. High-energy response detectors
2. Detectors located within the fuel pin matrix at axial locations along the full length of the core, including the axial blankets
3. Additional detectors, possibly 2π , located outside the fuel assembly to correlate gross fuel motion particularly in case of loss of signal from interpin detectors following fuel melt.

Specific details of the candidate detectors will be presented in the next paper.

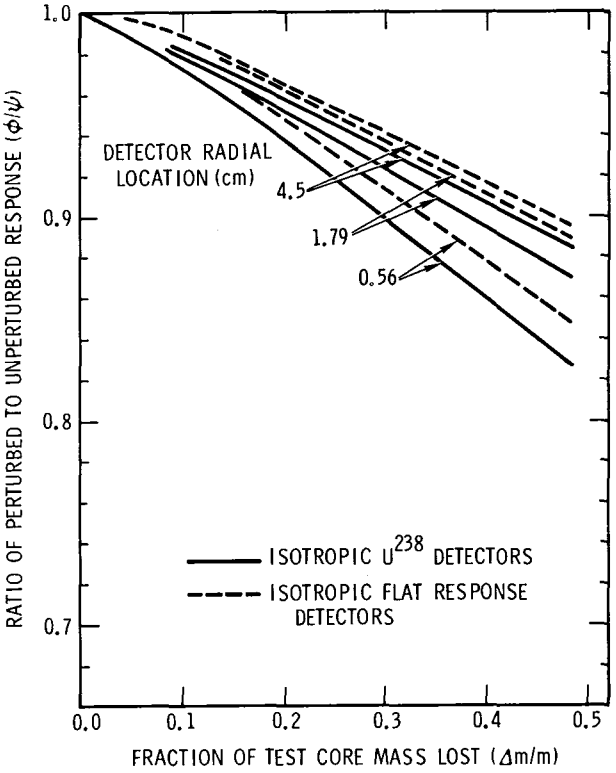

Figure 1. Detector Response to Fuel Motion in a One-Pin ACPR Experiment

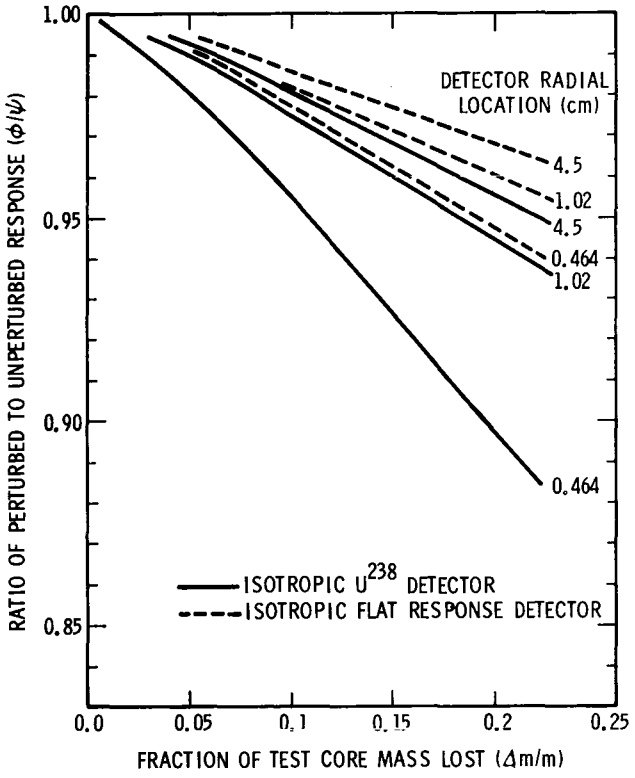

Figure 2. Detector Response to Fuel Motion in a 7-Pin ACPR Experiment

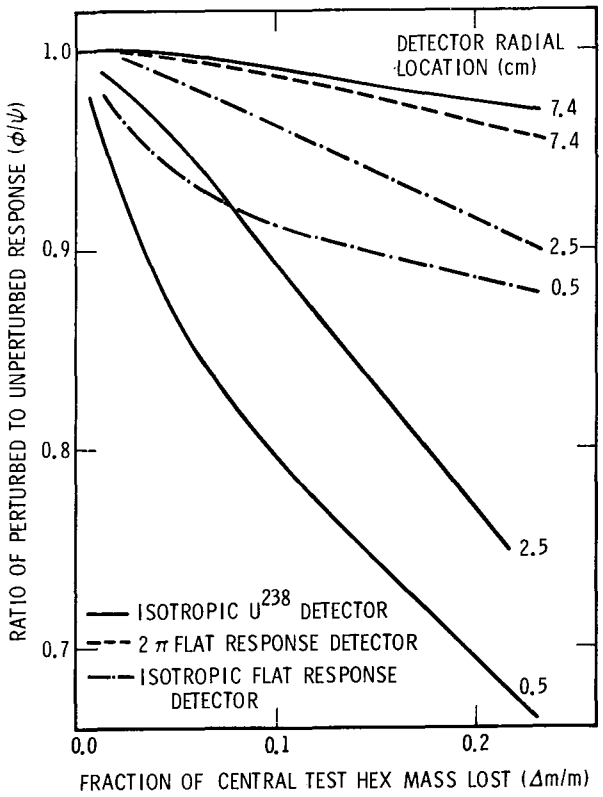

Figure 3. Detector Response to Fuel Motion in a Class I SAREF Reactor

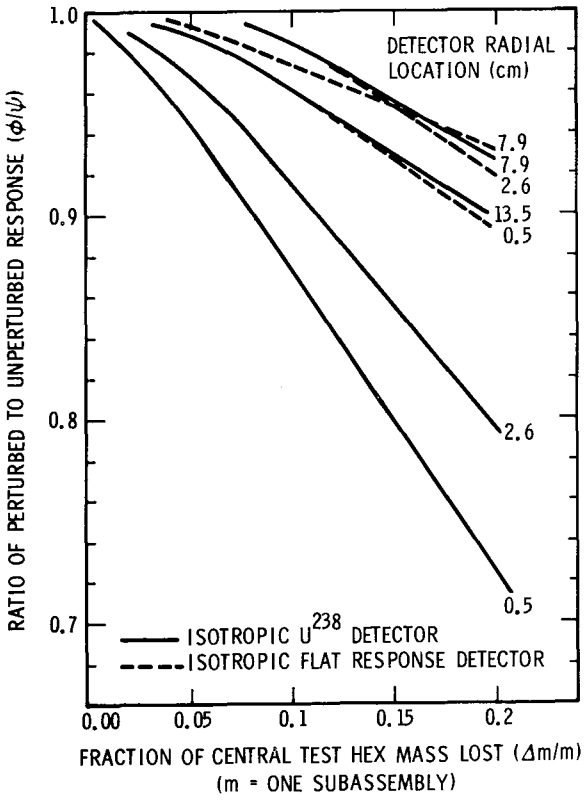

Figure 4. Detector Response to Fuel Motion in a Class III SAREF Reactor

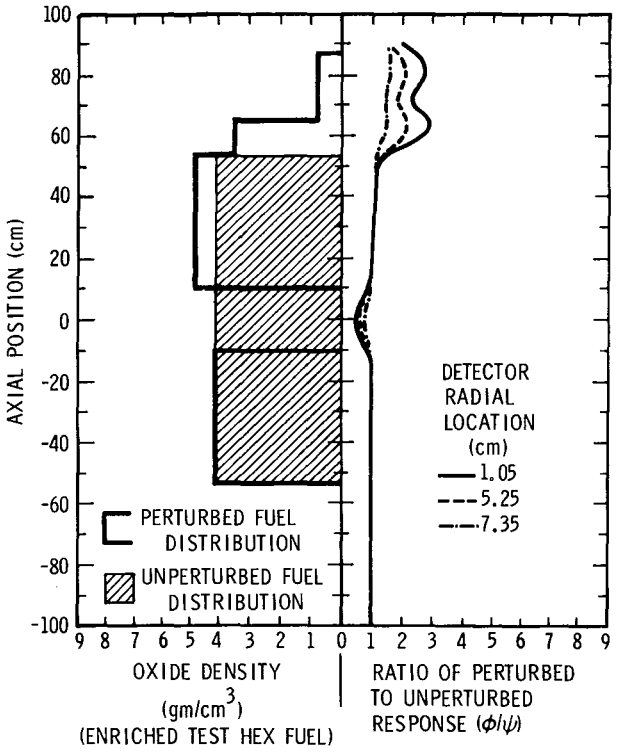

Figure 5. Detector Response to 6.48% Fuel Motion (Central Hex) in a Class III SAREF Reactor

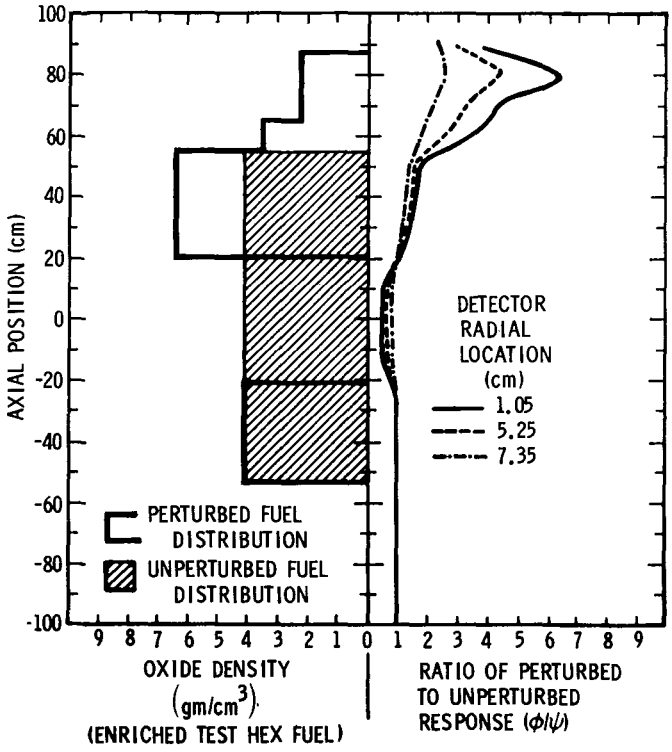

Figure 6. Detector Response to 12.25% Fuel Motion in a Class III SAREF Reactor

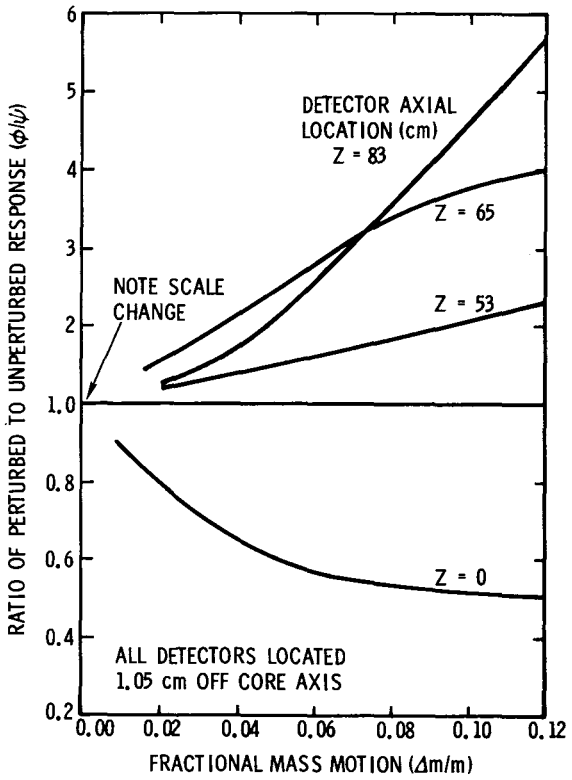

Figure 7. Detector Response to Fuel Motion in a Two-Dimensional Class III SAREF Reactor

Fuel Motion Measurements with In-Core Detectors*

by

L. R. Edwards

Sandia Laboratories
Albuquerque, New Mexico 87115

ABSTRACT

Two detection schemes which appear promising for in-core fuel motion monitoring in safety reactor facilities such as SAREF are described. The two types of detectors being considered are the diamond solid state ionization chamber and the fission couple. The pertinent physical properties of these detectors relative to their potential usage are discussed.

*This work supported by the U.S. Energy Research and Development Administration

I. Introduction

The analytical situation in regard to in-core fuel motion detection was presented by F. Biggs and J. H. Renken[1] and by S. A. Dupree.[2] As a sequel, this paper will be concerned with in-core detection systems that look qualitatively feasible. One of the advantages of the in-core concept is that the detectors are sampling a less sterile neutron flux than out-of-core detectors, where the neutron flux has interacted with the containment structure. The main problem associated with in-core detection is created by the high temperature, the high neutron and gamma fluxes, and the liquid metal coolant. Because of this hostile in-core environment severe constraints are imposed on both the selection of the type of detector and the selection of the detector materials.

It is clear from the analysis,[1,2] that the closer the detectors can be located to where the "action is" the better the accuracy to which fuel motion can be predicted. There are three different types of detectors which look feasible for in-core fuel motion studies in facilities such as the proposed SAREF reactor and Sandia's ACPR and SPR reactors. The first two types are the diamond detector and the fission chamber. These devices, although small, would have to be located radially just outside the test fuel pin bundle and on the axial blankets. The third type of detector, the fission couple, is extremely small and can be located inside the coolant channels within a test bundle. The discussion in this paper will focus only on the diamond detector and the fission couple. The fission chamber is a common detector and a description can be found elsewhere.[3]

II. Detector Properties

A. The Diamond Detector

For applications in a harsh environment, diamond appears to be the best candidate for use as a solid state ionization chamber. Many of the problems associated with diamond as a conduction counter have recently been solved.[4] The most recent work centers around the use of a diamond detector

in a reactor to measure the fission spectrum.[5] The results were very encouraging.

Some of the characteristics of diamond which are important for fuel motion detection are listed below.

Advantages

1. High temperature operation (∿600°C)
2. Small physical size (∿3 mm)
3. Fast response (∿ nsec)
4. Relatively insensitive to gammas (low Z)
5. Can be made sensitive to different types of radiation
6. Mechanically rugged
7. Can be used in corrosive media
8. Has above average resistance to neutron damage
9. Can be made directional

Disadvantages

1. Synthetic materials are not currently suitable (an adequate supply of suitable natural diamond exists)
2. Cannot simultaneously tailor both the energy response and the directional properties.

A schematic diagram of a diamond detector with directional properties is shown in Figure 1. The directional properties are achieved by the use of a forward scattering recoil mechanism, such as the proton recoil mechanism. For the active region a polyethylene film could be employed, or another section of diamond ion implanted with hydrogen or helium could be used. A diamond detector can either be operated in a pulse or a current mode. For the present types of applications where the flux levels and flux changes are very high, the current mode would probably be the most desirable.

Estimates of the carbon and proton recoil currents have made for a diamond with a volume ∿0.001 cm^3. The basic reaction rate equation and monoenergetic neutrons of energy 0.5 MeV were used in the calculations.

Sensitivities of 5 x 10^{-19} amp/unit flux and 2 x 10^{-18} amp/unit flux were obtained for the carbon and proton recoils, respectively. The directional response ratio is just the ratio of these sensitivities and is ∿4:1.

Currently, at Sandia, a research program has been initiated for developing diamond as an in-core detector. Procurement of high purity natural diamonds with nitrogen impurity concentrations less than 10^{20} nitrogen atoms/cm^3 has been no problem. Initial experiments have focused on charge injecting contacts. The preliminary results show that the counting rate does not saturate or deteriorate in time under α and β radiation. These results are consistent with the Russian work which demonstrates that the space charge polarization effects are virtually eliminated by use of appropriate charge injecting contacts. Future work will be directed toward neutron damage effects and ion implantation.

B. The Fission Couple

A fission couple is basically an intrinsic thermocouple with a junction that is comprized of some fissionable material. Sandia has had considerable experience in the design and development of these devices for neutron detection in reactor transient diagnostics and in underground tests at the NTS.[6] The important characteristics of fission couples are listed below.

Advantages

1. Extremely small size (∿0.75 mm)
2. Fast response (∿ μsec)
3. Adjustable energy response
4. High temperature operation (∿ 1000°C)
5. Can be used in corrosive media

Disadvantages

1. Intrinsically an integrating device
2. Cannot be made directional

The basic problem associated with the design of fission couples is the accounting of heat flux. The appropriate heat equations for these types of devices have been solved in detail.[6] The calculated time rate of change of the temperature as a function of neutron flux for various types of fissionable materials is shown in Figure 2. A considerable latitude in the choice of materials is available depending upon the applications. The fissionable material can be chosen to tailor the energy response, however, the maximum temperature extreme should not exceed the material's phase transition temperature. The observed linear relation here is important for simplifying the calibration.

In Figure 3 actual test results for a fission couple detection in Sandia's SPR reactor are shown.[7] The raw fission couple output is depicted by the open circle data points. Differentiation of the fission couple output yields the profile of the neutron flux pulse. The triangular data points for the fission couple compare very well with the photodiode response (solid curve). These results show that fission couples are sensitive and responsive devices for neutron detection.

III. Discussion

Intercomparing the various types of detectors show that each of them have individual advantages. In comparing the physical size, for example, the fission couples are extremely small and can be located directly in the liquid sodium coolant channels within the test fuel bundle; while the diamond detectors or the fission chamber detectors would have to be located outside of the fuel bundle. In considering the basic electrical properties the fission couple and the fission chamber have a common advantage in that the energy response can somewhat be tailored by the choice of fissionable material; and, on the other hand, the diamond detector can be made directionally responsive. In the overall design of a fuel motion diagnostic system, it may be advantageous to use combinations of these detectors in a complementary fashion.

Some of the following observations are based on the analytical studies.[2] For multiple subassembly tests a series of diamond detectors located radially on the outside of the test bundle and on the axial blanket would be effective in measuring gross fuel motions. This is because the neutrons originating from the central pin region are attenuated as they pass through many layers of fuel pins. Fission couples, on the other hand, located within the test bundle can detect fuel motion involving a few percent of the mass of the total test fuel. When melting occurs the fission couples would probably be destroyed, however, this is useful information for the unfolding analysis in that fiducial points are established. For times beyond which the fission couples exist, complementary detectors on the outside of the fuel bundle may be necessary.

In the case of small scale tests for 1-7 pins, diamond detectors may be feasible. Because the neutron signal from a few test pins is small compared to the background from the driver core collimination may be necessary. The analytical studies show, however, that a 2Π detector such as diamond would have a distinct advantage over 4Π detectors.

Obviously, further development work will be necessary for these in-core detection schemes. The previous conclusions are necessarily qualitative because the calculations are somewhat crude and because of the lack of adequate detector calibration data. Since these detectors would be operating in integrating modes, the accuracy of the calibrations will be of paramount importance. In any program to develop these schemes, the development of calibration techniques will play a major role.

Questions concerning the ability of detector materials to survive long term radiation exposure and very high fluxes need more detailed answers than are currently available. In the case of the fission couple, fission product buildup needs further study, along with determining useful detector life times.

Preliminary calculations for example, indicate that a U^{238} fission couple should survive a several months exposure to a flux of 10^{15} n/cm^2-sec, however, this effect needs to be quantified. In the case of the diamond

detector, radiation damage studies are incomplete for diamond. In particular, additional research is needed to determine the maximum neutron damage tolerance along with the temperature annealing mechanisms. These types of studies are being initiated on diamond.

As far as fabrication techniques are concerned, it is not anticipated that any new major technological developments will be required. In the case of the diamond detector, ion implantation studies will be needed; however, the technology of ion implantation is well established. For the fission couples electrical leads will probably pose some problems. Currently 0.010 in. O.D. stainless steel sheathed cable looks quite promising.

In summary, the types of detectors discussed here appear to be qualitatively feasible for in-core fuel motion diagnostics. In order to bring these detectors into reality, additional research and development will be needed.

REFERENCES

1. F. Biggs and J. H. Renken, Transactions of the Conference on Reactor Fuel and Clad Motion Diagnostics, Sandia Report (1975).

2. S. A. Dupree, ibid.

3. J. M. McKenzie, Nucleonics 17 (1959) 60.

4. S. J. Kozlov, R. Stuck, M. Hage-Ali, and P. Siffert, IEEE Trans. Nucl. Sci. NS-22, (1975) 160.

5. S. J. Kozlov, E. A. Konorova, A. L. Barinov, and V. P. Jarkov, ibid, p. 171.

6. T. S. Dahlstrom, J. A. Michael, E. L. Noon and H. A. Lamonds, "Final Report on the Sandia Intrinsic Thermocouple Developmental Program," Sandia Order No. ASB-59-0077 (1966).

7. L. D. Posey, private communication

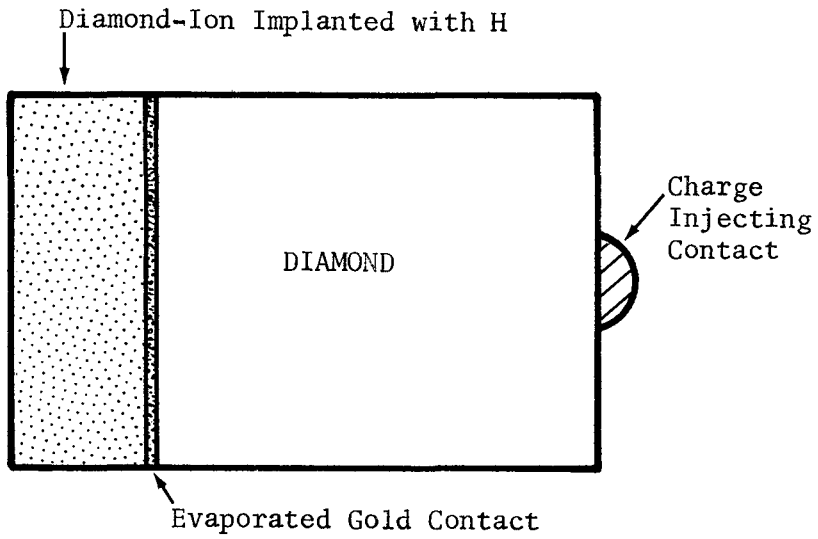

Figure 1. A Diamond detector with intrinsic vector properties

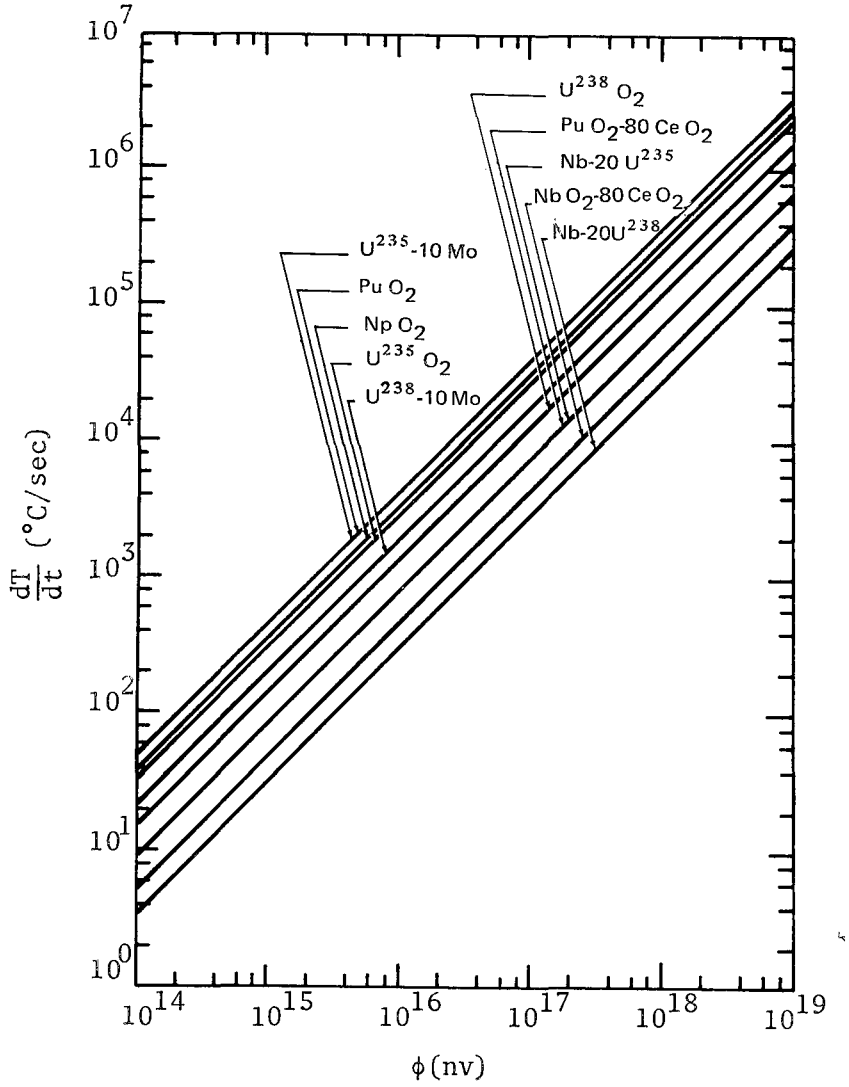

Figure 2. The time dependent temperature change as a function of neutron fluence for different fission couple junction materials.

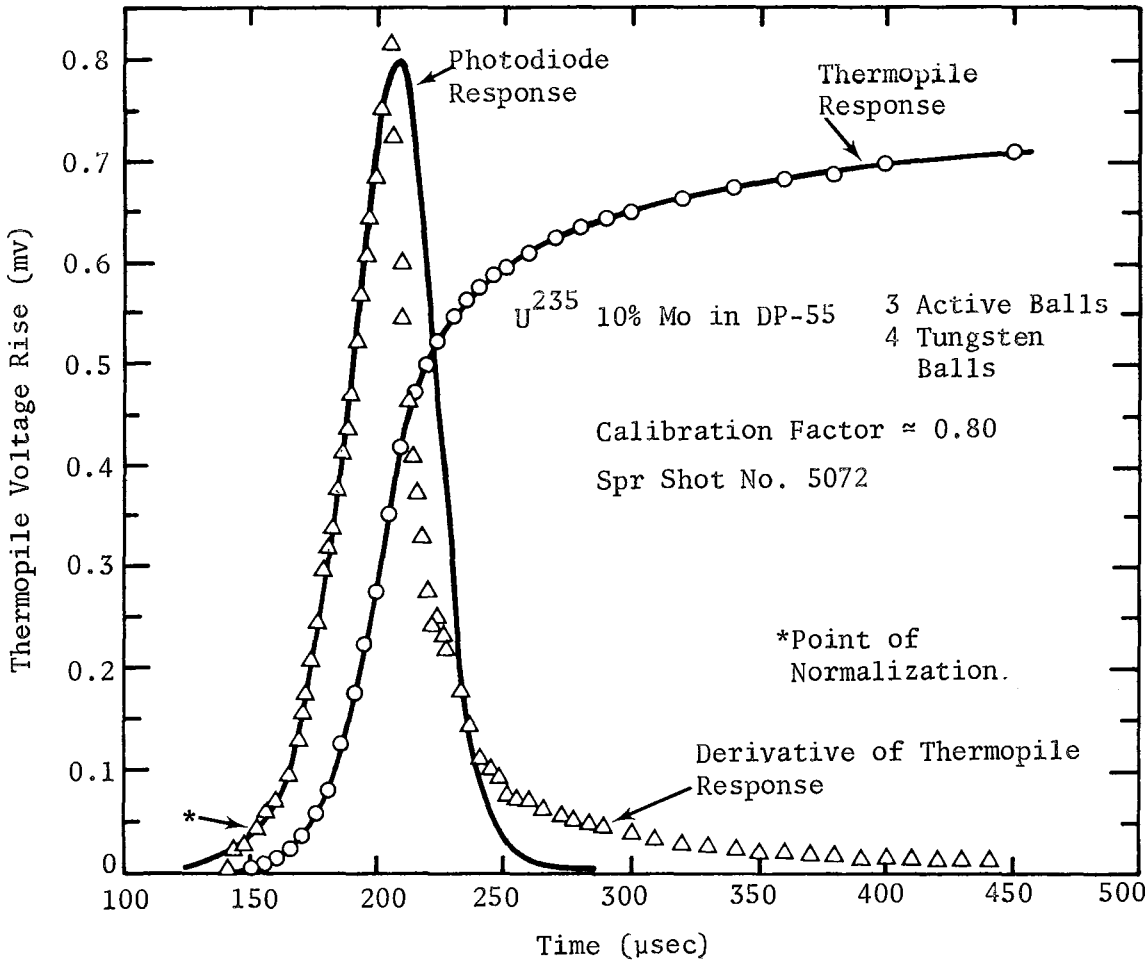

Figure 3. A typical fission couple response in Sandia SPR reactor. Courtesy of L. D. Posey.

Development of An In-Core Directional Fuel Motion Monitor*

by

S. A. Cox, R. A. Beyerlein, and F. E. LeVert

Applied Physics Division
Argonne National Laboratory
Argonne, Illinois 60439

A program has been undertaken at ANL to develop in-core instrumentation for fuel motion monitoring in connection with the Sodium Loop Safety Facility (SLSF) tests. Since the SLSF fuel bundle is to be inserted into a test hole in the Engineering Test Reactor (ETR), any monitor must be able to observe changes in flux from the fuel bundle in the presence of a large background flux from the ETR. A detector with directional sensitivity would enhance the signal from the fuel bundle. A detector with a threshold type behavior is also desirable in order to discriminate against the soft components of the neutron and gamma ray flux of the ETR. Current effort is concentrated in investigating the characteristics of two types of detector. The two detector types include a neutron detector which utilizes a hydrogenous layer as a proton recoil radiator, and a gamma ray detector which utilizes a thin lead layer to take advantage of the Z^5 dependence of the photoelectric effect. Z is the atomic number of the electrode material.

One of the models of the proton recoil type detector under study consists of three flat plates in an evacuated chamber. A 20-mil polyethylene radiator is attached to one side of the center electrode. Proton recoils from the radiator provide directional sensitivity through the $\cos(\theta)$ dependence of the (n, p) scattering cross section. Measurements to date have been made in the graphite pit of the Argonne Thermal Source Reactor (ATSR). A vertical

* This work supported by the U. S. Energy Research and Development Administration

strip of ^{235}U serves to convert the thermal neutrons into fast fission neutrons and fission gamma rays. The converter is thus a good simulation of a fuel bundle in the ETR. The detector is sensitive to the movement of the ^{235}U strip and shows a substantial amount of directional discrimination. The signal from the fission strip amounts to approximately 20% of the background signal from the ATSR thermal neutron flux and gamma-ray flux.

The gamma ray detector is also an evacuation detector. Within the vacuum container is a cylindrical stainless steel electrode which surrounds a flat plate electrode. The flat plate electrode consists of a plate of graphite bonded to a layer of lead. In one of the models the graphite plate is 1/8 inch thick and the lead layer is 0.020 inches thick. Because of the Z^5 dependence of the photo-electric effect the lead layer is much more efficient in producing photo-electrons than the graphite layer. As a result of the asymmetry the detector has a high degree of directional sensitivity. Because the compton cross section varies as Z and the range of the electrons produced varies as 1/Z the detector is highly compton compensated. Since the photo-electric cross section varies as Z^5 and the electron range varies as 1/Z the photo-electron current produced at a surface of the flat plate electrode should vary as Z^4. Since Z is 6 for graphite and 82 for lead the photo-electron current at the lead surface for a given gamma-ray flux should be approximately 35,000 times the photo-electron current at the graphite surface when the graphite is exposed at the same gamma-ray flux. Thus the photo-electron current from the graphite is negligible compared with the photo-electron current from the lead. At first it was expected that the largest induced current in the central flat plate electrode would occur with the electrode oriented so that the lead side of the electrode faced away from the gamma source. In this orientation some of the photo-electrons produced in the lead layer by the incident gamma rays would have sufficient range to escape and thus induce a positive current in the central electrode. In the orientation with the lead side facing toward the gamma source the photo-electrons produced in the lead would be trapped in the

graphite and no net current would result. However there is another process by which photo-electrons can be produced. This is a photo-electric interaction which occurs after the incident gamma ray has been compton scattered. Some of the incident gamma rays are backscattered in the graphite by the compton process. In the orientation with the lead side of the central electrode facing away from the gamma source these backscattered gamma rays interact only with graphite which has a very small photo-electric cross section and only a very small photo-electric current would be produced. In the orientation with the lead side facing toward the gamma source the backscattered gamma rays must pass through the lead layer where the photo-electric interaction is greatly enhanced because the energy of the backscattered gamma ray is much lower than the energy of the primary gamma ray. For 180-degree scattering the maximum energy of the scattered gamma ray is 0.256 MeV. For example, for an incident gamma-ray energy of 2 MeV the photo-electric cross section is 1.8 barns/atom; whereas the backscattered gamma ray with an energy of 0.227 MeV is subject to a photo-electric cross section of 250 barns/atom.

A detailed, if somewhat approximate, calculation which takes into consideration all of the cross sections involved, the relative intensity of the backscattered gamma rays, and the ranges of the photo-electrons produced does in fact predict that the photo-electron current produced by the backscattering is much larger than the current produced by the primary process. Measurements made using a 1 curie radium source confirm these conclusions. In the orientation with the lead side of the central electrode facing toward the radium source the inducted current is 20 times the current induced when the electrode is oriented with the lead side facing away from the source.

So far measurements of the detector performance have been made either in the ATSR or at the gamma irradiation facility. Both facilities are rather low-flux facilities and as such are not suitable for measuring the effect on the detector performance of a high-radiation field or an

elevated temperature. Experiments are scheduled in the Argonne Research Reactor (CP-5) to investigate these effects. The electrode structure for the detectors to be used in CP-5 must be modified from the detectors used in the ATSR to withstand the gamma heating which is present near the core region of CP-5. Measurements indicate that the gamma heating amounts to approximately 1/2 watt per gram in the heavy water region just outside the core. Two detectors will be placed in this region and measurements made as the detectors are rotated to confirm their directional sensitivity in the presence of intense gamma radiation and at a temperature in the vicinity of 100 degrees centigrade. One detector of the hydrogenous-radiator type and one of the lead-graphite type will be tested in this manner.

Preliminary Material Motion Assessment for SAREF*

by

D. Rose

Reactor Analysis and Safety Division
Argonne National Laboratory
Argonne, Illinois 60439

ABSTRACT

A description is provided of the basis for a comprehensive assessment of material motion for experiments in the Safety Research Experiment Facility (SAREF) that is being carried out, in which the projected capabilities of several instrumentation systems are to be compared against the requirements established by the desired experimental information. Preliminary requirements for fuel motion monitoring criteria are related to meaningful requirements for experiment interpretation and to analysis of postulated accidents. Preliminary projected capabilities are presented that focus on the initial emphasis of fuel motion assessment for the largest tests, particularly with respect to whether in-core detectors can achieve the desired capability, or whether devices requiring slots within the reactor core are essential. The conclusion from this initial effort is that a reasonable basis exists for expecting the hodoscope to satisfy the criteria for fuel-motion monitoring for these experiments in SAREF, while in-core detectors are likely to fall substantially short of meeting the requirement.

*This work supported by the U.S. Energy Research and Development Administration

Introduction

A comprehensive assessment of material motion for experiments in the Safety Research Experiment Facility (SAREF) is being carried out, in which the projected capabilities of several instrumentation systems are to be compared against the requirements established by the desired experimental information. The preliminary assessment thus far has focused largely on the monitoring of fuel motion. A description is provided of the basis for this assessment and of some preliminary results obtained to date. First, it may be appropriate to present briefly some background information on SAREF and on the safety experiments planned in the facility, particularly as they may impact diagnostic requirements.

The SAREF design concepts are motivated by the need to provide an in-pile testing capability for the LMFBR safety program beyond the range of available or firmly planned facilities. Under ERDA sponsorship, two conceptual design studies are nearing completion, one by Argonne National Laboratory and the other by General Electric Company. The ANL design concept, categorized as Class I, is capable of generating power bursts or time shaped transients without the need for significant heat removal during the test. The GE design concept, categorized as Class III, is capable of long-term steady-state operation and of superposing certain transients during the test. Although differing views may exist as to the key experiments each facility should be designed to perform, both are required to test fuel arrays up to full subassembly size and larger, with flat power distributions, and rated power test fuel operation for at least 30 sec or, alternatively, decay power levels for longer periods. Both facility designs provide a fast-flux spectrum reasonably prototypic of LMFBRs over the full test assembly. The following brief design description will be limited primarily to the ANL design concept.

The ANL SAREF reactor, which is helium cooled, is contained in a prestressed concrete reactor vessel. Figure 1 is a vertical cross section through the PCRV. The reactor has a central test hole surrounded by a neutron spectrum hardening zone, the converter, and an outer thermal driver zone.

The converter provides a neutron spectrum transition region to harden the spectrum in the experiment region and provide the very flat max/min power profile requirements for the experiments. One of three slots through the PCRV for fuel motion monitoring is seen in this figure. The three slots have a relative orientation of 0°, 90°, and 180° and allow full core height viewing.

The experiment test zone is defined by an experiment containment tube which separates the reactor environment from the experiment and within which an experiment test vehicle is inserted. The experiment containment tube is removable as is the converter region to accommodate different size test assemblies. Three different test assembly sizes are now contemplated - partial subassemblies (or small bundles, SB), single subassemblies, SS, and multisubassemblies, MS.

Figure 2 shows a schematic cross section through the core and test section in which the three viewing slots for fuel motion monitoring are seen. Provision is made to use any two of the three slots in any given experiment, and removable fuel boxes would be provided for, within the reactor core, both to provide this flexibility and to minimize the material interposed in the path of detectors which require slotted access. It is likewise important to minimize the amount of material, particularly steel, immediately surrounding the test fuel bundles.

Figure 3 shows a schematic of a test loop for a small bundle experiment as well as a cross section through the test assembly with 37 fuel pins. The space between the experiment containment tube and the outside of the test vehicle provides an annular region in which in-core detectors could be located. This provision is typical for all three sizes of test assemblies.

Figure 4 shows a test vehicle schematic in which a multisubassembly test is represented. A similar test vehicle, smaller in diameter, would accommodate a single subassembly test vehicle. Cross sections through such a single subassembly test section with 271 pins and a multisubassembly test

section are shown in Figure 5. The multisubassembly test section represented here consists of a full central subassembly of 271 pins surrounded by six approximately-half subassemblies.

To provide one additional perspective, the classes of experiments which we anticipate would be performed in the ANL-designed SAREF are listed in Figure 6.

Basis for Assessment

Returning to the main topic, it is desired to provide diagnostic capability for monitoring of all three significant materials included within typical test sections, i.e., fuel, cladding, and coolant. Monitoring is desired of material motion during transients and of quasistatic changes during nontransient conditions immediately prior to or just after a transient. To accomplish this, a wide spectrum of techniques is being considered, most of which have been the subject of papers presented at this meeting. Indeed, since the lead time required before such a major facility as SAREF becomes operational is quite long, it would be remiss not to explore new avenues for improved techniques. Thus, in evaluating the capabilities of candidate instrumentation systems, a reasonable projection of future developments should be taken into consideration. Insofar as possible, the facility design must include the flexibility to ultimately accommodate the spectrum of diagnostic techniques.

The disgnostic techniques under consideration can be placed in two categories, depending on whether or not slotted access through the core to the test section is required, and distinguished simply as in-core or ex-core detection. The ex-core detector systems can be further categorized as:

- Collimated detection systems, such as the hodoscope, which monitor induced radiation, both fast neutron and gamma, by means of detectors situated ex-core.

- Transmission schemes which require an external source (such as high-energy X-rays from an electron acceleration) and make use of penetration characteristics measured by an ex-core opto-electronic system after transmission through the test section.

- Coded aperatures, with which fission-induced neutron or gamma rays are monitored by ex-core psuedo-optical techniques, such as fresnel zone plates or pin holes.

To establish a reasonable basis for comparing the capabilities of candidate instrumentation systems with the requirements, a set of material monitoring criteria was formulated. The principal criteria established for the monitoring of fuel motion are shown in Figure 7.

A format for the intercomparison between requirements and projected capabilities was established in which the requirements are related to the three characteristic sizes of tests anticipated, namely, SB, SS, and MS test configurations. As will be seen later, there are other, nonarbitrary reasons for this categorization. We have also chosen to define three levels of requirements for each of the criteria being explored, as follows:

Necessary -- a requirement level which, if not achieved, means that the experiment probably should not be performed. This is a minimum requirement.

Acceptable -- the level of information which provides adequate data in conducting the experiment. Below this level, the value of the experiment becomes increasingly compromised. Every effort should be made to meet this requirement level.

Desirable -- a high information level which allows for optimal data recovery and possible furture improvements in analytical capability. This is a goal or ideal requirement.

It should be emphasized that these criteria are viewed from the narrow perspective of material motion monitoring requirements. Clearly other criteria enter into any composite evaluation of the desirability of performing specific experiments and whose importance could outweigh judgments reached on material monitoring alone.

Considerations that entered into establishing the criteria shown in Figure 7 are summaried below:

1. An overall field of view large enough to encompass the potential regions of interest during and after the experiment is required. For example, a multisubassembly test (consisting of a full single subassembly surrounded by a ring of six half-section subassemblies) requires a width and depth of ∿30 cm, at the desirable level. The total fuel height for prototypic FBR fuel elements is ∿100 cm, and it would be desirable to monitor the fuel motion of the order of a meter above and below the original core height. (These and corresponding values for SS and SB tests at all three levels are shown under "Requirements" on Table 1.)

2. The tests require material monitoring within

   (a) a certain resolution - i.e., the monitoring device must have a certain resolving power, and

   (b) a certain field of view or region inside which the resolution criteria can be met.

3. Resolution, average density, and time interval requirements are all interrelated and are keyed to a range of accident conditions.

Spatial resolution is set first, since there are practical limits on the size of regions in a finite element or finite difference model of the test region. These limits, based upon current analytical models and allowing for improvement, are 5 cm axially and 2-1/2 cm radially. The resulting ∿8000 regions, for MS tests, would certainly be an upper bound with ∿350 regions being a reasonable number. (These and corresponding values for SS and SB tests are shown under "Requirements" on Table 2.)

4. The time intervals can be separated into resolution and total intervals similar to field of view. Different time resolution will be required for different phases of the experiments. The near steady-state (i.e., preheat or nontransient) phase of a test will only require a coarse time monitoring of material location. The transient part, involving a heating of the test section but without rapid power bursts or material eructations, requires a finer time monitoring. The bursts require the shortest time resolution. The total time interval requirements, shown in Table 3, are readily set.

5. The requirement for monitoring material density changes in a region can be related to:

    (a) changes in reactivity affecting the course of an accident, and

    (b) the blocking or unblocking of coolant channels within fuel pin structure through solidification or remelting of materials.

The criterion for monitoring rates of change of region-averaged material densities (such as changes in fuel, coolant, clad or structure) is that the monitoring instrument is sensitive to those rates of change in densities

which would produce feedback reactivities (positive or negative) comparable to a postulated reactivity change in a particular phase of the accident analysis scenario.

Description of Requirements for Small Bundles

Further definition of the requirements, particularly for density and time resolutions, requires taking into account the specific purposes of the anticipated experiments. The description of the basis for selection of the specific values of requirements listed in Tables 1 through 4 must necessarily be limited to selected values, by way of illustration, in the limited time available. Further, the values of both requirements and projected capabilities are preliminary and are expected to change as the assessment is developed further.

In general the small bundle experiments are phenomenological tests. The small bundle experiments in SAREF will investigate such specific aspects of fuel pin behavior as:

(a) The probable fission-gas driven radial dispersal of unclad fuel in a loss-of-flow accident.

(b) The fission gas or fuel vapor driven radial dispersal of clad or unclad fuel during a power burst.

(c) The axial motion of molten fuel inside the cladding during an overpower situation.

(d) The location and coherence of cladding failure in an overpower situation.

(e) The ejection of fuel through cladding ruptures, with full sodium flow and with partially voided channels.

In order to investigate many of these phenomena it will be necessary to "see" what is happening in the molten region of the pins. For some it is also important to monitor the motion of the outer unmelted fuel which might be dispersed, for example, in the form of solid chunks. It therefore seems "acceptable" to have a width and depth resolution of one-third pin diameter, or about 0.25 cm. The "necessary" criterion for the width and depth resolution should be about the same because if one relaxes the above criterion one can no longer discriminate between pins and channels. If one wants to monitor the different microstructural regions in the pin a width and depth resolution of about 1/10 of a fuel pin diameter would be required, and this value is used as the "desirable" requirement. The height resolution is nominally set in correspondence with one or several fuel pellet heights.

The rate of fuel density changes in a molten pin region during an overpower excursion; that is, a slow transient can be determined from calculations with the PLUTO code and to a certain extent from experimental evidence. Typical PLUTO calculations show that the fuel density in the molten fuel region changes by more than 25% in 20 msec. Since one can relate this to the original smear density in the pin of about 8 g/cm^3, the rate of fuel density change (Table 4) is 0.1 g/cm^3/msec. This is taken as both an acceptable and necessary requirement. The desirable requirement is taken arbitrarily as one-half. Information from the H5 overpower experiment in TREAT indicated a larger rate of fuel density change.

The disintegration of fuel in a power burst is expected to lead to a radially homogeneous fuel distribution; i.e., the fuel density changes roughly from 0 to 4 g/cm^3 in the channel and from 8 to 4 g/cm^3 in the pin. Power burst situations may last up to 20 msec. The radial pin dispersal probably lasts for a much shorter time; a conservative time duration estimate is 10 msec. This would lead to a rate of fuel density change (Table 4) of 4 g/cm^3 over the 10 msec or 0.4 g/cm^3/msec. This is taken, likewise, as both an acceptable and necessary value, with the desirable value arbitrarily one-half.

The values for mass resolutions (in Table 4) for the fuel are obtained by multiplying the appropriate rate of fuel density change with the resolution volume (from Table 2) and the resolution time (from Table 3) from the respective category (necessary, acceptable, or desirable).

Description of Requirements for Single and Multisubassemblies

The type of experiments anticipated in single subassembly or multisubassembly size fuel bundles emphasize the capability to differentiate between noncoherent events and detect larger-scale phenomena. Less demanding time and space resolution criteria, with respect to monitoring material density changes, are required in studies of larger scale and/or slower phenomena such as: subassembly blockages, meltthrough of subassembly cans, and gross rearrangement or extended motion of subassembly materials. However, these studies have more demanding requirements in regard to overall instrumentation field of view.

To arrive at the rates of change in material densities required to affect significant positive or negative reactivity feedback, existing accident analysis calculations which describe the transient power history in reference LMFBR core-disruption accidents were examined.

One such accident analysis considered was that of a hypothetical transient undercooling (TUC) accident for a CRBR core. The reactivity and power traces calculated with the SAS code show that the first rapid reactivity and power decrease is due to fuel dispersal in several subassemblies. For a short time this fuel dispersal (calculated by the SLUMPY routine of the SAS code) leads to a large reactivity decrease. In order to verify the existence of such a dispersal mechanism one should be able to monitor this event quite precisely. From a SAS analysis of the fuel-steel mixture distributions at two different times, the average change in fuel density is found to be 0.48 g/cm^3. Since this change occurs during 26 msec, the rate of density change per msec is approximately 0.02 g/cm^3/msec. This can be

regarded as both an "acceptable" and "necessary" requirement for the case of a slow transient for both SS and MS. Further, since the fuel dispersal event lasted about 40 msec, 5 msec is regarded as an acceptable resolution time.

Another accident analysis considered was that of a transient overpower accident, likewise for a CRBR core. The fuel density distributions during this accident were calculated with the PLUTO code. The average absolute difference between the "total" fuel distributions at times 20 msec apart was approximately 0.4 g/cm^3. Thus the rate of density change is 0.02 g/cm^3/ msec, which corresponds to the above mentioned requirement.

Still another accident examined was that of a prompt critical excursion in a sodium-voided CRBR core in which a 50$/sec reactivity ramp at prompt critical was used and the disassembly calculation was performed with the VENUS code. The average absolute density change was determined by comparing the smear density distribution of the fuel-steel mixture over a major region of the core at the beginning of the disassembly calculation with that 4.75 msec later. The average fuel density change was 0.57 g/cm^3. With a time interval between the two configurations of 4.75 msec, the rate of fuel density change is 0.12 g/cm^3/msec. This rate of density change can be regarded as both an "acceptable" and "necessary" requirement for a fast or burst transient. In view of the 4.75 msec duration of the burst, 0.5 msec seems acceptable as a corresponding time resolution. Values of mass resolution are obtained as described previously.

Time does not allow for a comparably detailed definition of all the requirements established in the tables. However, before proceeding with other aspects of this preliminary material motion assessment, there is one further point to be noted, namely, the depth perception, rather than two-dimensional viewing, has been treated implicitly as an essential requirement. Two-dimensional viewing of large pin bundles cannot differentiate between signals resulting from changes in materials densities occuring either: (1) at the front, center, or far side of the bundle; or (2) homogeneously in the plane which is in a transverse direction to a two-dimensional detector array.

Projected Capabilities

In the preliminary assessment of instrument capabilities - to be compared with the experiment requirements - the initial emphasis has been place on the fuel motion assessment for multisubassembly and single-subassembly tests, and in particular whether in-core detectors could achieve the desired capability, or whether devices requiring slots within the reactor core are essential. This is due to the potentially significant impact of slots on both design concepts for SAREF presently under evaluation by ERDA. Their impact is most significant with respect to the MS test configurations, and the comparison of in-core and ex-core detectors has thus far been limited to this issue.

In the present assessment, the hodoscope has been taken as representative of the class of devices requiring slotted access through the core to the test section; subsequently, performance predictions for alternate ex-core devices (of which X-radiography and Fresnel plates are the primary candidates) will be evaluated. A final selection among the ex-core systems will depend upon which system is best able to meet or come close to meeting the fundamental requirements.

Hodoscope Evaluation

For the hodoscope, the field-of-view requirements for height and width in Table 1 can be met without difficulty by choice of design of collimator and detectors. (It is a separate question whether the most stringent requirements can be met in terms of impact of the required slot on the reactor and experiment design.) The depth requirement, however, requires a second hodoscope and slot, probably at 90°. Spatial resolution (Table 2) is generally adequately met.

Data collection time and time resolution (see Table 3) do not cause any difficulties; the most stringent criteria represent small extrapolations from current practice or from developments already underway.

The development of the density resolution capability for the hodoscope requires several intermediate steps. Extensive calculations were carried out that can only be briefly summarized here. The signal-to-background (S/B) detector response characteristics were determined for both SS and MS tests, using multigroup calculations in one-dimensional cylindrical geometry. S/B ratios were found to decrease when fuel is removed. As fuel is voided at the center of the test bundle, the S/B ratio decreases linearly with the number of pins removed. Also calculations show that S/B ratios in the range of 2 to 3.5 are possible for fuel monitoring in MS and SS size tests. These ratios are comparable or better than those achieved at TREAT, which suggests that the present techniques for hodoscope data visualizations and analysis may be applied to SAREF without extensive development.

Since the calculated results for the S/B ratio increases essentially linearly as pins are added to a test section, this indicates that hodoscope sensitivity can be extended from small bundles up to multisubassembly size tests. Further, since the calculations are based on a model which has been verified by determining measured parameters at TREAT, this lends confidence to scaling of data from TREAT to SAREF and places the estimates of sensitivity upon a reasonably sound foundation.

As indicated, the values of S/B ratio calculated provide a functional dependence on the cumulative total of fuel pins. This functional dependence can be translated into sensitivity as a function of the number of voided rings of fuel, beginning with a single pin at the center as the first "ring", and progressing outward to rings of 7, 19, etc., pins. In TREAT the current hodoscope sensitivity limit has been measured to be about 0.02 for S/B $\simeq$ 1 (corresponding to 50 mg of fuel in a single pin TREAT experiment). Based on this approximate sensitivity limit, and based on 100% density change* in a single volume element, the calculations for the SAREF hodoscope predict sensitivity thresholds corresponding to about 7 pins within the SS experiment and about 19 pins in the central subassembly of the MS experiment.

---

*The calculations, being derived from a one-dimensional model, only predict performance for full material voiding commencing at the center and propagating radially and uniformly outward.

These sensitivity threshold values, when converted to their mass equivalence, result in values of 25 gm and 80 gm, respectively, for the SS and MS test configurations, which is to be compared directly with the corresponding values of the requirements in Table 4. In the MS case the projected capability for fuel sensitivity is seen to approach the "acceptable" level of requirements. Although the projected capability in the SS case falls short of the "necessary" level of requirements, examination of several of the approximations made indicates a reasonable assurance that the necessary criterion can be met.

In-core Detector Evaluation

Consideration is being given in both SAREF conceptual designs to the use of in-core detectors. Specific provision must be made in either design to accommodate them. In the ANL design concept, provision is made for an instrument annulus surrounding the test section, within which it would be possible to place an in-core detector array for fuel motion monitoring during a transient. Each axial array about 50 in. in length, might consist of up to 50 discrete neutron detectors. This array then provides a 50-point axial profile of (fast) neutron population at the periphery of the test section. To achieve a high degree of azimuthal resolution, a large number of such axial arrays would be needed, requiring perhaps up to a total of 2500 detector channels. For the present purposes, the attendant design and engineering problems of accommodating such large numbers of signal cables, etc., are being ignored.

For the evaluation of the in-core detector capability, workable isotropic threshold detectors have been assumed as achievable and representing an upper limit projection of such detector capability. The axial profile generated from an in-core detector array has been calculated for the change due to 100% voiding of the central 15 cm height across a full MS test section. This is a volume of 21 liters, corresponding to about 100 kg of fuel. The profile is generated by some power normalization and is based on a comparison with the initial undisturbed profile prior to material motion.

There is a sizable component of the background which is caused by the contributions to the local population from neutrons not directly correlated with fuel in the test section. The signal/background ratio S_T/B for total signal over background has been calculated to be about 0.13. This composite signal is due to the net effects on neutron population at the detector produced by voiding of all fuel, coolant, and structure within the 15 cm height across the entire multisubassembly test section. If the purpose of monitoring with in-core detectors were to measure the combined effect of all materials, then the signal/background parameter of interest would be 0.13.

If in-core detectors are to be examined in terms of their ability to distinguish fuel from other materials in the test section, then a different "signal" to "background" condition applies. One must assume that there is some way of modeling the effects of coolant and structure on the fast neutron flux at the detectors. This is important because their effects are large. The S/B is estimated to increase to about 0.26 when only fuel is voided.

Without the advantage of in-reactor testing of detector configurations suitable to this application, it is difficult to ascribe a lower limit of sensitivity. Since the data processing codes will have to deal with rather small differences between large numbers, a high level of statistical accuracy will be required. If we assume that a sensitivity level of 0.01 in S/B can be achieved for in-core detectors, which is twice as good as been demonstrated for the hodoscope, then well over 10^8 cps per detector must be handled to achieve 0.1 msec time resolution with minimal confidence level.

To estimate the limiting level of fuel sensitivity, it is necessary to examine the response profile calculated for voiding of a single subassembly. It is estimated that voiding of fuel only in the central SS of a full MS experiment yeilds S/B of about 0.04. Although only one-fourth of the fuel (and one-fifth of the volume) was vacated from the full configuration, the calculated S/B dropped substantially (by a factor of six from 0.26 to 0.04); this decrement reflects the substantial shielding effect of fuel in the outer assemblies. Thus the mass sensitivity level associated with a S/B

value of 0.01 should be nearly that of a full subassembly, and corresponds to a volume of about 2.4 liters or 12 kg of fuel.

As can be seen from Table 4, this fails to meet the necessary fuel density resolution requirements by a large margin.

It should be emphasized that while in-core detectors may indeed be expected to provide sizable signal rates, the almost complete lack of directional or material discrimination (reflected in Tables 1 and 2) presents a formidable problem for interpretation. Also, these preliminary calculations were done with isotropic detectors, and it remains to be seen what improvement might be achievable with the directional detectors under development. In any case, their capability is not expected to alter the conclusion reached in this preliminary assessment.

Conclusion

The preliminary assessment described here has specifically addressed the question whether in-core detectors could achieve desired fuel motion monitoring capability, particularly for MS size tests, or whether devices requiring slots within the reactor are essential. The conclusion is clear that it would seriously compromise the future potential for meaningful experiments in SAREF to rely on in-core detectors as the primary devices. On the other hand, in-core detectors have the potential to supplement the ex-core detection devices and should continue under development and evaluation.

A number of additional factors that constitute important criteria to be evaluated as part of a complete assessment have not been discussed. These include, in addition to the monitoring of clad blockage and coolant voiding, such items as: (1) the impact of the detection devices on the reactor facility design and cost; (2) the relative feasibility or realizability of the candidate devices; and (3) the auxiliary capability for in-situ radiography and for pre- and posttransient monitoring that may be achievable with each candidate device.

Finally, I would like to point out that the work reported here is the result of a task force effort, which includes E. W. Barts, C. L. Beck, E. F. Bennett, W. A. Bezella, A. DeVolpi, A. B. Rothman, and H. Wider, all at ANL. In addition a supportive effort is underway at Sandia Laboratories, under cognizance of J. Powell, which will contribute toward completing this assessment.

TABLE 1. PRELIMINARY MATERIAL MONITORING ASSESSMENT

TRANSIENT FUEL MOTION DETECTION - FIELD OF VIEW

(TENTATIVE VALUES)

	REQUIREMENTS			PROJECTED CAPABILITIES			
	NECESSARY	ACCEPTABLE	DESIRABLE	HODOSCOPE	X-RADIOGRAPHY	FRESNEL	IN-CORE
HEIGHT, CM							
SB	130	180	280	✓			✓
SS	130	180	280	✓			✓
MS	130	180	280	✓			✓
WIDTH, CM							
SB	7	7	7	✓			*
SS	20	20	20	✓			*
MS	20	25	30	✓			*
DEPTH, CM							
SB	7	7	7	✓			**
SS	20	20	20	✓			**
MS	20	25	30	✓			**

✓ INDICATES ADEQUATE PROJECTED CAPABILITY.

* AZIMUTHAL COVERAGE AROUND INSTRUMENT THIMBLE.

** DOUBTFUL DEPTH (RADIAL) DISCRIMINATION.

TABLE 2. PRELIMINARY MATERIAL MONITORING ASSESSMENT

TRANSIENT FUEL MOTION DETECTION - SPATIAL RESOLUTION

(TENTATIVE VALUES)

	REQUIREMENTS			PROJECTED CAPABILITIES			
	NECESSARY	ACCEPTABLE	DESIRABLE	HODOSCOPE	X-RADIOGRAPHY	FRESNEL	IN-CORE
HEIGHT, CM							
SB	5	2.5	1.25	✓			
SS	10	5	2.5	✓			
MS	20	10	5	✓			✓
WIDTH, CM							
SB	0.25	0.25	0.07				
SS	1.5	1.5	0.5	✓			
MS	10	5	2.5	✓			*15°
DEPTH, CM							
SB	0.25	0.25	0.07				
SS	1.5	1.5	0.5	✓			
MS	10	5	2.5	✓			**
VOLUME, CM^3 (CYLINDRICAL)							
SB	0.25	0.12	0.005				
SS	18	9	0.5	✓			
MS	1600	200	25	✓			

* PROJECTED AZIMUTHAL COVERAGE. ** DOUBTFUL DEPTH (RADIAL) DISCRIMINATION.

TABLE 3. PRELIMINARY MATERIAL MONITORING ASSESSMENT

TRANSIENT FUEL MOTION DETECTION - TIME DEFINITION

(TENTATIVE VALUES)

	REQUIREMENTS			PROJECTED CAPABILITIES			
	NECESSARY	ACCEPTABLE	DESIRABLE	HODOSCOPE	X-RADIOGRAPHY	FRESNEL	IN-CORE
DURATION, SEC							
SB	30	45	60				
SS	30	45	60	✓			
MS	30	45	60	✓			✓
RESOLUTION, MSEC			I. NEAR STEADY STATE				
SB	1000	500	100				
SS	1000	500	100	✓			
MS	1000	500	100	✓			✓
			II. SLOW TRANSIENT				
SB	10	5	2				
SS	10	5	2	✓			
MS	10	5	2	✓			✓
			III. BURST				
SB	1	0.5	0.1				
SS	1	0.5	0.1	✓			
MS	1	0.5	0.1	✓			✓

TABLE 4. PRELIMINARY MATERIAL MONITORING ASSESSMENT

TRANSIENT FUEL MOTION DETECTION - DENSITY RESOLUTION

(TENTATIVE VALUES)

	REQUIREMENTS			PROJECTED CAPABILITIES			
	NECESSARY	ACCEPTABLE	DESIRABLE	HODOSCOPE	X-RADIOGRAPHY	FRESNEL	IN-CORE
RATE OF DENSITY CHANGE, GM/CM^3/MSEC (FOR SLOW TRANSIENT)							
SB	0.1	0.1	0.05				
SS	0.02	0.02	0.01				
MS	0.02	0.02	0.01				
MASS EQUIVALENT, GM (FOR SLOW TRANSIENT)							
SB	0.25	0.06	0.0005				
SS	3	0.9	0.01	25*			
MS	320	20	0.5	80**			12,000
RATE OF DENSITY CHANGE, GM/CM^3/MSEC (FOR BURST)							
SB	0.4	0.4	0.2				
SS	0.12	0.12	0.06				
MS	0.12	0.12	0.06				
MASS EQUIVALENT, GM (FOR BURST)							
SB	0.1	0.024	0.0001				
SS	2	0.5	0.003	25*			
MS	200	12	0.15	80**			12,000

NUMBER OF DETECTORS VIEWING OBJECT VOLUME: = 3*; = 4**

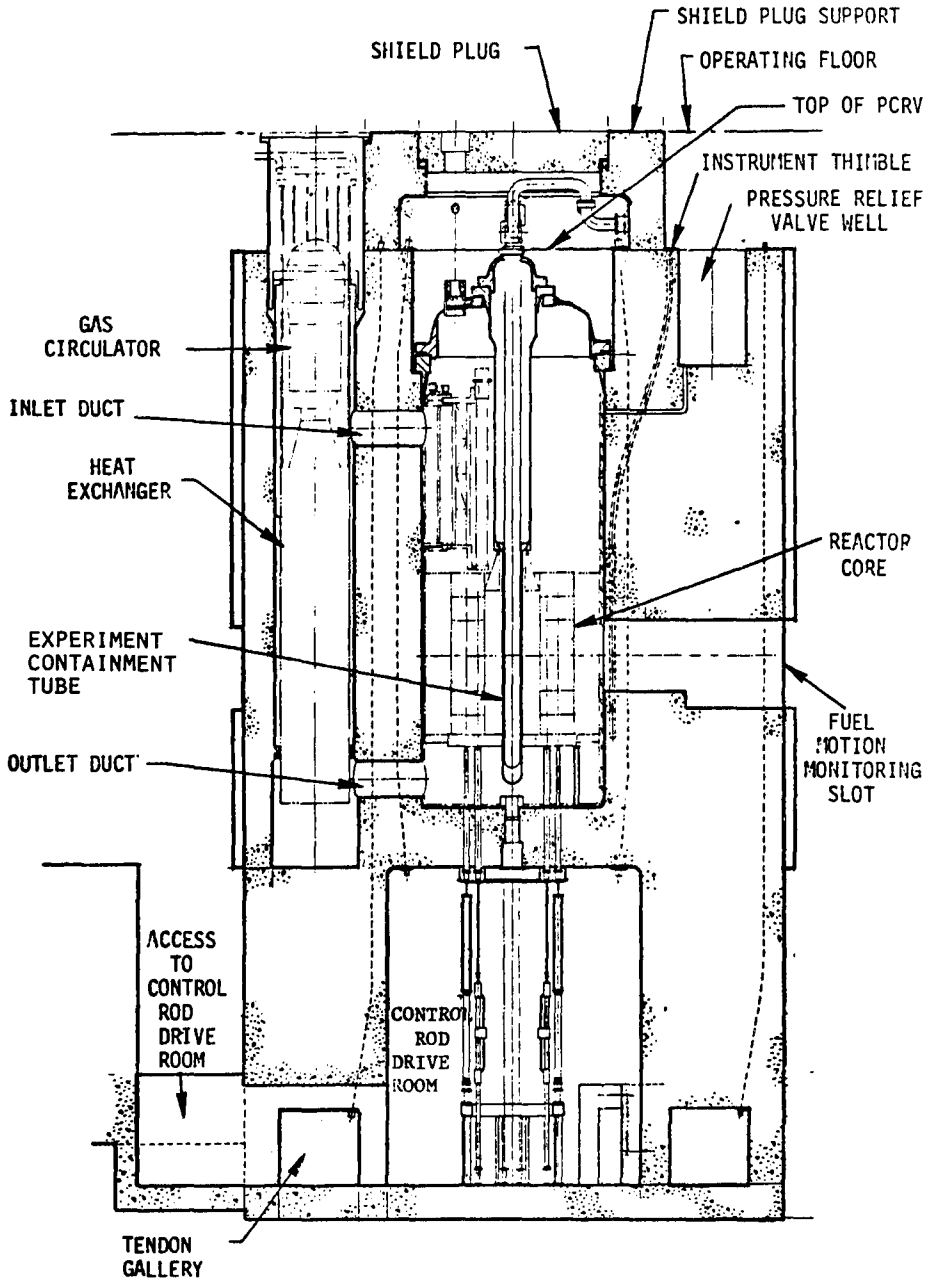

Figure 1. PCRV Vertical Section

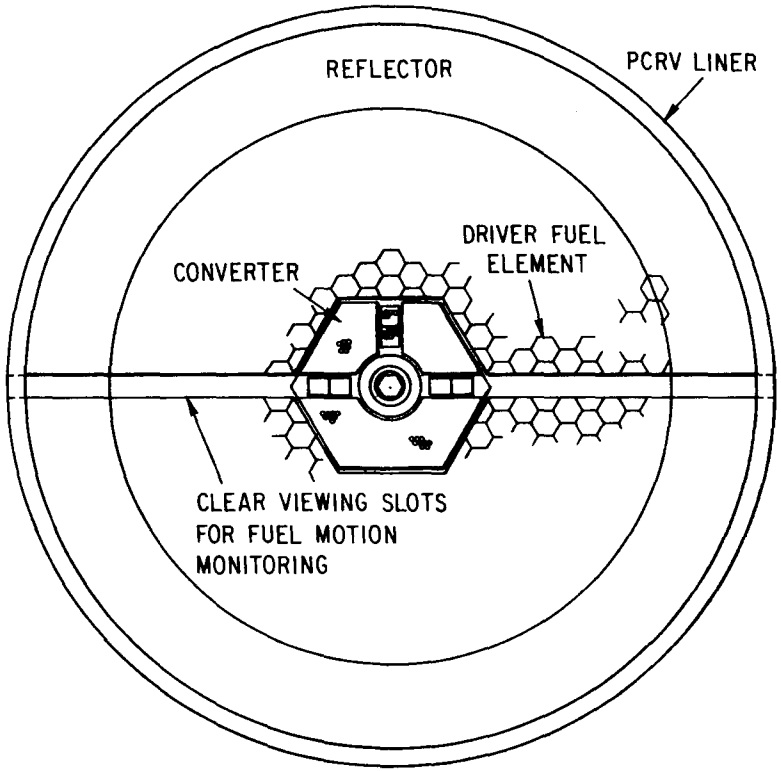

Figure 2. SAREF SS Schematic Core Cross Section

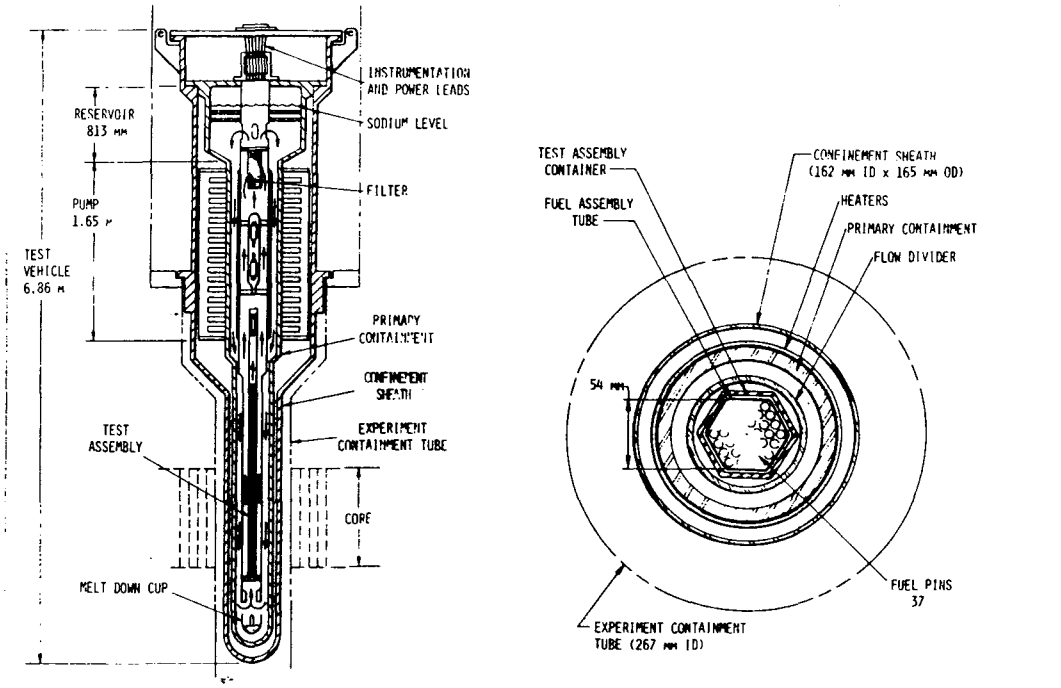

(a) Schematic

(b) Small-bundle, Test-assembly Cross Section

Figure 3. LMFBR Package Loop

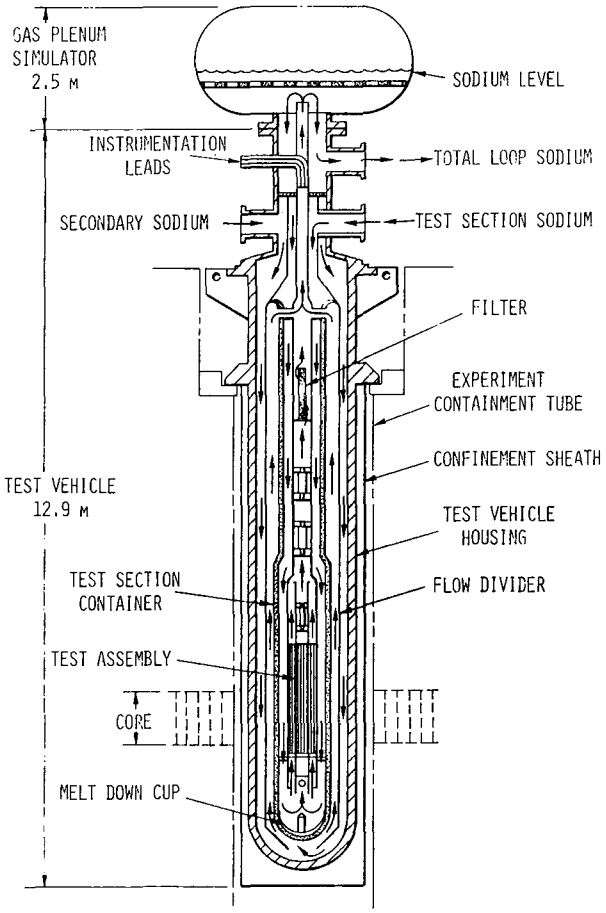

Figure 4. LMFBR Integral Test-Vehicle Schematic

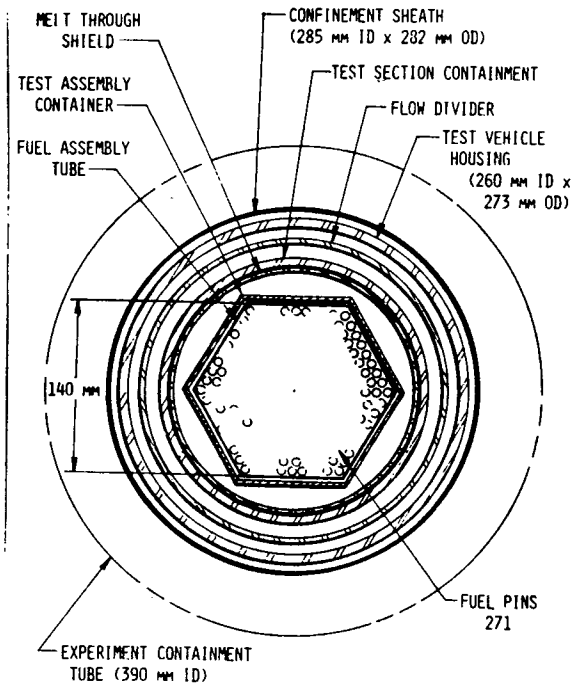

(a) Single Subassembly Test Assembly (SS) Cross Section

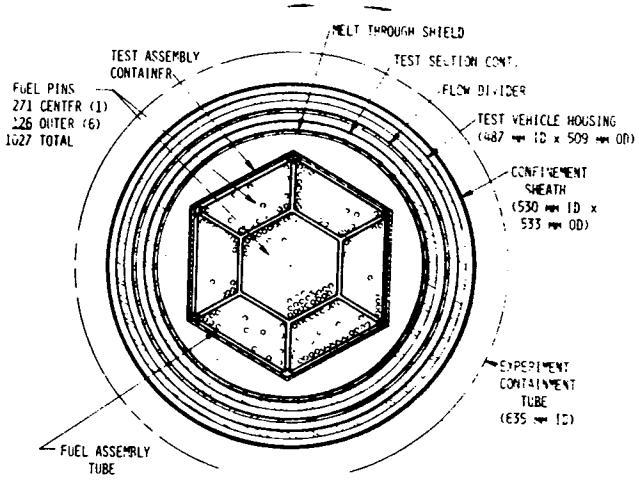

(b) Multi-subassembly Test Assembly (MS-4) Cross Section

Figure 5. LMFBR Integral Test Vehicle

- SUBASSEMBLY-TO-SUBASSEMBLY FAILURE PROPAGATION
- PROTOTYPIC FUEL FAILURE THRESHOLDS
- OVERPOWER TRANSIENTS, INCLUDING EFFECTS OF SUBASSEMBLY INCOHERENCE
- LOSS-OF-FLOW TRANSIENTS, INCLUDING EFFECTS OF SUBASSEMBLY INCOHERENCE AND INDUCED POWER BURST
- TRANSITION PHASE
- EFFECTS OF BUNDLE SIZE AND PERIOD ON FUEL-COOLANT INTERACTIONS
- FISSION-GAS EFFECTS ON FUEL DISPERSAL
- PAHR PHENOMENOLOGY

Figure 6. Experiment Classes

TRANSIENT FUEL MOTION DETECTION

1. FIELD OF VIEW

   HEIGHT/WIDTH/DEPTH

2. SPATIAL RESOLUTION

   HEIGHT/WIDTH/DEPTH/VOLUME

3. TIME DEFINITION

   DURATION

   TIME RESOLUTION

   NEAR STEADY STATE/SLOW TRANSIENT/BURST

4. DENSITY RESOLUTION

   RATE OF DENSITY CHANGE } SLOW TRANSIENT
   MASS EQUIVALENT }

   RATE OF DENSITY CHANGE } BURST
   MASS EQUIVALENT }

Figure 7. Material Monitoring Criteria for SAREF

Attendees

Ziya Akcasu
Argonne National Laboratory

Robert W. Albrecht
University of Washington

H. H. Barrett
University of Arizona

John P. Barton
Oregon State University

Edward W. Barts
Los Alamos Scientific Laboratory

George J. Berfins
Los Alamos Scientific Laboratory

Robert A. Beyerlein
Argonne National Laboratory

Frank Biggs
Sandia Laboratories

Paul B. Bleiweis
Los Alamos Scientific Laboratory

H. Bluhm
GPK/INR, Germany

James F. Boland
Argonne National Laboratory

Jay E. Boudreau
Los Alamos Scientific Laboratory

Albert L. Bowman
Aerojet Nuclear Co.

John O. Bradfute
General Electric Company

Richard L. Brehm
University of Arizona

Larry F. Burdge
Aerojet Nuclear Co.

Gary Carlson
Sandia Laboratories

Philip Champney
Physics International Co.

Larry M. Choate
Sandia Laboratories

R. L. Coats
Sandia Laboratories

Jean Costa
C. E. A., France

Samson A. Cox
Argonne National Laboratory

Dennis Damen
University of Washington

Sanders R. Dolce
Sandia Laboratories

A. DeVolpi
Argonne National Laboratory

Stephen A. Dupree
Sandia Laboratories

L. Roger Edwards
Sandia Laboratories

Albert E. Evans
Los Alamos Scientific Laboratory

Charles L. Fink
Argonne National Laboratory

George Fisher
Brookhaven National Laboratory

Attendees (Cont)

Jerry Griffith
U. S. Energy Research and Development Administration

John A. Halbleib
Sandia Laboratories

Ki S. Han
Los Alamos Scientific Laboratory

W. H. Hannum
U. S. Energy Research and Development Administration

K. R. Hessel
Sandia Laboratories

T. Hikido
Westinghouse Hanford Co.

Charles Kelber
U. S. Nuclear Regulatory Commission

John G. Kelly
Sandia Laboratories

David Lennox
Argonne National Laboratory

Francis E. Levert
Argonne National Laboratory

Richard A. Lewis
Argonne National Laboratory

Debu Majumdar
Brookhaven National Laboratory

John W. Mandler
Aerojet Nuclear Co.

John F. Marchaterre
Argonne National Laboratory

Ralph W. Marshall, Jr.
Aerojet Nuclear Co.

David A. McArthur
Sandia Laboratories

James McKenzie
Sandia Laboratories

Orlo McNary
Argonne National Laboratory

R. Leo McVean
Argonne National Laboratory

R. H. Meservey
Aerojet Nuclear Co.

Keiichi Mochizuki
PNC, Japan

F. M. Morris
Sandia Laboratories

J. W. Motz
National Bureau of Standards

John Orndoff
Los Alamos Scientific Laboratory

Joseph R. Parker
Los Alamos Scientific Laboratory

R. S. Peckover
U. K. Atomic Energy Authority

Dean R. Pedersen
Argonne National Laboratory

Jeffrey S. Philbin
Sandia Laboratories

Karl G. Porges
Argonne National Laboratory

Attendees (Cont)

Lawrence D. Posey
Sandia Laboratories

James E. Powell
Sandia Laboratories

James H. Renken
Sandia Laboratories

E. A. Rhodes
Argonne National Laboratory

L. N. Rib
U.S. Nuclear Regulatory Commission

J. W. Rogers
Aerojet Nuclear Co.

P. O. Rogers, Jr.
Sandia Laboratories

David Rose
Argonne National Laboratory

Paul Sasa
University of New Mexico

T. R. Schmidt
Sandia Laboratories

Robert L. Seale
University of Arizona

Bal Raj Sehgal
Electric Power Research Institute

Richard Simms
Argonne National Laboratory

A. W. Snyder
Sandia Laboratories

Bruce W. Spencer
Argonne National Laboratory

K. Terry Stalker
Sandia Laboratories

George S. Stanford
Argonne National Laboratory

William E. Stein
Los Alamos Scientific Laboratory

Michael G. Stevenson
Los Alamos Scientific Laboratory

Roy G. Stewart
Argonne National Laboratory

James G. Stone
U.S. Nuclear Regulatory Commission

W. H. Sullivan
Sandia Laboratories

A. Tattegrain
C.E.A. France

Steven V. Teague
ITRI

Walter Timmerman
General Electric Company

O. Tretiakoff
C.E.A., France

Joseph P. Tylka
Argonne National Laboratory

Jack V. Walker
Sandia Laboratories

David C. Williams
Sandia Laboratories

Robert W. Wright
U.S. Nuclear Regulatory Commission

DISTRIBUTION:

Ziya Akcasu
Argonne National Laboratory
9700 South Cass Avenue
Argonne, IL 60439

R. W. Albrecht
Department of Nuclear Engineering
University of Washington
Seattle, WA 98195

Prof. H. H. Barrett
Optical Sciences Center
University of Arizona
Tucson, AZ 85721

J. P. Barton
Radiation Center
Oregon State University
Corvallis, OR 97331

Edward W. Barts
Los Alamos Scientific Laboratory
P. O. Box 1663
Los Alamos, NM 87545

G. J. Berzins
Los Alamos Scientific Laboratory
P. O. Box 1663
Los Alamos, NM 87545

R. A. Beyerlein
Applied Physics Division
Argonnel National Laboratory
9700 South Cass Avenue
Argonne, IL 60439

P. B. Bleiweis
Los Alamos Scientific Laboratory
P. O. Box 1663
Los Alamos, NM 87545

H. Bluhm
KERNFORSCHUNGSZENTRUM KSRISRUHE
Institut fur Neutronenphysik und Reaktortechnik
Postfach 3640
West Germany

J. F. Boland
P. O. Box 2528
Argonne National Laboratory, West
Idaho Falls, ID 83401

J. E. Boudreau
MS 616
Los Alamos Scientific Laboratory
P. O. Box 1663
Los Alamos, NM 87545

A. L. Bowman
Aerojet Nuclear Company
550 Second street
Idaho Falls, ID 83401

J. O. Bradfute
Dynamics and Safety
General Electric Corporation
310 De Guigne Drive
Sunnyvale, CA 95086

R. L. Brehm
Department of Nuclear Engineering
College of Engineering
University of Arizona
Tucson, AZ 85719

L. F. Burdge
Aerojet Nuclear Company
550 Second Street
Idaho Falls, ID 83401

J. Costa
Commissariat A L'Energie Atomique
Centre D'Etudes Nucleaires de Grenoble
France

S. A. Cox
Applied Physics Division
Argonne National Laboratory
9700 South Cass Avenue
Argonne, IL 60439

D. Damen
Nuclear Engineering Department
University of Washington
Seattle, WA 98195

A. DeVolpi
Reactor Analysis & Safety Division
Argonne National Laboratory
9700 South Cass Avenue
Argonne, IL 60439

A. E. Evans
MS 540
Los Alamos Scientific Laboratory
Los Alamos, NM 87545

C. L. Fink
Reactor Analysis & Safety Division
Argonne National Laboratory
9700 South Cass Avenue
Argonne, IL 60439

G. J. Fisher
Fast Reactor Safety Division
Department of Applied Science
Brookhaven National Laboratory
Bldg 130
Upton, NY 11973

J. D. Griffith, Chief
Fast Reactor Safety Branch
Division of Reactor Research and Development
US Nuclear Regulatory Commission
Washington, DC 20555

DISTRIBUTION: (cont)

K. S. Han
MS 660
Los Alamos Scientific Laboratory
P. O. Box 1663
Los Alamos, NM 87545

W. H. Hannum
Assistant Director for Reactor Safety
Division of Reactor Research and Development
US Nuclear Regulatory Commission
Washington, DC 20555

T. Hikado
Westinghouse-Hanford
Richland, WA 99352

C. N. Kelber
Ass't Dir. for Advanced Reactor Safety Research
Division of Reactor Safety Research
U. S. Nuclear Regulatory Commission
Washington, DC 20555

David Lennox
Applied Physics Division
Argonne National Laboratory
9700 South Cass Avenue
Argonne, IL 60439

F. E. Levert
Reactor Analysis & Safety Division
Argonne National Laboratory
9700 South Cass Avenue
Argonne, IL 60439

R. A. Lewis
Applied Physics Division
Argonne National Laboratory
9700 South Cass Avenue
Argonne, IL 60439

Debaprasad Majumdar
Fast Reactor Safety Division
Department of Applied Science
Brookhaven National Laboratory
Bldg. 130
Upton, NY 11973

J. W. Mandler
Aerojet Nuclear Company
550 Second Street
Idaho Falls, ID 83401

J. F. Marchaterre
Reactor Analysis & Safety Division
Argonne National Laboratory
9700 South Cass Avenue
Argonne, IL 60439

R. W. Marshall, Jr.
Aerojet Nuclear Company
550 Second Street
Idaho Falls, ID 83401

O. McNary
Argonne National Laboratory
9700 South Cass Avenue
Argonne, IL 60439

R. L. McVean
P. O. Box 2528
Argonne National Laboratory, West
Idaho Falls, ID 83401

R. H. Meservey
ARA-3
Aerojet Nuclear Company
550 Second Street
Idaho Falls, ID 83401

K. Mochizuki
MONJO Group
PNCFBR
Akasaka 1-9-13
Minato-KC, Tokyo 107
Japan

J. W. Motz
Center for Radiation Research
National Bureau of Standards
Washington, DC 20234

J. Orndoff
Los Alamos Scientific Laboratory
P. O. Box 1663
Los Alamos, NM 87545

J. R. Parker
Los Alamos Scientific Laboratory
P. O. Box 1663
Los Alamos, NM 87545

R. S. Peckover
U. K. Atomic Energy Authority
Research Group
Culham Laboratory
Oxfordshire, England

D. R. Pedersen
Argonne National Laboratories
9700 South Cass Avenue
Argonne, IL 60439

K. G. Porges
Applied Physics Division
Argonne National Laboratory
9700 South Cass Avenue
Argonne, IL 60439

E. A. Rhodes
Reactor Analysis & Safety Division
Argonne National Laboratory
9700 South Cass Avenue
Argonne, IL 60439

DISTRIBUTION: (cont)

L. N. Rib
Chief, Experimental Fast Reactor Safety
Research Branch
Division of Reactor Safety Research
U. S. Nuclear Regulatory Commission
Washington, DC 20555

J. W. Rogers
Aerojet Nuclear Company
550 Second Street
Idaho Falls, ID 83401

David Rose
Reactor Analysis & Safety Division
Argonne National Laboratory
9700 South Cass Avenue
Argonne, IL 60439

Paul Sosa
Nuclear Engineering Department
University of New Mexico
Albuquerque, NM 87131

R. L. Seale
Department of Nuclear Engineering
College of Engineering
University of Arizona
Tucson, AZ 85719

B. R. Sehgal
Electric Power Research Institute
P. O. Box 10412
Palo Alto, CA 94303

Richard Simms
Reactor Analysis & Safety Division
Argonne National Laboratory
9700 South Cass Avenue
Argonne, IL 60439

B. W. Spencer
Reactor Analysis & Safety Division
Argonne National Laboratory
9700 South Cass Avenue
Argonne, IL 60439

G. S. Stanford
Reactor Analysis & Safety Division
Argonne National Laboratory
9700 South Cass Avenue
Argonne, IL 60439

W. E. Stein
Los Alamos Scientific Laboratory
P. O. Box 1663
Los Alamos, NM 87545

M. G. Stevenson
MS 616
Los Alamos Scientific Laboratory
P. O. Box 1663
Los Alamos, NM 87545

R. G. Stewart
Argonne National Laboratory
9700 South Cass Avenue
Argonne, IL 60439

J. G. Stone
Reactor Safety Research
U. S. Nuclear Regulatory Commission
Washington, DC 20555

A. Tattegrain
C. E. A.
Centre D'Etudes
Nucleaires de Cadarache
DeSaclay, France

S. V. Teague
IIT Research Institute
10 West 35th Street
Chicago, IL 60616

W. J. Timmerman
General Electric Corporation
310 De Guigne Drive
Sunnyvale, CA 94086

O. Tretiakoff
C. E. A.
Centre D'Etudes
Nucleaires de Cadarache
DeSaclay, France

J. P. Tylka
Reactor Analysis & Safety Division
Argonne National Laboratory
9700 South Cass Avenue
Argonne, IL 60439

R. W. Wright (10)
Division of Reactor Safety Research
U. S. Nuclear Regulatory Commission
Washington, DC 20555

M. Silberberg
Division of Reactor Safety Research
Office of Nuclear Regulatory Research
U. S. Nuclear Regulatory Commission
Washington, DC 20555

L. S. Rubensteign
Program Support Branch
Office of Nuclear Regulatory Research
U. S. Nuclear Regulatory Commission
Washington, DC 20555

T. P. Specis
LMFBR Branch
Office of Nuclear Regulatory Research
U. S. Nuclear Regulatory Commission
Washington, DC 20555

DISTRIBUTION: (cont)

Y. S. Tang
Westinghouse Corporation
Advanced Reactors Division
P. O. Box 158
Madison, PA 15663

General Electric Corporation (4)
310 De Guigne Drive
Sunnyvale, CA 94086
Attn: A. S. Gibson, Manager,
Product Engineering
R. Greebler, Manager
Reactor Studies
J. E. Mott, Senior Engineer,
Dynamics & Safety
M. I. Temme, Manager
Safety Analysis

Division of Military Applications (2)
Office of Safety and Facilities
USERDA
Washington, DC 20545
Attn: R. T. A. Bredderman
H. M. Busey

Reactor Safety Research Coordination (4)
USERDA
Washington, DC 20545
Attn: R. W. Barber, Acting Dir. (3)
T. E. McSpadden, Proj. Manager

J. R. Roeder, Director
Operational Safety Division
USERDA/ALO
Albuquerque, NM 87115

C. B. Quinn
Special Programs Division
USERDA/ALO
Albuquerque, NM 87115

Argonne National Laboratory (5)
9700 South Cass Avenue
Argonne, IL 60439
Attn: Robert Avery
R. G. Matlock
A. J. Goldman
L. Baker, Jr.
C. E. Dickerman

University of California
Energy and Kinetics Department
5530 Boelter Hall
Los Angeles, CA 90024
Attn: W. E. Kastenberg

A. W. Cronenberg
Department of Nuclear Engineering
University of New Mexico
Albuquerque, NM 87131

2 W. J. Howard
1000 G. A. Fowler
1100 C. D. Broyles
1111 S. R. Dolce
1112 P. O. Rogers, Jr.
1126 G. L. Ogle
1130 H. E. Viney
1133 R. D. Statler
1134 J. A. Brammer
1200 W. A. Gardner
1280 T. B. Lane
1300 D. B. Shuster
1424 J. S. Philbin
2541 K. T. Stalker
2542 K. R. Hessel
3242 P. E. Brewer
4010 C. Winter
5000 A. Narath
5100 J. K. Galt
5110 F. L. Vook
5120 G. J. Simmons
5130 G. A. Samara
5160 W. Herrmann
5200 E. H. Beckner
5230 M. Cowan, Jr.
5231 S. A. Dupree
5231 J. H. Renken
5231 J. A. Halbleib
5232 L. D. Posey
5240 G. Yonas
5271 J. H. Renken
5400 A. W. Snyder
5410 D. J. McCloskey
5411 D. A. Dahlgren
5420 J. V. Walker
5421 T. R. Schmidt
5422 R. L. Coats
5422 H. G. Plein
5422 J. B. Rivard
5422 D. J. Sasmor
5422 D. C. Williams
5423 J. E. Powell (50)
5423 G. A. Carlson
5423 L. M. Choate
5423 L. R. Edwards
5423 J. G. Kelly
5423 D. A. McArthur
5423 A. R. Phillips
5423 H. L. Scott
5423 W. H. Sullivan
5423 S. A. Wright
5424 J. A. Reuscher
5424 F. M. Morris
5424 P. S. Pickard
5430 R. M. Jefferson
5433 J. M. McKenzie
5440 H. D. Sivinski
5700 J. H. Scott
5800 R. S. Claassen
5820 R. L. Schwoebel

DISTRIBUTION: (cont)

5840 D. M. Schuster
8300 B. F. Murphey
8310 R. H. Meinken
8314 G. J. Thomas
8266 E. A. Aas (2)
3141 C. A. Pepmueller (Actg.) (5)
3151 W. L. Garner (3)
For ERDA/TIC (Unlimited Release)
ERDA/TIC (25)
(R. P. Campbell, 3171-1)

☆ US GOVERNMENT PRINTING OFFICE: 1976—677-358/505